

University of Sheffield

Investigation of the properties of MHD waves in the presence of non-uniform equilibria and flow using a unique numerical approach



Samuel Skirvin

Supervisors: Dr Viktor Fedun & Dr Gary Verth

A report submitted in partial fulfilment of the requirements
for the degree of doctor of philosophy in solar and space plasma physics

in the

Department of Automatic Control and Systems Engineering

April 25, 2022

Acknowledgements

First of all, I am grateful for the financial support provided by the Science and Technology Facilities Council (STFC UK) for funding the research presented in this thesis.

I extend my most sincere gratitude to my academic supervisors, Dr Viktor Fedun & Dr Gary Verth, for their fantastic support throughout my postgraduate journey. All that I have learned about research I owe to them.

Thank you to those that have contributed to my working environment over the course of this PhD project, whether that be in the office or at home. Thank you and good luck to those who are still on their postgraduate journeys: Matt, Max and Suzana. Thank you to those who have already moved on: Farhad, Fionnlagh and Jamie. In particular thank you to Farhad and the SunPy community for teaching me how to code using Python.

Thank you to my family who have had a major role in getting me to this point. Finally, thank you to my friends, both academic and non-academic, in particular to Lauren, for being by my side and someone who has made this PhD journey much less stressful than it otherwise would have been.

Declaration

I hereby declare that except where specific reference is made to the work of others, the contents of this dissertation are original and have not been submitted in whole or in part for consideration for any other degree or qualification in this, or any other university. All sentences or passages quoted in this document from other people's work have been specifically acknowledged by clear cross-referencing to author, work and page(s). Any illustrations that are not the work of the author of this report have been used with the explicit permission of the originator and are specifically acknowledged. I understand that failure to do this amounts to plagiarism and will be considered grounds for failure.

Name:

Signature:

Date:

Summary

In this thesis we have developed a numerical eigensolver, which is capable of obtaining the magnetoacoustic wave solutions of a given equilibrium in either a Cartesian or cylindrical geometry, for which it is applied to a number of different case studies in the context of waveguides in the solar atmosphere. The eigensolver is tested against known analytical results, with increasing complexity, where the previously obtained solutions are correctly retrieved. The equilibrium is allowed to be symmetrically non-uniform in the internal region of the waveguide, whereas the external region must be uniform. The development of this eigensolver has endless possibilities and greatly advances investigations of previous analytical studies.

Previous analytical studies of magnetoacoustic waves in solar waveguides have been restricted to consider only a limited selection of possible equilibria, such that a mathematical analysis can be conducted. If an equilibrium is too complex, an analytical description breaks down and a relationship describing the wave dispersion cannot be obtained. The work presented in this thesis aims to bridge the gap between realistic modelling of solar waveguides and providing a description of the waves that can propagate. In Chapter 2 we introduce the numerical eigensolver and describe the physics of the algorithm, along with the fundamental properties of MHD waves which it relies on. Additionally, we discuss potential avenues to improve the eigensolver that were not possible within the time frame of this project. Within the context of applying this numerical eigensolver, we have made an original contribution to knowledge in three areas:

- In Chapter 3 “The effect of non-uniform plasma density and flow on magnetoacoustic wave modes in a magnetic slab geometry”, we test the numerical eigensolver against previously obtained results for magnetoacoustic waves in photospheric and coronal slabs. Modelling the waveguide in a Cartesian geometry, we then extend this study to consider a non-uniform plasma with a density modelled as a series of Gaussian profiles and also a $\text{sinc}(x)$ function. The analysis is conducted under both photospheric and coronal conditions with the resulting eigenfunctions displayed for both scenarios. A magnetic slab in the presence of a non-uniform internal background plasma flow is then presented for which the governing equations are derived, eigenvalues obtained and eigenfunctions displayed. The implications that these results may have for observational interpretations of wave modes in the solar atmosphere is discussed.
- In Chapter 4 “The effect of non-uniform plasma density and flow on magnetoacoustic wave modes in a magnetic cylinder geometry”, we conduct a similar analysis to that presented in the previous chapter, however with a focus on the wave properties when the waveguide is modelled as a magnetic cylinder. The numerical eigensolver is again tested against previously obtained analytical results of a uniform cylinder before modelling the plasma density and background flow inside the waveguide as spatially non-uniform. The eigenfunctions are again obtained which then allows both a 2D and 3D visualisation of the perturbations to be shown. A discussion about the effect that a non-uniform equilibrium has on the perturbed eigenfunctions

is presented, with a focus on the possible onset of instabilities, comparison to previous similar studies and the implications for observational results.

- In Chapter 5 “Effect of non-linear twist and rotational flow on MHD wave modes of a magnetic cylinder”, we use the numerical eigensolver to retrieve the solutions of a more complicated scenario investigating a twisted magnetic flux tube. The previously obtained analytical results are retrieved and our analysis compliments that of previous studies by considering the modified continua due to the twisted magnetic field. We then investigate the wave modes that can exist in a rotating flux tube under both coronal and photospheric conditions where the rotational flow is modelled using a linear profile. This analysis is further extended to investigate the effect that a nonlinear rotational flow has on the properties of MHD waves and the resulting continuum regions. In both cases the eigenfunctions are calculated and we find that in the presence of a background rotational flow under photospheric conditions, the slow surface kink mode and the fast surface kink mode in the thin flux tube limit appear indistinguishable to observers.

These findings have implications for the theory of MHD waves in non-uniform plasmas and their use in providing accurate estimates of local plasma properties when used as a proxy for atmospheric-seismology.

We summarise our findings and discuss potential further investigations and improvements in Chapter 6.

Contents

1	Introduction	1
1.1	The Sun	2
1.2	The solar atmosphere	3
1.3	Ideal MHD equations	5
1.4	MHD waves in uniform plasmas of infinite extent	7
1.4.1	Magnetoacoustic waves	8
1.4.2	Alfvén waves	9
1.5	Analytical modelling of solar MHD waveguides	9
1.6	MHD waves in uniform waveguides	10
1.7	MHD waves in non-uniform waveguides	17
1.7.1	Governing equations for a non-uniform cylinder	17
1.7.2	Continuum modes	20
2	Numerical eigensolver	22
2.1	Obtaining an equilibrium	22
2.2	Magnetic Slab (Cartesian geometry)	23
2.2.1	Resonance locations	29
2.3	Magnetic Cylinder (cylindrical geometry)	31
2.4	Summary	32
3	MHD waves in non-uniform magnetic slabs	34
3.1	Introduction	35
3.2	Recovering previous analytical results	37
3.2.1	Uniform magnetic slab	37
3.2.2	Uniform magnetic slab with steady background plasma flow	38
3.3	Non-uniform density magnetic slab	40
3.3.1	Coronal non-uniform density magnetic slab case study	43
3.3.2	Photospheric non-uniform density magnetic slab case study	47
3.4	Uniform magnetic slab with a non-uniform background plasma flow	51
3.5	Summary & Discussion	57
4	MHD waves in non-uniform magnetic flux tubes	60
4.1	Introduction	61
4.2	Governing equations	62
4.3	Comparison with known solutions	64
4.3.1	Uniform magnetic cylinder	64
4.3.2	Magnetic cylinder with steady flow	65

4.4	Inhomogeneous plasma density	66
4.4.1	Photospheric conditions	68
4.4.2	Coronal conditions	71
4.5	Inhomogeneous flow in a coronal cylinder	79
4.6	Summary & Discussion	85
5	MHD waves in twisted and rotating flux tubes	87
5.1	Introduction	88
5.2	Governing equations	89
5.3	Linear magnetic twist	90
5.4	Linear rotational plasma flow	93
5.4.1	Rotating cylindrical magnetic flux tube under coronal conditions	94
5.4.2	Rotating cylindrical magnetic flux tube under photospheric conditions	100
5.5	Non-linear rotational plasma flow in a photospheric flux tube	105
5.5.1	Fixed azimuthal flow profile	108
5.5.2	Fixed azimuthal flow amplitude	111
5.6	Summary	111
6	Conclusions & Outlook	114
6.1	Future work	116
	Bibliography	117
	Appendices	132
A	Derivation of governing equation for a non-uniform flow in a magnetic slab	133

List of Figures

1.1	Sun’s structure. The distinct internal and atmospheric layers are labelled, along with some notable features observed in the solar atmosphere. Image courtesy of NASA.	3
1.2	Schematic diagram showing examples of how to model magnetic waveguides in the solar atmosphere analytically. (a) A magnetic waveguide in a Cartesian coordinate system can be modelled by a uniform magnetic slab, where the magnetic field is shown by the red arrows. (b) A magnetic waveguide in a cylindrical coordinate system is modelled by a uniform magnetic cylinder. The plasma both inside and outside the waveguide is uniform, however may be of different magnitudes. The magnetic field is assumed to be vertical and straight. If a background plasma flow is included, this is considered to be steady and aligned with the magnetic field. For a magnetic slab, the width of the waveguide is denoted as $2x_0$, whereas the radius of a magnetic cylinder is taken to be a	11
1.3	Schematic diagram of the magnetoacoustic wave modes observed in a magnetic cylinder taken from Jess et al. (2015). In this diagram the azimuthal wavenumber is denoted by n rather than m . The sausage ($m = 0$) and kink ($m = 1$) mode are shown as a periodic expansion/contraction and swaying motion of the waveguide, respectively. The solid lines outline the perturbation of the cylindrical waveguide with the corresponding arrows displaying the resulting velocity field. The magnetic field in all cases is considered vertical and uniform. A similar cartoon can be found in Morton et al. (2012).	14
1.4	The wave phase speeds plotted on a dispersion diagram. The solutions are obtained by solving the analytical dispersion relations from Edwin & Roberts (1982) for a magnetic slab and Edwin & Roberts (1983) for a magnetic cylinder. Solutions are shown for a magnetic slab under (a) photospheric conditions and (b) coronal conditions and also for a magnetic cylinder under (c) photospheric conditions and (d) coronal conditions. The blue dots denote the kink mode solutions whereas the red dots show solutions for the sausage mode.	16
2.1	Equilibrium profiles for uniform slab in coronal environment. (a) The density and characteristic speed profiles, (b) plasma properties including plasma pressure, temperature, magnetic field strength and total pressure. The dashed lines indicate the external value (outside the waveguide) for each variable shown in the separate panels.	24
2.2	Example of how initial sampling is divided up on dispersion diagram for numerical method as a function of (normalised) wavenumber for (a) phase speed (b) frequency. Only regions containing trapped modes are considered with narrower bands containing samples located closer together.	25

2.3 Example of how the numerical algorithm implements the bisection method when locating eigenvalues that are solutions to the governing differential equation. This case represents the sausage mode in a magnetic slab. In both plots sample can be seen indicated by the red dot on the top two panels, the resulting total pressure perturbation eigenfunction is shown in the bottom panel. In panel (a) the sample produces a value of $\delta\hat{P}_T$ which is positive, i.e. the value of \hat{P}_{Ti} at $x = x_0$ is greater than that of \hat{P}_{Te} at $x = x_0$. However, in panel (b), we have passed a known analytical solution (marked by the small red crosses) and the value of $\delta\hat{P}_T$ has changed sign. 27

2.4 Basic plot showing the obtained solutions, using a similar numerical technique to the eigensolver outlined in this chapter, applied to an ODE with complex coefficients. The yellow dots indicate the obtained roots of either the real part, or the imaginary component, of the governing function. These solutions trace out straight lines that intersect at the known full solution, denoted by the red cross. 30

3.1 A cartoon displaying a magnetic slab which is traditionally used to model waveguides in the solar atmosphere. The red arrows represent magnetic field lines and intend to show the different magnetic configurations in each regime internal and external to the waveguide. Blue arrows represent the vertical equilibrium velocity field which may be non-uniform in spatial coordinate x . The slab is assumed to be homogeneous and unbounded in the y -dimension. Parameters ρ , P , \mathbf{U}_0 and \mathbf{B} denote plasma density, pressure, background flow and magnetic field respectively. Subscripts i and e relate to internal and external properties respectively. The case studies considered in this Chapter investigate a spatially varying density profile $\rho_{0i}(x)$ and vertical background flow $U_{0i}(x)$. In reality any/all equilibrium background plasma variables are allowed to be inhomogeneous and the numerical eigensolver is capable of handling such a scenario. The specific spatial profiles considered in this chapter are shown in Figures (3.4), (3.9) and (3.12) for inhomogeneous equilibrium density and also Figure (3.15) for an inhomogeneous background flow. 36

3.2 The obtained numerical solutions for the case of a uniform magnetic slab under (a) photospheric conditions given by $c_e = 1.3c_i$, $v_{Ai} = 1.9c_i$ and $v_{Ae} = 0.8c_i$. (b) Coronal conditions given by $c_e = 0.4c_i$, $v_{Ai} = 1.2c_i$ and $v_{Ae} = 3c_i$. Red curves indicate the sausage mode solutions, whereas the blue curves show solutions for the kink mode. 37

3.3 The numerical solutions plotted on the dispersion diagram for a magnetic slab with a steady background plasma flow under (a) photospheric conditions given by $c_i = 0.67v_{Ai}$, $c_e = 0.75v_{Ai}$ and $v_{Ae} = 0$ with an external flow of $U_e = -0.15v_{Ai}$ and no internal flow. (b) Coronal conditions given by $c_i = 0.3v_{Ai}$, $c_e = 0.2v_{Ai}$ and $v_{Ae} = 2.5v_{Ai}$ with an internal flow of $U_i = 0.35v_{Ai}$ and no external flow. Same as Figure (3.2) but for a slab model with a steady background flow. 39

3.4 The profiles of internal non-uniform plasma density considered in this section. The density is modelled as a series of Gaussian's with varying inhomogeneity in a coronal slab. The profiles are normalised such that they possess their maximum value, which is equal to unity, at x_c . The width of the inhomogeneity is given by $W = 10^5$ (black), $W = 3$ (yellow), $W = 1.5$ (green), $W = 0.9$ (red). A spatial profile proportional to a sinc(x) (e.g. $\sin(x)/x$) function (blue) is also modelled. In all cases the density is discontinuous at the waveguide boundary and tends towards ρ_e (shown) at the boundary. The boundaries of the slab are located at $x = \pm 1$ and indicated by the red dashed lines. 41

3.5	Profiles of all plasma properties for the specific case of Gaussian density distribution with $W = 0.9$. Plots showing how the magnetic field, gas pressure, plasma temperature and total pressure along with the characteristic speeds of the system behave for the case of a non-uniform plasma density.	42
3.6	Dispersion diagrams showing the trapped solutions in a coronal slab with density structuring of a Gaussian form shown by the profiles in Figure 3.4. Here we show the cases when the width of the density profile, W , is, (a) $W \gg 2x_0$, (b) $W = 3$, (c) $W = 1.5$, (d) $W = 0.9$. The characteristic speeds at the boundaries are sub scripted 'B' with the maximum value of each characteristic speed denoted by the opposite edge of the shaded regions. The blue region corresponds to the slow continuum $c_{Ti}(x)$, green region the inhomogeneous sound speed band and orange region is the Alfvén continuum $v_{Ai}(x)$. Darker shades occur where there is an overlap of two inhomogeneous regions.	44
3.7	The dispersion diagram showing the eigenvalues for a spatial profile proportional to $\text{sinc}(x)$ under coronal conditions. Labels and colours are consistent with Figure 3.6.	45
3.8	Comparisons of the eigenfunctions \hat{P}_T and \hat{v}_x for all the spatial profiles considered in Figure 3.4. The colour scheme is consistent with Figure 3.4. (a) Fast sausage mode, (b) fast kink mode, (c) slow sausage mode and (d) slow kink mode. An eigenvalue of $k = 2$ was chosen for all plots. All curves are normalised such that their values are equal to unity at the boundary.	46
3.9	Density profile modelled as a Gaussian with a varying width in a photospheric slab. Width of inhomogeneity given by $W = 10^5$ (black), $W = 3$ (yellow), $W = 1.5$ (green), $W = 0.9$ (red). The spatial profile proportional to a $\text{sinc}(x)$ is shown by the blue curve. In all cases the density is discontinuous at the waveguide boundary and tends towards ρ_e (shown) at the boundary. The boundaries of the slab are indicated by the red dashed lines.	47
3.10	Dispersion diagrams showing the trapped solutions in a photospheric slab with density structuring given by a Gaussian profile. This figure is the same as Figure 3.6 with (a) $W \gg 2x_0$, (b) $W = 3$, (c) $W = 1.5$, (d) $W = 0.9$	48
3.11	Dispersion diagram for a spatial profile proportional to $\text{sinc}(x)$ (i.e. $\sin(x)/x$) under photospheric conditions.	49
3.12	Modified density profiles modelled as a Gaussian curve with a varying width in a photospheric slab. The width of the profile is given by $W = 10^5$ (black), $W = 3$ (yellow), $W = 2$ (magenta), $W = 1.5$ (green), $W = 1.25$ (indigo). In all cases the density is discontinuous at the waveguide boundary and tends towards ρ_e (shown) at the boundary. The boundaries of the slab are indicated by the red dashed lines.	50
3.13	Comparisons of the eigenfunctions \hat{P}_T and \hat{v}_x for all the photospheric spatial profiles considered in Figure 3.9. The colour scheme is consistent with Figure 3.9. (a) Eigenfunctions for the fast surface sausage mode, (b) eigenfunctions for the fast surface kink mode. An eigenvalue of $k = 2$ was chosen for all plots. In all plots the curves have been normalised such that their values are equal to unity at the boundary.	50
3.14	Comparisons of the eigenfunctions \hat{P}_T and \hat{v}_x for all the photospheric spatial profiles considered in Figure 3.12. The colour scheme is consistent with Figure 3.12. (a) Body sausage mode, (b) body kink mode. An eigenvalue of $k = 3$ was chosen for all plots. All curves normalised such that their values are equal to unity at the boundary.	51

- 3.15 Background plasma flow modelled as a Gaussian profile with a varying width in a uniform coronal slab. Width of inhomogeneity given by $W = 10^5$ (black), $W = 3$ (yellow), $W = 2.5$ (dark blue), $W = 2$ (magenta), $W = 1.75$ (red), $W = 1.5$ (green) and $W = 1.25$ (cyan). In all cases the flow is discontinuous at the waveguide boundary. The boundaries of the slab are indicated by the red dashed lines. The maximum flow speed is 0.3 such that the flow is both subsonic ($c_i = 1$) and sub Alfvénic ($v_{Ai} = 1.2$) to avoid any flow related instabilities. 53
- 3.16 The dispersion diagrams show the trapped solutions in a coronal slab with a background Gaussian flow of selected profiles from Figure 3.15. Diagrams are shown for cases where the width of flow profile is given by (a) $W \gg 2x_0$, (b) $W = 3$, (c) $W = 1.75$, (d) $W = 1.25$. The plasma slab under coronal conditions given by $c_i = 1$, $v_{Ai} = 1.2c_i$, $c_e = 0.4c_i$, $v_{Ae} = 3c_i$, $U_{0i} = 0.3c_i$. Red curves denote the sausage mode solutions and blue curves show the kink mode. 54
- 3.17 Same as Figure 3.16 but the figures show a zoom in on the region of forward and backward propagating slow body modes. For the cases when $W = 1.75$ and $W = 1.25$ we show a higher overtone of the attained body modes as the flow has shifted the fundamental modes into the continua. 56
- 3.18 Comparisons of the eigenfunctions \hat{P}_T and \hat{v}_x for all the flow profiles considered in Figure 3.15. (a) Fast forward sausage mode, (b) fast forward kink mode. An eigenvalue of $k = 3$ was chosen for all plots. All curves normalised such that their values are equal to unity at the boundary 57
- 3.19 Comparisons of the eigenfunctions \hat{P}_T and \hat{v}_x for all the flow profiles considered in Figure 3.15. (a) Slow forward sausage mode, (b) slow forward kink mode, (c) slow backward sausage mode, (d) slow backward kink mode. An eigenvalue of $k = 1.1$ was chosen for plots (a) and (b). An eigenvalue of $k = 0.9$ was chosen for plots (c) and (d). All curves normalised such that their values are equal to unity at the boundary. The eigenfunction plot for the case when $W = 1.25$ is not shown in (d) due to the kx_0 value beyond the cut off regime. 58
- 4.1 The numerical solutions plotted on the dispersion diagram for a uniform magnetic cylinder under (a) photospheric conditions given by $c_e = 1.5c_i$, $v_{Ai} = 2c_i$ and $v_{Ae} = 0.5c_i$, and (b) Coronal conditions given by $c_e = 0.5c_i$, $v_{Ai} = 2c_i$ and $v_{Ae} = 5c_i$. Red curves denote sausage mode, blue curves show kink mode. Figures replicate those shown in Figure 3 and Figure 4 in Edwin & Roberts (1983). 65
- 4.2 The numerical solutions plotted on the dispersion diagram for a uniform magnetic cylinder with a steady background plasma flow under (a) photospheric conditions given by $c_e = 0.6v_{Ai}$, $c_i = 0.53v_{Ai}$, $v_{Ae} = 0$ and $U_{0i} = 0.2v_{Ai}$. (b) Coronal conditions given by $c_e = 0.07v_{Ai}$, $c_i = 0.11v_{Ai}$, $v_{Ae} = 2v_{Ai}$ and $U_{0i} = 0.35v_{Ai}$. Red curves denote the sausage mode, blue curves show the kink mode. Figures (a) and (b) replicate those shown by Figure 10 and Figure 5 in Terra-Homem et al. (2003), respectively. 66

4.3	Cartoon depicting the equilibrium configuration of a radially dependant non-uniform magnetic flux tube in the solar atmosphere. Three separate cases are studied in this chapter. An inhomogeneous density magnetic flux tube under (a) photospheric conditions and (b) coronal conditions with no plasma flow. These types of equilibria may represent features observed in the solar atmosphere, e.g. sunspots and coronal loops, respectively. The equilibrium density profile inside the magnetic flux tube $\rho_{0i}(r)$ is denoted by the shaded contours, with a darker shade representing a (locally) more dense plasma. The actual profiles of $\rho_{0i}(r)$ investigated for the non-uniform density photospheric case are shown in Figure 4.4) and for the coronal case shown in Figure 4.8. Finally a uniform magnetic flux tube with a non-uniform internal background plasma flow ($U_{0i}(r)$) shown as 3D Gaussian shape (see panel (c)) is considered, with radial profiles as demonstrated in Figure 4.14. This case is applicable for some jet-like structures observed in the solar atmosphere.	67
4.4	The non-uniform background density modelled as a series of Gaussian profiles studied in this section for a non-uniform magnetic cylinder under photospheric conditions. $W = 10^5$ (black), $W = 3$ (yellow), $W = 1.5$ (green) and $W = 0.9$ (red).	68
4.5	The Alfvén (blue line) and cusp frequency (green line) are shown as a function of spatial variable r for a non-uniform cylinder under photospheric conditions. For frequencies lying inside this range, the discrete wave modes are swallowed by the continua. These continua are shown for different wavenumber k . (a) The frequencies for the uniform density case, (b) $W = 3$, (c) $W = 1.5$, (d) $W = 0.9$	69
4.6	Dispersion diagrams for magnetoacoustic waves in a photospheric cylinder with a background plasma density in the form of Gaussian profiles shown in Figure 4.4. (a) $W = 10^5$ corresponding to a uniform flow, (b) $W = 3$, (c) $W = 1.5$ and (d) $W = 0.9$. Red curves denote sausage mode, blue curves show kink mode. Shaded regions represent the non-uniform bands due to the equilibrium inhomogeneity. The slow continuum (blue shaded region), inhomogeneous sound speed band (green shaded region) and inhomogeneous kink speed band (orange shaded region) are all shown.	70
4.7	Resulting eigenfunctions for MHD wave modes in a photospheric cylinder with a non-uniform background plasma density given by the distributions shown in Figure 4.4 where the colour scheme is consistent. (a) Fast sausage surface mode for all cases with $ka = 2.7$, (b) fast kink surface mode for all cases with $ka = 1.3$, (c) slow sausage body mode with $ka = 2.7$, (d) slow kink body mode for three cases all with $ka = 3.2$. No azimuthal component is shown for the sausage mode as this wave mode does not produce an azimuthal perturbation. The case for $W = 0.9$ not shown in (d) as this wave mode is absorbed into the slow continuum. All plots are normalised to the external boundary value for each eigenfunction.	72
4.8	Gaussian background density profiles studied for a non-uniform cylinder under coronal conditions. $W = 10^5$ (black), $W = 3$ (yellow), $W = 1.5$ (green) and $W = 0.9$ (red).	73
4.9	Same as Figure 4.5 but for the case of a non-uniform density cylinder under coronal conditions.	74

4.10	Dispersion diagrams for magnetoacoustic waves in a coronal cylinder with a background plasma density in the form of Gaussian profiles shown in Figure (4.8). (a) $W = 10^5$ corresponding to a uniform flow, (b) $W = 3$, (c) $W = 1.5$ and (d) $W = 0.9$. Red curves denote sausage mode, blue curves show kink mode. Shaded regions represent the non-uniform bands due to the equilibrium inhomogeneity. The slow continuum (blue shaded region), inhomogeneous sound speed band (green shaded region), Alfvén continuum (pink shaded region) and inhomogeneous kink speed band (orange shaded region) are all shown.	75
4.11	Resulting eigenfunctions for MHD wave modes in a coronal cylinder with a non-uniform background plasma density given by the distributions shown in Figure 4.8 where the colour scheme is consistent. (a) Fast sausage body mode for all cases with $ka = 2.75$, (b) fundamental kink body mode for all cases with $ka = 1.5$. No azimuthal component is shown for the sausage mode as this wave mode does not produce an azimuthal perturbation in this case. All plots are normalised to the external boundary value for each eigenfunction.	76
4.12	Snapshots of the velocity field in time at the moment of maximum displacement for the different Gaussian profiles modelling plasma density for the fast fundamental kink mode. (a) $W = 10^5$, (b) $W = 3$, (c) $W = 1.5$ and (d) $W = 0.9$. The eigenfunctions shown in Figure 4.11b are converted into Cartesian components and shown in a Cartesian grid. The same value of $ka = 1.5$ is chosen in all plots. The colour contour shows the normalised total pressure perturbation where blue is negative and red is positive. The solid blue line outlines the shape of the perturbed boundary.	77
4.13	3D visualisation of \hat{P}_T and the perturbed velocity vector field in the presence of a uniform and non-uniform background plasma density for the fundamental kink mode with eigenfunctions shown in Figure 4.11b. These correspond to the 2D velocity field vectors shown in Figure 4.12a and Figure 4.12d respectively. (a) Case for uniform plasma density (b) case with Gaussian density with $W = 0.9$	78
4.14	Gaussian flow profiles inside an otherwise uniform coronal magnetic cylinder. $W = 10^5$ (black), $W = 3$ (yellow), $W = 1.5$ (blue), $W = 1$ (magenta) and $W = 0.6$ (red).	79
4.15	Zoom in on dispersion diagrams for forward and backward propagating slow body modes in a coronal cylinder with a background plasma flow in the form of Gaussian profiles shown in Figure 4.14. (a) $W = 10^5$ corresponding to a uniform flow, (b) $W = 3$, (c) $W = 1.5$ and (d) $W = 0.6$. Red curves denote sausage mode, blue curves show kink mode. The red shaded bands indicate the flow modified slow continuum where the modes become resonantly damped.	80
4.16	Eigenfunctions for a coronal cylinder with a background Gaussian flow as shown in Figure 4.14 where the colour scheme is consistent with the equilibrium profiles. (a) Fast sausage body mode with $ka = 3$, (b) fast kink body mode with $ka = 3$, (c) slow sausage body mode with $ka = 1$, (d) slow kink body mode with $ka = 2$	81
4.17	Background vorticity field (left), perturbed velocity field (middle) and background plus perturbed vorticity field (right) plots for all cases of Gaussian plasma flow shown in Figure 4.14. These snapshots all correspond to the slow body kink mode with eigenfunctions shown in Figure 4.16d. Top row corresponds to $W = 10^5$ with inhomogeneity increasing down the plot through $W = 3$, $W = 1.5$, $W = 1$ to bottom row where $W = 0.6$. The colour contour in centre plots shows the total pressure perturbation whereas the colour contours in the right column plots denote the vorticity component perpendicular to the xy plane.	82

4.18	3D visualisation of \hat{P}_T and the perturbed velocity vector field in the presence of a uniform and non-uniform background plasma flow for the slow body kink mode with eigenfunctions shown in Figure 4.16d. These correspond to the 2D velocity field vectors shown in the middle panel of Figure 4.17. (a) Case for uniform plasma flow ($W = 10^5$) (b) case with Gaussian flow with $W = 0.6$. Movies of these 3D visualisations can be found online on the PDG visualisations web-page.	83
5.1	A handful of chosen numerical solutions plotted on the dispersion diagram for a magnetic cylinder with uniform magnetic twist replicated from Erdélyi & Fedun (2010). (a) fast surface sausage modes in a photospheric cylinder (b) slow body sausage modes under coronal conditions (c) slow body and surface kink modes under photospheric conditions, (d) slow body kink mode under coronal conditions. The amplitude of linear twist in each case is shown in the legend, with increasing twist ranging from no twist $A = 0$ (black), $A = 0.001$ (red), $A = 0.01$ (blue) and $A = 0.1$ (green).	91
5.2	Slow body and slow surface kink mode solutions under photospheric conditions as shown in Figure 5.1c for the cases where $A = 0.01$ and $A = 0.1$. Here the modified slow continuum is highlighted by the red curve, showing how the slow surface modes and body modes follow the same trajectory of this continuum.	92
5.3	Plots of v_φ , plasma pressure, sound speed and plasma temperature inside the flux tube for an example configuration of a photospheric magnetic flux tube in the presence of a linear background rotational flow.	95
5.4	Equilibrium background rotational flow profiles for cases with increasing amplitude. In all cases the profiles are linear with respect to spatial coordinate r . The amplitude of the rotational flow increases from 0 (black line), 0.01 (green line), 0.025 (yellow line) and 0.05 (blue line).	96
5.5	Background velocity field for a magnetic cylinder in the presence of a background rotational flow for two cases considered with (a) $A = 0.01$ (b) $A = 0.05$	96
5.6	The y component of the background velocity field which would be seen by observers looking at the Doppler velocity of the structure from side on. (a) $A = 0.01$ (b) $A = 0.05$. Cross cut is taken at $y = 0$, i.e. across the centre of the flux tube.	97
5.7	Dispersion diagrams for all cases of linear anti-clockwise rotational flow with increasing amplitude under coronal conditions (a) $A = 0$ which corresponds to uniform case with no azimuthal flow component. (b) $A = 0.01$, (c) $A = 0.025$, (d) $A = 0.05$	98
5.8	Same as Figure 5.7, however, here we show a zoom region of the dispersion diagrams on the forward and backward slow body modes for all cases of linear anti-clockwise rotational flow with increasing amplitude. (a) $A = 0$, (b) $A = 0.01$, (c) $A = 0.025$, (d) $A = 0.05$	99
5.9	Eigenfunctions for all cases of linear clockwise rotational flow with increasing amplitude. The fast fundamental kink mode is shown in (a) whereas (b) shows the slow body kink mode. A wavenumber value of $ka = 0.55$ was chosen for all cases in both plots.	100
5.10	Equilibrium background rotational flow profiles for cases with increasing amplitude for a photospheric cylinder. In all cases the profiles are linear with respect to spatial coordinate r . The amplitude of the rotational flow increases from 0.01 (green line), 0.05 (black line), 0.1 (yellow line), 0.15 (red line) and 0.25 (blue line).	101

5.11	Dispersion diagrams for a photospheric cylinder with a background rotational flow of varying flow amplitudes. The different cases with varying amplitude, displayed on the top of each panel are shown corresponding to those in Figure 5.10. The red dots indicate solutions for the $m = 0$ sausage mode and the blue dots show the $m = 1$ kink mode.	102
5.12	Dispersion diagrams for the $m = 1$ kink mode for a photospheric cylinder with a background rotational flow. The different cases with varying amplitude are shown where the red shaded curve indicates the modified slow continuum due to the flow.	103
5.13	The resulting dispersion diagrams for all linear cases of rotational flow with the colour scheme consistent with Figure 5.10. These dispersion diagrams display the kink mode only, with the larger dots indicating the chosen eigenvalues for later analysis. The slow surface and slow body modes merge into a singular branch in the long wavelength limit.	104
5.14	The resulting eigenfunctions for the slow surface kink mode for all linear cases of rotational flow with the colour scheme consistent with Figure 5.10. A wavenumber value of $ka = 0.6$ was chosen for all plots.	105
5.15	Plots showing the eigenfunctions \hat{P}_T and $\hat{\xi}_r$ for the (a) fast and (b) slow magnetoacoustic kink mode solutions in a photospheric flux tube with a background rotational flow given by $v_\varphi = 0.1r^1$. Both plots are for the same $v_{ph} = \omega/k = 1.3$ indicated by the red dot on the dispersion diagram. For both cases the resulting eigenfunctions are indistinguishable from one another.	106
5.16	Plots of v_φ , plasma pressure, sound speed and plasma temperature inside the flux tube for an example configuration of a photospheric magnetic flux tube in the presence of a nonlinear background rotational flow given by the expression $v_\varphi = 0.5r^{0.5}$. The green shaded regions shows the inhomogeneous band of the internal sound speed, c_i , as a result of the background rotational flow.	107
5.17	Radial profiles of the rotational flow considered in this chapter. (a) Example case where the power of the profile is kept constant but the amplitude varies (b) example case when the flow amplitude is kept constant and the power of the profile varies.	108
5.18	Dispersion diagrams for the $m = 1$ kink mode for a photospheric cylinder with a non-linear background rotational flow with $p = 0.8$. The different cases with varying amplitude are shown where the red shaded curve indicates the modified slow continuum due to the flow.	109
5.19	Dispersion diagrams for the $m = 1$ kink mode for a magnetic photospheric cylinder with a non-linear background rotational flow with $p = 1.25$. The different cases with varying amplitude are shown where the red shaded curve indicates the modified slow continuum.	110
5.20	Dispersion diagrams for the $m = 1$ kink mode for a photospheric cylinder with a non-linear background rotational flow with $A = 0.05$. The different cases with varying power are shown where the red shaded curve indicates the modified slow continuum.	112

List of Tables

2.1	Properties for both the $m = 0$ sausage mode and $m = 1$ kink mode that are used in the shooting method of the numerical tool. The governing differential equations are for eigenfunctions which must be continuous across the boundary and have particular properties at the center of the waveguide also.	32
5.1	The relationship between the initial choice of equilibrium profile for rotational flow v_φ and the resulting integral in the pressure balance equation. For each choice of profile, the power p is indicated along with the expressions for the term inside the integral as well as the result after conducting the integration. The constant of integration is denoted by C and is absorbed into the gas pressure. The same relationship between the initial profile and resulting integration is obtained for all trial and error case studies.	94

Chapter 1

Introduction

Despite recent advances and successes in the field of solar physics as a result of increased spatial and temporal resolution of both ground and space based telescopes, there are still open questions about many unexplained solar phenomena. The two big questions that have evaded researchers for decades are the so called ‘coronal heating problem’ and the related issue of ‘solar wind acceleration’. Fine scale resolution observations have revealed details and features on the solar surface and in the solar atmosphere that has accelerated research into these two unsolved problems, however analytical theory has not developed at a similar pace.

Two promising possible scenarios have been proposed to explain the high temperatures in the corona both involve the magnetic field, one is magnetic reconnection and the other is magneto-hydrodynamic (MHD) waves. It should be noted that whilst these two mechanisms are the most common found in literature, that more scenarios do exist such as MHD turbulence and instabilities (Zirker 1993) and quasi-periodic oscillations (Walsh & Ireland 2003). This thesis has a particular focus on the properties of magnetic waves, in both a Cartesian and cylindrical geometry, however it should be noted that these may not be the only contributor to explain the coronal heating problem. MHD waves are considered to contribute to the solution of the coronal heating problem, as they can provide a source of energy which may be dissipated by a number of mechanisms which are discussed later in this section. This research addresses the coronal heating problem in the context of MHD waves by identifying the possible regimes within which dissipative processes can occur in observable non-uniform waveguides.

We first review (in the present chapter) basic concepts including an introduction to the solar atmosphere and MHD wave studies on which our investigations have concentrated. The numerical code developed over the course of the PhD project and implemented in later chapters is introduced and explained in Chapter 2. Chapter 3 discusses the wave properties in a Cartesian geometry to both (i) retrieve previously obtained analytical results and (ii) obtain new results for MHD wave properties in the presence of a non-uniform plasma density and also a non-uniform plasma flow. Chapter 4 compliments Chapter 3, however for the case of a cylindrical geometry with a non-uniform plasma density and a non-uniform field aligned plasma flow. Furthermore, we also present 3D visualisations of the wave perturbations in the non-uniform flux tube. Chapter 5 analyses the MHD wave behaviour in a magnetically twisted flux tube and the effect that a rotational flow has on the observational properties of these waves, in an attempt to mimic solar vortex structures. In Chapter 6 we draw our conclusions and summarise the obtained results, complemented by an outlook on promising future research.

1.1 The Sun

The Sun is one of many astrophysical objects which, in its hottest places, is made up of a fully ionised soup of electrons and nuclei known as plasma. The extreme temperatures found on the Sun cause thermal energy to overcome the electromagnetic force between protons and electrons preventing them from forming neutral atoms. The presence of these charged particles results in plasma being an efficient electrically conducting fluid and as a result has an associated magnetic field. This magnetic field interacts with the fluid in a nonlinear coupling with the magnetic field and with the motion of the plasma. The study of the interaction between the magnetic field and the plasma is known as magnetohydrodynamics (MHD). MHD theory provides an appropriate description of the physics and dynamics which is observed on the Sun. Throughout this thesis, a number of physical assumptions are made about the MHD framework which we consider and are summarised below.

1. In the analysis that follows, it is assumed that velocities are non-relativistic such that the plasma velocity and wave phase velocities are much smaller than the speed of light.
2. The plasma is assumed to be single-fluid in the sense that the plasma (fluid) is composed of one variety of particle, this assumption results in the plasma being collisionless.
3. The plasma is electrically neutral such that the total number density of particles comprising the plasma is much larger than the difference between the number densities of individual positive and negative ions.
4. The plasma is considered to be in thermodynamic equilibrium.
5. The characteristic length scales in our MHD framework are extremely large, that is, much larger than the mean free path which can be thought of as the average distance a particle will travel before colliding with another. Additionally, it is assumed that the length scales of interest are much larger than the Debye length, which is a measure of the distance between the deviation of number densities of positive and negative ions per unit volume.
6. The framework is under the assumption that the fluid is considered to fill up the space in which it is contained, such that small-scale inhomogeneities caused by particle dynamics are negligible. This means that local fluid properties such as pressure, temperature, velocity and density can be defined.
7. The characteristic time scales of our MHD framework are much larger than the collision times between particles in the plasma.

The Sun provides scientists with a large scale, functioning plasma laboratory with which to test our current understanding of MHD theory. Solar conditions are largely non-achievable in laboratories here on Earth, namely because it is too expensive to reproduce the temperatures of solar plasma and requires extremely complicated laboratory setups. Therefore, high-resolution observations of the Sun can aid our understanding of not only solar processes but MHD theory as a whole.

Studying the Sun is not only essential in terms of advancing human knowledge, it is also vital for protecting life on Earth. The Sun being such a massive body, located within a relatively (astronomically speaking) close proximity to Earth, also presents potentially dangerous risks. Large solar eruptions, such as coronal mass ejections and solar flares, launch energetic particles at very fast

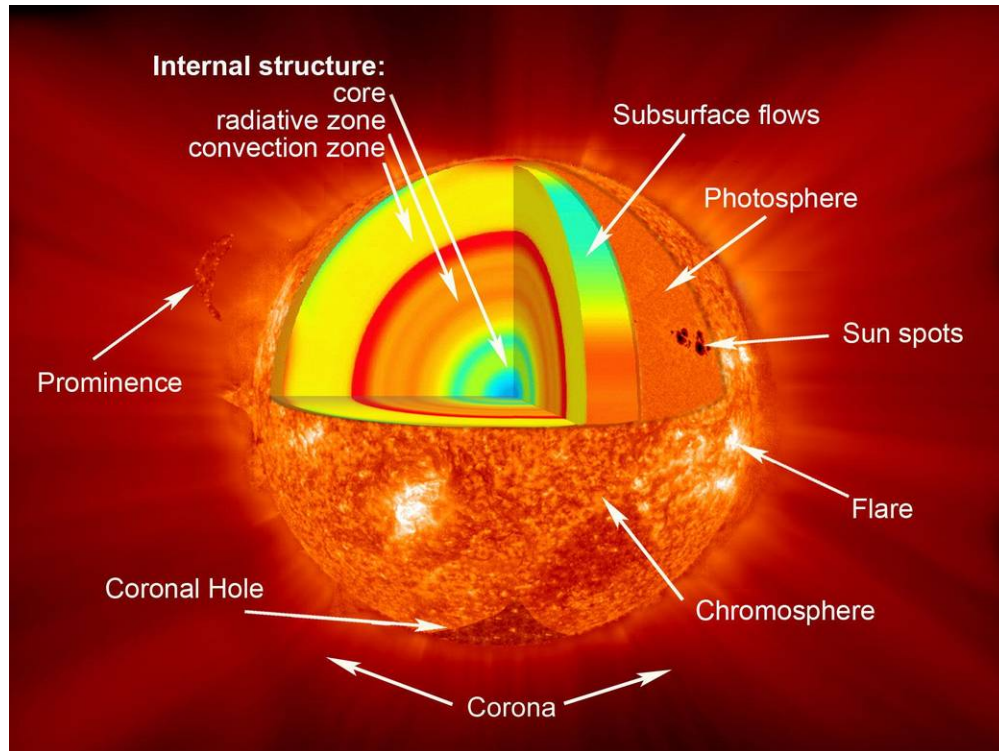


Figure 1.1: *Sun's structure. The distinct internal and atmospheric layers are labelled, along with some notable features observed in the solar atmosphere. Image courtesy of NASA.*

velocities towards Earth, which can interfere with satellite communications and damage electrical grids, as well as exposing pilots and astronauts to increased amounts of radiation. Whilst studying and predicting these events is a separate field of solar physics entirely, understanding the physical processes that occur on the Sun will provide another piece to the jigsaw.

1.2 The solar atmosphere

Inside the core of the Sun is where nuclear fusion ($H \rightarrow He$) occurs, releasing energy in the form of gamma ray photons. The energy produced here travels through the solar interior by means of radiation in the radiative zone and convection in the convection zone, the photons produced as a by-product from nuclear fusion in the core collide with atoms inside the solar interior and transfer some of their energy. By the time these photons reach the edge of the solar interior, they have lost sufficient energy such that their wavelength has increased into the visible part of the electromagnetic spectrum and released into space in the form of photons which we see here on Earth. The solar atmosphere is defined to begin at the 'layer' of the Sun beyond which photons can escape the interior and travel into space. The term layer is used to describe separate physical regions in the solar atmosphere although this word should not be taken explicitly, as these layers are not bounded regions as the height and depth of solar atmospheric layers are time and space dependant. The solar atmosphere can be thought of as consisting of three main layers namely the photosphere, the chromosphere and the corona, based on their physical plasma properties such as temperature and density. A sketch of the structure of both the Sun's interior and the solar atmosphere is shown in Figure 1.1.

The photosphere is the most dense region of the solar atmosphere and here the plasma temperature is relatively cool (≈ 6000 K), such that some of the plasma can be considered as only partially ionised. Partially ionised plasma is a mixture of charged particles (positive ions, electrons, and neutral atoms) interacting through collisions, and is not the main focus of this thesis, however there does exist excellent reviews discussing the importance of partially ionised plasma in the solar atmosphere (in e.g. Ballester et al. 2018, Srivastava et al. 2021). The photosphere, named as such as it emits most of the observable solar radiation, is optically thick in most spectral lines. As a result, using techniques based on the splitting of observable spectral lines such as Zeeman splitting, and quantum interference effects through e.g. the Hanle effect, the magnetic field is most reliably measured in the photosphere.

The chromosphere lies above the photosphere and much is still unknown about this region. The plasma temperature begins to rise in this region ($\approx 10^4$ K), increasing from the temperature minimum in the photosphere (4300 K), whilst the plasma density begins to decrease by approximately 4 orders of magnitude from the photosphere. The chromosphere is host to complex dynamical structures seen in observations, including a variety of plasma jets, such as spicules and fibrils.

A thin transition layer where the plasma density drops by 2 – 3 orders of magnitude and the plasma temperature increases by 2 – 3 orders of magnitude, leads to the outermost layer of the solar atmosphere - the solar corona. The temperature in the solar corona soars to above 10^6 K, roughly 3 orders of magnitude hotter than the visible solar surface - which is much closer to the core of the Sun where fusion occurs. This then raises the question of ‘why is the outermost layer of the solar atmosphere much hotter than the surface?’ This concept is counter-intuitive and can be imagined by being outside next to a campfire and feeling the air around you getting hotter the further away from the campfire that you sit. This thermodynamic mystery is known as the ‘coronal heating problem’ (Kuperus et al. 1981, Ionson 1984, Gudiksen & Nordlund 2005, Klimchuk 2006, Van Doorselaere et al. 2020). Previous studies, including work presented by Withbroe & Noyes (1977), have shown that in order for coronal plasma to be maintained at the observed high temperatures of roughly 2 MK, thermal losses due to the solar wind and radiation, must be balanced with a corresponding energy input of $10^2 - 10^4$ W m⁻².

Throughout the corona, a complex, inhomogeneous magnetic field dominates the plasma dynamics. This magnetic field is responsible for providing the energy that drives many of the most energetic events in the solar system, including blowout jets, coronal mass ejections, and solar flares. These events, as well as convective granular buffeting from the bubbling interior of the Sun, are important for wave excitation in the solar atmosphere (Hasan & Kalkofen 1999, Hasan et al. 2000, Chitta et al. 2012, Vigeesh et al. 2012) where the resulting waves can be guided by the inhomogeneous magnetic field. As the resulting waves are guided by the magnetic field, which contributes partly to their restoring force, the resulting waves are known as magnetohydrodynamic waves. It is widely accepted that MHD waves remain a strong candidate for explaining the unexpectedly high coronal temperatures however much is still unknown about the importance of the role that MHD waves may play. After the detection of ubiquitous MHD waves in the solar atmosphere, the following question arises: can they contribute to the energy budget of the solar atmosphere which ultimately results in the heating of the solar corona? To answer this fundamental question, it is vital that MHD waves possess sufficient energy required to heat the corona, and also that there exists a mechanism to convert this wave energy into thermal energy in the upper layers of the solar atmosphere?

Heating of the upper solar atmosphere as a result of waves was first proposed over half a century ago. Early work from Biermann (1946, 1948) and Schwarzschild (1948) suggested that sound waves generated by turbulence in the convection zone may steepen to form shock waves which propagate up through the solar atmosphere which may result in heating of the atmospheric plasma. Indeed,

this phenomena has been well modelled numerically (Verwichte et al. 2008, Bareford & Hood 2015, Arber et al. 2016), however, it is now known that the solar atmosphere, in particular the corona, is dominated by the magnetic field and consequently the relevant wave models are MHD in nature, as opposed to purely acoustic hydrodynamic waves. At this time, the widely accepted point of view in the solar community is that damping of acoustic wave modes, which have steepened into shocks, is the most probable mechanism of the lower chromospheric heating, however, it does not explain the heating of the upper chromosphere and corona. Some numerical studies have shown that sufficient energy, to heat the solar corona, can be found in other propagating MHD waves, e.g. Alfvén waves (Srivastava et al. 2017). A discussion of the proposed mechanisms that may allow MHD waves to dissipate their energy and heat local plasma is presented in Section 1.7.2. The primary aim of the work presented in this thesis does not intend to investigate the plasma heating potential of MHD waves, however a review of MHD wave heating can be found in a number of papers (see, e.g. Mathioudakis et al. 2013, De Moortel & Browning 2015, Arregui 2015).

Studying and understanding the properties of the observed MHD waves propagating through the solar atmosphere is important for a number of reasons. Firstly, MHD waves may be able to dissipate some of their energy as they travel through the upper layers of the solar atmosphere. If they are deemed to dissipate a sufficient amount of energy in the correct locations, they may play a vital role in the local heating of the chromosphere and corona. Secondly, not only may they contribute to the energy budget of the solar atmosphere, but they can also be used as a proxy to determine the properties of local plasma. Directly measuring certain properties of solar plasma, such as the magnetic field strength in the corona, is tremendously difficult through common techniques such as Zeeman splitting, because the coronal plasma is optically thin and intensity from the lower layers of the solar atmosphere would interfere with the splitting of observed spectral lines. Using a tool known as solar magnetoseismology, it is possible to infer properties such as the magnetic field strength, by combining observed wave properties with the corresponding analytical theory that models waveguides approximating those in the solar atmosphere.

1.3 Ideal MHD equations

In order to enable us to discuss MHD waves in detail, it is essential that the standard procedure for wave analysis is conducted. The starting point for all MHD wave motion analysis is a mathematical investigation which requires perturbing an established equilibrium and seeking wave-like solutions to the governing equations of MHD, to see whether the resulting disturbance propagates as a wave.

In MHD, the governing equations derive from the combination of the electromagnetic equations and plasma equations and describe the motion of a perfectly conducting fluid interacting with a magnetic field. A simplified form of Maxwell's equations combined with Ohm's law and the ideal gas law together with fundamental theorems in physics such as the conservation of mass, momentum and energy, form the basis for the ideal MHD equations.

The set of ideal, compressible MHD equations used in this thesis are the continuity equation describing the conservation of mass (Priest 2014):

$$\frac{d\rho}{dt} + \rho \nabla \cdot \mathbf{v} = 0, \quad (1.1)$$

the momentum equation (otherwise known as the equation of motion) describes the conservation of momentum:

$$\rho \left(\frac{d\mathbf{v}}{dt} \right) = -\nabla p + \frac{1}{\mu_0} (\nabla \times \mathbf{B}) \times \mathbf{B}, \quad (1.2)$$

the energy equation arising from the conservation of energy:

$$\frac{d}{dt} \left(\frac{p}{\rho^\gamma} \right) = 0, \quad (1.3)$$

the induction equation relates the motion of the plasma and the magnetic field:

$$\frac{\partial \mathbf{B}}{\partial t} = \nabla \times (\mathbf{v} \times \mathbf{B}), \quad (1.4)$$

and the solenoidal (divergence-free) condition requiring that any magnetic field entering a volume must also leave that volume:

$$\nabla \cdot \mathbf{B} = 0. \quad (1.5)$$

Here ρ is the plasma (gas) density, \mathbf{v} is the velocity field, p is the plasma pressure, \mathbf{B} is the magnetic field, μ_0 and γ are the magnetic permeability of free space and the ratio of specific heats respectively and $\frac{d}{dt} = \frac{\partial}{\partial t} + \mathbf{v} \cdot \nabla$ is the total (material) derivative. Traditionally, the value of γ is 5/3 in a model solar atmosphere however this value is dependant upon the degrees of freedom of the plasma.

The Lorentz force present in the momentum Equation (1.2) can be decomposed using a vector calculus identity into:

$$\frac{1}{\mu_0} (\nabla \times \mathbf{B}) \times \mathbf{B} = \frac{1}{\mu_0} (\mathbf{B} \cdot \nabla) \mathbf{B} - \nabla \left(\frac{\mathbf{B}^2}{2\mu_0} \right). \quad (1.6)$$

The first term on the right hand side of Equation (1.6) represents the magnetic tension force which acts perpendicular to \mathbf{B} . Tension acts to straighten out curved magnetic field lines and its magnitude is proportional to the field line curvature. The second term on the right-hand side represents the magnetic pressure force, which acts along a negative gradient in magnetic field strength. The effect of magnetic pressure is to spread out the magnetic field lines, in the sense that neighbouring magnetic field lines in close proximity will have a force pulling them apart.

The key properties of ideal MHD include that it must obey the ‘frozen-in’ condition (Alfvén 1942). This states that the magnetic field is frozen into the plasma such that the magnetic flux and magnetic field lines within a volume element is conserved over time, and that the magnetic topology is preserved over time. Furthermore, fundamental properties of the plasma such as mass, momentum, energy and helicity must be conserved. As a result of the magnetic field being ‘frozen-in’ to the plasma, plasma can move freely along magnetic field lines, however can not move perpendicular to magnetic field lines, resulting in a plasma which drags magnetic field lines, or magnetic field lines which push a plasma. The plasma is assumed to be adiabatic, such that there is no transfer of heat from the plasma to the surroundings, similarly, it is assumed that there is no dissipation in ideal MHD. The effects of gravity and the Coriolis force are ignored throughout. The Coriolis force alone acts perpendicular to the direction of plasma motion and is responsible for driving inertial waves. When the magnetic field is strong, such as in the solar atmosphere, the effect of the Coriolis force is negligible when compared to the magnetic field, as a result it is not considered in this thesis. Gravity would appear as an extra term in the equation of motion. However, it should be noted that equilibrium density stratification itself in the solar atmosphere can be a consequence of gravity, although gravity can be ignored if the gravitational scale height is large when compared to the wavelength of the oscillation and the thickness of the waveguide, which is an appropriate assumption for many small-scale solar atmospheric structures. Furthermore, non-ideal MHD effects are ignored in this thesis and thus not included in the set of Equations (1.1)-(1.5). Non-ideal MHD effects would appear as additional terms in the set of Equations (1.1)-(1.5) including resistivity, anisotropic thermal conduction and viscosity which describes the drag forces of the plasma resulting from collisions between particles and manifests as an additional term in Equation (1.2).

Without loss of generality, it is possible to linearise Equations (1.1)-(1.5) by writing each variable as $f = f_0 + f_1$ where f indicates a plasma variable such as density, pressure, magnetic field etc. and subscript 1 denotes a small perturbation to the equilibrium, shown by subscript 0 (Priest 1984, Goedbloed & Poedts 2004, Priest 2014). The perturbations are assumed to be small and thus any products of these perturbations are ignored as they will be small and negligible. The linearised set of Equations (1.1)-(1.5) for a spatially non-uniform equilibrium including a background plasma flow, but with a vertical straight magnetic field can be written as:

$$\frac{\partial \rho_1}{\partial t} + \rho_0(\nabla \cdot \mathbf{v}_1) + \rho_1(\nabla \cdot \mathbf{v}_0) = 0, \quad (1.7)$$

$$\rho_0 \frac{\partial \mathbf{v}_1}{\partial t} = -\nabla P_1 + \frac{1}{\mu}(\nabla \times \mathbf{B}_1) \times \mathbf{B}_0, \quad (1.8)$$

$$\frac{\partial P_1}{\partial t} - c^2 \frac{\partial \rho_1}{\partial t} = 0, \quad (1.9)$$

$$\frac{\partial \mathbf{B}_1}{\partial t} = \nabla \times (\mathbf{v}_1 \times \mathbf{B}_0) + \nabla \times (\mathbf{v}_0 \times \mathbf{B}_1), \quad (1.10)$$

where $c = \sqrt{\gamma p_0 / \rho_0}$ denotes the sound speed. The square of the sound speed in a plasma is proportional to the temperature of the plasma in an ideal gas which is assumed here.

Furthermore, it will be useful to define here some characteristic velocities that are commonly encountered in analytical studies of MHD waves describing the background state. The Alfvén speed, v_A , arises due to the magnetic field and is defined as:

$$v_A = \frac{B_0}{\sqrt{\mu_0 \rho_0}}. \quad (1.11)$$

Another common velocity in MHD is the tube (or cusp) speed, c_T , defined as:

$$c_T = \frac{v_{Ac}}{\sqrt{v_A^2 + c^2}}. \quad (1.12)$$

It would also be useful to define here the plasma- β which is the ratio of plasma pressure P_0 to magnetic pressure:

$$\beta = \frac{2\mu_0 P_0}{B_0^2}. \quad (1.13)$$

When plasma- $\beta \ll 1$, the local plasma is said to be ‘low plasma- β ’ and in this case the magnetic field dominates the dynamics of the local environment. In some studies, it is assumed that the plasma- $\beta = 0$, which can be a good approximation of coronal plasma (Ruderman & Roberts 2002, Arregui et al. 2005, Pascoe et al. 2009, Arregui & Goossens 2019, Duckenfield et al. 2021). By doing so, the plasma is taken to be ‘cold’ and the mathematical analysis is simplified with some permissible wave modes, namely slow magnetoacoustic modes, being ignored.

1.4 MHD waves in uniform plasmas of infinite extent

What differentiates MHD waves from waves in fluids, such as sound waves in air, is the contribution of the magnetic field to the waves’ restoring force. The properties of linear MHD waves in a uniform plasma of infinite extent are often used to characterise MHD waves in general (Goossens et al. 2019).

In this section, we will discuss the predicted waves from theory that can exist in a uniform plasma of infinite extent. The analysis in this section is based upon the assumption that the

medium within which the MHD waves propagate is uniform, which is valid if the wavelength (λ) is much smaller than the length scale of variations in the plasma properties. We can take the set of linearised ideal MHD equations shown in Equations (1.7)-(1.10) and seek a general solution in the form of a superposition of plane waves through:

$$\mathbf{v}_1, \rho_1, P_1, \mathbf{B}_1 \propto e^{i(\mathbf{k}\cdot\mathbf{r}-\omega t)},$$

where \mathbf{k} is the wavevector, \mathbf{r} the spatial vector which can take different forms depending upon the geometry of the mathematical model and ω is the angular frequency of the wave. By substituting into the system of linearised equations, one obtains the dispersion relation for MHD waves in a uniform plasma:

$$\omega^2 (\omega^2 - k^2 v_A^2 \cos^2 \theta) [\omega^4 - \omega^2 k^2 (v_A^2 + c^2) + k^4 v_A^2 c^2 \cos^2 \theta] = 0, \quad (1.14)$$

where θ denotes the angle between the wavevector and the magnetic field. Equation 1.14 provides the general dispersion relation describing waves in a uniform plasma of infinite extent. The dispersion relation contains the eight solutions of our system, one of which is a spurious solution corresponding to $\omega = 0$. The other seven, however, are physical solutions and for a more detailed discussion the interested reader is referred to Goedbloed & Poedts (2004). The first solution to Equation 1.14 is known as the entropy wave, and corresponds to $\omega = 0$ (not to be confused with the spurious solution), which only involves entropy perturbations (no perturbation in velocity, pressure or magnetic field). The second solution is the sound wave, which can be retrieved in the special case by setting the magnetic field to be zero. In this case, and neglecting the entropy wave, Equation 1.14 becomes:

$$\omega^2 = k^2 c^2, \quad (1.15)$$

which is the dispersion relation for sound waves travelling isotropically across the domain. The other solutions are found by the terms inside the brackets of Equation 1.14 and correspond to magnetoacoustic and Alfvén waves, which are discussed in more detail below.

1.4.1 Magnetoacoustic waves

MHD waves whose restoring force is a combination of the gas pressure gradient and the magnetic pressure gradient, but not other forces such as gravity and the Coriolis force, are known as magnetoacoustic waves. Magnetoacoustic waves are compressible perturbations and, as a result, their propagation can be inferred by indirectly observing periodic perturbations in plasma properties such as density and temperature. One of the two fundamental properties of magnetoacoustic waves include that they do not propagate parallel vorticity, however they do create horizontal vorticity. Vorticity, as used here, is defined as the curl of the velocity field and is a measure of the rotational behaviour of the plasma. By referring to ‘parallel’ and ‘horizontal’ we describe with respect to the magnetic field. In a uniform medium, the dispersion relation for magnetoacoustic waves has two solutions; which are retrieved from the bi-quadratic term in Equation 1.14:

$$\omega^4 - \omega^2 k^2 (v_A^2 + c^2) + k^4 v_A^2 c^2 \cos^2 \theta = 0.$$

The solutions for magnetoacoustic waves correspond to a higher frequency mode known as the fast magnetoacoustic wave (fast mode) and a lower frequency mode known as the slow magnetoacoustic wave (slow mode). The fast mode can propagate at any angle across the magnetic field lines and has a dominant transversal motion to the magnetic field, whereas the slow mode is restricted to propagation along the magnetic field lines only and has a dominant parallel motion. Both wave

modes are physically similar but different in the sense that the fast mode's restoring force has the magnetic pressure and gas pressure in phase with each other whereas for the slow mode, the gas pressure and magnetic pressure are out of phase with each other.

1.4.2 Alfvén waves

There is another type of MHD wave whose restoring force is solely magnetic tension, known as the Alfvén wave (Alfvén 1942), which is described by the second term in Equation 1.14 and has a dispersion relation:

$$\omega^2 = k^2 v_A^2 \cos^2 \theta.$$

The Alfvén wave exists purely due to the presence of the magnetic field. The perturbation in this case is incompressible, therefore this wave mode does not perturb plasma density or temperature and so can be difficult to detect directly in the solar atmosphere. Unlike magnetoacoustic waves, Alfvén waves do propagate parallel vorticity and do not have a component of the displacement parallel to the magnetic field. The waves are anisotropic since they transfer their energy along the magnetic field.

1.5 Analytical modelling of solar MHD waveguides

In Section 1.4, the typical MHD waves which exist in a magnetised plasma were introduced. That analysis assumed that the plasma was infinite, unbounded and homogeneous. However, it is clear that solar atmospheric plasma is not infinite and unbounded, neither is it homogeneous. A basic example of an inhomogeneous plasma would be to consider a tangential interface, created by a single discontinuity perpendicular to the magnetic field. A simple discontinuous jump in some plasma property such as density, creates two semi-infinite plasma regions separated by a tangential interface. This specific scenario was studied by e.g. Zajtsev & Stepanov (1975), Roberts (1981*b*), where the authors showed the existence of MHD surface waves that can be either fast or slow, depending on the phase difference between the pressure gradient and magnetic restoring forces. These waves are known as surface waves as they exhibit their maximum amplitude at the boundary of the tangential discontinuity. A more detailed discussion of these MHD waves is present in Section 1.6.

In reality, the plasma in the solar atmosphere is heavily structured, thanks to the magnetic field which permeates throughout plasma. These regions of inhomogeneities give rise to possible magnetic waveguides within which MHD waves can propagate. These waveguides provide a natural conduit for mass and energy transport from the lower solar atmosphere to the upper layers. Examples of magnetic waveguides commonly observed in the solar atmosphere include sunspots, pores, spicules, prominences and coronal loops. In the majority of cases, a boundary can be determined, either in intensity observations which is proportional to plasma density, or in the magnetic field strength. Therefore, it would be insightful to conduct an analytical investigation into the wave modes observed propagating throughout these waveguides by modelling these waveguides in a particular geometry.

Two appropriate models that are commonly used in the analytical analysis of MHD waves in solar structures are the magnetic slab (Cartesian geometry) and the magnetic cylinder (cylindrical geometry). Early analytical works have previously investigated the properties of MHD waves in uniform magnetic slabs and cylinders (Hain & Lüst 1958, Spruit & Zweibel 1979, Wilson 1980, Roberts 1981*b,a*, Spruit 1982, Edwin & Roberts 1982, 1983). Both methods have their individual advantages and disadvantages.

Firstly, consider modelling solar waveguides in a Cartesian geometry, alternatively the waveguide in this case is known as a magnetic slab. Usually in this case, the model is two dimensional, with x denoting the horizontal direction and z denoting the vertical direction. Therefore, the linearised ideal MHD Equations (1.7)-(1.10) can be Fourier decomposed with respect to the ignorable coordinate z . The benefits of modelling solar waveguides using a magnetic slab geometry are that it has mathematical simplicity over alternative geometries. The vector operators in Cartesian geometry adopt a simpler form than that of, e.g. cylindrical geometry which results in a Cartesian geometry providing a strong starting point to begin any analytical investigation. Furthermore, in principle, the magnetic slab model is a good approximation for some structures observed in the solar atmosphere, such as light bridges (Roupe van der Voort et al. 2010, Borrero & Ichimoto 2011, Sobotka et al. 2013). Rather contradictory, the magnetic slab model can also be a poor model of other observed waveguides in the solar atmosphere, such as jets, sunspots and coronal loops, because these waveguides are seen to have a curved boundary, which may be better modelled using a cylindrical model, see Figure 1.2b. Furthermore, the magnetic slab model is typically two dimensional. In this case the vector component into or out of the plane is ignored, and with it, so is a lot of physics, for example studies of the Alfvén wave and other torsional/rotational dynamics. On the other hand, modelling solar waveguides using a magnetic cylinder model has both benefits over the slab model and some complications. The benefits have already been briefly mentioned, including that a cylindrical geometry is a better approximation for the observed waveguides in the solar atmosphere with rounded-like boundaries. Additionally, the cylinder model is a three dimensional model which allows investigations into the azimuthal behaviour of the background and the perturbations. However, the cylinder model creates more complicated mathematical analysis, the results of which may be difficult to interpret without a good initial understanding.

MHD waves have been observed throughout features across all layers in the solar atmosphere such as pores, sunspots, spicules and coronal loops (Morton et al. 2012, 2013, Verth & Jess 2016, Jess et al. 2017, Keys et al. 2018). The observable signatures of MHD waves depends on the type of mode and a more detailed discussion on this with additional observational evidence is found in Section 1.6.

1.6 MHD waves in uniform waveguides

Solar atmospheric plasma is in reality extremely non-uniform both spatially and temporally. However, it is instructive to conduct an analysis into wave modes in a uniform waveguide first, to create the foundations upon which to build an understanding into the MHD waves observed in the solar atmosphere.

In this section, let us introduce a waveguide where the MHD waves can be trapped, which is represented by an discontinuous inhomogeneity in, e.g. density, magnetic field strength, temperature etc. The analysis in this section assumes a cylindrical geometry where the boundary of the waveguide is located at $r = a$, with a being the tube radius. The magnetic field in both regions ($r > a$ and $r < a$) is taken to be straight and uniform although of different magnitudes in each region. Likewise the equilibrium plasma density and pressure inside and outside the tube are taken to be ρ_i, ρ_e and P_i, P_e respectively, (see Figure 1.2b). The subscript i indicates plasma inside the waveguide whereas the subscript e indicates plasma outside the waveguide. There are numerous studies which investigate wave propagation in such an equilibrium (see, e.g. Wilson 1979, Wentzel 1979, Wilson 1980, Edwin & Roberts 1983).

Traditionally, conducting an analytical study into waves in the solar atmosphere is carried out analytically. This requires solving the (ideal or non-ideal) linearised MHD Equations (1.7)-(1.10)

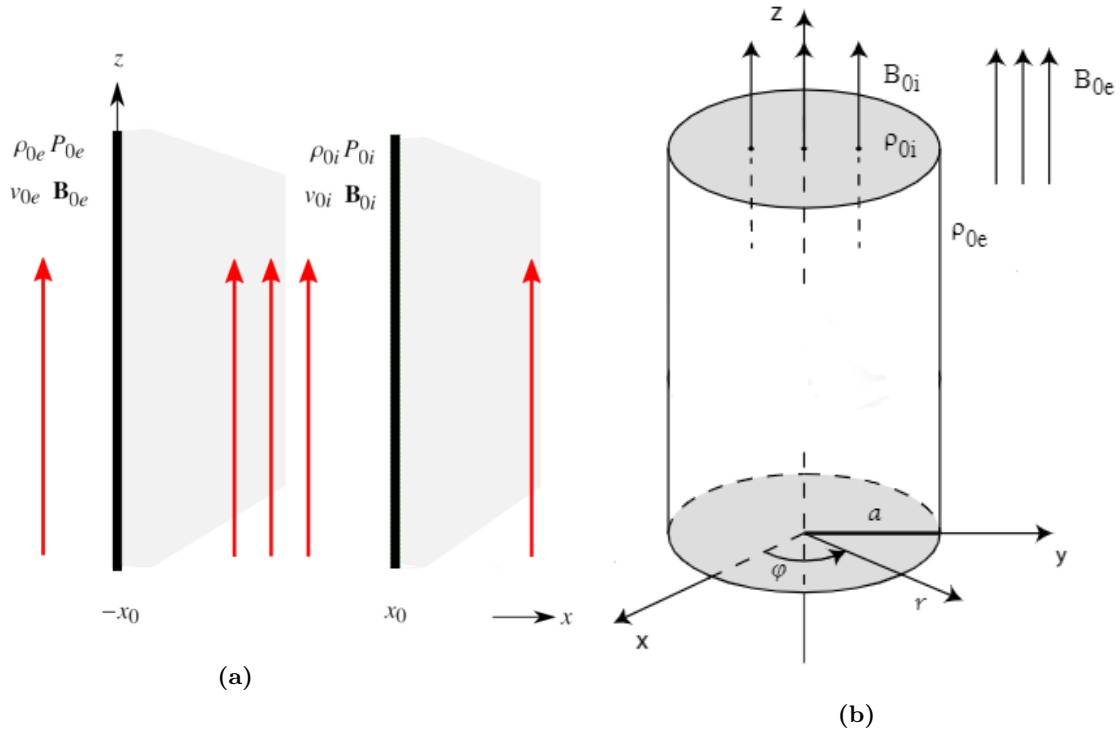


Figure 1.2: Schematic diagram showing examples of how to model magnetic waveguides in the solar atmosphere analytically. (a) A magnetic waveguide in a Cartesian coordinate system can be modelled by a uniform magnetic slab, where the magnetic field is shown by the red arrows. (b) A magnetic waveguide in a cylindrical coordinate system is modelled by a uniform magnetic cylinder. The plasma both inside and outside the waveguide is uniform, however may be of different magnitudes. The magnetic field is assumed to be vertical and straight. If a background plasma flow is included, this is considered to be steady and aligned with the magnetic field. For a magnetic slab, the width of the waveguide is denoted as $2x_0$, whereas the radius of a magnetic cylinder is taken to be a .

and seeking plane wave solutions that are oscillatory in space and time. Equations (1.7)-(1.10) are Fourier analysed by taking the perturbations proportional to $\exp(i\mathbf{k} \cdot \mathbf{r} - i\omega t)$ as before. In this section we will analyse the equilibrium in a cylindrical geometry, however, it should be noted that a similar analysis can be carried out in Cartesian geometry by simply modifying the vector operators.

Assuming a cylindrical geometry, the spatial vector can be written in component form as $\mathbf{r} = (r, \varphi, z)$ and the wavevector can be written as $\mathbf{k} = (k_r, m, k_z)$ where k_r is the radial wavenumber, m is the azimuthal wavenumber and k_z the longitudinal wavenumber. From now on, the longitudinal wavenumber k_z will be expressed as k .

After some algebra, and seeking wave-like solutions, the linearised MHD Equations (1.7) - (1.10) yield the governing equations:

$$D \frac{d}{dr} (r \hat{\xi}_r) = (v_A^2 + c^2) (\omega^2 - k^2 c_T^2) \left(\kappa^2 + \frac{m^2}{r^2} \right) r \hat{P}_T, \quad (1.16)$$

$$\frac{d\hat{P}_T}{dr} = \rho_0 (\omega^2 - k^2 v_A^2) \hat{\xi}_r, \quad (1.17)$$

$$D = \rho_0 (v_A^2 + c^2) (\omega^2 - k^2 v_A^2) (\omega^2 - k^2 c_T^2),$$

$$\text{and } \kappa^2 = \frac{(k^2 v_A^2 - \omega^2) (k^2 c^2 - \omega^2)}{(v_A^2 + c^2) (k^2 c_T^2 - \omega^2)},$$

where \hat{P}_T is the total pressure perturbation and $\hat{\xi}_r$ denotes the radial displacement perturbation. Equations (1.16)-(1.17) apply to both the internal and external regions of the cylinder, however, characteristic quantities will be denoted by subscripts i or e respectively. The effective internal radial wavenumber, κ_i , also controls an important aspect regarding the physical properties of the resulting waves. The square of the effective internal radial wavenumber κ_i^2 can be expressed as:

$$\kappa_i^2 = \frac{(k^2 c_i^2 - \omega^2) (k^2 v_{Ai}^2 - \omega^2)}{(c_i^2 + v_{Ai}^2) (k^2 c_{Ti}^2 - \omega^2)}. \quad (1.18)$$

If this quantity is positive ($\kappa_i^2 > 0$) then the amplitude of the resulting eigenmodes is located near the boundary $r = a$ of the flux tube, these are called ‘surface modes’. However, when $\kappa_i^2 < 0$ then the resulting spatial behaviour of the eigenmodes is oscillatory in nature, and the solution may possess an infinite number of radial nodes within the waveguide, these wave modes are referred to as ‘body modes’.

It is possible to combine Equations (1.16)-(1.17) to form a single differential equation in one eigenfunction, for example \hat{P}_T . Inside the waveguide, this equation takes the form:

$$(\omega^2 - k^2 v_{Ai}^2) \left[\frac{d^2}{dr^2} + \frac{1}{r} \frac{d}{dr} - \left(\kappa_i^2 + \frac{m^2}{r^2} \right) \right] \hat{P}_T = 0. \quad (1.19)$$

Equation 1.19 takes the same form outside the cylinder, however, the subscript i will be replaced by subscript e . It can be seen from Equation 1.19 that these are two unique solutions. The first solution which satisfies Equation 1.19 can be written as:

$$\omega = k v_{Ai},$$

$$v_{ph} = \frac{\omega}{k} = v_{Ai},$$

and corresponds to torsional Alfvén waves propagating with a phase speed v_{ph} at the local internal Alfvén velocity. It can be seen from Equation 1.19 that the solution for the Alfvén wave is independent on the azimuthal wavenumber m . This means that there exists an infinite number of Alfvén wave solutions for the uniform magnetic cylindrical waveguide. The second solution is given by the solution of the differential equation in square brackets and corresponds to the magnetoacoustic waves with different azimuthal wavenumber m . In previous studies, such as that analysed in this section by Edwin & Roberts (1983), the differential equation describing magnetoacoustic wave modes in Equation 1.19 has coefficients which are of sufficient mathematical simplicity that a known closed form analytical solution exists. The solution to the differential equation under consideration takes the form of Bessel functions of different kinds, dependant upon the sign of the effective radial wavenumber κ_i^2 . Furthermore, it is required by the model that waves must be trapped inside the flux tube, therefore there must be no wave energy infinitely far from the waveguide. Mathematically speaking, this means that the solution outside the cylinder must be evanescent, i.e. the wave energy must decay as it approaches $r = \infty$ such that the energy is spatially concentrated within the waveguide. This can be achieved by requiring the external effective wavenumber, κ_e^2 , to be positive. Waves which propagate energy away from the waveguide are known as ‘leaky waves’ and are discussed in Section 1.7.2. The resulting dispersion relation can be derived in a relatively straight forward way by applying relevant boundary conditions on the boundary of the waveguide. There are two physical boundary conditions in this case; the continuity of the perturbation of total pressure across the interface $r = a$, and the continuity of the perturbation of radial displacement. If the initial model does not take into account any background plasma flow, then the second boundary condition here can be replaced by the continuity of radial velocity perturbation, arising from the MHD stress tensor describing the forces acting on the boundary of the waveguide. Application of these boundary conditions yields the dispersion relation for surface magnetoacoustic modes in a uniform cylindrical waveguide (Edwin & Roberts 1983).:

$$\rho_e (\omega^2 - k^2 v_{Ae}^2) \kappa_i \frac{I'_m(\kappa_i a)}{I_m(\kappa_i a)} - \rho_i (\omega^2 - k^2 v_{Ai}^2) \kappa_e \frac{K'_m(\kappa_e a)}{K_m(\kappa_e a)} = 0, \quad (1.20)$$

where I_m and K_m are modified Bessel functions of order m and a prime denotes a derivative with respect to the argument of the Bessel function. Solutions to Equation (1.20) provide the discrete magnetoacoustic modes that exist in a uniform magnetic cylinder and the dispersion relation gives a relationship between ω and k . As the frequency of the resulting waves depends on the wavenumber, these waves are said to be dispersive. Wave dispersion is caused by a well defined geometric boundary, in this case by the waveguide. Finally, with regards to Equation (1.20), for body mode solutions that are oscillatory in nature, $\kappa_i^2 < 0$ will result in the modified Bessel function I_m becoming Bessel J_m .

Magnetoacoustic waves can be divided into sub classes by their azimuthal wavenumber. Setting $m = 0$ yields the ‘sausage mode’ solution which has no nodes in the azimuthal direction. This wave mode can be observed in e.g. density or velocity perturbations as a periodic expansion and contraction of the waveguide and does not perturb the axis of the waveguide. The sausage mode solution has a total pressure perturbation which is a maximum or minimum at the centre of the tube. Whilst the sausage mode is fundamental in theory, it has proven to be difficult to observe in the solar atmosphere until recent times, due to limitations in the spatial resolution of many observing instruments. These waves are typically identified through simultaneous periodic intensity and area fluctuations in magnetic waveguides, and recently have interpretations of the $m = 0$ sausage mode has been reported propagating in solar pores (Morton et al. 2011, Gilchrist-Millar et al. 2021) and in chromospheric fibrils on the solar disk (Gafeira et al. 2017).

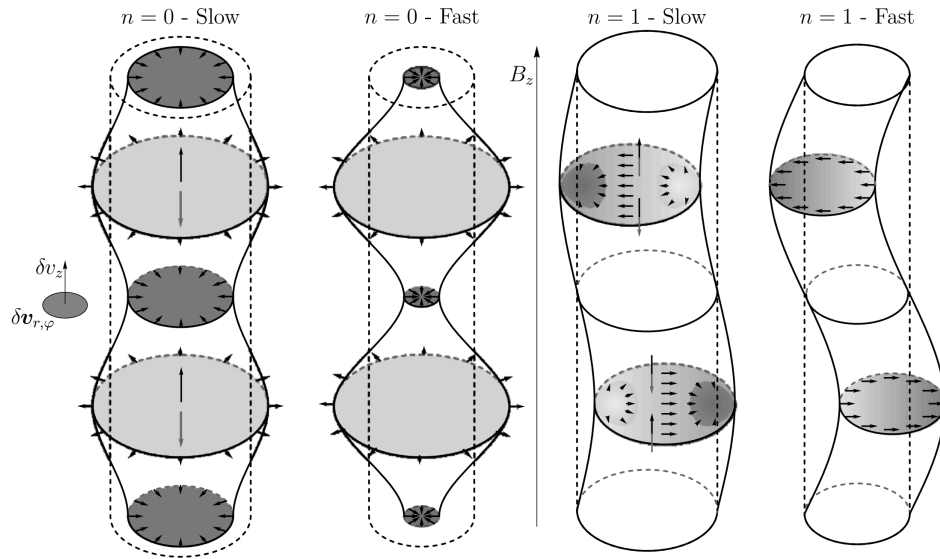


Figure 1.3: Schematic diagram of the magnetoacoustic wave modes observed in a magnetic cylinder taken from Jess et al. (2015). In this diagram the azimuthal wavenumber is denoted by n rather than m . The sausage ($m = 0$) and kink ($m = 1$) mode are shown as a periodic expansion/contraction and swaying motion of the waveguide, respectively. The solid lines outline the perturbation of the cylindrical waveguide with the corresponding arrows displaying the resulting velocity field. The magnetic field in all cases is considered vertical and uniform. A similar cartoon can be found in Morton et al. (2012).

On the other hand, the $m = 1$ wave mode, which has one node in the azimuthal direction, retrieves a solution known as the ‘kink mode’. The kink mode corresponds to a waveguide that appears to undergo a periodic transverse ‘swaying’ motion. This mode does not perturb the axial structure of the waveguide and the total pressure perturbation is zero at the centre of the flux tube. Conversely, the radial displacement perturbation is a maximum at $r = 0$. A cartoon depicting the fast and slow $m = 0$ and $m = 1$ magnetoacoustic modes is shown in Figure 1.3. Kink waves have been observed in coronal loops (Aschwanden et al. 1999, Nakariakov et al. 1999, Li et al. 2017) in spicules (Kukhianidze et al. 2006, De Pontieu, McIntosh, Carlsson, Hansteen, Tarbell, Schrijver, M., Shine, Tsuneta, Katsukawa, Ichimoto, Suematsu, Shimizu & Nagata 2007, Ebadi & Ghiassi 2014, Tavabi et al. 2015), in their on-disk counterparts Rapid Blue- (Red-) shifted Excursions (RBE/RREs) (Roupe van der Voort et al. 2009), in mottles (Kuridze et al. 2012) and in fibrils (Pietarila et al. 2011). A mix of both propagating and standing transverse waves along spicule structures was reported by Okamoto & De Pontieu (2011). The observational study by Sekse et al. (2013) revealed that transverse displacements along with rotational motions and mass plasma flows, a common characteristic of solar spicules, are present in RBE/RREs (Kuridze et al. 2016).

It is possible to plot the solutions to Equation (1.20) for different values of m (e.g. for the sausage and kink modes) but also for different values of characteristic speed orderings. The choice of characteristic speed orderings determines the plasma environment of which the magnetic flux tube is embedded. For example, speed orderings of the choice $v_{Ae} < c_i < c_e < v_{Ai}$ would represent plasma embedded in a photospheric environment. On the other hand, speed orderings of the choice $c_e < c_i < v_{Ai} < v_{Ae}$ would be representative of plasma embedded in a coronal environment.

In Figure 1.4 we show the solutions for the uniform magnetic slab and cylinder model by solving the analytical dispersion relation, for example Equation (1.20) for the case of a uniform magnetic cylinder. Modes with phase speeds larger than the minima of the sound and Alfvén speeds are fast mode solutions, whereas those with phase speeds slower than one minimum or the other are slow mode solutions. The regions of different types of modes are labelled in Figure 1.4 based upon whether the solution is a surface mode (maximum perturbation at the boundary) or a body mode (internal oscillatory perturbation). It can be seen that only body mode solutions are present under coronal conditions for both a magnetic slab and cylinder. Under photospheric conditions, fast surface modes are present for speeds greater than c_i and slower than c_e and slow surface modes for speeds slower than c_{Ti} and faster than v_{Ai} (see Figure 1.4a). The slow surface kink mode approaches v_{Ai} in the long wavelength limit (as kx_0 tends to 0). Both the slow body kink and sausage modes are trapped between $c_{Ti} < \omega/k < c_i$ and tend towards c_{Ti} in the long wavelength limit. For the case of a uniform magnetic cylinder, as shown in Figure 1.4c, the slow body waves are trapped within the same regions as their slab counterparts and possess similar properties. However, the fast surface kink mode approaches the kink speed c_k in the long wavelength limit and the slow surface sausage and kink modes are almost identical in a cylindrical geometry. The kink speed c_k is an average of the internal and external Alfvén speeds relative to the magnetic waveguide:

$$c_k = \sqrt{\frac{\rho_{0i}v_{Ai}^2 + \rho_{0e}v_{Ae}^2}{\rho_{0i} + \rho_{0e}}}. \quad (1.21)$$

Under coronal conditions for a magnetic slab, shown in Figure 1.4b, and a magnetic cylinder, shown in Figure 1.4d, the eigenvalues are similar. However, there is one main difference, which is the appearance of the fundamental kink mode in the magnetic cylinder case. This mode tends to c_k in the long wavelength limit and is widely believed to be the mode reported in the majority of coronal loop oscillations. For both a magnetic slab and a magnetic cylinder under coronal conditions, the slow body sausage and kink modes are bounded by the interval $c_{Ti} < \omega/k < c_i$, the same as slow

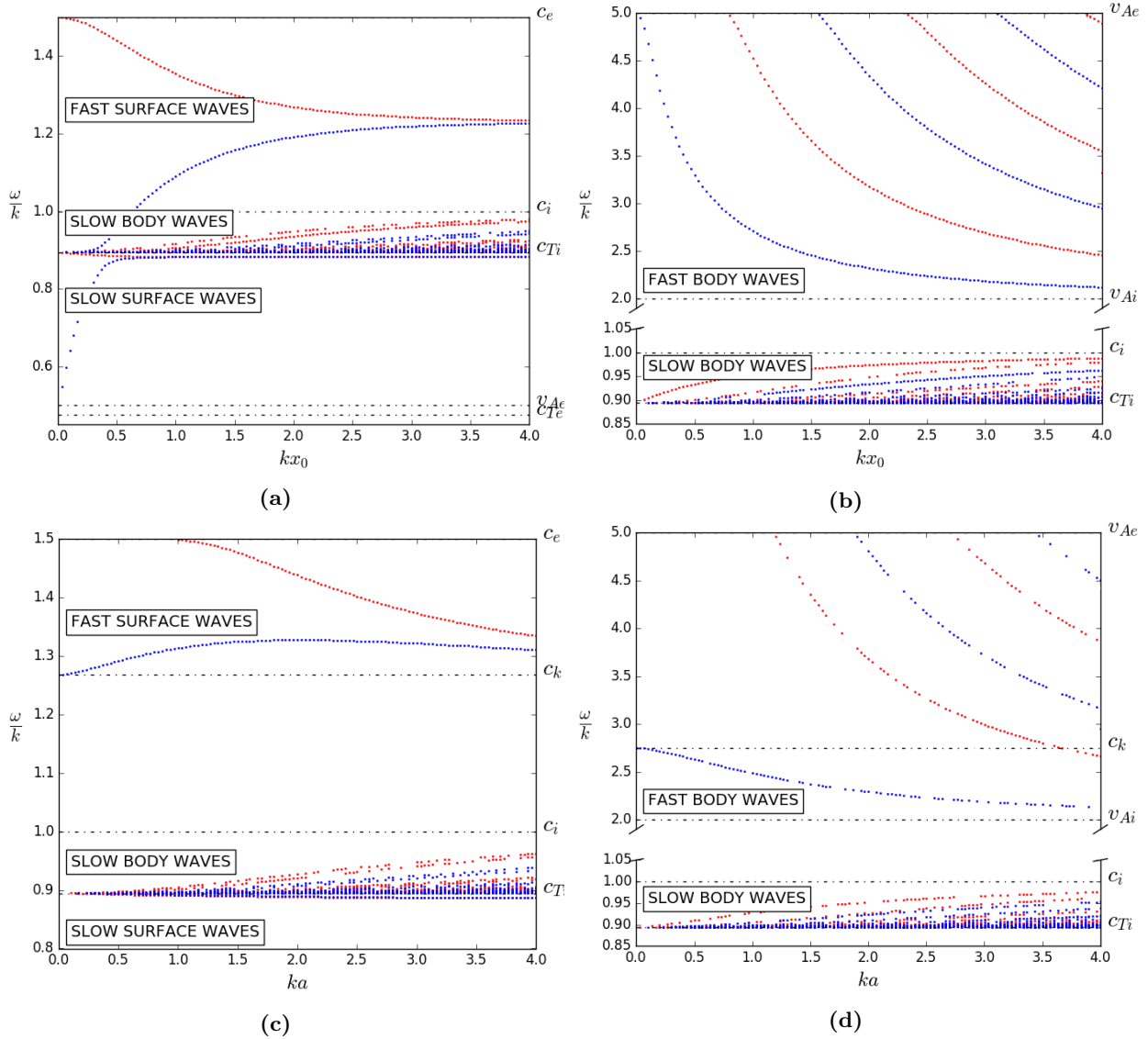


Figure 1.4: The wave phase speeds plotted on a dispersion diagram. The solutions are obtained by solving the analytical dispersion relations from Edwin & Roberts (1982) for a magnetic slab and Edwin & Roberts (1983) for a magnetic cylinder. Solutions are shown for a magnetic slab under (a) photospheric conditions and (b) coronal conditions and also for a magnetic cylinder under (c) photospheric conditions and (d) coronal conditions. The blue dots denote the kink mode solutions whereas the red dots show solutions for the sausage mode.

body modes under photospheric conditions. The $m = 0$ sausage mode and $m = 1$ kink mode are not the only magnetoacoustic modes predicted by theory. In principle, there can be an infinite number of nodes in the azimuthal direction of the resulting MHD wave, therefore the azimuthal wave number m can be infinitely large. Magnetoacoustic waves which have azimuthal wavenumber $m \geq 2$ are known as fluting modes, however, they are not analysed in this thesis.

1.7 MHD waves in non-uniform waveguides

In the Section 1.6, we have discussed the possible modes that can exist in simple magnetic geometries such as slabs or flux tubes. We have discussed how the modes that exist in magnetic waveguides can be identified by their distinguishing properties, such as body, surface, sausage and kink modes. However, in reality, due to the inhomogeneous magnetic field which permeates the solar atmosphere, the plasma is likely to be spatially non-uniform. This makes observations difficult to interpret, but also consequently rich in diagnostic potential. In a non-uniform plasma, MHD waves have different properties to their uniform counterparts, such that there is no longer a clear division between Alfvén, magnetoacoustic, body and surface waves. MHD waves in non-uniform plasmas have mixed properties and can propagate both parallel vorticity, such as the classical Alfvén wave, and compression, such as classical magnetoacoustic waves. In other words, in a non-uniform plasma, wave modes with different azimuthal wavenumbers will be coupled and hence display mixed properties. For example, the torsional Alfvén wave in a cylindrical flux tube can only be described as a ‘pure’ wave when it is not coupled to another wave (e.g. kink mode), and only then the nature of the wave remains the same as it propagates along the tube. Recently Giagkiozis et al. (2015) and Giagkiozis et al. (2016) showed that, even in the linear regime, the presence of a magnetic background twist could couple the $m = 0$ torsional Alfvén wave to the sausage mode, resulting in wave modes of mixed properties.

The properties of MHD waves in a non-uniform plasma have been investigated before and the general formalism for any 1D inhomogeneity, including stratification along the direction of non-uniformity, has previously been presented in (see e.g. Goedbloed et al. 2010, Goedbloed et al. 2019, Roberts 2019). In some circumstances, such as in the plasma- $\beta = 0$ approximation, the fast kink mode is almost completely incompressible, similar to that of the Alfvén wave. These nearly incompressible kink modes are referred to as Alfvénic and have ubiquitous presence in the solar atmosphere (Tomczyk et al. 2007, Morton et al. 2015, 2019). Previous reports regarding the detection of Alfvén waves in the corona (Tomczyk et al. 2007) are, in fact, likely to have been kink waves (Van Doorselaere et al. 2008). More probable reports of Alfvén waves have since been made in X-ray jets (Cirtain et al. 2007) and in magnetic bright points (Jess et al. 2009). A review of the theory and observations of solar Alfvén waves can be found in Mathioudakis et al. (2013).

1.7.1 Governing equations for a non-uniform cylinder

The guided waves within a waveguide are otherwise known as the trapped modes. These modes correspond to solutions with a purely real wave frequency, such that it has no imaginary component. The guided wave modes are traditionally obtained by finding the solutions to a transcendental dispersion relation, such as Equation (1.20) as shown in Section 1.6. In the previous section it was assumed that the waveguide was spatially uniform, that is, in each region (internal and external to the waveguide) the plasma properties were radially constant, although the plasma was inhomogeneous due to a discontinuity at the waveguide boundary. In a non-uniform waveguide, where all variables are a function of the radial component only, the initial magnetic field can be written as $\mathbf{B}_0 = (0, B_\varphi(r), B_z(r))$ with equilibrium velocity field modelled as $\mathbf{v}_0 = (0, v_\varphi(r), v_z(r))$.

From here, for simplicity, we drop the notation that all variables may depend on r and the ideal MHD equations can be Fourier decomposed with respect to the invariant directions φ and z to yield:

$$D \frac{d}{dr} \left(r \hat{\xi}_r \right) = C_1 r \hat{\xi}_r - C_2 r \hat{P}_T, \quad (1.22)$$

$$D \frac{d \hat{P}_T}{dr} = C_3 \hat{\xi}_r - C_1 \hat{P}_T, \quad (1.23)$$

where,

$$D = \rho (c^2 + v_A^2) (\Omega^2 - \omega_A^2) (\Omega^2 - \omega_c^2), \quad (1.24)$$

$$\Omega = \omega - \frac{m}{r} v_\varphi - k v_z, \quad (1.25)$$

$$\omega_A^2 = \frac{f_B^2}{\mu \rho}, \quad \omega_c^2 = \frac{\omega_A^2 c^2}{(c^2 + v_A^2)}, \quad (1.26)$$

$$f_B = \frac{m}{r} B_\varphi + k B_z, \quad (1.27)$$

$$C_1 = Q \Omega^2 - 2m (c^2 + v_A^2) (\Omega^2 - \omega_c^2) \frac{T^2}{r^2}, \quad (1.28)$$

$$C_2 = \Omega^4 - (c^2 + v_A^2) \left(\frac{m^2}{r^2} + k^2 \right) (\Omega^2 - \omega_c^2), \quad (1.29)$$

$$C_3 = D \left\{ \rho (\Omega^2 - \omega_A^2) + r \frac{d}{dr} \left[\frac{1}{\mu} \left(\frac{B_\varphi}{r} \right)^2 - \rho \left(\frac{v_\varphi}{r} \right)^2 \right] \right\} + Q^2 - 4 (c^2 + v_A^2) (\Omega^2 - \omega_c^2) \frac{T^2}{r^2}, \quad (1.30)$$

$$Q = - (\Omega^2 - \omega_A^2) \frac{\rho v_\varphi^2}{r} + \frac{2\Omega^2 B_\varphi^2}{\mu r} + \frac{2\Omega f_B B_\varphi v_\varphi}{\mu r}, \quad (1.31)$$

$$T = \frac{f_B B_\varphi}{\mu} + \rho \Omega v_\varphi. \quad (1.32)$$

This full set of Equations (1.22)-(1.32) was previously introduced in literature by Goossens et al. (1992). The quantities c^2 , v_A^2 , ω_A^2 and ω_c^2 define the squares of the local sound speed, Alfvén speed, Alfvén frequency and cusp frequency respectively. Equation (1.25) describes the Doppler shifted frequency due to the presence of the background plasma flow. It is clear that with no plasma flow present in the model that this equation simply reduces to the wave frequency. Furthermore, it can be seen that if the plasma flow is bulk and steady, i.e., spatially uniform and unchanging in time, then this expression describes the Doppler shift shown previously in Nakariakov & Roberts (1995*a*) and Terra-Homem et al. (2003). Finally, the presence of a background rotational flow will have no effect on Ω for the $m = 0$ sausage mode. The set of Equations (1.22)-(1.32) provide the full set of equations for any cylindrical equilibrium with magnetic twist and plasma flow either rotational or aligned with the axis. It should also be noted that Equations (1.22)-(1.32) describe any cylindrical equilibrium which is non-uniform in the direction of spatial coordinate r , as a result all quantities would also depend on r in such an equilibrium.

The Doppler shifted frequency due to background plasma flow, Ω , and the characteristic frequencies ω_A , ω_c all depend on the spatial variable r . Under these conditions, the differential Equations (1.22)-(1.23) become singular as $\omega \rightarrow \omega_A$ and $\omega \rightarrow \omega_c$, giving rise to a continuous spectrum of

wave frequencies. These two continua are closely related to resonant processes which are discussed in more detail in Section 1.7.2.

The Doppler shifted continua, where wave modes can be resonantly damped due to the presence of a background plasma flow, are bounded within the regions:

$$\omega = \omega_f(r) \pm \omega_A(r), \quad (1.33)$$

$$\omega = \omega_f(r) \pm \omega_c(r), \quad (1.34)$$

where $\omega_f = mv_\varphi/r + kv_z$. Within these regions the wave frequency becomes a complex quantity, as a result these are the regions which are not considered in this work. For an equilibrium which models a uniform plasma, such as constant density and magnetic field, Equations (1.33) - (1.34) define the flow continuum (or resonance location), however in the absence of equilibrium flow, Equation (1.33) describes the Alfvén continuum and Equation (1.34) describes the slow/cusp continuum.

Equations (1.22)-(1.23) can be combined to create a single differential equation in either $r\hat{\xi}_r$:

$$\frac{d}{dr} \left[f(r) \frac{d}{dr} (r\hat{\xi}_r) \right] - g(r) (r\hat{\xi}_r) = 0, \quad (1.35)$$

where,

$$f(r) = \frac{D}{rC_2}, \quad (1.36)$$

$$g(r) = \frac{d}{dr} \left(\frac{C_1}{rC_2} \right) - \frac{1}{rD} \left(C_3 - \frac{C_1^2}{C_2} \right), \quad (1.37)$$

or:

$$\frac{d}{dr} \left[\tilde{f}(r) \frac{d\hat{P}_T}{dr} \right] - \tilde{g}(r) \hat{P}_T = 0, \quad (1.38)$$

where,

$$\tilde{f}(r) = \frac{rD}{C_3}, \quad (1.39)$$

$$\tilde{g}(r) = -\frac{d}{dr} \left(\frac{rC_1}{C_3} \right) - \frac{r}{D} \left(C_2 - \frac{C_1^2}{C_3} \right). \quad (1.40)$$

Both the governing differential Equations (1.35) and (1.38) are analytically complicated in the sense that, similar to the case of a non-uniform magnetic slab, no closed form analytical solution exists for them. Ultimately, boundary conditions cannot be matched analytically and a dispersion relation cannot be derived. For later use it may be important to note that the components of the displacement vector of magnetic surfaces both parallel to the magnetic field lines $\hat{\xi}_{\parallel} = \hat{\xi} \cdot \mathbf{B}/B$ and perpendicular to the magnetic field lines $\hat{\xi}_{\perp} = (\hat{\xi}_\varphi B_z - \hat{\xi}_z B_\varphi)/B$ can be related to $\hat{\xi}_r$ and \hat{P}_T by:

$$(\Omega^2 - \omega_A^2) \hat{\xi}_{\perp} = \frac{i}{\rho B} \left(g_B \hat{P}_T - \frac{2B_z T \hat{\xi}_r}{r} \right), \quad (1.41)$$

$$\begin{aligned} (\Omega^2 - \omega_c^2) \hat{\xi}_{\parallel} &= \frac{if_B}{\rho B} \left(\frac{c^2}{c^2 + v_A^2} \right) \frac{(\Omega^2 \hat{P}_T - Q \hat{\xi}_r)}{\Omega^2} - \\ &\quad - i \frac{(\Omega^2 - \omega_c^2) (2\Omega B_\varphi v_\varphi + f_B v_\varphi^2) \hat{\xi}_r}{B\Omega^2 r}, \end{aligned} \quad (1.42)$$

where $B = \sqrt{B_\varphi^2 + B_z^2}$ and

$$g_B = (\mathbf{k} \times \mathbf{B})_r = \frac{m}{r} B_z - k B_\varphi,$$

as given in Sakurai et al. (1991), Goossens et al. (1992). It is possible to combine Equations (1.41) and (1.42) to isolate the component of perturbed azimuthal displacement $\hat{\xi}_\varphi$ or the component of perturbed vertical displacement $\hat{\xi}_z$:

$$\begin{aligned} \hat{\xi}_\varphi = \frac{i}{B} \left\{ \frac{B_z}{\rho(\Omega^2 - \omega_A^2)} \left(g_B \hat{P}_T - \frac{2B_z T \hat{\xi}_r}{r} \right) + \right. \\ \left. + \frac{B_\varphi}{\Omega^2} \left[\frac{f_B}{\rho} \left(\frac{c^2}{c^2 + v_A^2} \right) \left(\frac{\Omega^2 \hat{P}_T - Q \hat{\xi}_r}{(\Omega^2 - \omega_c^2)} \right) - \frac{(2\Omega B_\varphi v_\varphi + f_B v_\varphi^2) \hat{\xi}_r}{r} \right] \right\}, \end{aligned} \quad (1.43)$$

$$\begin{aligned} \hat{\xi}_z = \frac{i}{B_z} \left\{ \frac{f_B}{\Omega^2 \rho} \left(\frac{c^2}{c^2 + v_A^2} \right) \left(\frac{\Omega^2 \hat{P}_T - Q \hat{\xi}_r}{(\Omega^2 - \omega_c^2)} \right) - \frac{(2\Omega B_\varphi v_\varphi + f_B v_\varphi^2) \hat{\xi}_r}{r} \right\} \left(1 - \frac{B_\varphi^2}{B^2} \right) - \\ - \frac{i B_\varphi B_z}{B^2 \rho (\Omega^2 - \omega_A^2)} \left(g_B \hat{P}_T - \frac{2B_z T \hat{\xi}_r}{r} \right). \end{aligned} \quad (1.44)$$

For the case of a uniform cylinder, Equation (1.43) reduces to:

$$\hat{\xi}_\varphi = \frac{i}{\rho(\omega^2 - k^2 v_A^2)} \frac{m}{r} \hat{P}_T, \quad (1.45)$$

which is a previously obtained analytical result for the traditional uniform cylinder (Goedbloed & Poedts 2004, Goossens et al. 2009, Ruderman & Erdélyi 2009, Priest 2014).

The components of the Eulerian perturbation of velocity can be related to the components of the Lagrangian displacement by (see, e.g. Goossens et al. 1992):

$$\hat{v}_r = -i\Omega \hat{\xi}_r, \quad (1.46)$$

$$\hat{v}_\varphi = -i\Omega \hat{\xi}_\varphi - \hat{\xi}_r r \frac{d}{dr} \left(\frac{v_\varphi}{r} \right), \quad (1.47)$$

$$\hat{v}_z = -i\Omega \hat{\xi}_z - \hat{\xi}_r \frac{dv_z}{dr}, \quad (1.48)$$

where v_φ and v_z are the azimuthal and vertical components of the background plasma flow respectively. Equations (1.46)-(1.48) describe the velocity perturbations of the plasma due to a combination of the background environment and the resulting displacement perturbations. For an equilibrium that is uniform, Equations (1.46)-(1.48) remain uncoupled and independent of each other. However, for an equilibrium that has a nonlinear v_φ in the sense that the azimuthal component of flow is not proportional to r , the radial plasma motions become coupled to the azimuthal plasma motions, an interesting scenario which is discussed in further detail in Chapter 5.

1.7.2 Continuum modes

In Section 1.7.1, we have discussed how, in reality, the plasma in the solar atmosphere is non-uniform in nature. As a result, a broad spectrum, i.e. a continuous spectra given by a broad range of frequencies, of MHD waves is likely to exist within such a medium. This includes waves with

frequencies that lie within either the Alfvén or slow continua described by Equations (1.33) - (1.34). Waves inside these regions are expected to undergo resonant processes. Analytically this is due to the regular singularities that are present in the governing Equations (1.35) and (1.38). In order for wave based models to be a genuine suggestion as a way to heat local plasma, there must exist a mechanism that can rapidly transfer the wave energy from large to small length scales, where classical dissipation, such as resistive or viscous dissipation, is effective.

Many physical mechanisms have been proposed as a possible way for waves to damp and/or dissipate their energy including, but not limited to, the transformation of waves via parametric processes (Voitenko & Goossens 2002, Fedun et al. 2004, Voitenko & Goossens 2004, Váscónez et al. 2015), resonant absorption and phase mixing. Perturbations of the plasma by a sideways driver from e.g. eruptions in the solar atmosphere such as flares or CMEs, would generate waves that propagate (on the whole) at an angle across the magnetic field. Waves propagating across a non-uniform plasma are likely to heat the local plasma by resonant absorption when the waves reach a location where their frequency matches the local Alfvén or slow frequency (Ionson 1978, Hollweg & Yang 1988, Ruderman & Roberts 2002, Aschwanden et al. 2003, Howson et al. 2019). We can see, from Equation 1.17, that when the excited mode has a frequency which falls inside one of the two continua, this results in $D = 0$. The physical location of the resonance is called the resonant layer, and is located within the region where the plasma is non-uniform. In many studies, both analytical and numerical, a magnetic flux tube is modelled with a thin non-uniform boundary layer at the edge of the magnetic flux tube, where resonant absorption can occur and has been proposed as a possible explanation behind the observed damping of coronal loop oscillations (Goossens et al. 2002, Magyar & Van Doorselaere 2016, Van Doorselaere et al. 2021). Resonant absorption can only take place for modes with $m \geq 1$, because for $m = 0$ Equation (1.45) decouples from Equations (1.16) and (1.17), making resonance impossible. We need to stress that resonant absorption is not a true energy dissipation mechanism, but a damping mechanism. Resonant absorption is an ideal MHD method to transfer energy from the global mode to the localised Alfvén wave, leading to damping of the global mode. In order to dissipate the enhanced wave energy, much smaller spatial scales need to be created, for example via the mechanism of phase mixing.

On the other hand, another proposed mechanism of wave dissipation is the concept of phase mixing, as described by Heyvaerts & Priest (1983), which aims to enhance the rate of wave dissipation through the creation of small length scales in an inhomogeneous medium. Phase mixing is most likely to affect waves propagating along the magnetic field lines, excited by footpoint driving motions. Phase mixing occurs when a local gradient in the Alfvén speed is present; as waves propagate along field lines with different Alfvén speeds, the wave front turns and the waves become increasingly out of phase (Ofman & Aschwanden 2002, Pagano et al. 2020). Although resonant absorption and phase mixing are often discussed as individual mechanisms, there is a natural link between these mechanisms, as both rely on the presence of a variation in the local Alfvén speed profile (Soler & Terradas 2015). Hence, the small-scale oscillations in the non-uniform region will naturally undergo phase mixing due to local variation in the Alfvén speed (e.g. Ruderman et al. 1997). However, the damping caused by phase mixing depends on the actual value of the resistivity, while the damping of resonant absorption does not (as resonant absorption itself is an ideal process).

Whilst it is not the main aim of this thesis to investigate the properties of waves that exist within the continua, there are excellent reviews regarding the processes behind local heating of solar plasma (Erdélyi & Ballai 2007, Klimchuk 2015, Van Doorselaere et al. 2020).

Chapter 2

Numerical eigensolver

In this chapter the numerical procedure utilised throughout this thesis will be introduced and explained. This numerical eigensolver obtains the eigenvalues and resulting eigenfunctions for any symmetric radially non-uniform waveguide in either a slab or cylindrical geometry. The code assumes that the internal region can be inhomogeneous, whereas the external region must be uniform. The code was written in Python programming language from scratch.

2.1 Obtaining an equilibrium

Structures observed in the solar atmosphere that are thought to be effective waveguides (e.g. coronal loops, sunspots, spicules etc.), must be in equilibrium in order to exist on the timescales which they are seen to live for. Therefore, when conducting any study into waves propagating within such structures, it is essential that the mathematical model is in a stable equilibrium before small perturbations are considered. A stable equilibrium is obtained by ensuring that the spatial gradient of total pressure is equal to zero. In a uniform plasma, this is numerically straightforward as there are only two variables that need to be balanced, namely the plasma pressure and the magnetic field. However, for more complicated equilibria that may include e.g. inhomogeneous plasma, magnetic twist and/or rotational background flows, obtaining an equilibrium can be more difficult. The gas pressure is determined by an equation of state simply defined by the ideal gas law:

$$P = \frac{k_B}{m} \rho T, \quad (2.1)$$

where k_B is the Boltzmann constant (1.381×10^{-23} J deg⁻¹), m is the mean particle mass and T the temperature of the plasma. Therefore, from Equation (2.1) it is possible to keep the background gas pressure radially constant, even with a non-uniform plasma density, by, for example, balancing the change with a spatial variation of temperature. This scenario is investigated in later chapters.

It is vital to ensure that, no matter if the equilibrium is uniform or non-uniform, that a pressure balance is maintained across the boundary of the waveguide of choice. Consider first a simple case of a uniform magnetic slab. In each region there is a contribution to the total pressure by both the plasma and the magnetic field, the expression ensuring that these are equal across the boundary can be written as:

$$\frac{d}{dx} \left(P + \frac{B^2}{2\mu_0} \right) = 0, \quad \text{or,} \quad P_i + \frac{B_i^2}{2\mu_0} = P_e + \frac{B_e^2}{2\mu_0}, \quad (2.2)$$

where subscript i denotes plasma variables inside the waveguide and with subscript e for external parameters. Equation (2.2) yields a relationship between the equilibrium plasma densities, sound

speeds and Alfvén speeds across the waveguide boundary, which can be expressed by:

$$\frac{\rho_e}{\rho_i} = \frac{c_i^2 + \frac{1}{2}\gamma v_{Ai}^2}{c_e^2 + \frac{1}{2}\gamma v_{Ae}^2}. \quad (2.3)$$

Numerically speaking it is possible to obtain a simple equilibrium by defining ρ_i , c_i , v_{Ai} , c_e and v_{Ae} for either photospheric or coronal conditions, and by using Equation (2.3), the necessary value of ρ_e can be calculated such that the waveguide is in equilibrium. For example, under coronal conditions given by $c_e < c_i < v_{Ai} < v_{Ae}$, we can assign a value of $c_i = 1$ and say let $c_e = 0.4c_i$, $v_{Ai} = 1.2c_i$ and $v_{Ae} = 3c_i$ with $\rho_i = 1$. These conditions will result in a value for $\rho_e = 0.287$ and resulting equilibrium plasma profiles as shown in Figure 2.1. The equilibrium density profile and characteristic speed profiles of the example case of a uniform magnetic slab under coronal conditions are shown in Figure 2.1a. Meanwhile, the radial profiles for plasma parameters such as temperature, pressure and magnetic field are displayed in Figure 2.1b. Furthermore, Figure 2.1b shows the spatial distribution of total pressure, which can be seen to be both continuous across the boundary of the waveguide located at $x_0 = 1$ and $-x_0 = -1$ and also spatially constant. This is the ultimate requirement for obtaining an MHD equilibrium. Once an equilibrium is obtained, the relevant analysis of MHD waves can begin as it can be assured that small perturbations will behave in a wave-like manner with no contribution from background perturbations.

The previous discussion had a focus on a magnetic slab geometry. In that scenario, it is only possible to have non-uniformity in one direction, the radial direction (as y direction is infinite and homogeneous and the MHD equations are Fourier decomposed with respect to z). However, if a cylindrical geometry is considered, there is now an additional direction which may have plasma properties that can be radially non-uniform. In the more complicated case of a magnetic cylinder, it is likely that the background magnetic field and velocity field will have both azimuthal and vertical components which are radially dependant. In such a scenario, the pressure balance equation would be (Goossens et al. 1992):

$$\frac{d}{dr} \left(P + \frac{B^2}{2\mu_0} \right) = \frac{\rho v_\varphi^2}{r} - \frac{B_\varphi^2}{\mu_0 r}, \quad (2.4)$$

with v_φ and B_φ the azimuthal components of the velocity and magnetic field respectively.

Now that an equilibrium has been established, for both a Cartesian and cylindrical geometry, let us now go into more detail describing the physics of the numerical algorithm to obtain the eigenvalues of the system.

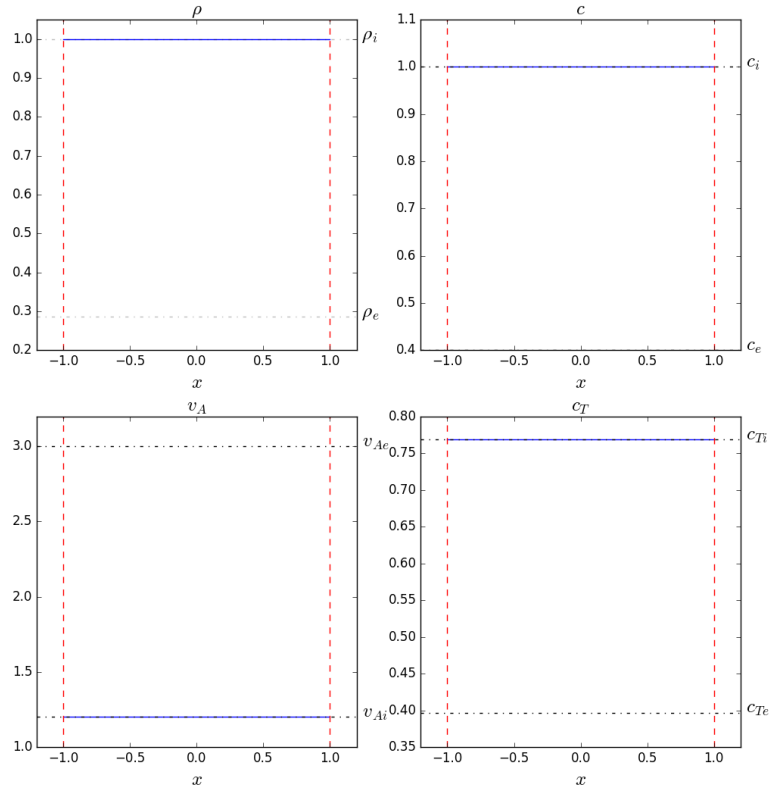
2.2 Magnetic Slab (Cartesian geometry)

In this section the numerical approach which adopts the shooting method to solve the relevant boundary conditions of a magnetic slab in the presence of a spatially non-uniform density is described. Due to the presence of a non-uniform plasma, the equilibrium sound, Alfvén and cusp speeds may all be spatially non-uniform, too. The general differential equation for the eigenfunction, \hat{v}_x , takes the following form for a non-uniform density magnetic slab:

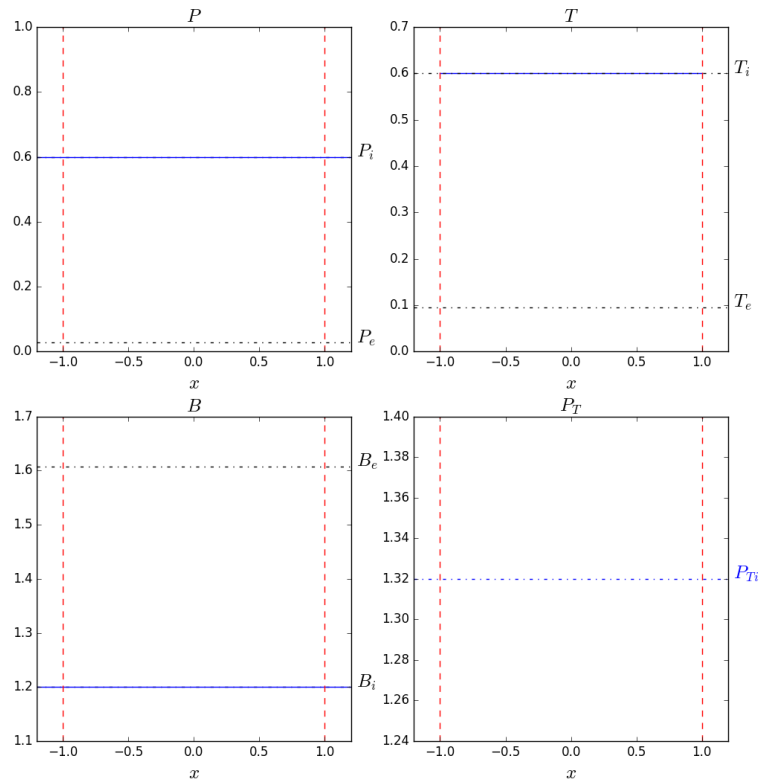
$$\hat{v}_x'' + F(x, \omega, k, c_0, v_A, c_T) \hat{v}_x' + G(x, \omega, k, c_0, v_A, c_T) \hat{v}_x = 0, \quad (2.5)$$

where F and G are both arbitrary functions. The corresponding total pressure perturbation expression for a non-uniform density magnetic slab takes the form:

$$\hat{P}_T = A(x, \omega, k, c_0, v_A, c_T) B(x, \hat{v}_x, \hat{v}_x'), \quad (2.6)$$



(a)



(b)

Figure 2.1: Equilibrium profiles for uniform slab in coronal environment. (a) The density and characteristic speed profiles, (b) plasma properties including plasma pressure, temperature, magnetic field strength and total pressure. The dashed lines indicate the external value (outside the waveguide) for each variable shown in the separate panels.

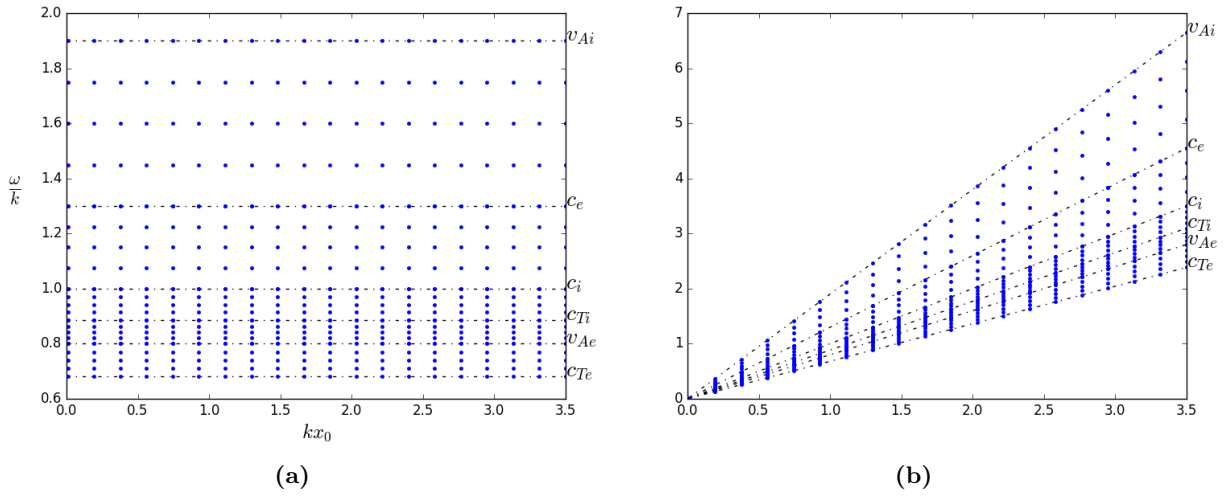


Figure 2.2: Example of how initial sampling is divided up on dispersion diagram for numerical method as a function of (normalised) wavenumber for (a) phase speed (b) frequency. Only regions containing trapped modes are considered with narrower bands containing samples located closer together.

with A and B again arbitrary general functions. Utilising the known properties of the sausage and kink modes, namely those of \hat{P}_T or \hat{v}_x , it is possible to solve for the symmetric or anti-symmetric solutions in \hat{P}_T or \hat{v}_x dependant upon what the initial governing equation is (see Section 1 for information about kink and sausage solutions being symmetric or anti symmetric). MHD waves can be classified into ‘trapped’ or ‘leaky’ modes based on the physical nature of their wave frequencies. If the frequency is purely real, then this wave mode is said to be ‘trapped’ and can be an observed eigenmode. However if the wave frequency has an imaginary component (e.g. $\omega = \omega_R + i\omega_i$) then the wave will radiate energy away from the waveguide and is said to be ‘damped’ if $\omega_i < 0$, will be unstable if $\omega_i > 0$ and for the case of trapped modes $\omega_i = 0$. There is one more requirement that this work considers which is that the waves under investigation are all trapped modes. This allows the frequency domain used in the investigation to consider only real values of both the wave frequency and wavenumber. The eigenvalues (wave frequency and wavenumber) are initially unknown, therefore it is required to sample through values of $\omega = \omega_R$ and k to locate solutions that satisfy both boundary conditions. In Figure 2.2 we show an example of the initial sampling of the eigenvalues that are fed into the code. For example, the value of k can be fixed and the code will loop/scan through the values of ω . The more samples used in the initial sampling (initial resolution) then the greater the number of obtained solutions.

Restricting the investigation to purely trapped modes provides a physical constraint on the waves infinitely far away from the waveguide boundary that they must be evanescent, that is, the amplitude of wave perturbation and the gradient of the perturbation must be zero. Numerically it is not convenient to consider a point located at infinity with a value of zero, as such, ‘numerical infinity’ is considered as a point sufficiently far away from the waveguide boundary that allows the wave amplitude to decay outside the waveguide. Using the condition that waves must be evanescent outside the waveguide provides the initial conditions at infinity needed to numerically solve the governing differential equation outside the waveguide. In all cases, we consider that the external medium is uniform, therefore, a known analytical expression exists describing perturbations in this region. The known initial conditions at ‘numerical infinity’ and the closed form analytical solution

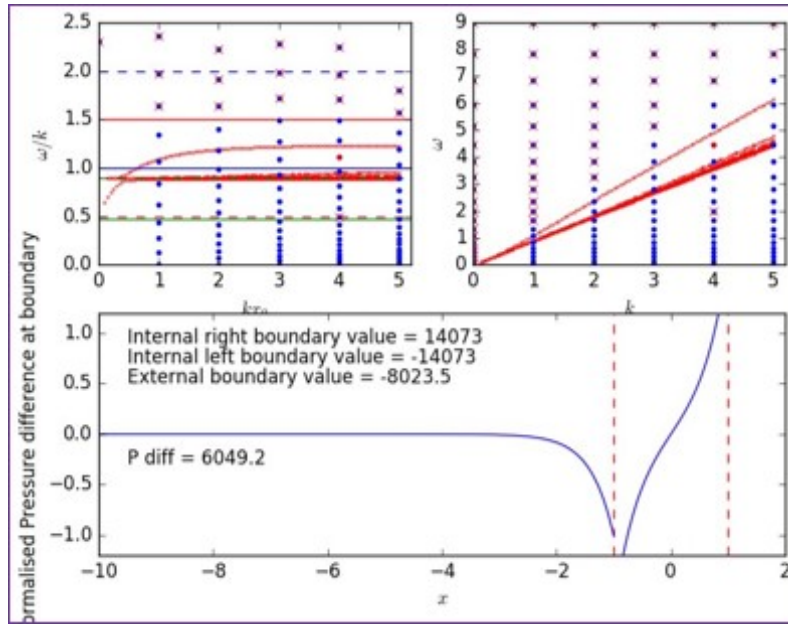
describing the dynamics outside the waveguide are combined to solve for \hat{v}_x externally up to and including the boundary location. The differential equation such as that provided in Equation (2.5) can be reduced to a first order ordinary differential equation (ODE) by a simple change of variables which simplifies the numerical solver.

The external region to the waveguide can be considered an Initial Value Problem (IVP). The governing ODE can be solved numerically by using a numerical integrator. In Python, a function that can achieve this is *ODEINT* which stands for **o**rdinary **d**ifferential **e**quation **i**ntegration. *ODEINT* adopts a number of different numerical schemes to find an approximate solution for such ODEs but mainly implements explicit methods from a number of families including explicit ‘Runge-Kutta’, extrapolating techniques and for implicit schemes it uses implicit ‘Runge-Kutta’. In addition to these families of algorithms, *odeint* introduces stepper categories corresponding to the functionality of the method to optimise the iteration time step. Solving the ODE in the external domain provides a value located at $x = -x_0$ for both \hat{P}_T and \hat{v}_x which, for trapped modes, must be continuous across the boundary. The value of \hat{P}_T or \hat{v}_x at the opposite boundary $x = x_0$ is known for both the sausage and kink mode solutions using their (anti)symmetric properties discussed in Chapter 1. Therefore, inside the waveguide we have a Boundary Value Problem (BVP), however, not enough initial information is known at the boundary to allow an IVP solver to be used. What is unknown are the gradients at each spatial location in the domain to obtain the correct boundary value at $x = x_0$, therefore, the shooting method approach can be applied as the opposite boundary value is known. The values of \hat{P}'_T and \hat{v}'_x do not need to be continuous across the boundary, so even though the gradients are known in the external region, their values inside need to be found. The shooting method takes the initial value of \hat{P}_T or \hat{v}_x at the location $x = -x_0$ and estimates the derivatives such that an integration can be carried out. If the derivative estimation is good, then the eigenfunction \hat{P}_T or \hat{v}_x will satisfy the condition for either the kink or sausage mode at $x = x_0$. It could be possible to try and guess the correct gradient at the boundary, however, this would either require remarkable luck or an incredible amount of trial and error, therefore we use a numerical integrator. In Python, the function *FSOLVE* can aid with obtaining the correct gradient. *FSOLVE* finds the roots of a given linear or non-linear function using Powell’s method (Powell 1964). Obviously, this method is conducted for one eigenfunction so far, for the differential equation of choice, which in this case is \hat{v}_x . However, it is a requirement for trapped waves that both \hat{P}_T and \hat{v}_x are continuous across the boundary. Therefore a technique to satisfy the other eigenvalue \hat{P}_T must be considered. The expression for the total pressure perturbation inside a non-uniform magnetic slab is:

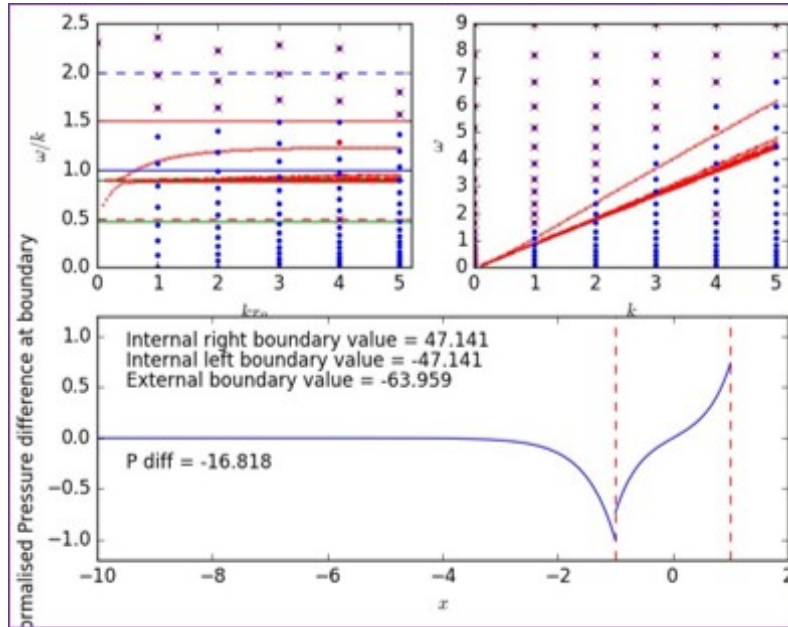
$$\hat{P}_{Ti} = i \frac{\rho_i(x)}{\omega} (c_i(x)^2 + v_{Ai}(x)^2) \frac{(k^2 c_{Ti}(x)^2 - \omega^2)}{(k^2 c_i(x)^2 - \omega^2)} \frac{d\hat{v}_x}{dx}, \quad (2.7)$$

and the same expression for the total pressure perturbation outside but variables will possess subscript e . Fortunately, when calculating the spatial values of \hat{v}_x using the shooting method, the gradient \hat{v}'_x (where a prime denotes a derivative with respect to space) is also calculated at each point in the spatial domain as the governing differential equation has been reduced to a first order differential equation. Therefore it is straightforward to calculate the value of \hat{P}_T everywhere inside the magnetic slab as all the variables in Equation (2.7) are now known. The value of \hat{v}_x is trivially matched at the boundary due to the shooting method using the known boundary value obtained from the external region as the starting point for the internal shooting method. However, for \hat{P}_T , the value at the boundary depends on \hat{v}'_x and will only be continuous for a specific combination of ω and k .

The numerical algorithm continuously loops through wave frequency when the wavenumber is fixed. Therefore, for each eigenvalue combination, the values for \hat{P}_{Ti} and \hat{P}_{Te} at $x = x_0$ are calcu-



(a)



(b)

Figure 2.3: Example of how the numerical algorithm implements the bisection method when locating eigenvalues that are solutions to the governing differential equation. This case represents the sausage mode in a magnetic slab. In both plots sample can be seen indicated by the red dot on the top two panels, the resulting total pressure perturbation eigenfunction is shown in the bottom panel. In panel (a) the sample produces a value of $\delta\hat{P}_T$ which is positive, i.e. the value of \hat{P}_{Ti} at $x = x_0$ is greater than that of \hat{P}_{Te} at $x = x_0$. However, in panel (b), we have passed a known analytical solution (marked by the small red crosses) and the value of $\delta\hat{P}_T$ has changed sign.

lated. Using this information it is possible to calculate the difference in total pressure perturbation $\delta\hat{P}_T$ across the boundary:

$$\delta P_T = P_{Te} \Big|_{x=x_0} - P_{Ti} \Big|_{x=x_0}. \quad (2.8)$$

Using Equation (2.8), the variable $\delta\hat{P}_T$ will be either positive or negative for a specific combination of eigenvalues. Consider a case, say $\omega = \omega_1$ and $k = k_1$ returns a values of $\delta\hat{P}_T < 0$. In this particular example, the value of \hat{P}_{Ti} at the boundary is greater than that of \hat{P}_{Te} at the same location. In this assumption we also consider that, so far, the two values of \hat{P}_{Ti} and \hat{P}_{Te} are not very close to each other. With this information, the code will not do anything special, because the total pressure perturbation is not continuous across the boundary, it will continue onto the next eigenvalue pair to seek a solution. However, lets suppose that the second iteration for $\omega = \omega_2$ and $k = k_1$, that $\delta\hat{P}_T$ is now positive. It is clear that now the difference in total pressure perturbation has changed sign in between the two sample eigenvalues ω_1 and ω_2 . This change in sign across the boundary indicates that a root lies somewhere in between ω_1 and ω_2 , this is the same physical procedure applied in the bisection method for solving transcendental equations. Now that this change in sign of $\delta\hat{P}_T$ has occurred, the numerical code will recognise this and assume that a solution lies somewhere in the range $\omega_1 < \omega_{\text{root}} < \omega_2$, where ω_{root} represents a root satisfying the eigenvalue problem. As a result, the code will return to eigenvalue ω_1 and repeat the shooting method process, solving the governing differential equation for ω_1 and k_1 , however, the frequency range is now divided into two such that the second iteration will solve the governing differential equations for $\omega = \omega_{1.5}$ and $k = k_1$. By doing so, the value of $\delta\hat{P}_T$ will change sign again, either between $\omega_1 < \omega < \omega_{1.5}$ or between $\omega_{1.5} < \omega < \omega_2$. This will isolate the root within one of the two regimes. When the value of δP_T changes sign again, the bisection method is implemented again, until the frequency range is narrowed to isolate the root. Numerically, it can be computationally expensive to repeat this process to locate the root to a high level of precision. Therefore, a new variable is introduced that determines how small the absolute value of $\delta\hat{P}_T$ must be such that the eigenvalues being sampled can be classified as a solution. This variable denoted by ϵ can be altered, however, must provide a reasonable balance between the accuracy and precision of the solution. Setting ϵ to be a very large number will result in the code running faster and being less computationally expensive, however, will also result in a poor accuracy of solution. On the other hand, setting ϵ very small may result in a highly accurate solution, however, may take a long time to find it, which is not ideal particularly in the case when a lot of sample points are considered. Of course the boundary conditions should be analytically continuous anyway, however, numerically this may not be possible, which is the purpose of the variable ϵ . Figure 2.3 outlines the method adopted by the numerical eigensolver to locate solutions to the governing differential equations by implementing the bisection method. The bottom panel shows the spatial structure of the total pressure perturbation eigenfunction. The value of $\delta\hat{P}_T$ changes sign when the sample eigenvalue passes a known solution, in doing so, the internal eigenfunction solution passes the external value at the boundary. This process repeats until $\delta\hat{P}_T < \epsilon$ in which case this condition satisfies that of a solution and the code moves onto the next eigenvalue pair.

Finally, due to the linearity of this problem, it would be a wise idea to expand the numerical code to include multiprocessing techniques to optimise the algorithm. At an early stage in the development, it became obvious that multiprocessing would significantly improve the quality of the code. As a result, multiprocessing commands were added such that each wavenumber k value would be submitted to a separate processor where the algorithm could be run independently. This would allow the integration and shooting method to be conducted for multiple wavenumber values at once until an eigenvalue pair is located. Once this is achieved the solutions are saved to an array on that processor and the next available wavenumber value is sent to that same processor.

When all eigenvalues are located, the eigenvalue arrays are combined from all processors where the elements of each array correspond to the eigenvalue pairs. It is then straightforward to sort the arrays in ascending (or descending) values of, e.g. wavenumber.

2.2.1 Resonance locations

It is expected that when considering a non-uniform plasma, where the inhomogeneity is transversal to the magnetic field, that there are going to be locations at which the governing differential equation(s) become singular, that is, the eigenfunction tends to infinity. Physically, this represents a resonant point where interesting physics can occur, including resonant absorption and phase mixing (see Section 1.7.2). The regions within which this phenomenon can occur are known as the Alfvén and cusp continuum's. Unfortunately, when considering only the ideal MHD equations, the shooting method fails when it encounters a resonant point, as these correspond to singularities in the governing equations. Derivatives at these locations become very large over a very small spatial step and the solution is no longer defined. Numerically this is an issue and can be complicated to fix without including non-ideal effects in the MHD equations to remove these resonances.

During part of the PhD a short practical investigation was conducted to determine whether it was possible to solve this problem during the time frame of the project. This involved considering a variety of thought experiments that could be conducted within a short time frame.

Initially, the step size of the spatial domain was decreased such that the spatial array inside the non-uniform region consisted of more points, located closer to each. The idea was that reducing the step size could reduce the size of gradients in between each point where calculations had to be made. The problem with this is that by increasing the size of the spatial arrays in the numerical calculation, the time required to complete the calculation is also increased. However, it was found that decreasing the step size alone did not make a sufficient improvement to compensate the additional computation run time. It appeared that even with decreasing the step size in the spatial domain and interpolating the result, that it was not sufficient to avoid the singularities and provide a smooth solution.

One approach that was not investigated that may be useful in future improvements of the code involves applying jump conditions (Sakurai et al. 1991, Goossens et al. 1992), this classifies as a driven problem. The jump conditions were derived to provide an analytical expression which keeps the continuity of the relevant eigenfunctions across a singular point. It considers taking a point at either side of the resonance point and ensuring that the relevant boundary conditions on the continuity of total pressure perturbation and radial displacement perturbation are maintained across the resonance point.

Finally, another approach that was explored was to consider the wave frequency as a complex quantity, which corresponds to an eigenvalue problem. By doing this, it would allow the eigenvalue solution to stray away from the real axis and possess an imaginary component. The benefit of doing this would be that solutions inside the continua could still be obtained and investigated. However, numerically integrating the ODE such that both the real and imaginary components of the ODE were continuous across the waveguide boundary was complicated. A short analysis into whether this would be possible was undertaken and although some early results were positive, which is explained in more detail below, the progress was slow and a decision was made to ignore the complex components for the time being and focus solely on the real part of the solutions corresponding to trapped wave modes. A simple case study which considered a second order ODE in the form $y'' + Ay' + By = 0$, where A and B can be coefficients with imaginary components, e.g. $\omega = \omega_r + i\omega_i$, was modelled. The ODE was solved analytically between two spatial values, 0 and 1, with known initial conditions, with the aim to use the numerical shooting method to match

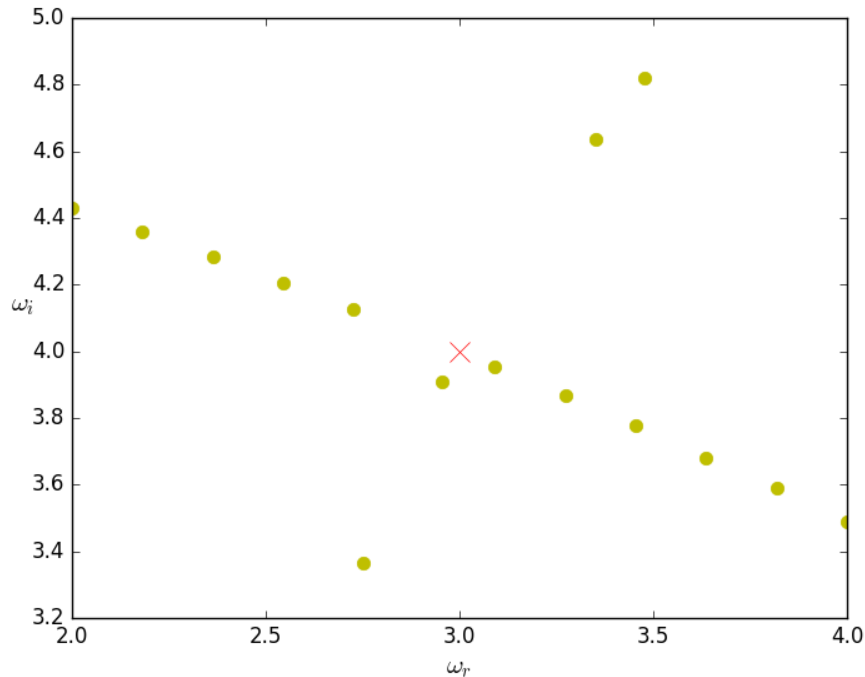


Figure 2.4: Basic plot showing the obtained solutions, using a similar numerical technique to the eigensolver outlined in this chapter, applied to an ODE with complex coefficients. The yellow dots indicate the obtained roots of either the real part, or the imaginary component, of the governing function. These solutions trace out straight lines that intersect at the known full solution, denoted by the red cross.

the required value at the second spatial point, to test the feasibility of the shooting method when the wave frequency is modelled as an imaginary value. We found that it is possible to apply the bisection method for the real and imaginary component simultaneously to eventually converge at the correct solution. It was deduced that, in the frequency plane with the real part, ω_r , plotted over one axis and the imaginary part, ω_i , on the other, each component has roots that trace out a diagonal line intersecting at the solution upon which the root of the function y is obtained for both the real and complex components. Therefore, the actual solution that satisfies both conditions on the real and imaginary components is where these two lines intersect. By examining the change in sign in the difference between the known analytical value and the numerical value of either the real or imaginary component these two lines can be obtained. For example, the very basic plot shown in Figure 2.4 displays the obtained solutions (the yellow dots) for frequency values where either the real or imaginary root is found. It can be seen clearly that these obtained solutions path out a straight diagonal line. The exact solution (given analytically from the start of the investigation) lies where these lines intersect each other denoted by the red cross in Figure 2.4. Applying this to the boundary conditions of a solar waveguide would require using this method to match the boundary conditions of the external values of each eigenfunction \hat{P}_T and $\hat{\xi}_r$ separately. This scenario is more complicated than the single ODE study presented here, however it offers exciting future work to extend the endless capabilities of this numerical tool.

Our results show that whilst it is definitely possible to overcome this problem, the strict time frame of the project and the other objectives that wanted to be achieved, resulted in this target

being beyond the scope of the PhD project. Using the ideas presented in this section, inclusion of a method to investigate resonance behaviour should definitely be considered in future work.

2.3 Magnetic Cylinder (cylindrical geometry)

Similar to the scenario encountered in the magnetic slab analysis, the governing differential Equations (1.35) and (1.38) in a cylindrical geometry have no known closed form analytical solutions without making assumptions that somehow reduce the mathematical complexity. Therefore, investigating the properties of wave modes propagating within a cylindrical equilibrium which is non-uniform must be carried out numerically.

In this case, the fundamental procedure to obtain the eigenvalues for any symmetrically non-uniform equilibria is essentially the same for that of a magnetic slab. However, due to the changes in geometry between Cartesian and cylindrical, minor adaptations must be made to overcome any new numerical issues which may arise. The major numerical implication of switching to cylindrical geometry can be seen in Equations (1.35) and (1.38). At the centre of the cylinder, where $r = 0$, both these equations become singular due to the coefficients tending towards an infinite value. Following the brief discussion in Section 2.2.1 the shooting method will ultimately fail when trying to calculate gradients at or across the regular singularity ($r = 0$). Therefore, an alternative approach must be adopted in a cylindrical geometry in order to obtain the permissible eigenvalues in a non-uniform cylinder. In the scenario for a magnetic slab, the relevant boundary conditions on total pressure perturbation and continuity of radial displacement were applied at the opposite boundary for both the sausage and kink modes. In a cylindrical geometry, a vertical cross cut through the centre of the cylinder would reveal a ‘slab like’ structure in the sense that two boundaries would exist. However, as mentioned previously, it is not possible to solve at the opposite boundary in a magnetic cylinder as the shooting method will fail before the opposite radius value is reached. Therefore, instead of the second boundary condition being applied at the opposite boundary, it is applied at the (numerical) centre of the waveguide. Obviously, for numerical reasons, the second boundary value cannot be applied at $r = 0$ because this is where the governing equations become singular, instead a value as close as numerically possible to $r = 0$ is chosen. Assuming that the waveguide is symmetric about $r = 0$ means that the opposite region (in Cartesian geometry) does not need to be solved, as this is taken care of by the azimuthal wavenumber m . Note that the same approach could have been applied in the Cartesian case however as no fundamental issue occurred at $x = 0$ it was not a problem at that time.

Properties of the sausage and kink mode also apply at the centre of the cylinder. It is well known that the sausage mode is the axisymmetric mode, as a result it does not perturb the axis of the waveguide. Therefore, the first boundary condition is that for the sausage mode, $\hat{\xi}_r = 0$ at the numerical centre of the waveguide, where the numerical centre is taken to be somewhere close to $r = 0$, for example $r = 0.001$. On the other hand, it is known that the kink mode does perturb the axis of the structure and as a result has a maximum value at the numerical centre. As this exact value is unknown, an alternative variable must be used, which is the spatial gradient $\hat{\xi}_r'$. If the displacement is a maximum at the centre of the waveguide, then mathematically, the gradient must be equal to zero (the same mathematical principle applies for a minimum value of a function too).

In Table 2.1 we show a summary of the physical properties for the sausage and kink modes that are used in the numerical shooting method. The conditions in Table 2.1 satisfy the governing differential equations (1.22) and (1.23) for both the sausage and kink modes. Equation (1.22) is satisfied trivially for the $m = 1$ kink mode at $r = 0$, whereas Equation (1.23) reduces to $C_1 = 0$.

Azimuthal mode number	\hat{P}_T at $r = 0$	\hat{P}'_T at $r = 0$	$\hat{\xi}_r$ at $r = 0$	$\hat{\xi}'_r$ at $r = 0$
$m = 0$ - sausage	min/max	0	0	min/max
$m = 1$ - kink	0	min/max	min/max	0

Table 2.1: *Properties for both the $m = 0$ sausage mode and $m = 1$ kink mode that are used in the shooting method of the numerical tool. The governing differential equations are for eigenfunctions which must be continuous across the boundary and have particular properties at the center of the waveguide also.*

For a uniform cylinder with no background magnetic twist or plasma flow, this condition is also satisfied trivially for the sausage mode using Equation (1.31). However, when background magnetic twist or plasma flow is present, care must be taken to ensure that this condition is still satisfied such that the code retrieves the correct eigenvalues. In this work, we consider profiles of either v_φ or B_φ to be proportional to the radial distance r . When this is the case, the variable Q in Equation (1.31) has the presence of r in the numerator of each term, which will satisfy the condition in Table 2.1 trivially. In this thesis, we do not study higher order wave modes ($m > 1$), however this may be possible to study in future work as the value of m can be explicitly given, the only other conditions that would need to be known would relate to those shown in Table 2.1.

We need to stress that the numerical eigensolver presented in this chapter is not unique in that we suggest it presents new analytical or numerical methods to solve an eigenvalue problem in the context of MHD. The simple numerical procedure which we present has been applied before, in a similar fashion, in solar physics by, e.g. Tirry & Goossens (1996), Pinter et al. (1998), Andries et al. (2000), Taroyan & Erdélyi (2002, 2003), although the precise application may vary slightly on a case by case basis. It should also be noted that these works utilise the jump conditions, briefly discussed in Section 2.2.1, such that they can conduct their analysis by considering the wave frequency as an imaginary quantity, providing a greater insight into instabilities and wave damping. On the other hand, one aspect of novelty in the present methodology is the application of multiprocessing in seeking solutions to the eigenvalue problem. As the problem is linear, solutions can be numerically obtained on separate processors and combined later on, significantly reducing computation time. The benefit of this is that either the solutions can be obtained in a shorter timescale to previous studies, or more samples can be analysed in the same timescale to improve the resolution (data points) of the resulting dispersion diagram.

2.4 Summary

A summary of the procedure which the numerical eigensolver follows is:

1. Set up the initial equilibrium ensuring that radial pressure balance is achieved across the boundary of the waveguide, either in Cartesian or cylindrical geometry.
2. Define the initial sampling grid by creating arrays for wavenumber k and wave frequency ω . It is possible to split the frequency ranges such that the same number of samples are considered in different phase speed bands (i.e. 10 samples between c_{Ti} and c_i and also 10 samples between c_i and v_{Ai}).
3. Using multiprocessing, separate wavenumbers are sent to different processors such that the procedure is more numerically efficient. As the eigenvalues are independent on k for each eigenvalue pair this is permissible. When the procedure is complete, the solution arrays from each processor are combined.

4. The code then solves for the $m = 0$ sausage mode and the $m = 1$ kink mode separately using the relevant boundary conditions and/or conditions at the centre of the waveguide. The governing differential equations are solved using the shooting method and the bisection method to locate the solutions.
5. If the condition $\delta\hat{P}_T < \epsilon$ is satisfied, then the current values for k and ω are saved to separate arrays but take the same element number in each array.
6. The solution arrays, for both k and ω , are saved and then are read into a separate script for further analysis.

Chapter 3

The effect of non-uniform plasma density and flow on magnetoacoustic wave modes in a magnetic slab geometry ¹

Abstract

Realistic analytical models of MHD wave propagation in different solar magnetic configurations are required to explain observational results, allowing magneto-seismology to be conducted and provide more accurate information about local plasma properties.

The numerical approach described in Chapter 2 allows the eigenvalues to be obtained for any arbitrary symmetric model of solar atmospheric features. In this chapter the magnetic slab model of a solar waveguide is considered. The dispersion diagrams for a number of analytic cases which model magnetohydrodynamic waves in a magnetic slab are successfully reproduced. These include a uniform slab under both photospheric and coronal conditions, with and without the inclusion of a bulk background plasma flow. A discussion between the obtained numerical solutions and the previously obtained analytical solutions is included.

This study is then extended by considering a non-uniform background plasma density modelled as a series of Gaussian profiles and a $\text{sinc}(x)$ function. These specific profiles cannot be studied analytically. A further case study investigates properties of MHD wave modes in a uniform coronal slab with a non-uniform background plasma flow, for which the governing equations are derived. For all cases the eigenvalues are obtained and compared to the uniform slab. Following this, the resulting eigenfunctions are calculated and analysed with respect to the equilibrium inhomogeneity.

We find that the dispersive properties of slow body modes are more greatly altered than those of fast modes when any equilibrium inhomogeneity is increased, including background flow. The spatial structure of the eigenfunctions is also modified, introducing extra nodes and points of inflexion which may be of interest to observers. Furthermore, regions of continua are identified and waves with frequencies within this range will undergo resonant processes.

¹The content of this chapter appeared as S. Skirvin, V. Fedun and G. Verth, 2021, MNRAS, 504, 4077S (Skirvin et al. 2021)

3.1 Introduction

The understanding of excitation and propagation of MHD waves (see Chapter 1.6) is an important field of research in solar and plasma physics. It is thought that these waves may contribute to coronal heating due to their observed ubiquity throughout the solar atmosphere. These waves may be able to transfer sufficient amounts of energy to the upper layers of the solar atmosphere and undergo dissipation, consequently locally heating up the plasma. A complete understanding of the properties of these waves including their dispersive nature is essential in determining their contribution to the energy budget of the solar atmosphere.

The dispersion diagram provides a useful tool in understanding the properties of various MHD waves. It indicates the permissible phase speeds at which trapped waves propagate and provides information about their dispersive characteristics. Previously, there has been a number of studies devoted to the analysis of MHD wave properties in different magnetic configurations. As discussed previously in Chapters 1.5, Roberts (1981*a*) and Edwin & Roberts (1982) investigated MHD waves in Cartesian geometry modelled as a magnetic interface and a magnetic slab, respectively. The magnetic slab has been investigated in both magnetic and a field-free environment. A visual representation of the uniform slab was shown earlier in this thesis in Figure 1.2a and a cartoon of the non-uniform magnetic slab is shown in Figure 3.1.

These theoretical studies have provided the fundamental models which describe wave propagation for magnetic waveguides found in the solar atmosphere. Further extensions of these models were provided by introducing steady background plasma flows (Nakariakov & Roberts 1995*a*), linear background flows (Zaqarashvili 2011) and also moving to cylindrical geometry (Edwin & Roberts 1983) which is discussed further in Chapter 4, with magnetic twist (Erdélyi & Fedun 2007*b*, 2010) (discussed in Chapter 5) and curvature of the waveguide (Verwichte et al. 2006*a,b*, Van Doorselaere et al. 2009), to name but a few.

Generalising the traditional slab model of a solar waveguide to a more realistic case has been an extensive area of research. For example, coronal loops have been modelled in planar geometry with smooth density profiles (Lopin & Nagorny 2015*a*), although these studies consider a continuous background plasma profile and do not match any boundary conditions, simply because there are no distinct boundaries in the model. The period ratio of the fundamental mode to twice the first overtone $P_1/2P_2$ was investigated by Macnamara & Roberts (2011) for a coronal loop with an Epstein density profile. The authors found that there were striking similarities to that of the step function considered traditionally, suggesting that the step function profile for density may actually be a useful model for wave investigations. Chen et al. (2018) derived a generalised dispersion relation for fast waves in a coronal slab with a finite plasma- β and compared the results to those for fast waves in zero plasma- β coronal slabs. However, in this investigation, continuous transverse profiles are considered to be split into three regions where the outer two regions are uniform separated by the middle regime which is allowed to be arbitrarily non-uniform.

Previous works have developed a number of techniques to numerically solve the differential equation with carefully chosen profiles for plasma density or Alfvén speeds (Oliver et al. 1993, Verwichte et al. 2006*a*, Soler et al. 2017, Thackray & Jain 2017). These studies also focus on coronal structures, namely coronal loops, where plasma pressure is assumed negligible and the plasma- β is zero. The cold plasma- β limit restricts these investigations to fast magnetoacoustic waves only as it is assumed that the Lorentz force dominates. The behaviour of MHD waves propagating in coronal loops with specific inhomogeneous density profiles has also been studied before in both planar and cylindrical geometries, see, e.g. Edwin & Roberts (1988), Nakariakov & Roberts (1995*b*), Lopin & Nagorny (2015*a,b*), Li, Guo, Yu & Chen (2018). The specific choice of the density profile could result in an analytical derivation of the dispersion relation. However,

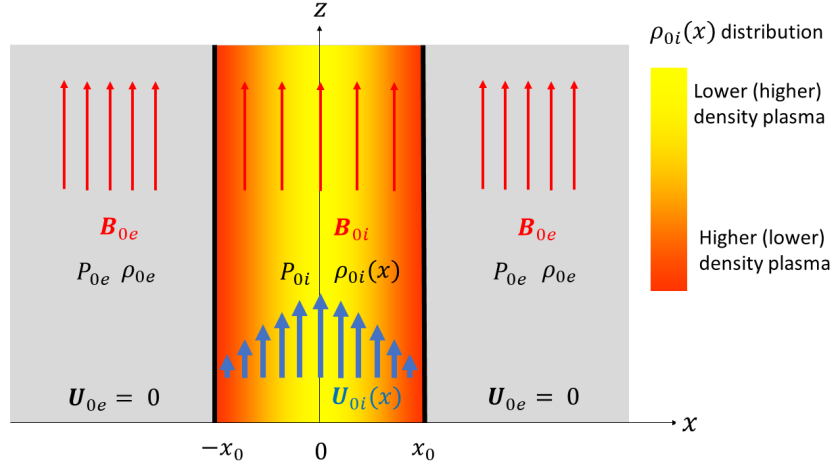


Figure 3.1: A cartoon displaying a magnetic slab which is traditionally used to model waveguides in the solar atmosphere. The red arrows represent magnetic field lines and intend to show the different magnetic configurations in each regime internal and external to the waveguide. Blue arrows represent the vertical equilibrium velocity field which may be non-uniform in spatial coordinate x . The slab is assumed to be homogeneous and unbounded in the y -dimension. Parameters ρ , P , \mathbf{U}_0 and \mathbf{B} denote plasma density, pressure, background flow and magnetic field respectively. Subscripts i and e relate to internal and external properties respectively. The case studies considered in this Chapter investigate a spatially varying density profile $\rho_{0i}(x)$ and vertical background flow $U_{0i}(x)$. In reality any/all equilibrium background plasma variables are allowed to be inhomogeneous and the numerical eigensolver is capable of handling such a scenario. The specific spatial profiles considered in this chapter are shown in Figures (3.4), (3.9) and (3.12) for inhomogeneous equilibrium density and also Figure (3.15) for an inhomogeneous background flow.

in the majority of these cases a continuous density profile is considered, such that there are no boundaries of the waveguide and as a result, no boundary conditions to be matched. In this case, the kink and sausage mode are not determined by the motion of the waveguide, but instead the behavior of the driver of the perturbations, as kink and sausage modes appear only in waveguides.

Studies of wave behaviour in the context of different realistic background plasma profiles are important as they provide information on group velocity as a function of density structure (Edwin & Roberts 1988), and, therefore, on how the waves may transfer their energy. Whilst this research has greatly advanced understanding of wave phenomena in coronal structures, the dispersion relation is derived in all cases through carefully chosen plasma profiles allowing an analytical solution to be obtained. To model wave propagation in a realistic magnetic configuration with a spatially varying plasma equilibrium in the presence of background flows, a numerical approach has to be used. Very recently Claes et al. (2020) have developed a numerical code to solve the full MHD spectrum for any given 1D equilibrium. In the approach presented by the authors a finite element method (FEM) was implemented to identify the permissible eigenvalues.

In this chapter, the numerical methodology for obtaining solutions located on the dispersion diagram based on the shooting method approach will be compared to previous studies of wave propagation and analytically derived dispersion relations in a magnetic slab geometry. These comparisons are carried out under the context of both static background plasma and steady background plasma flow. In Section 3.3 the developed method will be applied to inhomogeneous density profiles which take the form of a Gaussian distribution and a $\text{sinc}(x)$ function, better known as $\sin(x)/x$,

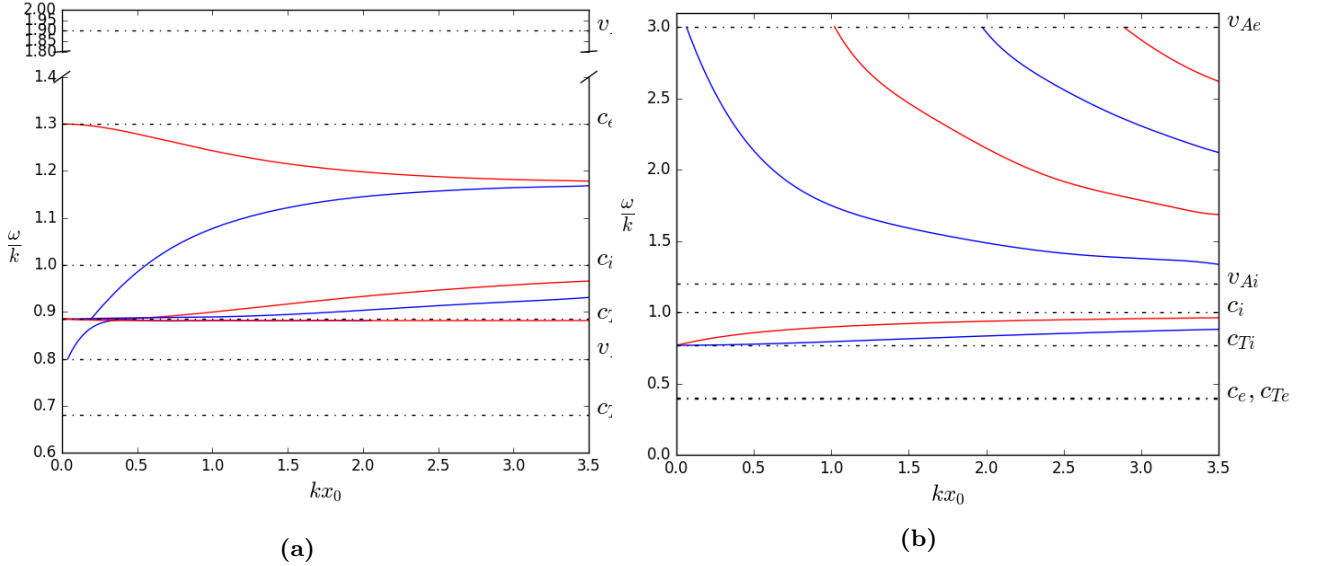


Figure 3.2: The obtained numerical solutions for the case of a uniform magnetic slab under (a) photospheric conditions given by $c_e = 1.3c_i$, $v_{Ai} = 1.9c_i$ and $v_{Ae} = 0.8c_i$. (b) Coronal conditions given by $c_e = 0.4c_i$, $v_{Ai} = 1.2c_i$ and $v_{Ae} = 3c_i$. Red curves indicate the sausage mode solutions, whereas the blue curves show solutions for the kink mode.

which have not been previously investigated and can not be solved analytically. Finally, in Section 3.4 the properties of MHD waves in a coronal slab in the presence of a Gaussian non-uniform background flow is investigated. A graphical representation of a non-uniform magnetic slab can be seen in Figure 3.1. In this cartoon, the non-uniform internal plasma density is denoted by the contour inside the waveguide, which is free to vary provided it remains symmetric around $x = 0$. The slab is uniform in the z direction and the waveguide boundaries are shown by the solid lines at $x = \pm x_0$. In all cases the plasma outside the waveguide is uniform. The blue arrows show the vertical profile of the background plasma flow, which can be non-uniform in the transversal direction, again providing symmetry around $x = 0$. In all cases the magnetic field is taken to be vertical and uniform in each region, shown by the red arrows.

3.2 Recovering previous analytical results

3.2.1 Uniform magnetic slab

In this section the results of the method will be compared to results previously obtained by Edwin & Roberts (1982) in which a magnetic slab embedded in a magnetic environment in the absence of background plasma flow is investigated. The visual model of this problem is shown in Figure 1.2a where the plasma in the internal and external regions is assumed to be uniform. The boundaries of the slab are located at $\pm x_0$ and by matching the necessary boundary conditions with an analytical expression, the dispersion relation can be derived. The analytic dispersion relation is derived with a closed form solution by assuming that all plasma quantities including sound and Alfvén speed are uniform in all regions. The known analytic dispersion relation is given by Equation (11) in Edwin & Roberts (1982) and is written below for reference:

$$\rho_e (k^2 v_{Ae}^2 - \omega^2) m_i \left\{ \begin{array}{l} \tanh \\ \coth \end{array} \right\} (m_i x_0) + \rho_i (k^2 v_{Ai}^2 - \omega^2) m_e = 0, \quad (3.1)$$

where the *tanh* function corresponds to sausage mode solution, whereas the *coth* function corresponds to kink mode solution.

The solutions of Equation (3.1) give the resulting dispersion diagram. Here, the functions F and G in Equation (2.5) are constant and, therefore, Equation (2.5) describing motions inside the slab can be written as:

$$\hat{v}_x'' - m_i^2 \hat{v}_x = 0, \quad (3.2)$$

where

$$m_i^2 = \frac{(k^2 v_{Ai}^2 - \omega^2) (k^2 c_i^2 - \omega^2)}{(c_i^2 + v_{Ai}^2) (k^2 c_{Ti}^2 - \omega^2)}.$$

The corresponding total pressure perturbation inside the slab, given by Equation (2.6), can be written as:

$$\hat{P}_T = i \frac{\rho_i}{\omega} (c_i^2 + v_{Ai}^2) \frac{(k^2 c_{Ti}^2 - \omega^2)}{(k^2 c_i^2 - \omega^2)} \frac{d\hat{v}_x}{dx}, \quad (3.3)$$

which is proportional to the derivative in the velocity perturbation. Equations (3.2) and (3.3) provide the two expressions that must be matched, both inside and outside, at the waveguide boundary. All variables outside of the slab will have indexes e but take the same form as Equations (3.2) and (3.3). Following the procedure outlined in Section 2, the shooting method is applied to solve equation (3.2). A solution will only be obtained if a value of frequency and wavenumber simultaneously satisfies Equations (3.2) and (3.3) for \hat{v}_x and \hat{P}_T .

Using the numerical tool, the obtained solutions can be seen in Figure 3.2a that the obtained solutions for surface waves and body waves fits well those results found previously by Edwin & Roberts (1982, see Figure 3) under photospheric conditions ($v_{Ae} < c_i < c_e < v_{Ai}$). Typically, obtaining solutions for body modes, located between $c_{Ti} < v_{ph} < c_i$ ($v_{ph} = \omega/k$) for the photospheric case, tends to be more difficult due to the reduced step size required when numerically solving the dispersion relation by the bisection method, however, this method finds the exact solutions with no alterations in the algorithm. More MHD wave modes could be retrieved by increasing the number of samples in the domain, however this comes at a cost of increased numerical intensity, so a balance must be found. This also includes higher harmonics of body modes which will be retrieved also with increasing resolution.

The results of the calculation for the scenario of a magnetic slab under coronal conditions ($c_e < c_i < v_{Ai} < v_{Ae}$) are shown in Figure 3.2b and can be compared to Figure 4 in Edwin & Roberts (1982). Similarly to the photospheric case, the phase speed solutions are recovered well for both the sausage and kink modes. Under coronal conditions as stated by Edwin & Roberts (1982) only body modes exist, indicating here the power of this method to recover body mode solutions with no additional steps required in the algorithm. It can be seen that only specific branches of the fast body waves are recovered, presumably these are the first harmonics and higher harmonics will be identified with greater resolution.

3.2.2 Uniform magnetic slab with steady background plasma flow

The magnetic slab model can be further extended to investigate observed features in the solar atmosphere such as jets, by the inclusion of a background steady flow. In this case, a steady flow

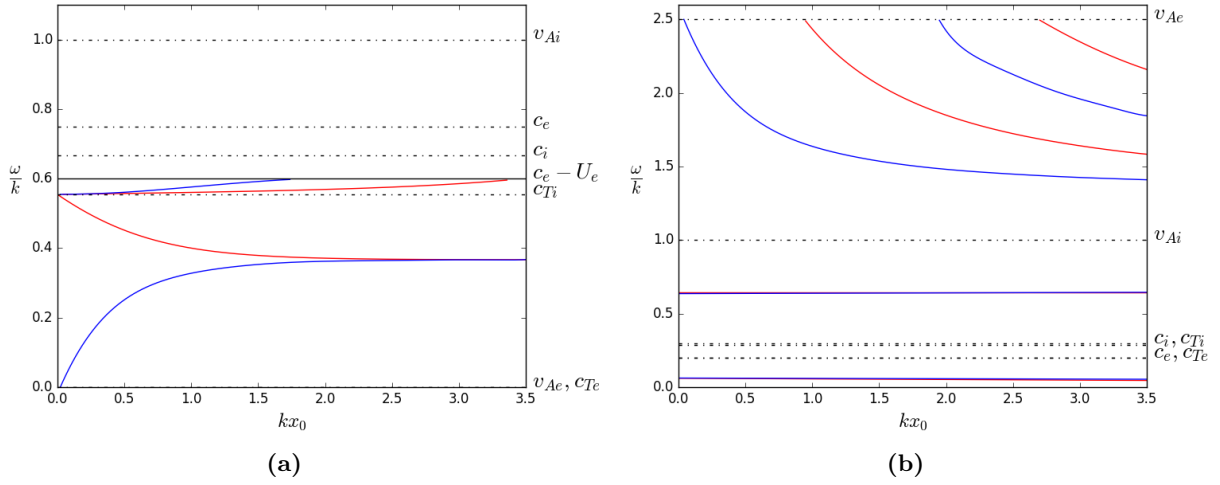


Figure 3.3: The numerical solutions plotted on the dispersion diagram for a magnetic slab with a steady background plasma flow under (a) photospheric conditions given by $c_i = 0.67v_{Ai}$, $c_e = 0.75v_{Ai}$ and $v_{Ae} = 0$ with an external flow of $U_e = -0.15v_{Ai}$ and no internal flow. (b) Coronal conditions given by $c_i = 0.3v_{Ai}$, $c_e = 0.2v_{Ai}$ and $v_{Ae} = 2.5v_{Ai}$ with an internal flow of $U_i = 0.35v_{Ai}$ and no external flow. Same as Figure (3.2) but for a slab model with a steady background flow.

refers to a plasma flow that is spatially and temporally constant. Previous studies have included the addition of a steady background plasma flow, see e.g. Nakariakov & Roberts (1995a), Zaqrashvili (2011), Ebadi et al. (2011) and found that the introduction of a background flow into the model increases the amplitude of the wave perturbations. Furthermore, the flow also gives the waves an observed Doppler shift when compared to the static magnetic slab model, a frequency shift which is proportional to the speed of the flow. Furthermore, introducing a background flow supports development of the KHI at the boundary of the flux tube. A study into the evolution of the KHI is beyond the scope of this thesis as this would correspond to a value $\omega_i > 0$, which, as discussed in Chapter 2, is not supported by the numerical code as of yet.

In the presence of a steady background plasma flow, the structure of Equation (2.5) remains the same, but the wave frequency, ω , is now shifted by a magnitude proportional to the plasma flow speed U_0 , i.e. $\omega - kU_0$. As a result the coefficient in Equation (2.5) becomes:

$$m_i^2 = \frac{(k^2 v_{Ai}^2 - \Omega^2)(k^2 c_i^2 - \Omega^2)}{(c_i^2 + v_{Ai}^2)(k^2 c_{Ti}^2 - \Omega^2)},$$

with:

$$\Omega_{0i} = \omega - kU_{0i},$$

where Ω is the Doppler shifted frequency. A similar variable for the region external to the slab takes the same form but is concerned with the external flow, U_{0e} . Now that a flow has been introduced, two conditions at the boundaries of the slab are still required to be satisfied. Whereas before, in the case of a static magnetic slab, the continuity of total pressure and transversal velocity perturbation were the conditions, the latter is replaced by the continuity of the horizontal displacement perturbation in a slab model which includes a background flow. This is because the homogeneous background flow, U_0 , can locally amplify the wave displacement at the boundary and must be

accounted for. Therefore the new boundary conditions which need to be satisfied are given by:

$$\frac{v_{xi}(x = \pm x_0)}{\Omega_{0i}} = \frac{v_{xe}(x = \pm x_0)}{\Omega_{0e}}, \quad (3.4)$$

as explained in Nakariakov & Roberts (1995a) where $\pm x_0$ are the locations of the slab boundaries (see Figure 3.1).

Equations (2.5) and (2.6) along with the condition in Equation (3.4) are used in order to attempt to retrieve the eigenvalues ω and k to be plotted on the dispersion diagram. Nakariakov & Roberts (1995a) have found that the properties of magnetoacoustic waves in a magnetic slab with a background flow were similar to those of the static model. Although, for specific values of external flow, some eigenvalues disappeared from the dispersion diagram and can be absorbed into the shifted continua modified by the background flow.

Figure 3.3a shows the results of the methodology under photospheric conditions with a downward steady flow external to the slab. The phase velocity axis is normalised relative to the internal Alfvén speed so that direct comparison can be made with the results of Figure 2b in Nakariakov & Roberts (1995a). The obtained results show a good agreement of those first retrieved by Nakariakov & Roberts (1995a) and it is possible to sample regions between specific characteristic speeds such that higher resolution can be obtained in the regions of trapped modes which are narrowed due to the presence of the background flow. The corresponding coronal solutions are shown in Figure 3.3b with a steady internal flow of $v_0 = 0.35v_{Ai}$ and no external flow. Again, the same solutions are obtained as those shown in Figure 1c in Nakariakov & Roberts (1995a) including the backward propagating body modes at small v_{ph} . It is reassuring that the numerical tool can recover previously obtained analytical eigenvalues for waveguides modelled as a magnetic slab in both a uniform plasma and with the inclusion of a background flow. In these cases the ideal MHD equations have analytical solutions, therefore the next step is to model a scenario which cannot be investigated analytically by implementing our numerical tool.

3.3 Non-uniform density magnetic slab

In this section, a transversal dependant internal plasma density is introduced into the model. This significantly changes the expression given by Equation (2.5) from the case of a uniform slab, namely the function $F(x)$ is no longer equal to zero. The governing equation now reads:

$$\hat{v}_x'' + \frac{F'(x)}{F(x)} \hat{v}_x' + m_i^2(x) \hat{v}_x = 0, \quad (3.5)$$

where:

$$F(x) = \rho_i(x) \frac{(c_i^2(x) + v_{Ai}^2(x)) (k^2 c_{Ti}^2(x) - \omega^2)}{(k^2 c_i^2(x) - \omega^2)},$$

and

$$m_i^2(x) = \frac{(k^2 v_{Ai}^2(x) - \omega^2) (k^2 c_i^2(x) - \omega^2)}{(c_i^2(x) + v_{Ai}^2(x)) (k^2 c_{Ti}^2(x) - \omega^2)}.$$

The equivalent expression for \hat{P}_T is given by equation (3.3) where all quantities are now a function of x .

Consider a magnetic slab embedded in a stationary, uniform and magnetised environment under coronal conditions ($c_e < c_i < v_{Ai} < v_{Ae}$). Background plasma flow is ignored and the characteristic speeds are chosen to match those given in the coronal case in Section 3.2.1. Shown in Figure 3.4

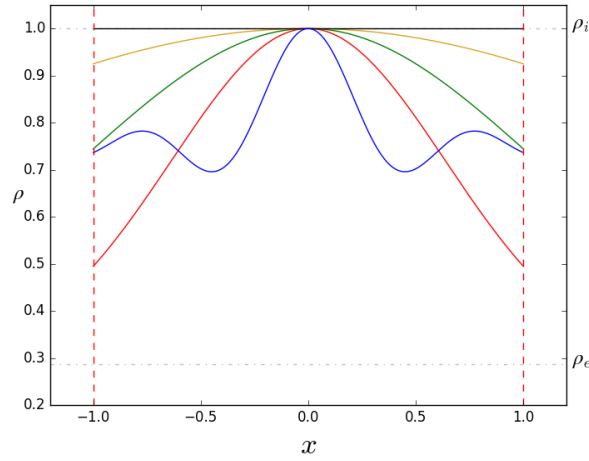


Figure 3.4: The profiles of internal non-uniform plasma density considered in this section. The density is modelled as a series of Gaussian's with varying inhomogeneity in a coronal slab. The profiles are normalised such that they possess their maximum value, which is equal to unity, at x_c . The width of the inhomogeneity is given by $W = 10^5$ (black), $W = 3$ (yellow), $W = 1.5$ (green), $W = 0.9$ (red). A spatial profile proportional to a $\text{sinc}(x)$ (e.g. $\sin(x)/x$) function (blue) is also modelled. In all cases the density is discontinuous at the waveguide boundary and tends towards ρ_e (shown) at the boundary. The boundaries of the slab are located at $x = \pm 1$ and indicated by the red dashed lines.

are the radial profiles for the plasma density structuring considered in this section. A number of cases modelling the density as a Gaussian profile with a varying standard deviation are shown. A case study with a large width (i.e. orders of magnitude larger than the width of the waveguide) corresponds to a uniform plasma as the gradients of inhomogeneity are extremely small. The analytical expression describing the Gaussian profiles is given by:

$$\rho_i(x) = \rho_e + (\rho_{0i} - \rho_e) \exp\left(-\frac{(x - x_c)^2}{W^2}\right),$$

where x_c is the centre of the Gaussian located at $x_c = 0$, W is the standard deviation (i.e. the width) of the density distribution and ρ_{0i} is the maximum internal density given by the value in Section 3.2.1.

When the equilibrium density is non-uniform, then of course, to maintain pressure balance and achieve a stable system, this non-uniform plasma density must be balanced by changing other properties of the plasma. Figure 3.5 shows how the other parameters of the plasma behave for the specific case study when the coronal slab is modelled with a background plasma density with a Gaussian profile and $W = 0.9$. The non-uniform plasma density is compensated by a change in temperature of the plasma such that the gas pressure remains constant across the slab. In the specific case of a slab under coronal conditions where the plasma density decreases towards the boundary of the slab, then the plasma temperature possesses a minimum at the centre of the slab, increasing up to the boundary. This overdense waveguide, balanced by the plasma temperature manages to keep a constant magnetic field across the slab and as a result the total pressure is still continuous across the boundaries.

The other equilibrium density structuring investigated in this section considers a $\text{sinc}(x)$ function. The motivation behind modelling a $\text{sinc}(x)$ profile comes from observations of magnetic bright points (MBP's) which have been observed to have spatial intensity distributions similar to such a

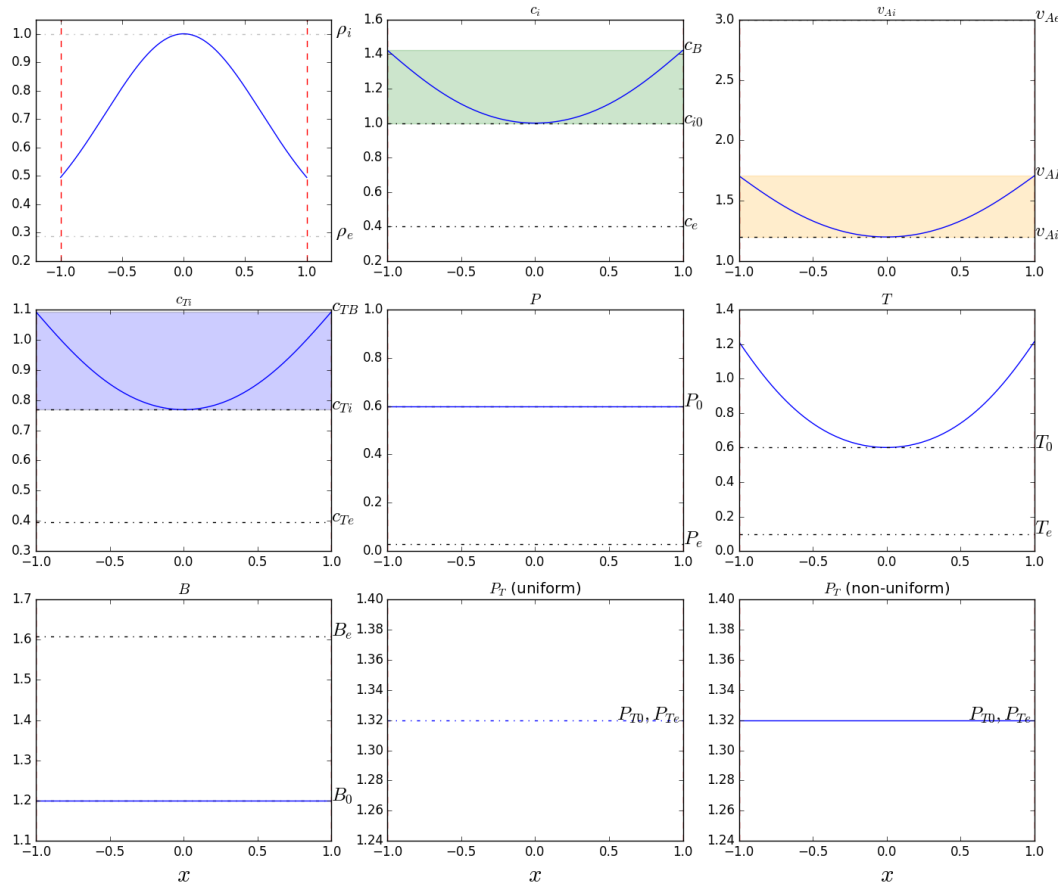


Figure 3.5: Profiles of all plasma properties for the specific case of Gaussian density distribution with $W = 0.9$. Plots showing how the magnetic field, gas pressure, plasma temperature and total pressure along with the characteristic speeds of the system behave for the case of a non-uniform plasma density.

profile (see, e.g. Jess et al. 2010). To fit the numerical domain, the normalised $\text{sinc}(x)$ function is modelled here using:

$$\rho_i(x) = \frac{\rho_{0i}}{4} (\text{sinc}(10x) + 3),$$

for a coronal slab and is normalised such that the maximum is comparable to the uniform slab case. Pressure balance is accounted for by a change in temperature inside the slab. The width of the Gaussian profile determines the gradient of the inhomogeneity. The characteristic speeds are therefore also spatially dependant. This specific case corresponds to a cool magnetic flux tube.

3.3.1 Coronal non-uniform density magnetic slab case study

The solar atmosphere is highly inhomogeneous and types of inhomogeneity could arise from non-uniform density and magnetic field structuring, or unsteady flows. Investigating the trapped wave modes of a solar waveguide within a non-uniform background plasma is relevant to study from a theoretical point of view such that models can be created which more accurately represent those seen in observations. Typically this investigation is done analytically, however, when plasma variables are non-uniform in space, the governing MHD equations become more complicated to solve. Some specific plasma profiles have been previously extensively investigated, chosen such to allow the derivation of an analytic dispersion relation and retrieve solutions on the dispersion diagram. A review of the density profiles which have been studied before are given in Table 4 of Li, Guo, Yu & Chen (2018). Here, the proposed numerical approach will be applied to investigate density profiles which can not be analysed analytically.

For a wide Gaussian profile, the inhomogeneity inside the slab is weak and the plasma is the same as the uniform case described in Section 3.2.1, therefore corresponding to the same results as the uniform case. This case is shown in Figure 3.6a, where the characteristic speeds at the boundary (subscript 'B') correspond to the uniform speeds in Figure 3.2b. The width of the profile here is chosen to be $W \gg 2x_0$, i.e. many orders of magnitude larger than the width of the waveguide. By changing the width of the inhomogeneity (i.e. the standard deviation W), the value of ρ_{0i} decreases at the boundary compared to the uniform case and alters the trapped modes of the system. Figures 3.6b, 3.6c, 3.6d show the resulting dispersion diagrams for the density profiles given by Figure 3.4. The fast body solutions are still bounded between v_{Ae} and v_{Ai} , however, these are cut off by the internal Alfvén speed at the boundary for a narrow Gaussian profile ($W < 1$) as it is not possible for trapped modes with purely real global eigenfrequencies to enter this continua. Slow body waves in an inhomogeneous coronal slab are bounded between the tube speed at the boundary of the waveguide (c_{TB}) and the maximum internal sound speed due to the density structuring for small inhomogeneity. This can be seen in Figures 3.6b and 3.6c, unlike the uniform case, where the slow body waves are trapped between c_i and c_{Ti} . Furthermore, the band located between c_{TB} and maximum c_{Ti} is a continuous spectrum known as the cusp (slow) continuum. This band is due to the singularity in Equation (3.5), when $\omega = kc_{Ti}$ which provides great interest as resonant absorption can occur here and has been subject to previous analytical investigation. Keppens (1996) studied this effect in a cylinder with an unmagnetised surrounding and later Yu et al. (2017b,a) in a photospheric slab with a weakly magnetised surrounding. It is worth further noting that the work by Keppens (1996) also investigated the leaky modes, which can radiate energy away from the waveguide. This study however is beyond the scope of the current study and will be investigated in future work.

Let us now focus on the spatial profile modelled as a $\text{sinc}(x)$ function. This profile is shown by the blue line in Figure 3.4. The value of ρ_{0i} at the boundary for the $\text{sinc}(x)$ profile is similar to that

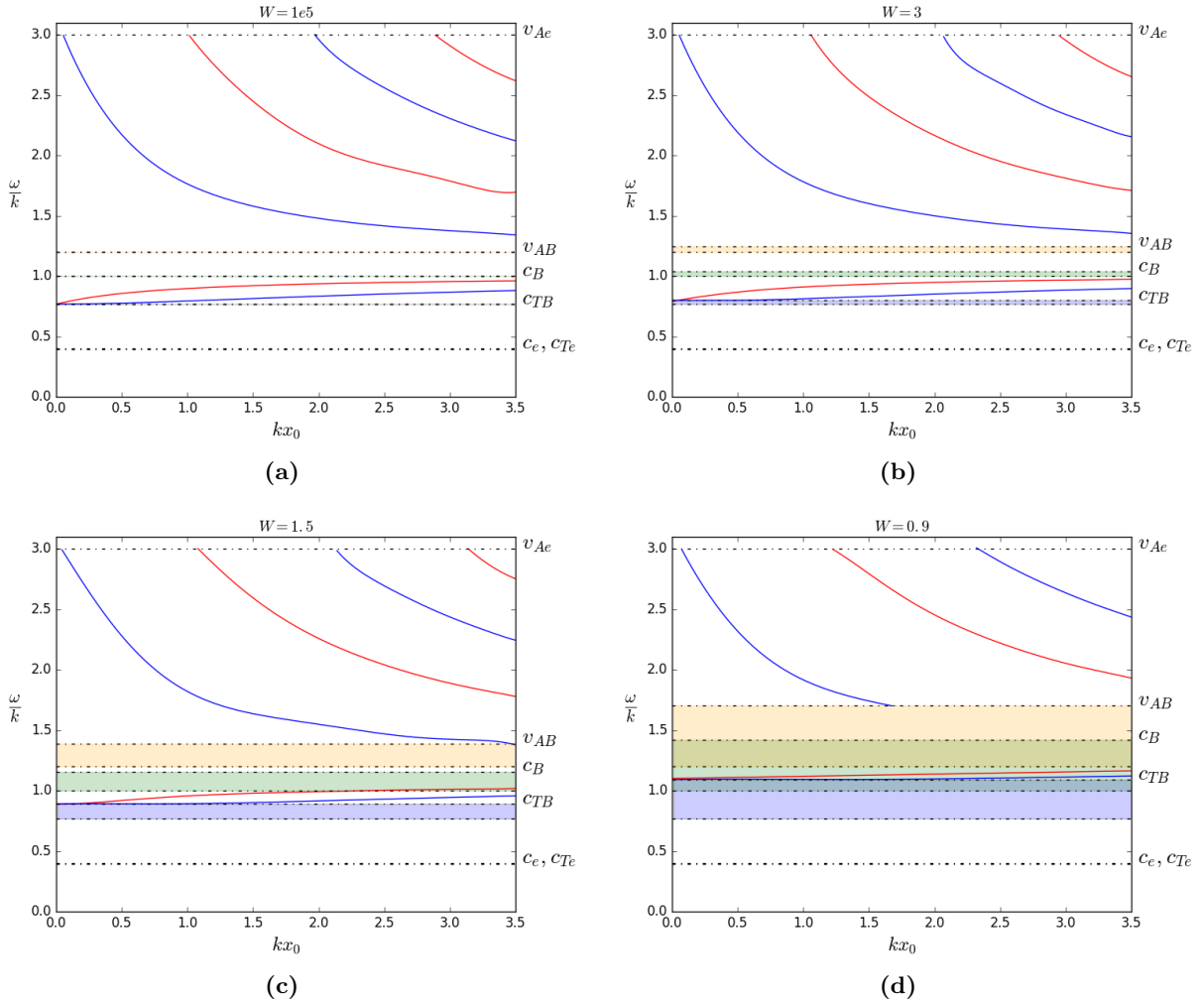


Figure 3.6: Dispersion diagrams showing the trapped solutions in a coronal slab with density structuring of a Gaussian form shown by the profiles in Figure 3.4. Here we show the cases when the width of the density profile, W , is, (a) $W \gg 2x_0$, (b) $W = 3$, (c) $W = 1.5$, (d) $W = 0.9$. The characteristic speeds at the boundaries are sub scripted 'B' with the maximum value of each characteristic speed denoted by the opposite edge of the shaded regions. The blue region corresponds to the slow continuum $c_{Ti}(x)$, green region the inhomogeneous sound speed band and orange region is the Alfvén continuum $v_{Ai}(x)$. Darker shades occur where there is an overlap of two inhomogeneous regions.

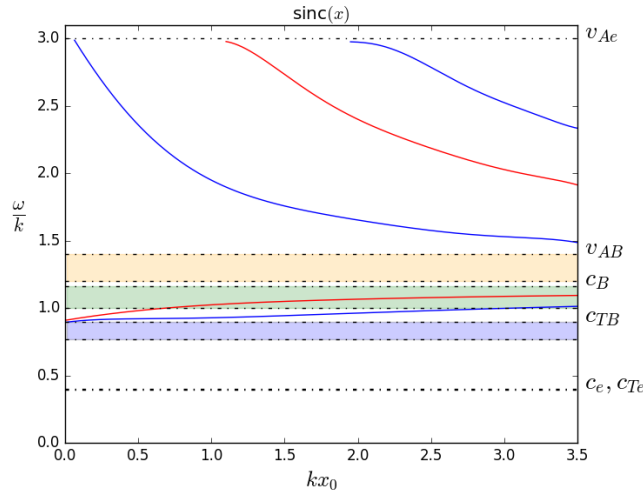


Figure 3.7: The dispersion diagram showing the eigenvalues for a spatial profile proportional to $\text{sinc}(x)$ under coronal conditions. Labels and colours are consistent with Figure 3.6.

of a Gaussian profile with $W = 1.5$, however, the structuring inside the slab is much different. The dispersion diagram shown in Figure 3.7 has similar characteristics to those shown in Figure 3.6c with slight change in the positioning of slow body modes such that the majority of these branches now lie inside the green shaded region which represents the spatial sound speed band.

Comparisons of the eigenfunctions \hat{P}_T and \hat{v}_x for all possible modes are shown in Figure 3.8. For the fast modes, both sausage and kink, equilibrium inhomogeneity has a minor effect on the physical properties of the wave mode. It can be seen in Figure 3.8a that as the Gaussian inhomogeneity is increased, the anti-nodes of the fast sausage mode shift towards the center of the waveguide, an effect which has been shown in coronal loop analysis by Verth et al. (2007). The amplitude of the total pressure perturbation is also locally increased at the centre of the waveguide as the Gaussian inhomogeneity is increased. Figure 3.8b indicates the nodes of the total pressure perturbation become more pronounced as the inhomogeneity increases, a similar albeit more minor effect can be seen in the spatial structure of the \hat{v}_x eigenfunction. It is worth mentioning here that the profile proportional to $\text{sinc}(x)$, similar to varying the width of the Gaussian profiles, does not appear to affect the physical spatial distribution of the eigenfunctions for fast modes in a coronal plasma, suggesting that these fast modes may not be a suitable choice to use for spatial coronal-seismology.

However for the slow modes, the inhomogeneity has a much greater effect. Figure 3.8c shows the perturbed eigenfunctions for the slow body sausage mode. It is obvious that increasing the inhomogeneity away from a uniform plasma has a clear effect on the physical properties of this mode. Decreasing the Gaussian width creates extra nodes and anti-nodes in the resulting \hat{v}_x perturbation, these extra anti-nodes may be misinterpreted in observational data as an entirely different mode. Increased inhomogeneity also has an effect on \hat{P}_T , changing the center of the waveguide from having a maximum to having a minimum at this location for the slow sausage mode. The slow body kink mode is also greatly affected by small inhomogeneity compared to the uniform slab. As the Gaussian width is decreased, the maximum of the \hat{v}_x perturbation is achieved closer to the boundaries of the waveguide, rather than obtaining a single maximum at the centre in the uniform scenario. The total pressure perturbation shown in Figure 3.8d is still zero at the center of the waveguide as expected for the kink mode however displays an anti-symmetric

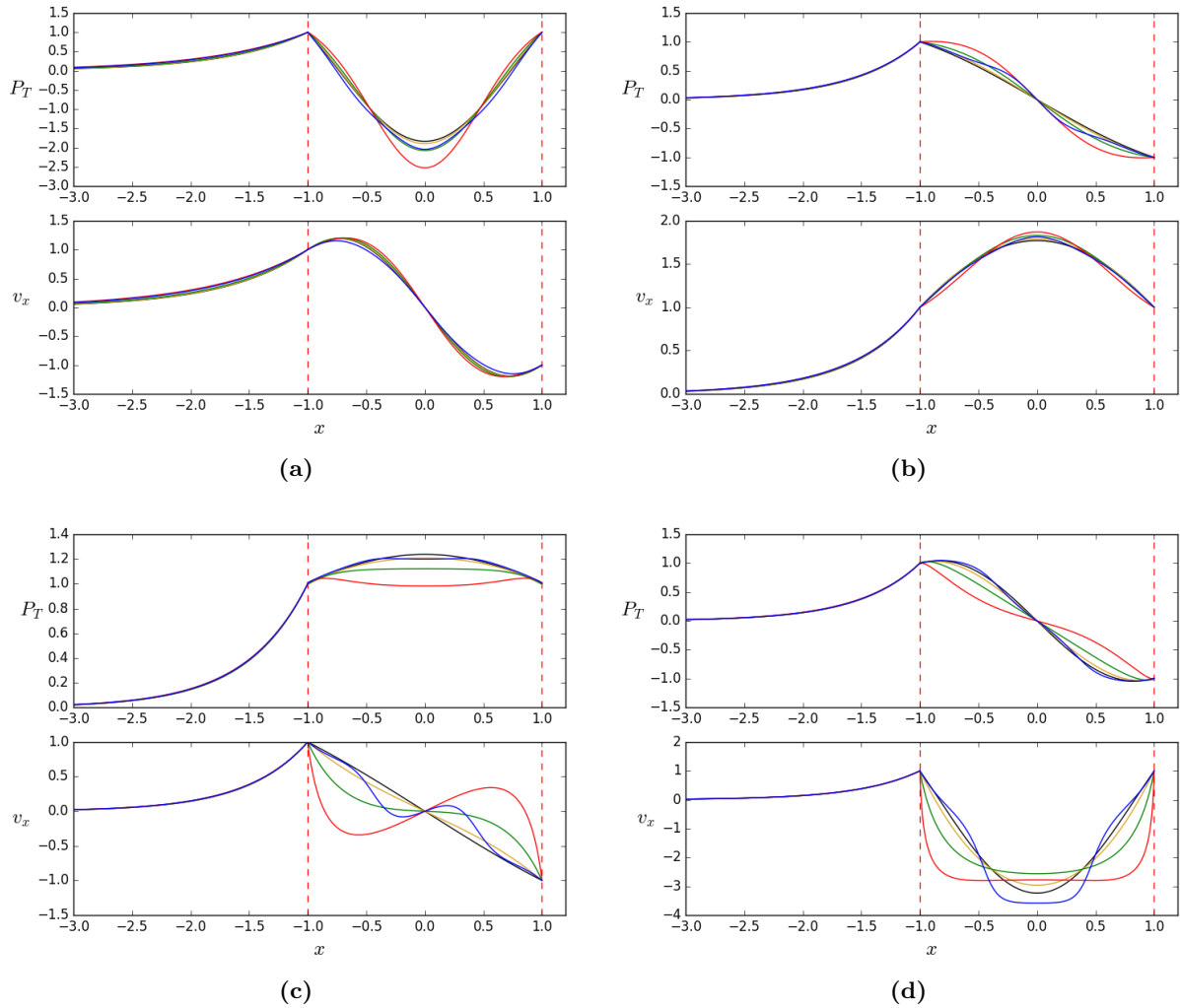


Figure 3.8: Comparisons of the eigenfunctions \hat{P}_T and \hat{v}_x for all the spatial profiles considered in Figure 3.4. The colour scheme is consistent with Figure 3.4. (a) Fast sausage mode, (b) fast kink mode, (c) slow sausage mode and (d) slow kink mode. An eigenvalue of $k = 2$ was chosen for all plots. All curves are normalised such that their values are equal to unity at the boundary.

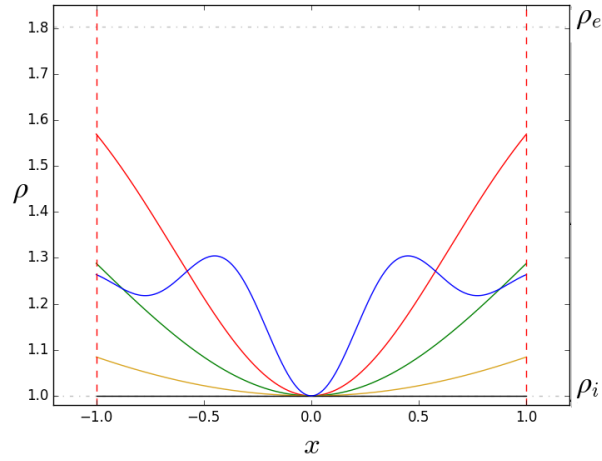


Figure 3.9: Density profile modelled as a Gaussian with a varying width in a photospheric slab. Width of inhomogeneity given by $W = 10^5$ (black), $W = 3$ (yellow), $W = 1.5$ (green), $W = 0.9$ (red). The spatial profile proportional to a $\text{sinc}(x)$ is shown by the blue curve. In all cases the density is discontinuous at the waveguide boundary and tends towards ρ_e (shown) at the boundary. The boundaries of the slab are indicated by the red dashed lines.

behaviour to the uniform scenario as the Gaussian profile in density becomes more pronounced. The slow body modes in a coronal plasma may be a good indicator into the underlying plasma density structure. The distributions of \hat{v}_x in Figure 3.8c appear to be proportional to the derivative of the corresponding equilibrium density profiles shown in Figure 3.4.

3.3.2 Photospheric non-uniform density magnetic slab case study

For photospheric conditions (i.e. $v_{Ae} < c_i < c_e < v_{Ai}$), the density profiles investigated are shown in Figure 3.9 to model an evacuated magnetic slab. Under these conditions, the Gaussian density maintains the same expression as that for the coronal case, however the $\text{sinc}(x)$ function must be normalised to the numerical domain and now takes the form:

$$\rho_i(x) = \frac{\rho_{0i}}{4} (\text{sinc}(10x) + 5).$$

This model may better represent those conditions found in sunspot umbrae and penumbrae, with a continuous internal density profile. The case when the width of the profile is large compared to the width of the waveguide is shown in Figure 3.10a and is comparable to the uniform case shown in Figure 3.2a, as expected. Adding extra density inhomogeneity into the internal region alters the plasma properties at the boundary compared to the centre.

The shaded regions in Figures 3.10b, 3.10c and 3.10d denote the area covered by the inhomogeneity for each characteristic speed, which is dependent on the non-uniform background density. Slow surface waves are trapped at speeds below c_{TB} and above v_{Ae} . This result is expected from theory presented by Edwin & Roberts (1982). In Figure 3.10c we show that the value of c_{TB} surpasses v_{Ae} and, as a result, slow surface waves cease to exist. An interesting region to note is the area contained within $c_B < v_{ph} < c_i$, where $c_i = 1$ is shown by the opposite edge of the green shaded region. As extra inhomogeneity is added into the equilibrium, this region becomes larger. Due to the presence of the inhomogeneity in the model, this region varies continuously between the

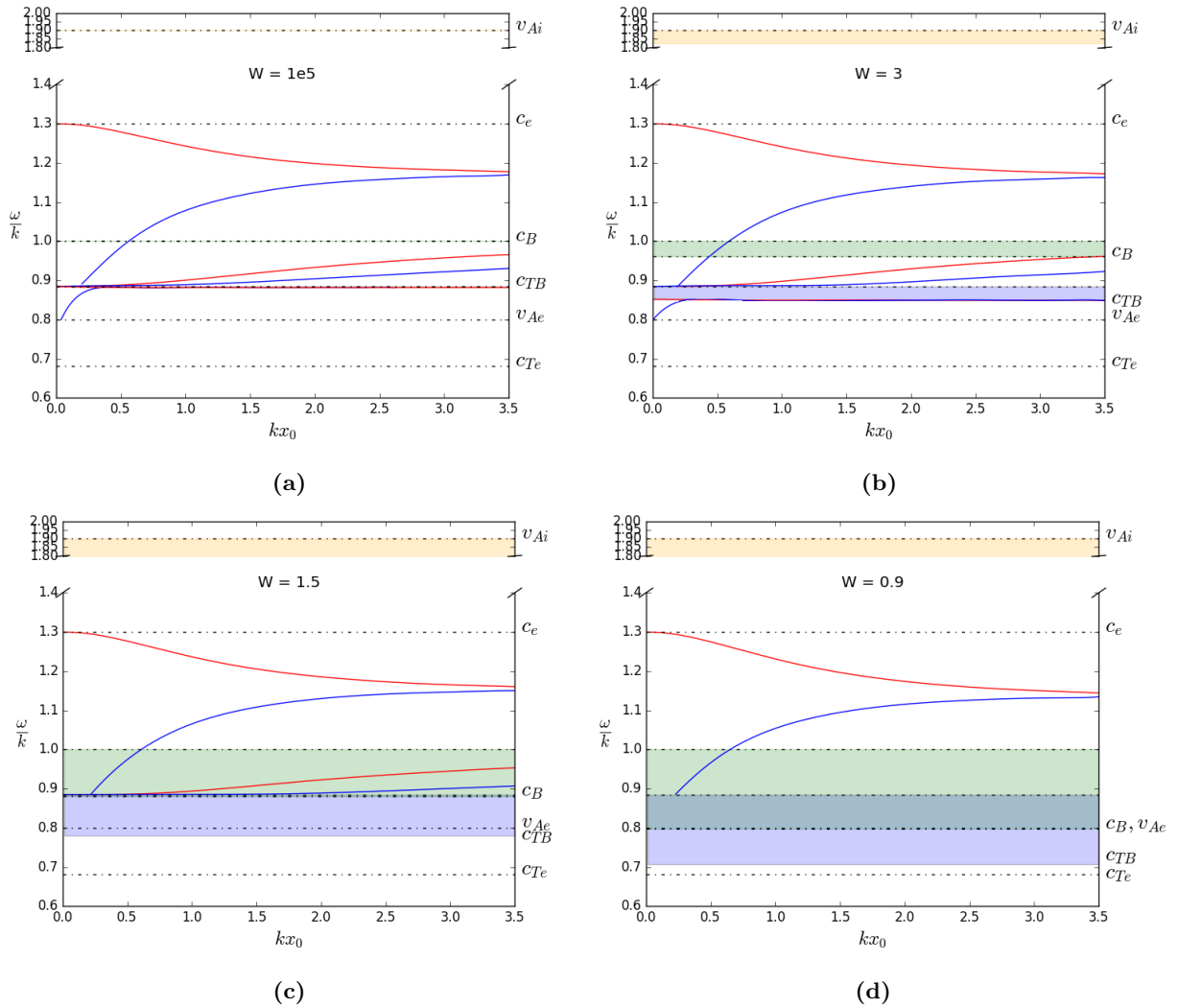


Figure 3.10: Dispersion diagrams showing the trapped solutions in a photospheric slab with density structuring given by a Gaussian profile. This figure is the same as Figure 3.6 with (a) $W \gg 2x_0$, (b) $W = 3$, (c) $W = 1.5$, (d) $W = 0.9$.

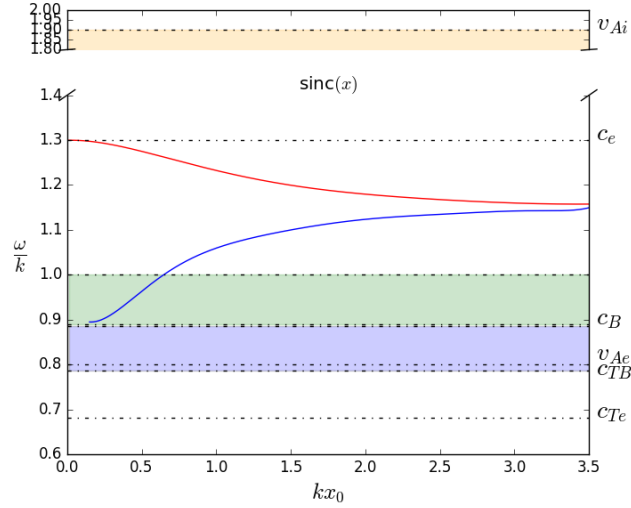


Figure 3.11: Dispersion diagram for a spatial profile proportional to $\text{sinc}(x)$ (i.e. $\sin(x)/x$) under photospheric conditions.

boundary, c_B , and minimum value of internal sound speed, c_i . Similarly, compared to the coronal case this introduces regular singularities in the governing differential equations and provides the possibility for dissipation processes to occur. Figure 3.11 is the resulting dispersion diagram for a photospheric equilibrium with a density structure modelled as a $\text{sinc}(x)$ function. The algorithm finds eigenvalues very similar to the Gaussian scenario with a width equal to 0.9 as shown in Figure 3.10d. Interestingly, the shape of the equilibrium inhomogeneity, does not appear to have a great affect on the eigenvalues of the equilibrium system. Similar to the coronal case, the resulting eigenfunctions appear very similar for fast modes, which may not feel the inhomogeneity as much as slow modes, as they are able to travel across magnetic field lines and as such travel more freely across any inhomogeneity.

Figure 3.13 shows the perturbed eigenfunctions for the fast surface sausage and fast surface kink mode under photospheric conditions. It is clear that inhomogeneity in the form of a Gaussian or a $\text{sinc}(x)$ function has very little effect on the physical behaviour of the total pressure and velocity perturbation.

Due to the decreasing density ratio at the boundary for Gaussian widths with larger inhomogeneity, the cusp continuum band becomes larger, therefore cutting off the slow surface and body modes. To investigate these further, we consider initial density profiles with a similar Gaussian width but smaller inhomogeneity, see Figure 3.12.

Displayed in Figure 3.14 are the perturbed eigenfunctions for body sausage and body kink modes under photospheric conditions and equilibrium density structure shown in Figure 3.12. Again, it is clear that any equilibrium inhomogeneity, even minor changes in the form of a Gaussian profile, has a significant effect on the properties of slow modes. The \hat{v}_x perturbation for the sausage mode has anti-nodes which shift again towards the centre of the waveguide, an affect mirrored by the \hat{P}_T perturbation of the kink mode, due to the asymmetry of the kink and sausage modes.

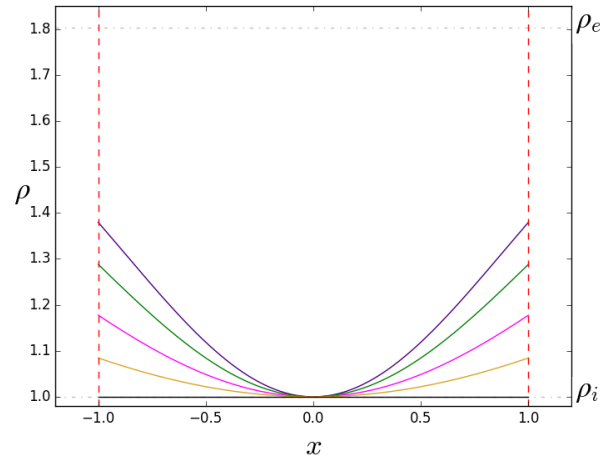


Figure 3.12: Modified density profiles modelled as a Gaussian curve with a varying width in a photospheric slab. The width of the profile is given by $W = 10^5$ (black), $W = 3$ (yellow), $W = 2$ (magenta), $W = 1.5$ (green), $W = 1.25$ (indigo). In all cases the density is discontinuous at the waveguide boundary and tends towards ρ_e (shown) at the boundary. The boundaries of the slab are indicated by the red dashed lines.

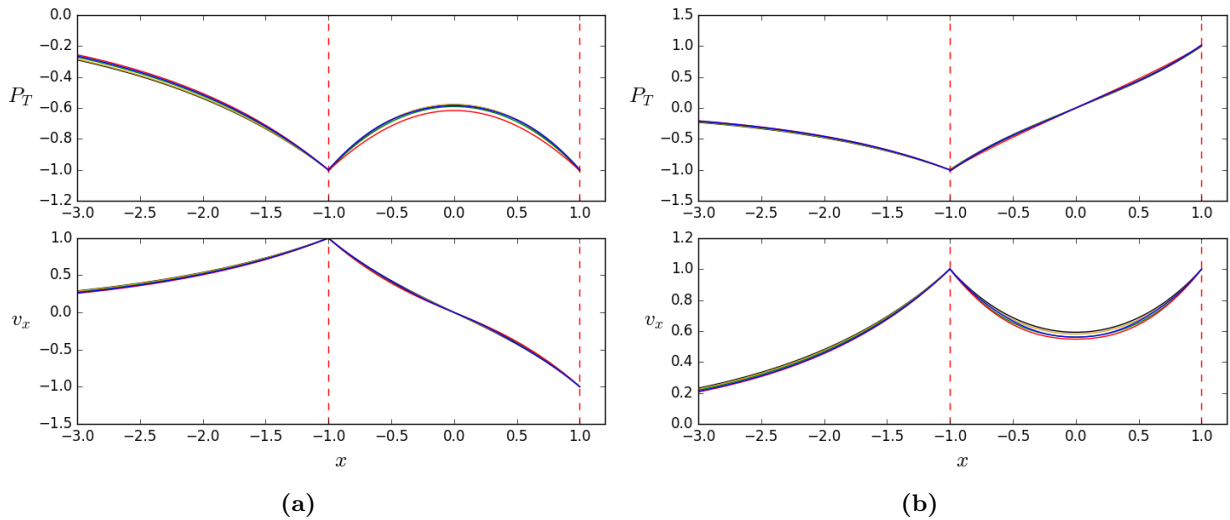


Figure 3.13: Comparisons of the eigenfunctions \hat{P}_T and \hat{v}_x for all the photospheric spatial profiles considered in Figure 3.9. The colour scheme is consistent with Figure 3.9. (a) Eigenfunctions for the fast surface sausage mode, (b) eigenfunctions for the fast surface kink mode. An eigenvalue of $k = 2$ was chosen for all plots. In all plots the curves have been normalised such that their values are equal to unity at the boundary.

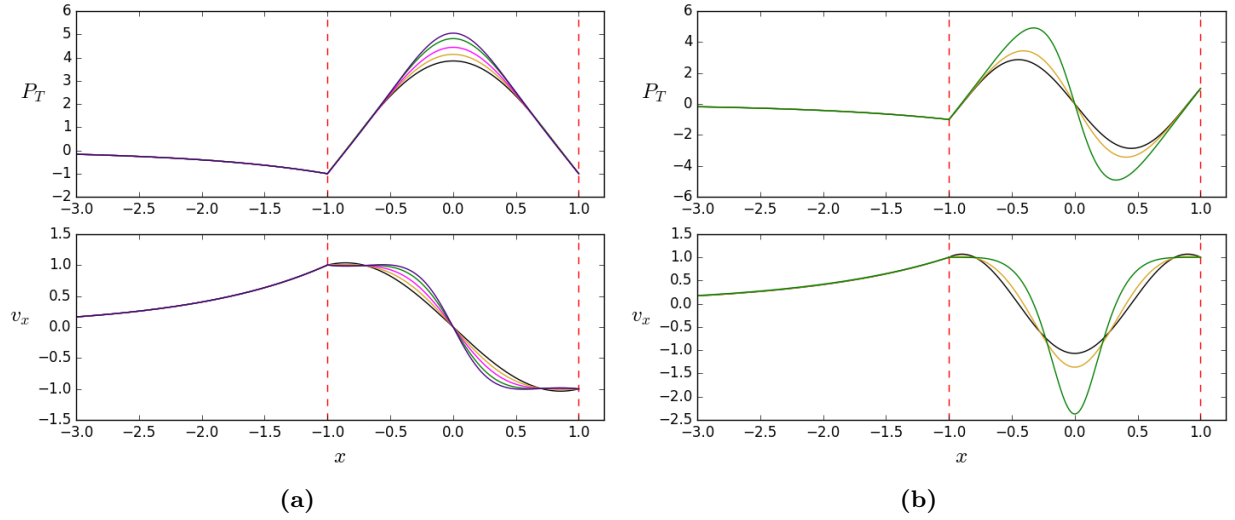


Figure 3.14: Comparisons of the eigenfunctions \hat{P}_T and \hat{v}_x for all the photospheric spatial profiles considered in Figure 3.12. The colour scheme is consistent with Figure 3.12. (a) Body sausage mode, (b) body kink mode. An eigenvalue of $k = 3$ was chosen for all plots. All curves normalised such that their values are equal to unity at the boundary.

3.4 Uniform magnetic slab with a non-uniform background plasma flow

In this section, an analysis of magnetoacoustic wave properties in the case of a magnetic slab of uniform plasma in the presence of a non-uniform background flow will be conducted. The governing equations are derived under the context that the background plasma flow is symmetrically-arbitrary and spatially varying. This situation may be encountered in features in the solar atmosphere as jet-like features and other waveguides with a background plasma flow are routinely observed in the solar atmosphere, including spicules, fibrils and prominences to name a few (De Pontieu, McIntosh, Hansteen, Carlsson, Schrijver, Tarbell, Title, Shine, Suematsu, Tsuneta, Katsukawa, Ichimoto, Shimizu & Nagata 2007, Berger et al. 2010, Pereira et al. 2011). Due to current spatial resolution limits of ground and space based telescopes, the spatial profiles of these flows are still unknown, however, it is common in fluid dynamics that flows are not steady (e.g. Orszag & Kells 1980).

The discussed magnetic configuration in the form of a uniform magnetic slab in the presence of a non-uniform plasma flow is shown in Figure 3.1. In this model, it is assumed that the plasma flow is aligned with the background magnetic field and the plasma flow is present only inside the magnetic slab, e.g. $\mathbf{v}_{0i} = (0, 0, U_{0i}(x))$. This particular choice of equilibrium flow profile does not effect the initial pressure balance of the equilibrium. As a vertical flow, even one that is radially non-uniform, does not introduce any additional radial forces, the pressure balance equation still maintains the same form as Equation (2.2). Furthermore, the divergence of this equilibrium velocity field is zero, resulting in the linearised ideal MHD equations taking a simplified form.

The governing equation attained exterior to the slab is the same as that shown in by Equation (3.2) in Section 3.2.1. The general formulation for a non-uniform equilibrium, including background plasma flow, has been previously derived in Frieman & Rotenberg (1960), Goedbloed et al. (2019). Here we present a specific case of Equation (13.11) from Goedbloed et al. (2019), in which the plasma properties are uniform expect for a symmetric inhomogeneous background plasma flow,

which unlike previous studies, is allowed to be discontinuous across the slab boundary. This chosen configuration of an inhomogeneous vertical background flow aligned with the magnetic field eliminates any magnetic shear effects, including those associated with the background flow.

The set of linearised, Fourier-decomposed MHD Equations (1.1)-(1.5) for each perturbed quantity in the presence of an inhomogeneous background plasma flow described above are:

$$-i\Omega(x)\hat{\rho}_1 + \rho_0(\hat{v}'_x + ik\hat{v}_z) = 0, \quad (3.6)$$

$$-i\rho_0\Omega(x)\hat{v}_x = -\hat{P}'_1 + \frac{B_0}{\mu_0}(ik\hat{B}_x - \hat{B}'_z), \quad (3.7)$$

$$-i\rho_0\Omega(x)\hat{v}_z + \rho_0 U'_{0i}(x)\hat{v}_x = -ik\hat{P}_1, \quad (3.8)$$

$$-i\Omega(x)\hat{P}_1 + c_0^2\rho_0(\hat{v}'_x + ik\hat{v}_z) = 0, \quad (3.9)$$

$$-i\Omega(x)\hat{B}_x = ikB_0\hat{v}_x, \quad (3.10)$$

$$-i\Omega(x)\hat{B}_z = \hat{B}_x U'_{0i}(x) - B_0\hat{v}'_x, \quad (3.11)$$

where $\Omega(x) = \omega - kU_{0i}(x)$ is the Doppler shifted frequency and a prime denotes a differentiation with respect to the spatial coordinate x .

Equations (3.6)-(3.11) can be combined by eliminating all perturbed quantities but \hat{v}_x , and as such, the governing equation for velocity amplitude becomes:

$$\hat{v}''_x + D(x)\hat{v}'_x + \left[-\frac{\Omega''(x)}{\Omega(x)} - \frac{\Omega'(x)}{\Omega(x)}D(x) - m_i^2(x) \right] \hat{v}_x = 0. \quad (3.12)$$

The coefficient $D(x)$ can be expressed as,

$$D(x) = \frac{2\Omega'(x)}{\Omega(x)} \left[\frac{\Omega^2(x)}{\Omega_c^2(x)} - \frac{k^2 c_{Ti}^2}{\Omega_T^2(x)} \right], \quad (3.13)$$

where,

$$\begin{aligned} \Omega_s^2(x) &= k^2 c_i^2 - \Omega^2(x) \\ \Omega_T^2(x) &= k^2 c_{Ti}^2 - \Omega^2(x) \\ \Omega'(x) &= -kU'_{0i}(x), \quad \Omega''(x) = -kU''_{0i}(x), \\ m_i^2(x) &= \frac{[k^2 v_{Ai}^2 - \Omega^2(x)] [k^2 c_i^2 - \Omega^2(x)]}{(c_i^2 + v_{Ai}^2) [k^2 c_{Ti}^2 - \Omega^2(x)]} = \frac{\Omega_A^2(x) \Omega_s^2(x)}{(c_i^2 + v_{Ai}^2) \Omega_T^2(x)}, \end{aligned}$$

with,

$$\Omega_A^2(x) = k^2 v_{Ai}^2 - \Omega^2(x).$$

Equation (3.12) has no known closed-form analytical solution due to its complicated nature caused by the spatially varying coefficients. A detailed derivation of Equation (3.12) is given in Appendix A. It can be seen that if the spatial dependence on flow is removed (i.e. an initial constant flow) that $\Omega(x) \rightarrow \omega - kU_{0i} = \Omega$, and $m_i^2(x)$ is also no longer a function dependant on space. Furthermore, $\Omega''(x) = \Omega'(x) = 0$ such that Equation (3.13) becomes equal to zero. Equation (3.12) now becomes:

$$\hat{v}''_x - m_i^2 \hat{v}_x = 0, \quad (3.14)$$

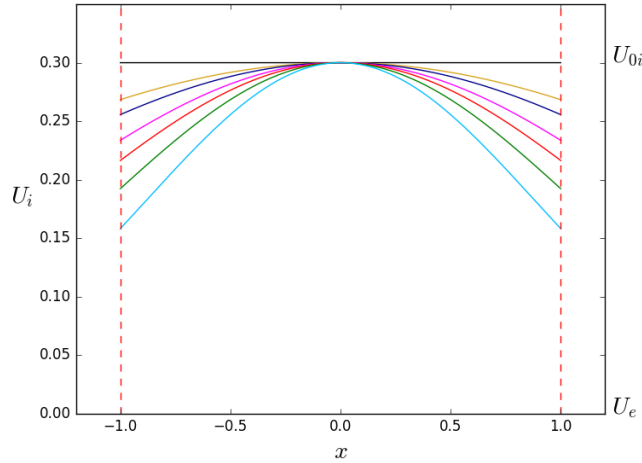


Figure 3.15: Background plasma flow modelled as a Gaussian profile with a varying width in a uniform coronal slab. Width of inhomogeneity given by $W = 10^5$ (black), $W = 3$ (yellow), $W = 2.5$ (dark blue), $W = 2$ (magenta), $W = 1.75$ (red), $W = 1.5$ (green) and $W = 1.25$ (cyan). In all cases the flow is discontinuous at the waveguide boundary. The boundaries of the slab are indicated by the red dashed lines. The maximum flow speed is 0.3 such that the flow is both subsonic ($c_i = 1$) and sub Alfvénic ($v_{Ai} = 1.2$) to avoid any flow related instabilities.

which is the same result as shown in Equation (3.2) but with a Doppler shifted frequency in the expression of m_i^2 . If magnetic field is neglected ($B = 0$) such that $v_{Ai}, c_{Ti} = 0$ and assume an incompressible plasma ($c_i \rightarrow \infty$), the governing Equation (3.12) becomes:

$$\hat{v}_x'' - \left(\frac{\Omega''(x)}{\Omega(x)} + k^2 \right) \hat{v}_x = 0, \quad (3.15)$$

as given in Timofeev (2000). Equation (3.15) is a form of Rayleigh's equation (see e.g Chandrasekhar 1961), a well-known expression in hydrodynamics concerning inviscid shear flows (Rayleigh 1879, Hirota et al. 2014). The corresponding expression for the total pressure perturbation, \hat{P}_T , inside a magnetic slab with a spatially varying background plasma flow is given by:

$$\hat{P}_T = -i \frac{\rho_i}{\Omega(x)} (c_i^2 + v_{Ai}^2) \frac{\Omega_T^2(x)}{\Omega_s^2(x)} \left(\hat{v}_x' - \frac{\Omega'(x)}{\Omega(x)} \hat{v}_x \right), \quad (3.16)$$

The set of Equations (3.12) and (3.16) provides the required expressions for the numerical analysis. Similar to the analysis conducted in Section 3.3, an internal Gaussian flow profile is considered with the spatial profiles analysed shown in Figure 3.15 given by the expression:

$$U_{0i}(x) = A \exp \left(-\frac{(x - x_c)^2}{W^2} \right),$$

where A is the velocity amplitude and similar to the previous case $x_c = 0$ and W are the center of the waveguide and the width of the Gaussian profile, respectively. In all cases studied in this section there is assumed to be no plasma flow exterior the slab.

The resulting dispersion diagrams for a magnetic slab under coronal conditions for the inhomogeneous internal background plasma flow cases considered in this section are shown in Figure 3.16.

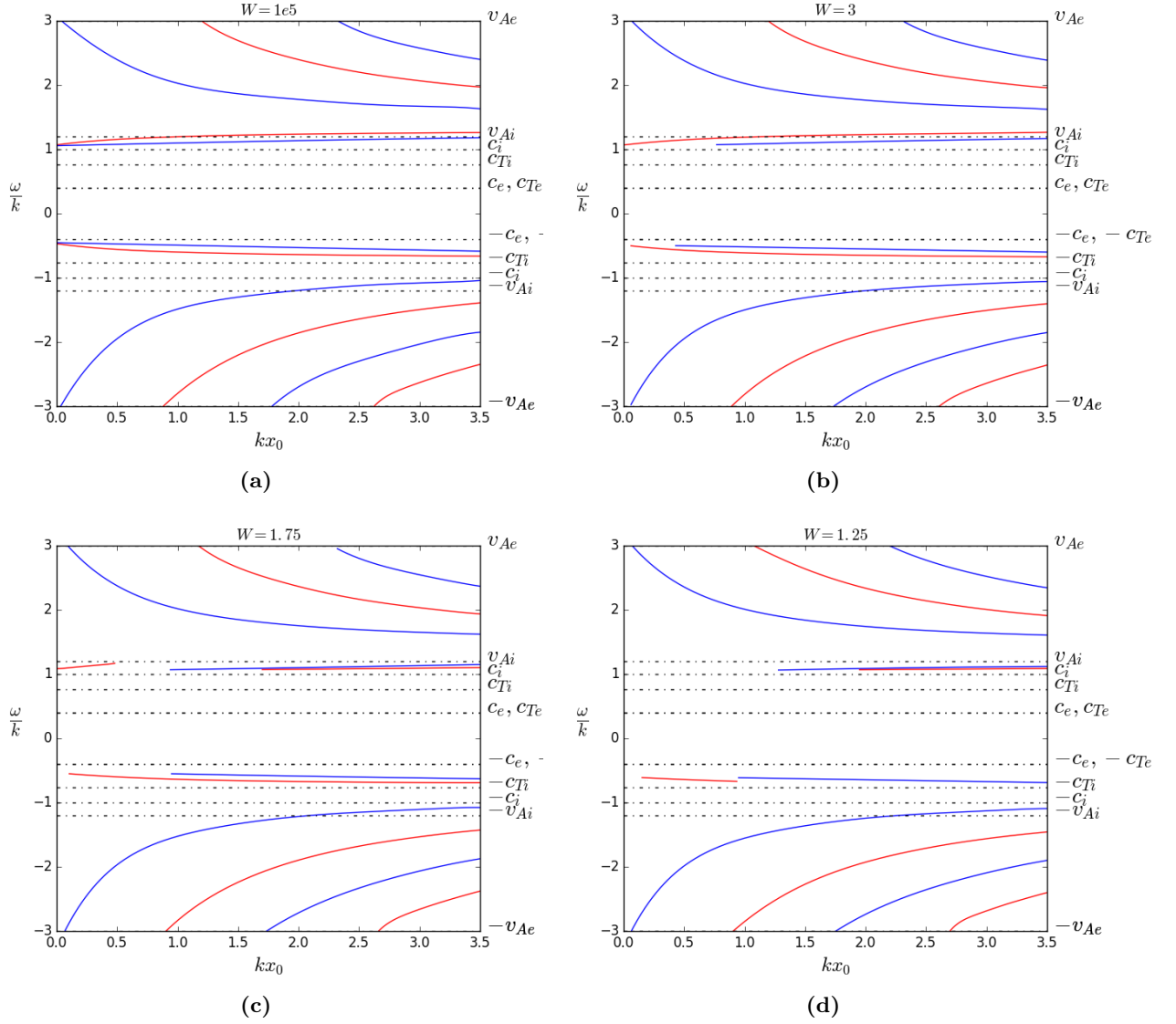


Figure 3.16: The dispersion diagrams show the trapped solutions in a coronal slab with a background Gaussian flow of selected profiles from Figure 3.15. Diagrams are shown for cases where the width of flow profile is given by (a) $W \gg 2x_0$, (b) $W = 3$, (c) $W = 1.75$, (d) $W = 1.25$. The plasma slab under coronal conditions given by $c_i = 1$, $v_{Ai} = 1.2c_i$, $c_e = 0.4c_i$, $v_{Ae} = 3c_i$, $U_{0i} = 0.3c_i$. Red curves denote the sausage mode solutions and blue curves show the kink mode.

As the maximum of the Gaussian flow located at $x_c = 0$ remains constant for all cases, the maximum Doppler shift on the waves in all cases also remains constant. There is not much difference in the dispersive properties between the fast body modes - both forward and backward propagating, as the inhomogeneity is increased. The dispersive properties of the slow body modes however, are much more affected by the non-uniformity of the background plasma flow. The region bounded between $-c_{Ti} + U_B < v_{ph} < -c_{Ti} + U_{0i}$ is a band in which resonances due to the background flow are present. This region is not shown in Figure 3.16, and although this phenomena is not investigated further in this section, it has been studied before analytically (Taroyan & Erdélyi 2002).

In Figure 3.17, we display enlarged regions of the dispersion diagrams in Figure 3.16 to highlight the region of forward and backward propagating slow body modes in detail. In Figure 3.17a, we plot the slow body modes for a magnetic slab under coronal conditions with a background plasma flow which is effectively uniform, i.e. $W \gg 2x_0$. The forward and backward propagating waves in this case are symmetric in the sense that they are trapped between the respective positive and negative phase speed bands, but asymmetric around the wave frequency caused by the Doppler shift of the steady background flow. A more detailed explanation of this can be found in Nakariakov & Roberts (1995a). In their study, equations (7) – (8) provide the dispersion relations for surface and body magnetoacoustic waves, which can be algebraically derived due to the uniformity of their model. The dispersion relations are similar to that of a uniform magnetic slab in the absence of plasma flow given in Edwin & Roberts (1982), however, they are modified in the presence of a steady background flow. It can be seen that the dispersion relations are now not symmetric for forward (aligned with the magnetic field) and backward (against the magnetic field) propagations in the slender slab limit, which is provided by an expansion in the limit where $kx_0 \rightarrow 0$ in their equations (16) – (17). It should be noted that these expressions are independent on the wavenumber, and instead, depend on the value of the flow. We also retrieve this result which is shown in Figure 3.17a. As the inhomogeneity of the background flow is increased, this symmetry is further broken as shown in Figures 3.17b, 3.17c, 3.17d. This is due to forward propagating slow modes being trapped between $c_{Ti} + U_{0i}$ and $c_i + U_B$, where U_{0i} is the maximum flow speed and U_B being the flow speed at the boundary of the slab. The backward propagating modes are trapped between $-c_{Ti} + U_B$ and $-c_i + U_{0i}$. Furthermore, this causes certain branches on the dispersion diagram to be absorbed into the slow continuum modified due to the non-uniform background plasma flow.

The eigenfunctions \hat{P}_T and \hat{v}_x in the presence of an inhomogeneous background flow are shown in Figure 3.18. Similar to the study of inhomogeneous density profiles, the equilibrium inhomogeneity appears to have little effect on the spatial properties of fast propagating wave modes. In Figure 3.19 we show the eigenfunctions for the slow forward and backward propagating sausage and kink modes for the model shown in Figure 3.15. Figures 3.19a and 3.19b show the spatial behaviour of the eigenfunctions for a forward propagating slow body mode. The perturbation of \hat{v}_x corresponding to the sausage mode obtains an extra point of inflexion caused by the inhomogeneity of the background plasma flow, which may be of interest for interpreting observational results. For both the \hat{v}_x perturbation, which corresponds to the sausage mode, and the \hat{P}_T perturbation corresponding to the kink mode, the maximum value of the eigenfunction anti-node shifts towards the centre of the waveguide, where the flow speed is a maximum and its gradient is zero. If it were possible to model a Gaussian flow stretching to infinity, the corresponding spatial eigenfunctions would become discontinuous at the centre of the waveguide.

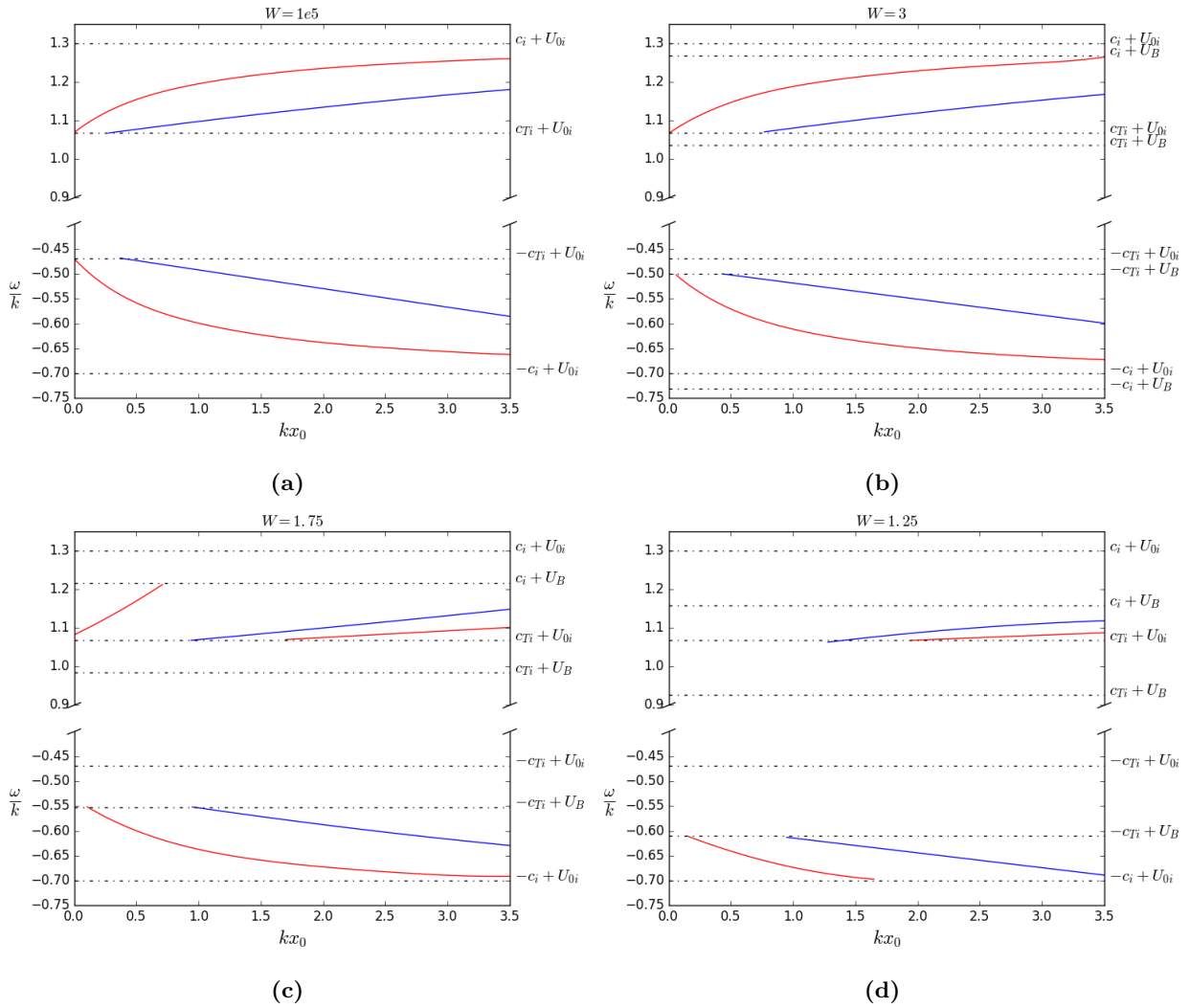


Figure 3.17: Same as Figure 3.16 but the figures show a zoom in on the region of forward and backward propagating slow body modes. For the cases when $W = 1.75$ and $W = 1.25$ we show a higher overtone of the attained body modes as the flow has shifted the fundamental modes into the continua.

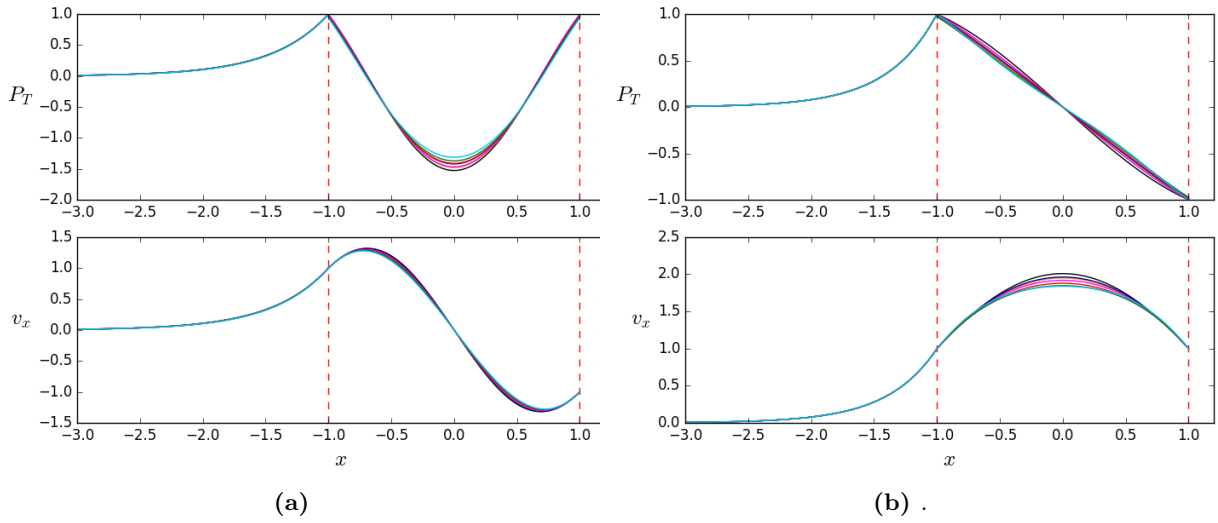


Figure 3.18: Comparisons of the eigenfunctions \hat{P}_T and \hat{v}_x for all the flow profiles considered in Figure 3.15. (a) Fast forward sausage mode, (b) fast forward kink mode. An eigenvalue of $k = 3$ was chosen for all plots. All curves normalised such that their values are equal to unity at the boundary

3.5 Summary & Discussion

In this chapter the numerical technique presented in Chapter 2 has been tested against previously obtained analytical results for magnetoacoustic waves in a uniform magnetic slab under different atmospheric environments. Additional tests included the addition of a constant steady field aligned plasma flow, for which the solutions (known from analytical studies) were retrieved under both photospheric and coronal conditions.

The method was then applied to a waveguide in which the internal plasma structuring is non-uniform and modelled as a Gaussian profile. The dispersion relation cannot be derived analytically when modelling the plasma density as a Gaussian function, therefore the numerical technique is applied instead. We find that the cut-off values for slow body modes are dependant upon the values of the sound speed at the boundary, c_B , cusp speed at the boundary, c_{TB} , and the size of internal inhomogeneity in both coronal and photospheric conditions. This technique can be useful to identify the bands in which resonance can occur and potentially lead to dissipation processes such as resonant absorption and phase mixing. Whilst fast surface and body modes are not modified by the equilibrium inhomogeneity when compared with the uniform magnetic slab case, the physical eigenfunctions of slow body modes are more significantly altered. We have found that even for an equilibrium Gaussian density distribution of sufficient width, an extra node and point of inflexion appears in the spatial structure of the eigenfunctions. This result is important for the interpretation of observational signatures of MHD wave modes as it shows non-uniform equilibria may lead to the misunderstanding of their spectral patterns.

A possible explanation for this observed behaviour in slow modes rather than fast modes could be as follows. Fast magnetoacoustic modes propagate perpendicular to the magnetic field, which in all of our case studies is taken to be vertical, straight and uniform. Furthermore, the non-uniformity in all of our case studies are taken to be in the horizontal direction, which is also perpendicular to the magnetic field. Due to the nature of fast modes, they can propagate across the magnetic field lines and, thus, across the inhomogeneity, therefore feeling less of the effect of the non-uniform

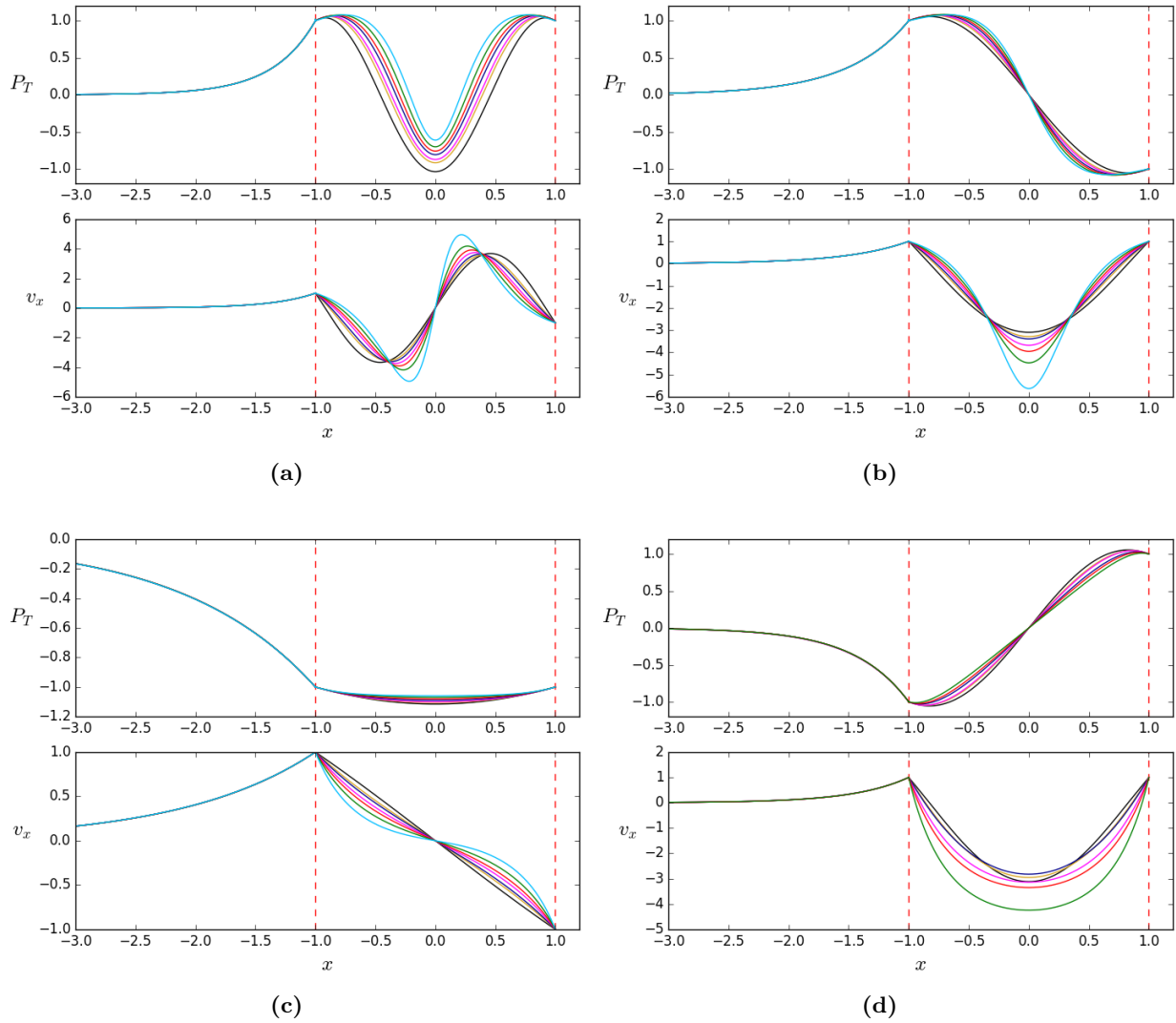


Figure 3.19: Comparisons of the eigenfunctions \hat{P}_T and \hat{v}_x for all the flow profiles considered in Figure 3.15. (a) Slow forward sausage mode, (b) slow forward kink mode, (c) slow backward sausage mode, (d) slow backward kink mode. An eigenvalue of $k = 1.1$ was chosen for plots (a) and (b). An eigenvalue of $k = 0.9$ was chosen for plots (c) and (d). All curves normalised such that their values are equal to unity at the boundary. The eigenfunction plot for the case when $W = 1.25$ is not shown in (d) due to the kx_0 value beyond the cut off regime.

plasma. On the other hand, slow magnetoacoustic modes, which propagate along the magnetic field lines, will feel the effect of the non-uniform plasma, as neighbouring magnetic field lines will be under a different local plasma environment. As a result, the properties of slow modes could be affected more than those of the fast modes, as our analysis of the eigenfunctions show in Figures 3.8, 3.14 and 3.19. Another possible explanation may be that the plasma non-uniformity shifts the phase speeds of the modes into different propagation windows. This may explain the observed additional nodes and anti-nodes in the resulting eigenfunctions when the inhomogeneity is increased. As the non-uniformity is increased, the wave modes we recover may actually be higher harmonics of the fundamental mode in the uniform scenario. This observed shifting of the phase speed with increasing non-uniformity may be a result of the changing density ratio at the boundary between the internal and external value.

To further show the strength of this technique, an example of a coronal slab with a non-uniform background flow was investigated. The general governing equations for the perturbations of total pressure and velocity were derived, which reduce to the known expressions when inhomogeneity is ignored. These equations were then solved numerically to obtain eigenvalues and plot the dispersion diagrams for a number of different non-uniform background flow profiles. The non-uniform flow created an asymmetry between the bands in which forward and backward propagating slow body waves are trapped within the waveguide. A similar behaviour to a non-uniform plasma density is observed with the resulting eigenfunctions. As the inhomogeneity of the background flow is increased, by decreasing the width of the Gaussian profile, the spatial structure of slow body waves - both forward and backward propagating - become distorted, while the fast modes remain unaltered.

The major benefit of the presented methodology is that more complicated plasma equilibrium can be introduced into the original slab model. Non-uniform plasma flow profiles which more accurately reflect those observed in, e.g. sunspots can be included and the resulting wave analysis can be conducted. It is well-known that the resonant absorption and phase mixing mechanisms rely upon the presence of a non-uniform transversal plasma or inhomogeneous boundary layer - for which this method could locate the appearance of the resulting continua. This would previously not have been achievable due to the complicated mathematics involved and the numerous simplifications and assumptions needed to be able to obtain an analytical solution to the MHD equations.

Immediate future steps involve extending the current work to investigate the wave properties in a cylindrical model, which more accurately models solar features such as sunspots, jets and coronal loops. This will be possible using the introduced methodology as the physics remains the same, however, the differential operators take a different form in cylindrical geometry. Further extensions could include modelling asymmetric profiles, for example non-steady asymmetric background plasma flows, in which the physics for MHD wave modes would be modified slightly. Another very important aspect which can be studied is the behaviour of complex wave frequencies. Complex frequencies would provide more information on the physical behaviour of wave damping and any instabilities that are present in a static or steady equilibrium. Implementation of asymmetry, extra geometries and complex frequencies will help move a step closer to developing a technique which can be used in wave analysis for a general arbitrary model. The power of our numerical eigensolver is that it can be used alongside observational data to conduct magnetoseismology with a realistic model to best fit observational results and provide a greater insight into the physical properties of these waves and their potential contribution to the energy budget of the solar atmosphere.

Chapter 4

The effect of non-uniform plasma density and flow on magnetoacoustic wave modes in a magnetic cylinder geometry ¹

Abstract

In this chapter, a natural extension of the study considered in Chapter 3 is presented. The magnetic slab model is replaced by a magnetic cylinder model and a similar investigation into the properties of MHD waves is presented using the numerical eigensolver presented in Chapter 2.

In this chapter we investigate the properties of magnetoacoustic waves under non-uniform equilibria in a cylindrical geometry. Again, previously obtained analytical results are retrieved to emphasise the power and applicability of this numerical technique in multiple geometries. Further case studies investigate the effect that a radially non-uniform plasma density and non-uniform plasma flow, modelled as a series of Gaussian profiles, have on the properties of different MHD waves. For all cases the dispersion diagrams are obtained and spatial eigenfunctions calculated which display the effects of the equilibrium inhomogeneity. It is shown that as the equilibrium non-uniformity is increased, the radial spatial eigenfunctions are affected and extra nodes introduced, similar to the results of a non-uniform magnetic slab, as seen in Chapter 3. Furthermore, it is found that the azimuthal perturbations are increased with increasing equilibrium inhomogeneity which introduces vortical motions inside the waveguide. These excited vortical motions due to the equilibrium inhomogeneity may be responsible for exciting torsional MHD waves inside magnetic waveguides.

Finally, 2D and 3D representations of the velocity fields are shown which may be useful for observers for wave mode identification under realistic magnetic waveguides with ever increasing instrument resolution.

¹The content of this chapter appeared as S. Skirvin, V. Fedun, S. Silva and G. Verth, 2021, MNRAS, 510(2), 2689–2706 (Skirvin et al. 2022)

4.1 Introduction

Observations of the solar atmosphere show that it is replete with MHD waves (see, e.g. Nakariakov et al. 1999, Aschwanden et al. 1999, De Pontieu, McIntosh, Carlsson, Hansteen, Tarbell, Schrijver, M., Shine, Tsuneta, Katsukawa, Ichimoto, Suematsu, Shimizu & Nagata 2007, Morton et al. 2012, Keys et al. 2018). The combination of observational data with analytical models allows for the practice known as ‘solar atmospheric seismology’. This technique allows researchers to calculate properties of the solar atmospheric plasma, that may be difficult to determine directly from observations, by analysing the propagation of waves through the medium. However, for this to be a useful technique, there is a need for a high degree of accuracy in both the observations and the theoretical models. Whilst great improvement has been made on the observational side, there is still a large amount unknown about modelling wave propagation in general realistic solar waveguides.

Adaptations and extensions of the uniform magnetic waveguide studies have been undertaken to explore the properties of MHD waves under more complicated yet realistic plasma configurations. A non exhaustive list includes investigating waves in non-uniform magnetic slabs (Arregui et al. 2007, Lopin & Nagorny 2015*a,b*, Li, Zhang, Yang, Hou & Erdélyi 2018, Skirvin et al. 2021), curved magnetic slabs (Verwichte et al. 2006*c*), twisted magnetic cylinders (Erdélyi & Fedun 2007*b*, 2010, Terradas & Goossens 2012, Terradas et al. 2018) and magnetic cylinders with vortex flows (Cheremnykh et al. 2017, 2018, Tsap et al. 2020). It is widely known that within a non-uniform plasma in ideal MHD, waves propagating at specific frequencies may resonate with the local plasma. This occurs in continuum regions where the wave propagates at either the local Alfvén speed or the local tube (cusp) speed. At these locations, wave energy can be extracted by processes such as resonant absorption (Goossens et al. 1995, Keppens 1996, Goossens et al. 2011). Undertaking an investigation into wave damping mechanisms relies on treating the wave frequency as a complex quantity, where the imaginary component provides information on either wave damping or any wave related instabilities, (see e.g. Section 1.7.2). This phenomenon is not considered in this chapter, however, relevant studies can be found in, e.g. Heyvaerts & Priest (1983), Yu et al. (2021). The present study includes plasma (gas) pressure in the analysis however avoids resonantly damped modes by assuming that the wave frequency is purely real. It should be noted that previous works have investigated the resonantly damped modes, however, in their analysis assume that the plasma- β is zero, which ultimately removes the slow magnetoacoustic modes from their analysis (Van Doorselaere et al. 2004, Soler et al. 2013, Soler 2017, 2019).

It is well-known that the solar atmosphere and features within are highly non-uniform, mainly due to the fine magnetic fields which permeate throughout (e.g. Williams et al. 2020). This non-uniformity has an important affect on the propagation and observation of MHD waves. It was shown in Chapter 3 (Skirvin et al. 2021) that an inhomogeneous plasma equilibrium changes the eigenvalues for trapped modes dependant upon the scale of the inhomogeneity. If the plasma is highly non-uniform, then the permittable bands within which MHD waves can propagate become narrower, whereas the continuum regions, where physical damping processes can take place, spread a wider range of phase speeds. The non-uniform equilibrium can also affect the spatial distributions of observable eigenfunctions produced by MHD wave propagation. It was found that in non-uniform coronal slab structures, slow body modes are more affected by large inhomogeneities in density over the width of a magnetic slab, the same is true for the body modes of a non-uniform photospheric slab.

Furthermore, the effect of non-uniformity has important implications for identifying wave modes in observations. It is well known that the theoretical Alfvén mode along with the slow and fast magnetoacoustic modes only exist in pure form in a uniform plasma of an infinite extent. In such a scenario the Alfvén wave propagates as a purely incompressible vortical perturbation with only

magnetic tension acting as the restoring force. Furthermore, magnetoacoustic waves propagate as compressible disturbances which can be identified through observations of plasma intensity perturbations with a combination of magnetic tension and total pressure acting as the restoring forces. In reality however, the solar atmosphere is highly non-uniform and not infinite. Consequently it is difficult to interpret observations of MHD wave modes as one of the three distinct wave modes in a uniform plasma. In a non-uniform plasma, MHD waves have mixed properties and cannot be classified as pure Alfvén or pure magnetoacoustic waves (Goossens et al. 2019).

It has been shown analytically that even a simple discontinuity in plasma equilibrium such as a piece-wise true discontinuous density (similar to that modelled as a magnetic cylinder) that the fundamental radial non-axisymmetric magnetoacoustic mode (kink mode) should in fact be interpreted as a surface Alfvén wave (Wentzel 1979, Goossens et al. 2012). The analytical investigation conducted by Goossens et al. (2012) focused on the role that vorticity plays when the plasma is non-uniform. For a pure Alfvén wave the displacements are vortical everywhere, however, for a pure magnetoacoustic wave we have zero vorticity. As the piece-wise discontinuity is replaced with a continuous profile, vorticity is spread out over the whole interval covered by the Alfvén continuum, where the density is inhomogeneous. We investigate further the role of vorticity in a non-uniform magnetic flux tube for both a non-uniform equilibrium density and a non-uniform background plasma flow.

The effect of a steady background plasma flow on the properties of MHD waves has been previously studied in a cylindrical geometry. An investigation by Terra-Homem et al. (2003) derived and solved the dispersion relation for MHD waves in a uniform magnetic cylinder with a uniform background plasma flow. Further studies have looked at the potential a steady flow may have for the onset of the Kelvin-Helmholtz instability, which may provide a turbulent cascade of energy that could heat localised plasma (Zhelyazkov 2012, 2013). However, little research has been conducted which investigates the effect a non-steady plasma flow may have on the properties of MHD waves in a magnetic cylinder due to the difficulty of analytically deriving a dispersion relation.

In this Chapter, the approach to that described in Chapter 3 is slightly modified with the main difference in the coordinate system used which affects the vector operators in the analytical analysis. In this investigation, the numerical technique developed previously is applied to initially uniform cylindrical waveguides to reproduce previously obtained analytical results including also a steady background flow. Thereafter, the internal spatial profile of plasma density and background flow is allowed to be non-uniform in the shape of a series of Gaussian profiles, which cannot be investigated purely analytically, with discussions about the observable differences in wave properties due to this non-uniform equilibria.

This Chapter is organised as follows: the simplified ideal MHD equations describing motions in a radially non-uniform cylinder are presented in Section 4.2. In Section 4.3 the numerical tool is applied to previously studied cases with known analytical results, the analytical and numerical results are compared. Further investigations of non-uniform density cases which cannot be studied analytically are discussed in Section 4.4. The MHD wave behaviour in a uniform coronal cylinder with a non-uniform background plasma flow is analysed in Section 4.5. Lastly, a summary and discussion of the results obtained in this chapter can be found in Section 4.6.

4.2 Governing equations

The studies presented in this chapter adopt a cylindrical geometry, with coordinates in the form (r, φ, z) . The initial equilibrium is allowed to be radially spatially dependant for plasma density and background plasma flow and has background magnetic field vector components in the form

$(0, 0, B_{0z})$ with the background velocity field vector components $(0, 0, U_{0z}(r))$. The flow, U_{0z} , is taken to be positive which corresponds to a flow in the positive vertical direction.

The system of linearised ideal MHD equations in a cylindrical geometry for a radially non-uniform equilibrium is described by Equations (1.22)-(1.32). It should be noted that these equations consider an equilibrium that includes background magnetic and velocity azimuthal components. The case studies considered in this section, do not assume that all plasma properties are taken to be inhomogeneous, therefore the system of Equations (1.22)-(1.32) reduces to a simplified form:

$$D \frac{d}{dr} \left(r \hat{\xi}_r \right) = -C_1 r \hat{P}_T, \quad (4.1)$$

$$D \frac{d \hat{P}_T}{dr} = C_2 \hat{\xi}_r, \quad (4.2)$$

where,

$$D = \rho (c^2 + v_A^2) (\Omega^2 - \omega_A^2) (\Omega^2 - \omega_c^2), \quad (4.3)$$

$$\Omega = \omega - k U_{0z}(r), \quad (4.4)$$

$$\omega_A^2 = \frac{k^2 B_{0z}^2}{\mu \rho}, \quad \omega_c^2 = \frac{\omega_A^2 c^2}{(c^2 + v_A^2)}, \quad (4.5)$$

$$C_1 = \Omega^4 - (c^2 + v_A^2) \left(\frac{m^2}{r^2} + k^2 \right) (\Omega^2 - \omega_c^2), \quad (4.6)$$

$$C_2 = D \rho (\Omega^2 - \omega_A^2). \quad (4.7)$$

Equation (4.4) describes the Doppler shifted frequency due to the presence of the background plasma flow considered in this model. This quantity is now a function of radially variable r and, as a result, the effect of the Doppler shifted frequency depends on the local background plasma flow at that location. The set of Equations (4.1)-(4.7) provide the full equations for any cylindrical equilibrium with a radially varying field aligned flow. It should also be noted that they describe any cylindrical equilibrium which is non-uniform in the direction of spatial coordinate r , as a result all quantities would also depend on r in such an equilibrium. Equations (4.1)-(4.2) can be combined to create a single differential equation in either $r \hat{\xi}_r$:

$$\frac{d}{dr} \left[f(r) \frac{d}{dr} \left(r \hat{\xi}_r \right) \right] - g(r) \left(r \hat{\xi}_r \right) = 0, \quad (4.8)$$

where,

$$f(r) = \frac{D}{r C_1}, \quad (4.9)$$

$$g(r) = -\frac{C_2}{r D}, \quad (4.10)$$

or \hat{P}_T :

$$\frac{d}{dr} \left[\tilde{f}(r) \frac{d \hat{P}_T}{dr} \right] - \tilde{g}(r) \hat{P}_T = 0, \quad (4.11)$$

where,

$$\tilde{f}(r) = \frac{r D}{C_2}, \quad (4.12)$$

$$\tilde{g}(r) = -\frac{r C_1}{D}, \quad (4.13)$$

similar to the governing Equations (1.35) and (1.38).

As in the previous chapter, investigating the properties of wave modes propagating within an equilibrium which is non-uniform, such as the case presented here, must be done numerically. The numerical algorithm, described in Chapter 2, employed in the following studies is the cylindrical approach presented in Section 2.3. The numerical shooting method is implemented to solve Equations (4.8) and (4.11) ensuring continuity of \hat{P}_T and $\hat{\xi}_r$ across the boundary.

The component of the displacement vector of magnetic surfaces perpendicular to the magnetic field lines $\hat{\xi}_\varphi$ can be related to \hat{P}_T and general plasma properties by modifying Equation 1.43 to yield:

$$(\Omega^2 - \omega_A^2) \hat{\xi}_\varphi = \frac{i}{\rho B_{0z}} (g_B \hat{P}_T), \quad (4.14)$$

where,

$$g_B = (\mathbf{k} \times \mathbf{B})_r = \frac{m}{r} B_{0z}.$$

4.3 Comparison with known solutions

In this section the numerical approach is tested against analytical results previously obtained for MHD waves in a uniform magnetic cylinder, which may represent the majority of structures observed in the solar atmosphere that may support the propagation of such waves. In all of these cases, the analytical dispersion relation is not required and the eigenvalues are obtained purely numerically. These numerically obtained solutions can be directly compared to their analytical counterparts which can be found in the respective references from previous studies.

4.3.1 Uniform magnetic cylinder

The foundations of investigating MHD waves in a cylindrical geometry with an application to solar physics were presented by Edwin & Roberts (1983) where the dispersion relations were derived for MHD waves propagating in a uniform cylinder embedded in a magnetic environment under both photospheric and coronal conditions. This work was an extension of previous studies by Wentzel (1979), Spruit (1982), which analysed specific types of oscillations in a magnetic cylinder. Recovering the dispersion diagrams introduced by Edwin & Roberts (1983) is the starting point for testing the numerical algorithm in a cylindrical geometry. Both photospheric and coronal dispersion diagrams are shown in Figure 4.1 and can be directly compared to Figure 3 and Figure 4 in Edwin & Roberts (1983). Figure 4.1a shows the resulting dispersion diagram for a uniform cylinder under photospheric conditions, where the correct eigenvalues are identified that agree with the analytical results of Edwin & Roberts (1983). The branches of fast kink and surface sausage waves are trapped between c_k and c_e , slow body modes are trapped between c_{Ti} and c_i and slow kink and sausage surface waves are seen propagating at speeds just below c_{Ti} . Figure 4.1b displays the obtained dispersion diagram for a uniform cylinder under coronal conditions. Fast body modes propagate at speeds above v_{Ai} and experience a cut-off at v_{Ae} where at speeds faster than this they become leaky (Wilson 1981, Stenuit et al. 1998, 1999), also see Section 1.7.2. The fundamental kink branch can be seen trapped between v_{Ai} and c_k which tends towards c_k in the long wavelength limit, in agreement with the analytical results of Edwin & Roberts (1983). Furthermore, in a coronal environment, slow body modes are found to be trapped between c_{Ti} and c_i . This uniform cylinder

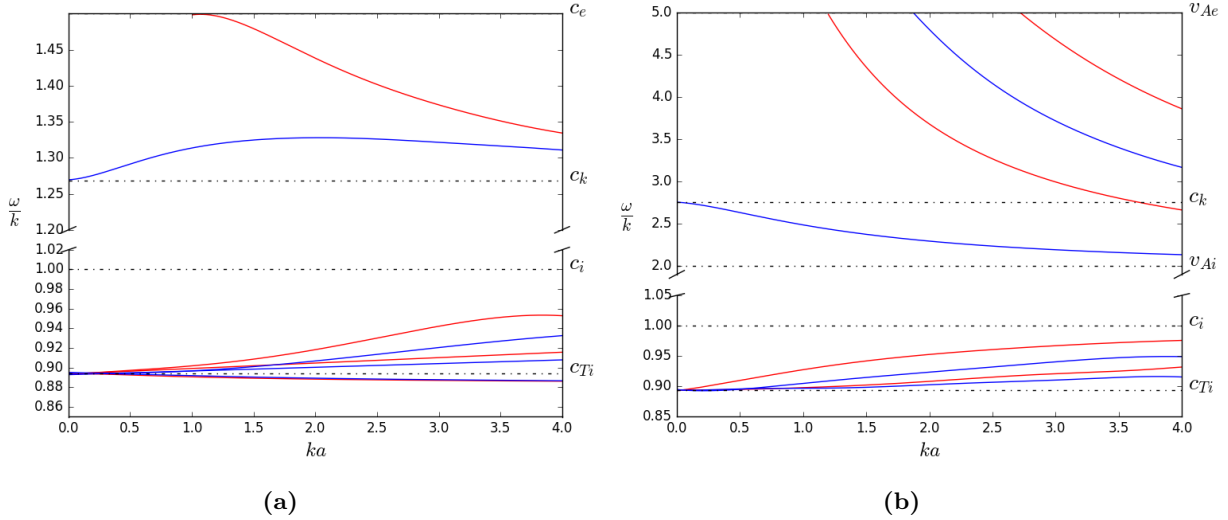


Figure 4.1: The numerical solutions plotted on the dispersion diagram for a uniform magnetic cylinder under (a) photospheric conditions given by $c_e = 1.5c_i$, $v_{Ai} = 2c_i$ and $v_{Ae} = 0.5c_i$, and (b) Coronal conditions given by $c_e = 0.5c_i$, $v_{Ai} = 2c_i$ and $v_{Ae} = 5c_i$. Red curves denote sausage mode, blue curves show kink mode. Figures replicate those shown in Figure 3 and Figure 4 in Edwin & Roberts (1983).

is a very basic model of waveguides observed in the solar atmosphere, yet it is reassuring that the numerical algorithm obtains the known real eigenvalues under the new geometry and relevant boundary conditions.

4.3.2 Magnetic cylinder with steady flow

It is well known that the addition of a bulk background plasma flow introduces new physics into the observed wave modes. Nakariakov & Roberts (1995a) conducted an analytical study into the effect that a steady plasma flow has on magnetoacoustic waves in a magnetic slab. The authors found that the presence of a background flow introduces an observed Doppler shift of the wave frequency. This frequency shift alters the physics slightly as wave modes may be shifted into windows where they are not permitted to propagate as trapped modes. These results were also recovered in Chapter 3 using the numerical shooting method rather than the analytical approach.

In this section, the analytical results from a previous study (Terra-Homem et al. 2003) are recovered which investigates the effect that a steady flow has on the MHD wave modes of a magnetic cylinder. In this work, the authors took a uniform magnetic cylinder model adopted from Edwin & Roberts (1983) and incorporated a steady background plasma flow, similar to that done by Nakariakov & Roberts (1995a) but in a cylindrical geometry. The authors came to a very similar conclusion to that of the magnetic slab with a steady flow counterpart. Namely, the inclusion of a steady background plasma flow changes the properties of magnetoacoustic waves, in the sense that the flow provides an observed Doppler shift to the wave modes which may shift the cut off values and propagation speeds in both the short and long wavelength limits. In Figure 4.2, we display the resulting dispersion diagrams obtained using the numerical technique for waves under photospheric and coronal conditions in a magnetic cylinder with a background steady flow. Figure 4.2a shows the dispersion diagram for a magnetic cylinder under typical photospheric conditions with an internal plasma flow of $U_{0i} = 0.2v_{Ai}$. This Figure is representative of Figure 10 in Terra-Homem et al. (2003). The asymmetry between forward propagating and backward propagating waves can be

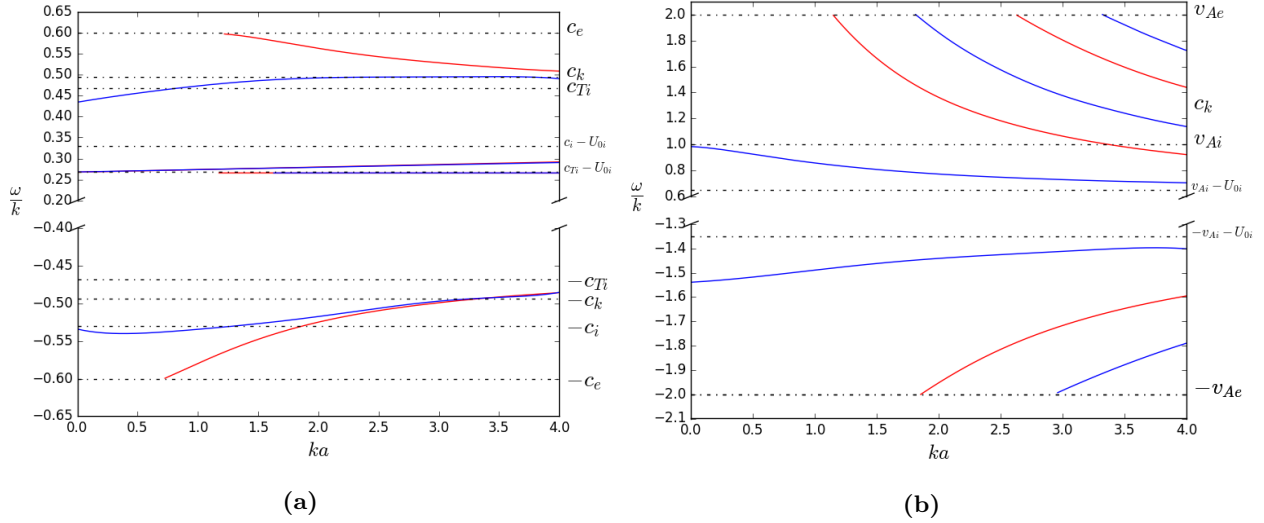


Figure 4.2: The numerical solutions plotted on the dispersion diagram for a uniform magnetic cylinder with a steady background plasma flow under (a) photospheric conditions given by $c_e = 0.6v_{Ai}$, $c_i = 0.53v_{Ai}$, $v_{Ae} = 0$ and $U_{0i} = 0.2v_{Ai}$. (b) Coronal conditions given by $c_e = 0.07v_{Ai}$, $c_i = 0.11v_{Ai}$, $v_{Ae} = 2v_{Ai}$ and $U_{0i} = 0.35v_{Ai}$. Red curves denote the sausage mode, blue curves show the kink mode. Figures (a) and (b) replicate those shown by Figure 10 and Figure 5 in Terra-Homem et al. (2003), respectively.

clearly seen by the structure and cut-off values of the fast forward and backward surface modes. A more qualitative explanation of this is given by the expression in equation (24) in Terra-Homem et al. (2003), which shows the expansion of the dispersion relation in the thin-tube limit, albeit for the incompressible case. Due to the non-uniformity of our model, an analytical description in this limit is not possible, however this study provides a good insight into the behavior of the waves in this regime and more importantly, shows how the behaviour of the waves is dependent on the flow, creating the asymmetry between forward and backward propagating modes, similar to the magnetic slab case (Nakariakov & Roberts 1995a). Under these conditions the backward sausage and kink body modes are shifted into a region where they no longer exist as trapped modes. However, the background plasma flow is not strong enough to shift the forward body and surface modes into the leaky regime, instead these modes are shifted relative to the flow speed. Figure 4.2b shows the dispersion diagram for magnetoacoustic waves in a coronal magnetic cylinder with an internal steady background flow of $U_{0i} = 0.35v_{Ai}$. Similar to the photospheric case, it is clear that all wave modes are shifted by a constant frequency due to the background flow. This effect can be clearly seen by the cut-off wavenumbers between the forward and backward propagating fast body modes.

In this section, the numerical approach has been further tested against previously obtained analytical results in a cylindrical geometry. The predicted eigenvalues have been correctly obtained and it would now be instructive to investigate a scenario which cannot be investigated analytically.

4.4 Inhomogeneous plasma density

In this section, the equilibrium internal plasma density is considered to be inhomogeneous in the radial direction r . For all the following case studies, the spatially non-uniform plasma density is modelled as a series of Gaussian profiles, exactly the same principle as the investigation in Chapter

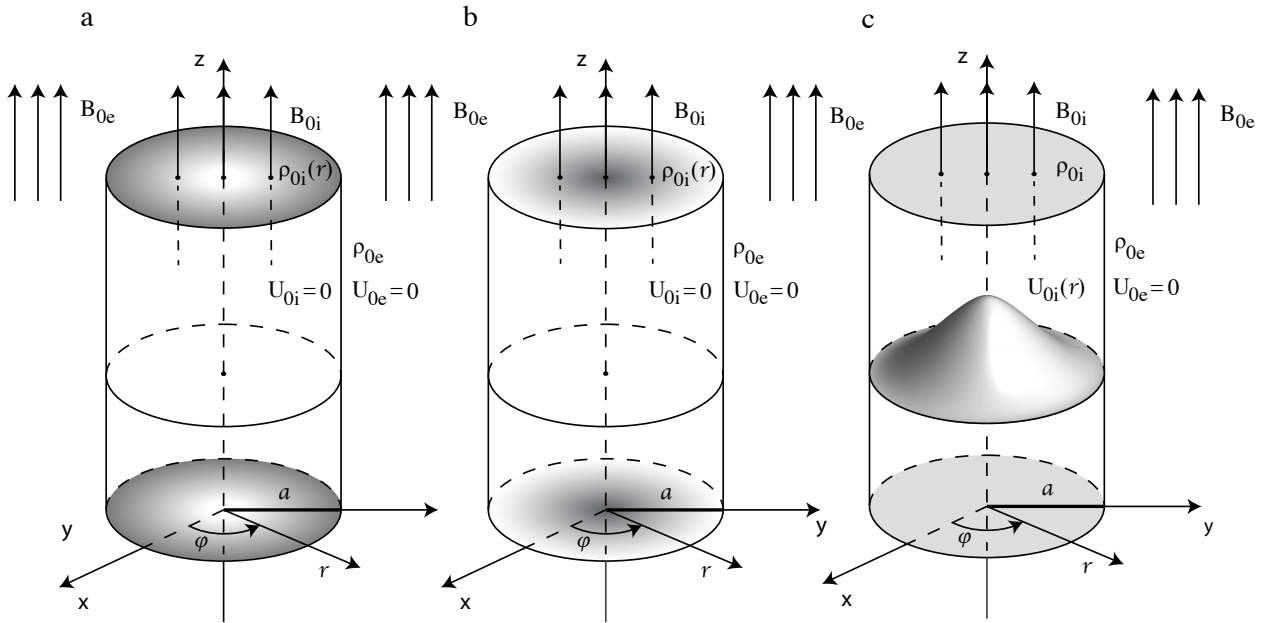


Figure 4.3: Cartoon depicting the equilibrium configuration of a radially dependant non-uniform magnetic flux tube in the solar atmosphere. Three separate cases are studied in this chapter. An inhomogeneous density magnetic flux tube under (a) photospheric conditions and (b) coronal conditions with no plasma flow. These types of equilibria may represent features observed in the solar atmosphere, e.g. sunspots and coronal loops, respectively. The equilibrium density profile inside the magnetic flux tube $\rho_{0i}(r)$ is denoted by the shaded contours, with a darker shade representing a (locally) more dense plasma. The actual profiles of $\rho_{0i}(r)$ investigated for the non-uniform density photospheric case are shown in Figure 4.4) and for the coronal case shown in Figure 4.8. Finally a uniform magnetic flux tube with a non-uniform internal background plasma flow ($U_{0i}(r)$) shown as 3D Gaussian shape (see panel (c)) is considered, with radial profiles as demonstrated in Figure 4.14. This case is applicable for some jet-like structures observed in the solar atmosphere.

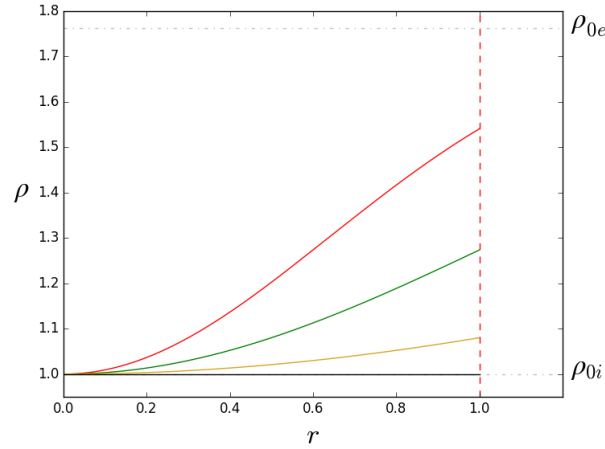


Figure 4.4: The non-uniform background density modelled as a series of Gaussian profiles studied in this section for a non-uniform magnetic cylinder under photospheric conditions. $W = 10^5$ (black), $W = 3$ (yellow), $W = 1.5$ (green) and $W = 0.9$ (red).

3. These profiles are modelled using the expression:

$$\rho_i(r) = \rho_{0e} + (\rho_{0i} - \rho_{0e}) \exp\left(-\frac{(r - r_0)^2}{W^2}\right),$$

where r_0 is the centre of the Gaussian profile located at $r = 0$. The width of the inhomogeneity is again controlled by W . ρ_{0i} is the internal plasma density at r_0 and ρ_{0e} is the uniform value of the external plasma density. A sketch of the non-uniform cylinder is shown in Figure 4.3. Total pressure balance is achieved by a variation in equilibrium temperature to maintain a constant gas pressure across the flux tube, through the ideal gas law, similar to that shown in Figure 3.5.

4.4.1 Photospheric conditions

In this section, we consider a photospheric magnetic flux tube with a non-uniform background density profile. Under photospheric conditions, the non-uniform background density is shown in Figure (4.4). Here, the centre of the flux tube is a local minimum for the internal density distribution, where the density increases towards the boundary at a rate which depends on the width of the Gaussian distribution. In all non-uniform cases the density at the boundary tends towards the external density. This also introduces bands on the dispersion diagrams for all characteristic speeds which depend on the plasma density. The internal sound, Alfvén and tube speeds all now range from the value at the centre of the flux tube to the value at the boundary, denoted as c_B , v_{AB} and c_{TB} . The resulting characteristic frequencies where the discrete wave modes are resonantly damped are shown in Figure 4.5. The frequency where the waves are resonantly damped is single-valued for the case of a uniform density, as would be expected, and is linear in k . As the equilibrium inhomogeneity is increased, the resonant frequencies occupy a larger range and possess a maximum at the centre of the cylinder

As would be expected, the case for a large Gaussian width, Figure 4.6a, corresponding to a uniform distribution produces the same dispersion diagram as shown for the uniform scenario in Figure 4.1a. As the width of the Gaussian density profile is decreased, the fast sausage and kink modes remains relatively unaffected, however are shifted to slightly slower phase speeds with increasing

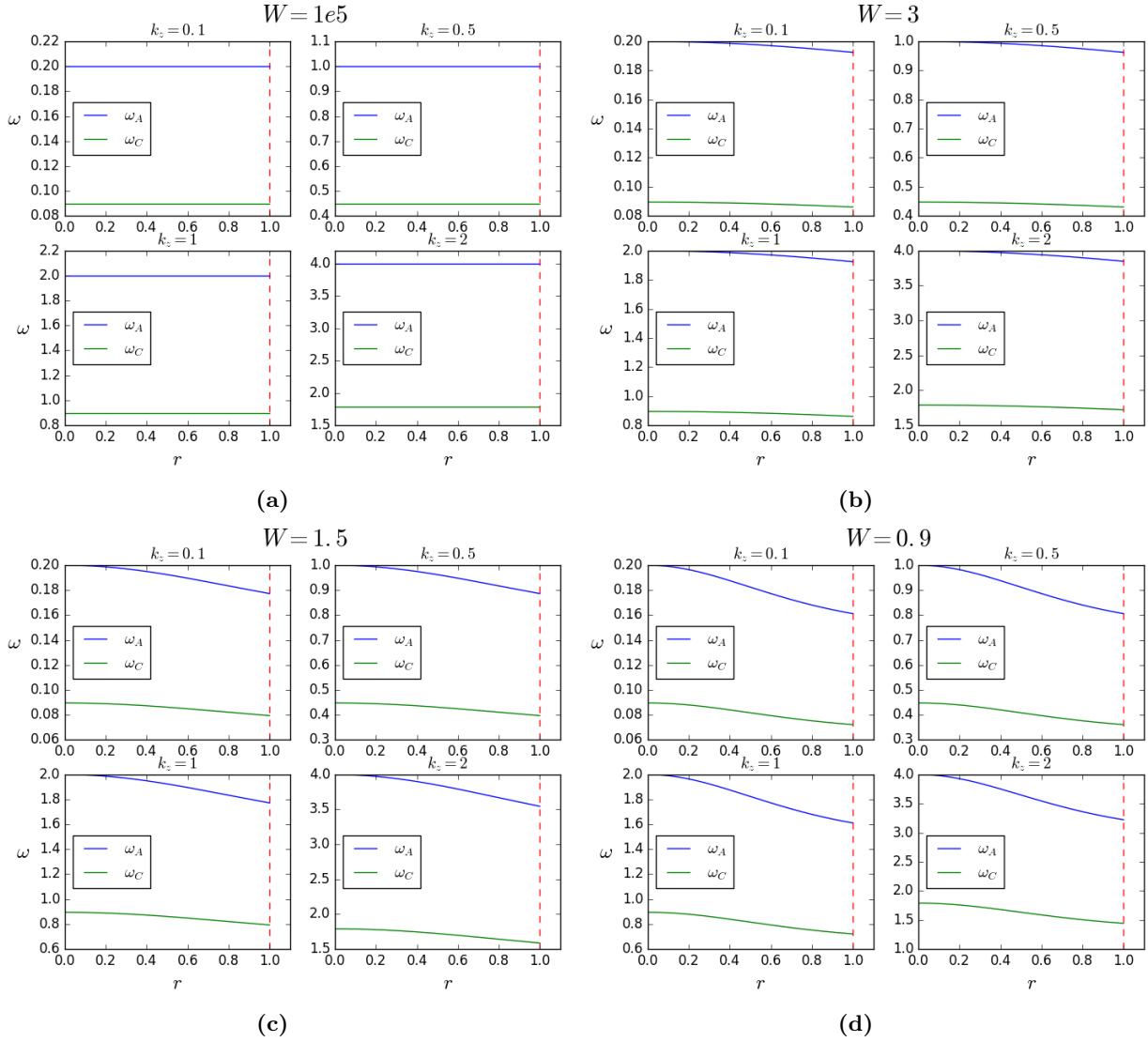


Figure 4.5: The Alfvén (blue line) and cusp frequency (green line) are shown as a function of spatial variable r for a non-uniform cylinder under photospheric conditions. For frequencies lying inside this range, the discrete wave modes are swallowed by the continua. These continua are shown for different wavenumber k . (a) The frequencies for the uniform density case, (b) $W = 3$, (c) $W = 1.5$, (d) $W = 0.9$.

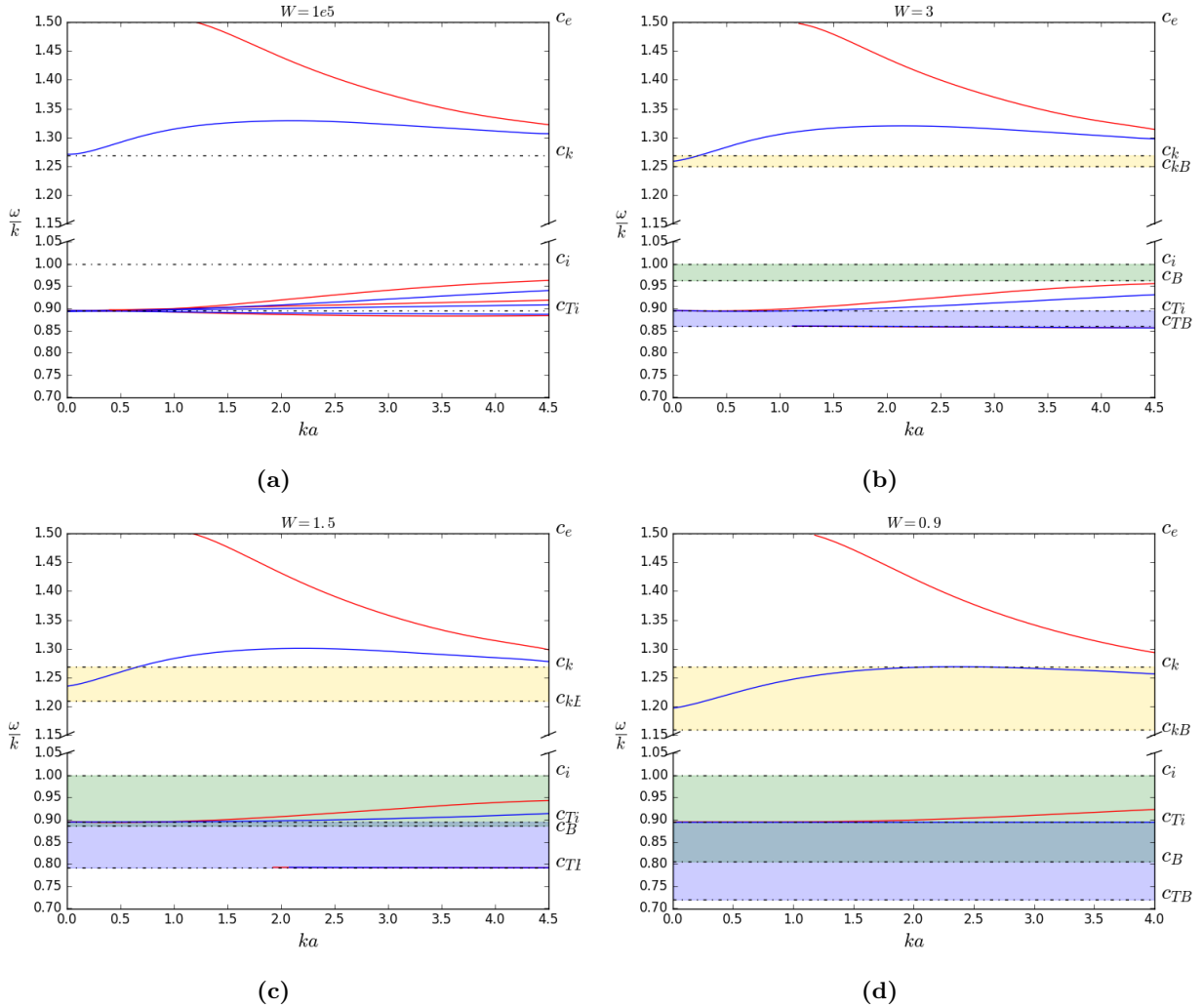


Figure 4.6: Dispersion diagrams for magnetoacoustic waves in a photospheric cylinder with a background plasma density in the form of Gaussian profiles shown in Figure 4.4. (a) $W = 10^5$ corresponding to a uniform flow, (b) $W = 3$, (c) $W = 1.5$ and (d) $W = 0.9$. Red curves denote sausage mode, blue curves show kink mode. Shaded regions represent the non-uniform bands due to the equilibrium inhomogeneity. The slow continuum (blue shaded region), inhomogeneous sound speed band (green shaded region) and inhomogeneous kink speed band (orange shaded region) are all shown.

background non-uniformity. Figure 4.6 shows the behaviour of all wave modes as the inhomogeneity of background plasma density is increased. The slow body modes remain trapped between c_{Ti} and c_i although appear to also have slower phase speeds as the inhomogeneity is increased. For sufficient non-uniformity certain slow body modes can be cut off below c_{Ti} . Similar to the study in Chapter 3 into waves in a non-uniform density photospheric slab these modes exist within a band shown by the green shaded region but this band does not represent a continuum therefore this is physically permissible. Furthermore, as the level of background density non-uniformity is increased, the slow surface modes in the photospheric case propagate with speeds similar to c_{TB} , which obviously changes with the inhomogeneity. At sufficiently large inhomogeneity, these modes disappear from the dispersion diagram, as they are shifted into the slow continuum. It is clear from Figure 4.6 that a non-uniform background density has the effect of decreasing the phase speeds of wave modes in a photospheric cylinder.

Turning attention now to the physical appearance of the eigenfunctions of the wave modes in a non-uniform photospheric magnetic cylinder. Figure 4.7 shows the spatial behaviour of fast surface and slow body modes for both the kink and sausage mode in a photospheric cylinder under all scenarios displayed in Figure 4.4. Similar to the results of a magnetic slab, both the kink and sausage fast surface modes appear to be unaffected by the background inhomogeneity for \hat{P}_T and $\hat{\xi}_r$. However Figure 4.7b shows that the azimuthal perturbation $\hat{\xi}_\varphi$ becomes more pronounced at the boundary as the background plasma inhomogeneity is increased. The slow body modes for both sausage and kink are shown in Figures 4.7c and 4.7d. Coinciding with the previously obtained results for a non-uniform magnetic slab, it was found that these modes were most affected by the background inhomogeneity, this is again true for a cylindrical waveguide. Both \hat{P}_T and $\hat{\xi}_r$ are greatly affected for both sausage and kink modes and show the appearance of extra nodes and points of inflexion as the background inhomogeneity is increased. The azimuthal component, $\hat{\xi}_\varphi$, also shows this behaviour for the slow kink mode. Finally, Figure 4.7 highlights the differences that a non-uniform background plasma density has on surface modes and body modes. Surface modes are defined as having a positive squared radial wavenumber and have maximum amplitude at the surface of the waveguide. Body modes have a negative squared radial wavenumber and, as such, exhibit oscillatory behaviour throughout the waveguide, possessing nodes inside the cylinder. Introducing a non-uniform background plasma density changes the spatial behaviour of surface modes at the boundary, most notably the azimuthal component, with the internal structure near the centre remaining locally constant. On the other hand a non-uniform background plasma density changes the local internal structure of the eigenfunctions for body modes, with the boundary values remaining unchanged no matter the scale of inhomogeneity of background equilibrium.

4.4.2 Coronal conditions

Unlike the similar case studied in Section 3.3 for a magnetic slab, the characteristic speeds chosen to represent coronal conditions are slightly changed in the case of a cylindrical magnetic flux tube, to be comparable to previous studies. This changes the characteristics of the dispersion diagram, namely that the slow body modes are absorbed into the slow continuum at certain values of inhomogeneity, which was not present in Section 3.3 due to the smaller speed of v_{Ae} used in the analysis. The background density profiles investigated in this paper are the same as before and displayed in Figure 4.8 for increasing non-uniformity where the internal density gradually tends towards the external density at the boundary. In Figure 4.9, we show the resulting characteristic frequencies where the wave modes are resonantly damped in the non-uniform coronal cylinder cases investigated in this section.

Figure 4.10 shows the behaviour of sausage and kink modes in a coronal cylinder with a back-

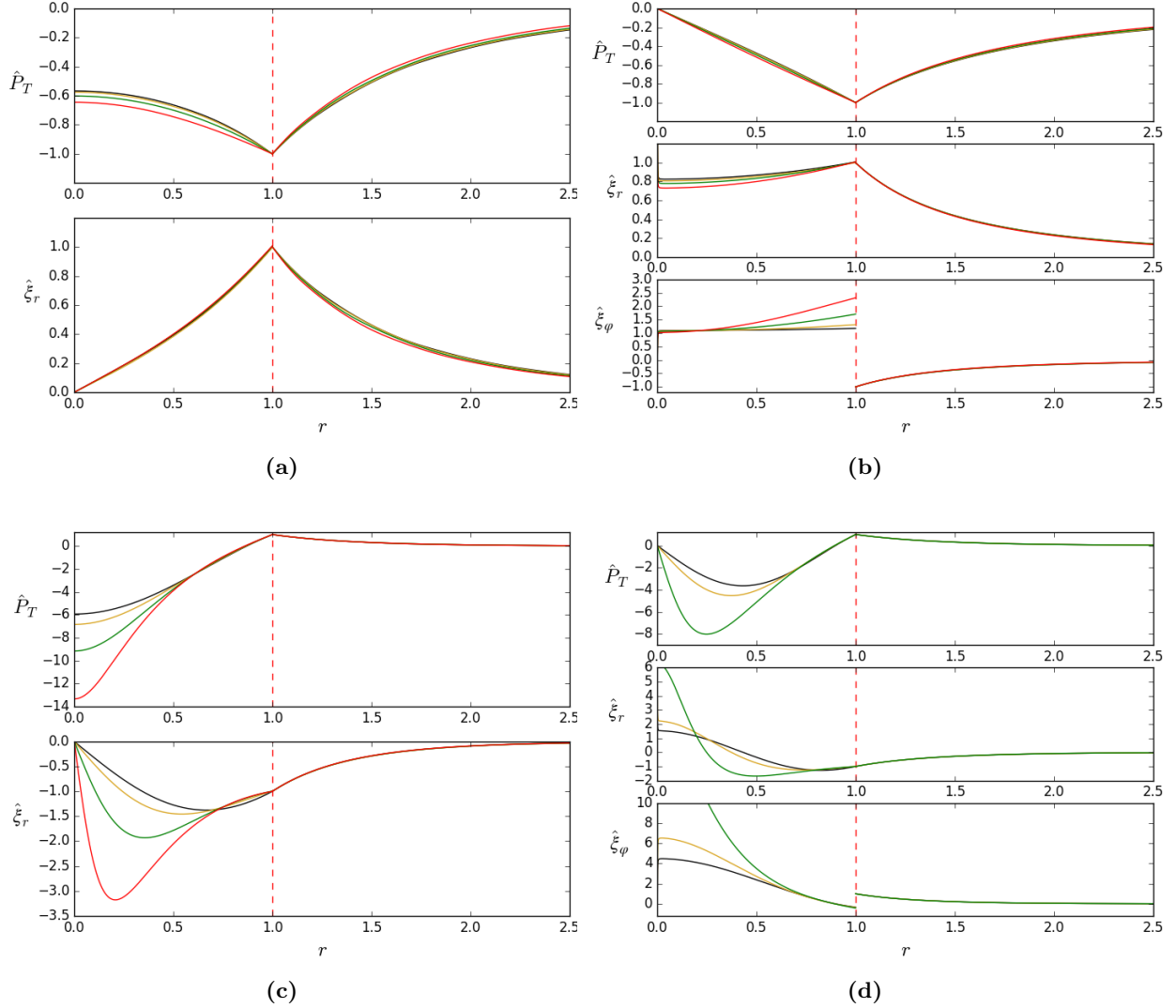


Figure 4.7: Resulting eigenfunctions for MHD wave modes in a photospheric cylinder with a non-uniform background plasma density given by the distributions shown in Figure 4.4 where the colour scheme is consistent. (a) Fast sausage surface mode for all cases with $ka = 2.7$, (b) fast kink surface mode for all cases with $ka = 1.3$, (c) slow sausage body mode with $ka = 2.7$, (d) slow kink body mode for three cases all with $ka = 3.2$. No azimuthal component is shown for the sausage mode as this wave mode does not produce an azimuthal perturbation. The case for $W = 0.9$ not shown in (d) as this wave mode is absorbed into the slow continuum. All plots are normalised to the external boundary value for each eigenfunction.

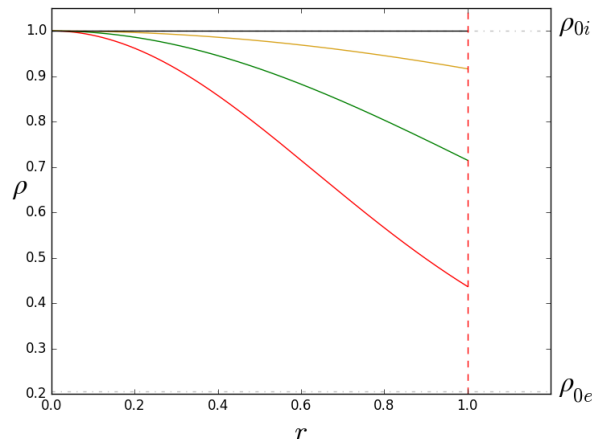


Figure 4.8: Gaussian background density profiles studied for a non-uniform cylinder under coronal conditions. $W = 10^5$ (black), $W = 3$ (yellow), $W = 1.5$ (green) and $W = 0.9$ (red).

ground spatial density profile as a Gaussian distribution. The case of a large width when the Gaussian distribution is given by $W = 10^5$ and the resulting dispersion diagram is shown in Figure 4.10a. As expected, this case produces the exact result as the uniform investigation by Edwin & Roberts (1983) and shown earlier in this chapter in Figure 4.1b. As the inhomogeneity of the background plasma density is increased, the density value at the boundary becomes smaller (tends towards the external value however is still discontinuous across $r = a$). As a result, the variables which depend on density such as c_i , v_{Ai} and c_{Ti} become a continuous band across multiple possible phase speeds, these are shown by the shaded regions in Figure 4.10. It is well known that the Alfvén and cusp continuum are regions in which dissipative processes are possible, such as phase mixing and resonant absorption, due to local resonances occurring within these bands. The wave frequency becomes complex here and, as such, the solution no longer appears on the dispersion diagram between v_{AB} and c_{TB} , as the solution moves away from being a purely real value. In a cylinder with a large enough inhomogeneity of plasma density, the slow body modes disappear from the dispersion diagram as no real frequency band exists in which they can propagate, without becoming resonantly damped.

In a non-uniform plasma, it is well known that a smooth inhomogeneity such that the density varies linearly from one value (ρ_1) to another (ρ_2), that quasi-modes are introduced (Sedláček 1971, Tirry & Goossens 1996, Priest 2014). The real part of the quasi mode phase speed is defined as $\sqrt{(\rho_1 v_{A1}^2 + \rho_2 v_{A2}^2)/(\rho_1 + \rho_2)}$, which is simply the kink speed between the minimum and maximum value. Replacing the smooth linear non-uniform density by an external ρ_{0e} and internal ρ_{0i} value yields the well known kink speed for a uniform cylinder. In Figure 4.10, we show that the fundamental kink branch does not tend to either of these values in the thin-tube limit. Instead, it tends towards a value in between which is due to the fact that the inhomogeneity is not smooth from outside to inside the cylinder, in all cases the density is discontinuous across $r = a$.

Figure 4.11 displays the spatial eigenfunctions for both the fast sausage mode and fundamental kink mode in a coronal cylinder with a non-uniform background density. We have previously concluded that fast modes are unaffected by the background inhomogeneity in a magnetic slab, however, their behaviour may be different in a magnetic cylinder, therefore we investigate the behaviour of their eigenfunctions here. It can be seen clearly in Figure 4.11 that, as the plasma

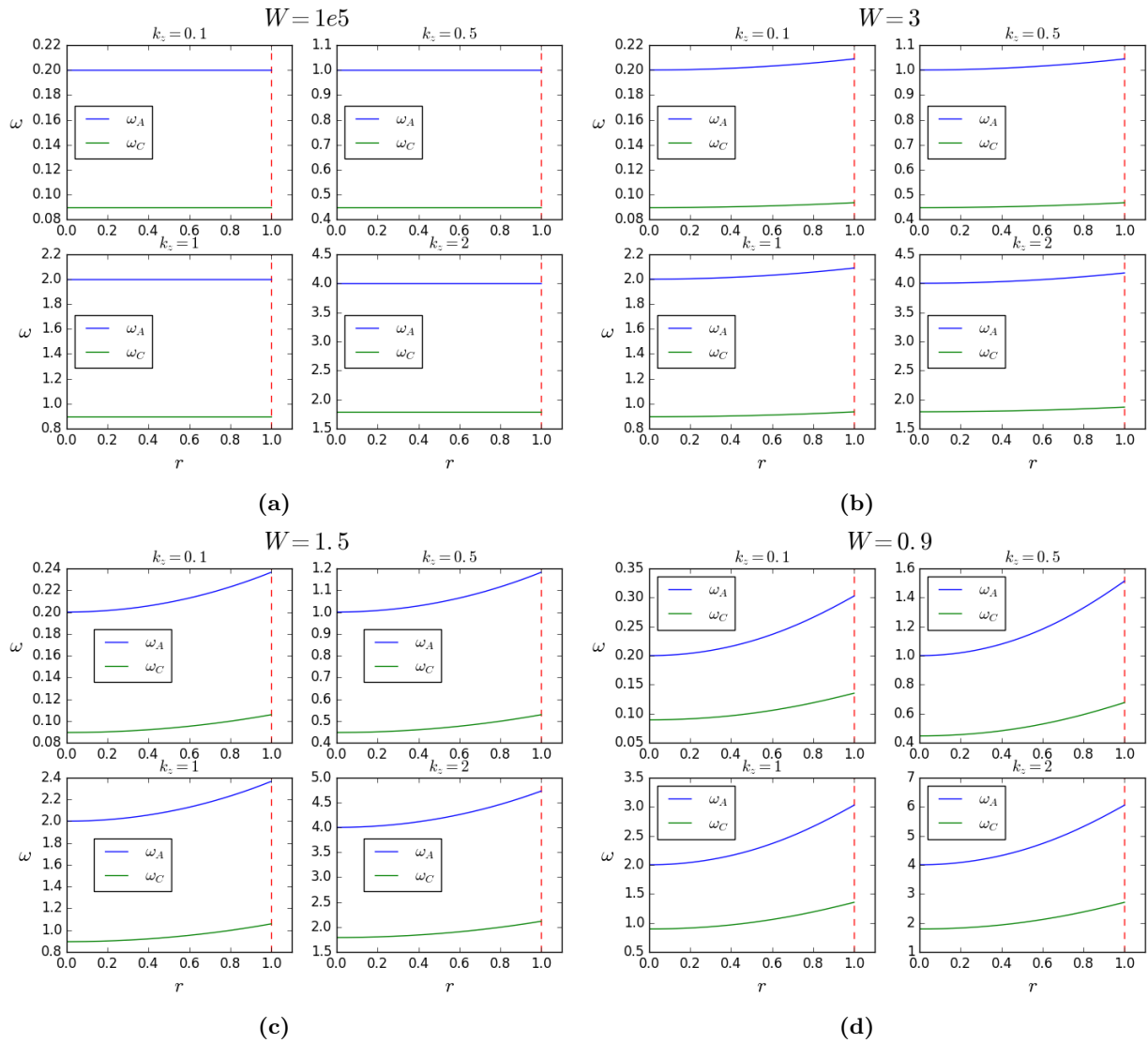


Figure 4.9: Same as Figure 4.5 but for the case of a non-uniform density cylinder under coronal conditions.

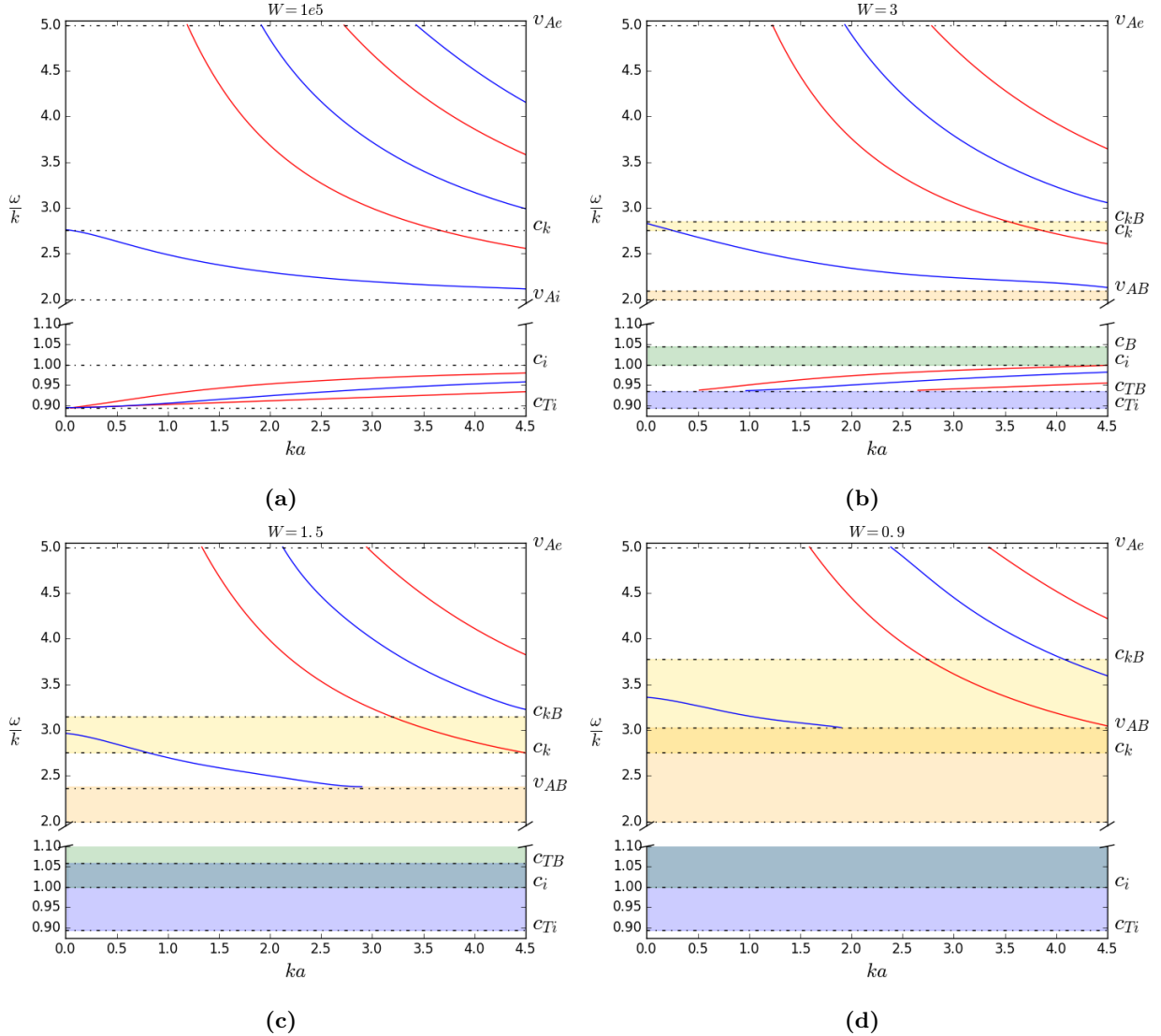


Figure 4.10: Dispersion diagrams for magnetoacoustic waves in a coronal cylinder with a background plasma density in the form of Gaussian profiles shown in Figure (4.8). (a) $W = 10^5$ corresponding to a uniform flow, (b) $W = 3$, (c) $W = 1.5$ and (d) $W = 0.9$. Red curves denote sausage mode, blue curves show kink mode. Shaded regions represent the non-uniform bands due to the equilibrium inhomogeneity. The slow continuum (blue shaded region), inhomogeneous sound speed band (green shaded region), Alfvén continuum (pink shaded region) and inhomogeneous kink speed band (orange shaded region) are all shown.

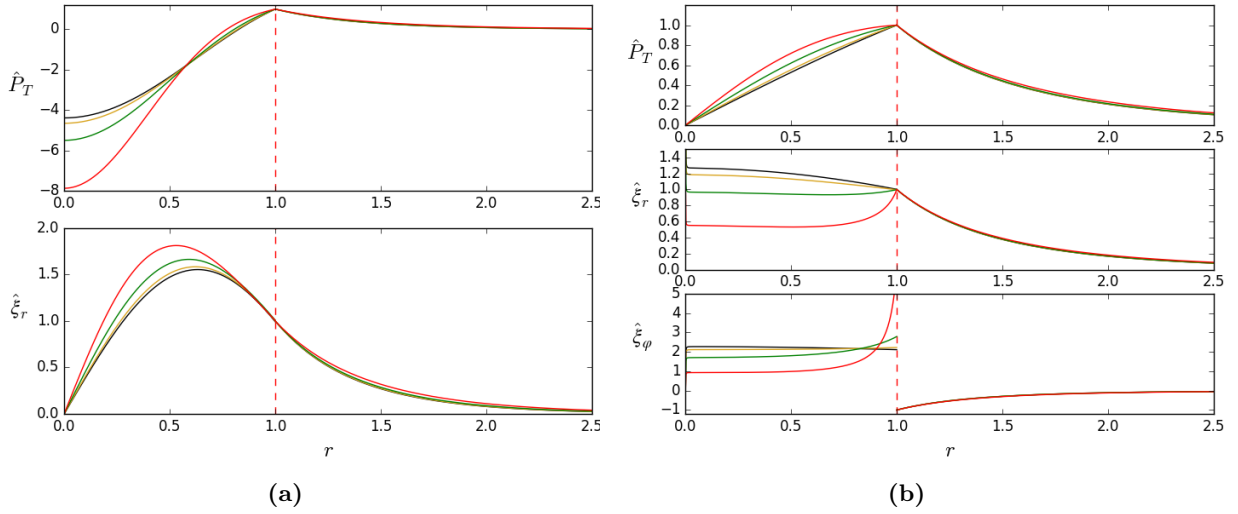


Figure 4.11: Resulting eigenfunctions for MHD wave modes in a coronal cylinder with a non-uniform background plasma density given by the distributions shown in Figure 4.8 where the colour scheme is consistent. (a) Fast sausage body mode for all cases with $ka = 2.75$, (b) fundamental kink body mode for all cases with $ka = 1.5$. No azimuthal component is shown for the sausage mode as this wave mode does not produce an azimuthal perturbation in this case. All plots are normalised to the external boundary value for each eigenfunction.

density inhomogeneity is increased, both the fast sausage mode and fundamental kink mode display different spatial characteristics for both \hat{P}_T and $\hat{\xi}_r$ and also $\hat{\xi}_\varphi$ for the kink mode. The fundamental kink mode was not present in the magnetic slab analysis and this is the mode which is routinely observed in the thin-tube limit in the solar atmosphere when a cylindrical analytical model is considered. The difference in spatial eigenfunction behaviour is also more pronounced for $ka < 1$ for the fundamental kink mode. As the fast sausage mode experiences a cut-off around $ka = 1.5$, it is unlikely that these eigenfunctions would be observed for this mode in non-uniform coronal structures, which are frequently observed in the thin-tube limit.

A snapshot in time of the resulting velocity field at maximum displacement for the fundamental kink mode is shown in Figure 4.12 for all cases of equilibrium Gaussian density. The velocity field corresponds to the eigenfunctions shown in Figure 4.11b converted into Cartesian components to be visualised in a uniform Cartesian grid. Any given vector $\mathbf{Q} = (Q_r, Q_\varphi, Q_z)$ in a cylindrical geometry can be easily converted to a similar vector $\mathbf{Q} = (Q_x, Q_y, Q_z)$ in a Cartesian geometry through the transformation:

$$Q_x = Q_r \cos \varphi - Q_\varphi \sin \varphi, \quad (4.15)$$

$$Q_y = Q_r \sin \varphi + Q_\varphi \cos \varphi, \quad (4.16)$$

$$Q_z = Q_z. \quad (4.17)$$

The case for uniform density retrieves the theoretical kink mode displacement in that the velocity field is uniform inside the cylinder and has a dipole configuration in the external region as seen in Figure 4.12a. As the equilibrium inhomogeneity is increased, the resulting velocity field inside the cylinder becomes curved, as azimuthal perturbations dominate the plasma motions. For the case of maximum inhomogeneity given by $W = 0.9$ shown in Figure 4.12d, this increasing azimuthal component results in the boundary of the cylinder becoming distorted. This result can be understood

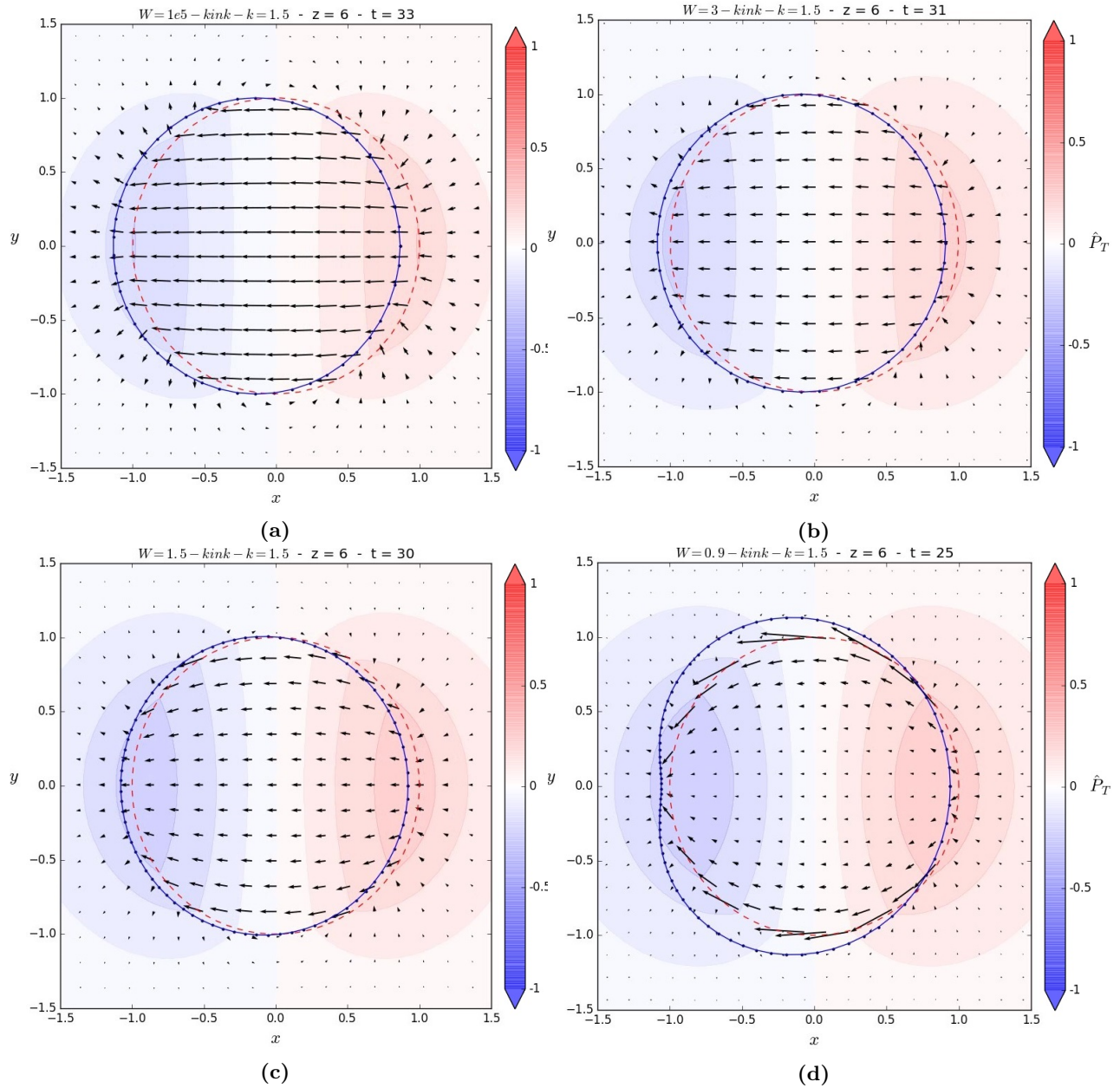


Figure 4.12: Snapshots of the velocity field in time at the moment of maximum displacement for the different Gaussian profiles modelling plasma density for the fast fundamental kink mode. (a) $W = 10^5$, (b) $W = 3$, (c) $W = 1.5$ and (d) $W = 0.9$. The eigenfunctions shown in Figure 4.11b are converted into Cartesian components and shown in a Cartesian grid. The same value of $ka = 1.5$ is chosen in all plots. The colour contour shows the normalised total pressure perturbation where blue is negative and red is positive. The solid blue line outlines the shape of the perturbed boundary.

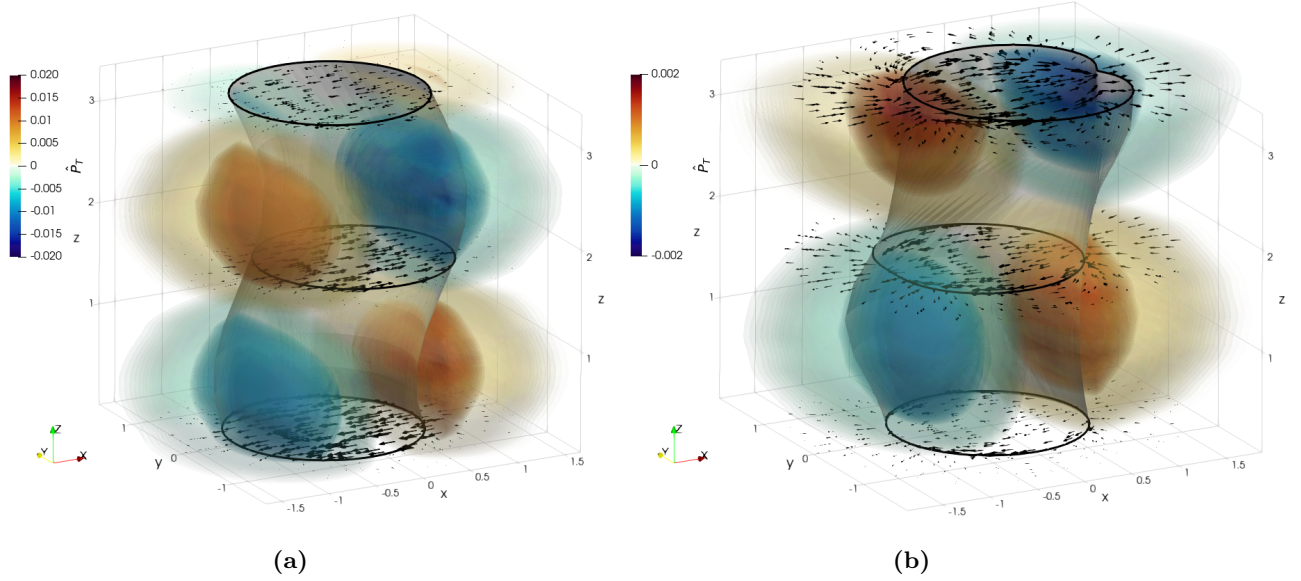


Figure 4.13: 3D visualisation of \hat{P}_T and the perturbed velocity vector field in the presence of a uniform and non-uniform background plasma density for the fundamental kink mode with eigenfunctions shown in Figure 4.11b. These correspond to the 2D velocity field vectors shown in Figure 4.12a and Figure 4.12d respectively. (a) Case for uniform plasma density (b) case with Gaussian density with $W = 0.9$.

by looking at the azimuthal component of the eigenfunction in Figure 4.11b where the magnitude of discontinuity at the boundary increases with increasing inhomogeneity. The nature of the azimuthal displacement component for the kink mode can be understood by examining Equation (4.14) when the location $r = 1$ is crossed. At this position, $\omega^2 - k^2 v_A^2$ changes sign discontinuously whereas the total pressure perturbation \hat{P}_T remains continuous. Furthermore, in the case for maximum inhomogeneity, the frequency, ω , approaches the local resonant Alfvén frequency $k^2 v_A^2$ which results in the large amplitude for $\hat{\xi}_\varphi$. The increased discontinuity in displacement creates counter-streaming flows that can generate the Kelvin-Helmholtz instability (KHI). These results can be compared to the linear stage of Antolin et al. (2014) (see their Figure 1) in which similar behaviour of the boundary is seen but in the case of a thinner boundary layer with a non-uniform density profile. This behaviour has also been detected in previous numerical studies investigating straight cylinders with a non-uniform density layer in the radial direction (Terradas et al. 2008) including non-ideal MHD (Howson et al. 2017) and also an analytic study with a velocity shear in the azimuthal component across the boundary (Soler et al. 2010).

Figure 4.13 shows a 3D representation of the 2D velocity fields seen in Figure (4.12) for a propagating wave in vertical coordinate z . It can be clearly seen in Figure 4.13b that at maximum displacement for the kink mode, the boundary becomes distorted due to the non-uniform equilibrium plasma density. This perturbation of the boundary propagates with the wave vertically through the magnetic flux tube, unlike the uniform scenario shown in Figure 4.13a which maintains the structure of the tube. It was suggested that the fundamental kink mode in a non-uniform plasma should actually be called a surface Alfvén wave due to the mixed properties and increased vorticity, which is not a property associated with magnetoacoustic waves (Goossens et al. 2012). The results presented in this section further strengthen this debate as the kink mode does not display traditional properties when the equilibrium plasma is non-uniform.

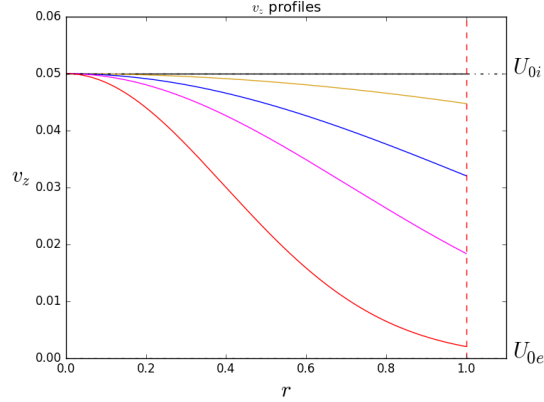


Figure 4.14: *Gaussian flow profiles inside an otherwise uniform coronal magnetic cylinder. $W = 10^5$ (black), $W = 3$ (yellow), $W = 1.5$ (blue), $W = 1$ (magenta) and $W = 0.6$ (red).*

4.5 Inhomogeneous flow in a coronal cylinder

In this section, a magnetic cylinder of uniform plasma is modelled with a vertical straight magnetic field with a field-aligned and radially non-uniform internal background plasma flow embedded in a coronal environment. A sketch of this equilibrium configuration is shown by panel (c) of Figure 4.3. A similar case study was investigated in a magnetic slab in a Cartesian geometry in Section 3.4. The flow magnitude is chosen to be small in comparison with the internal sound speed, i.e. $U_{0i} = 0.05c_i$. This allows a clearer investigation into the physical effects of the spatial flow to be undertaken as a large flow magnitude will shift certain wave modes into the leaky regime. Adopting a small magnitude of the background plasma flow speed also avoids the possibility of the onset of flow related instabilities such as Kelvin-Helmholtz. Similar to the previous investigation of a non-uniform plasma density, the background plasma flow in this section is also modelled as a series of Gaussian profiles, of the form:

$$U_{0i}(r) = U_{0e} + (U_{0i} - U_{0e}) \exp\left(-\frac{(r - r_0)^2}{W^2}\right),$$

where U_{0e} is the flow outside the waveguide, assumed to be 0.

These inhomogeneous flow profiles investigated are shown in Figure 4.14. The case of a large width (i.e. $W = 10^5$) corresponds to a uniform steady flow which is well-known to create an observed Doppler shift to the waves in the direction of flow (Nakariakov & Roberts 1995a). Due to the small amplitude of flow chosen, it is found that there is very little effect on the fast modes in the dispersion diagram, there is a more observable affect on the slow body modes. A zoom in region of the resulting dispersion diagrams are shown in Figure 4.15 for the forward and backward propagating slow body modes. As expected, these waves are shifted with respect to the maximum flow speed. As the non-uniformity of flow is increased, the branches of the forward and backward propagating slow body modes are shifted with a clear asymmetry between the forward and backward propagating modes. With increasing spatial non-uniformity of the background plasma flow, the permissible backward propagating kink and sausage slow body modes propagate in the thin tube limit, whereas the opposite is true for forward propagating slow body modes. This effect is due to the flow speed at the boundary U_B which depends on the initial non-uniformity of the background plasma flow, therefore, a non-uniform background plasma flow may further shift some modes into possible

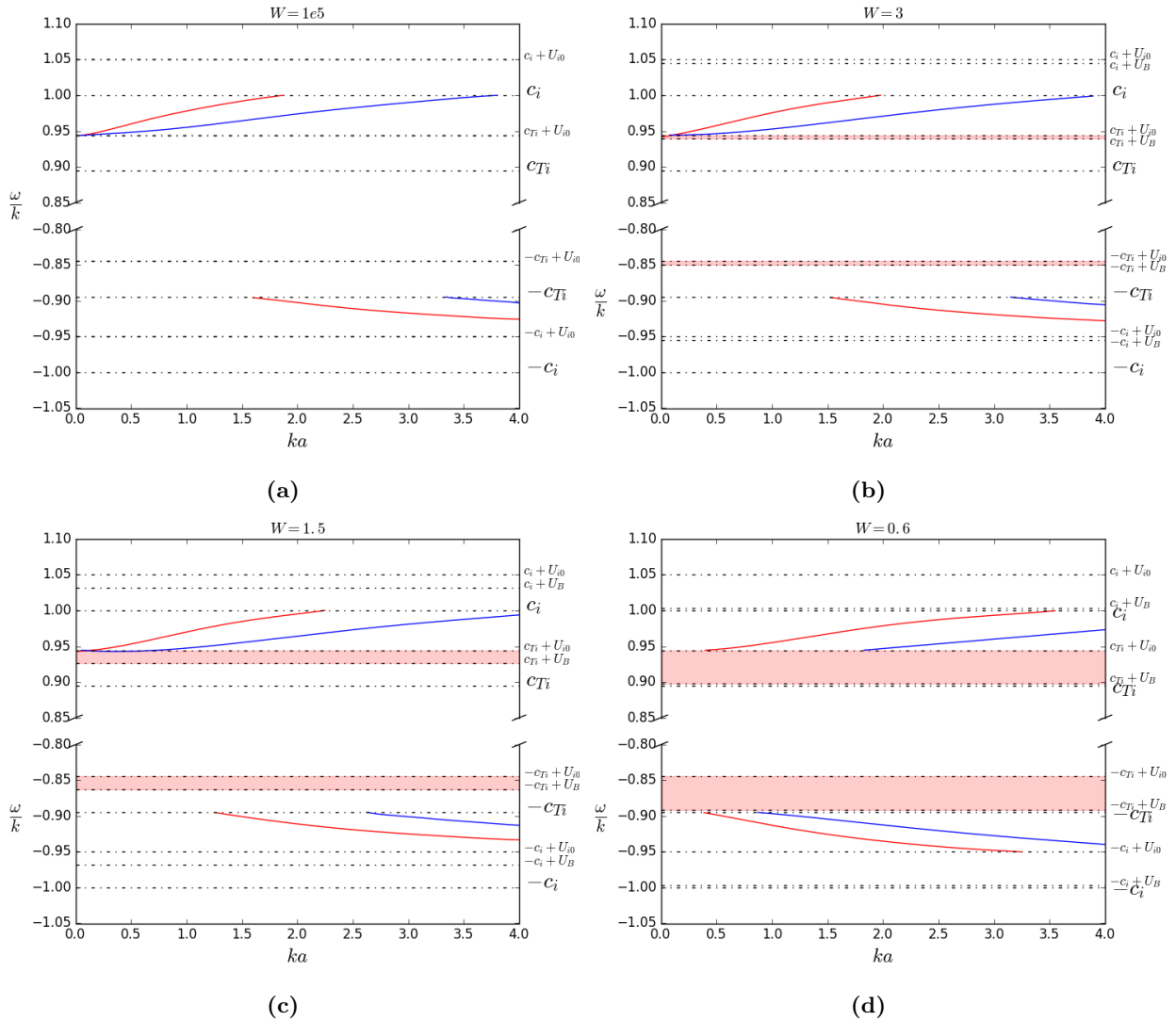


Figure 4.15: Zoom in on dispersion diagrams for forward and backward propagating slow body modes in a coronal cylinder with a background plasma flow in the form of Gaussian profiles shown in Figure 4.14. (a) $W = 10^5$ corresponding to a uniform flow, (b) $W = 3$, (c) $W = 1.5$ and (d) $W = 0.6$. Red curves denote sausage mode, blue curves show kink mode. The red shaded bands indicate the flow modified slow continuum where the modes become resonantly damped.

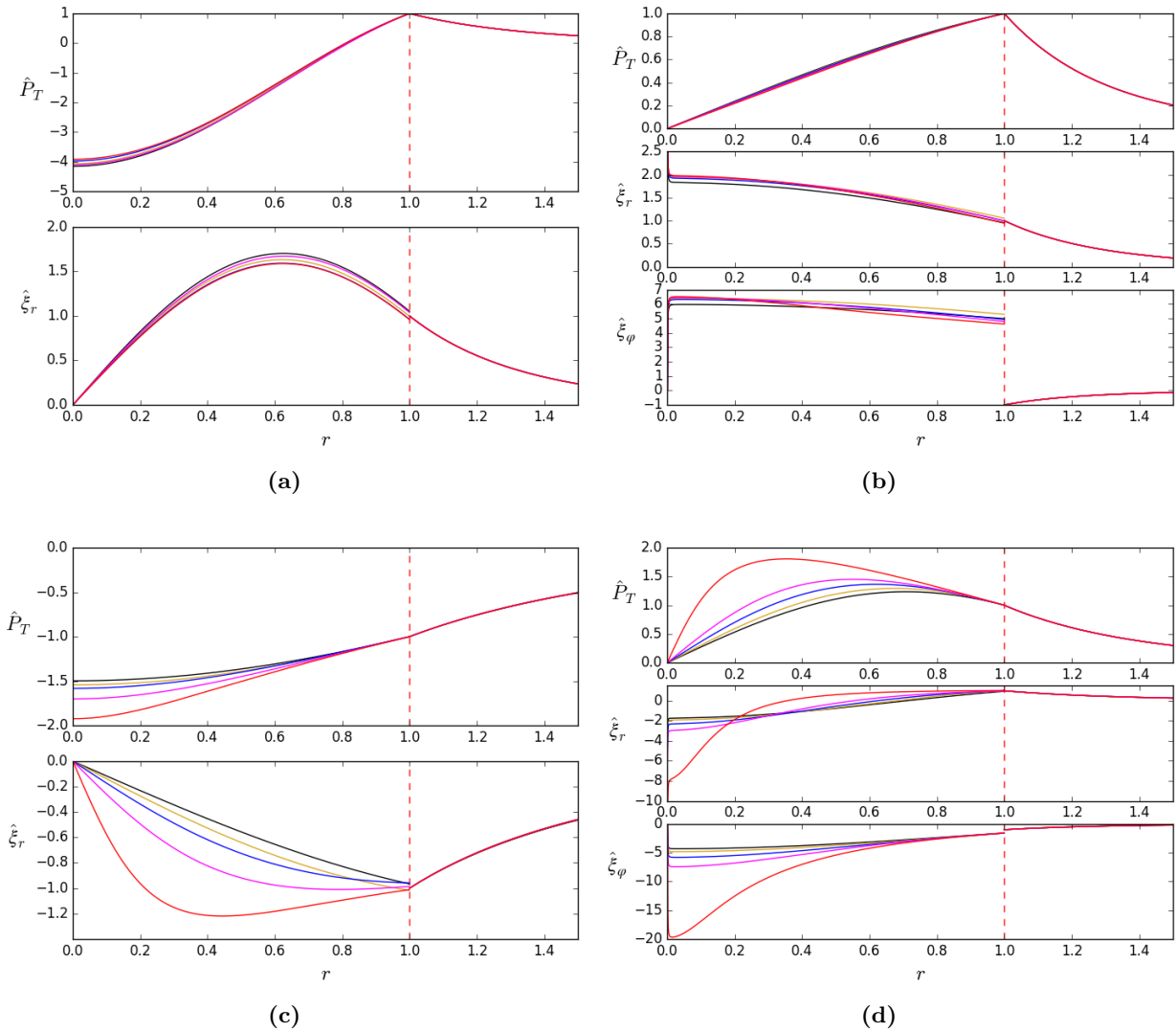


Figure 4.16: Eigenfunctions for a coronal cylinder with a background Gaussian flow as shown in Figure 4.14 where the colour scheme is consistent with the equilibrium profiles. (a) Fast sausage body mode with $ka = 3$, (b) fast kink body mode with $ka = 3$, (c) slow sausage body mode with $ka = 1$, (d) slow kink body mode with $ka = 2$.

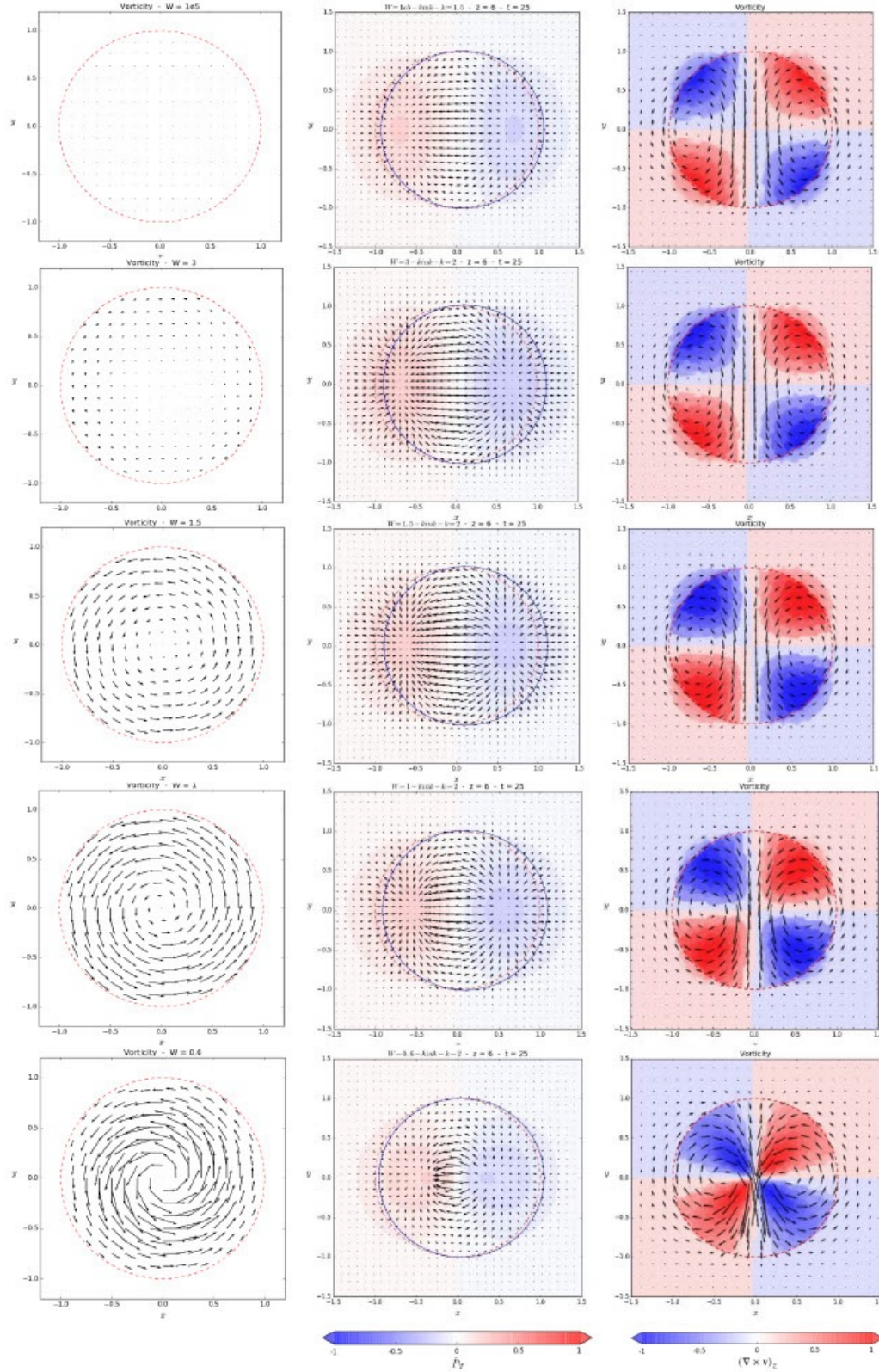


Figure 4.17: Background vorticity field (left), perturbed velocity field (middle) and background plus perturbed vorticity field (right) plots for all cases of Gaussian plasma flow shown in Figure 4.14. These snapshots all correspond to the slow body kink mode with eigenfunctions shown in Figure 4.16d. Top row corresponds to $W = 10^5$ with inhomogeneity increasing down the plot through $W = 3$, $W = 1.5$, $W = 1$ to bottom row where $W = 0.6$. The colour contour in centre plots shows the total pressure perturbation whereas the colour contours in the right column plots denote the vorticity component perpendicular to the xy plane.

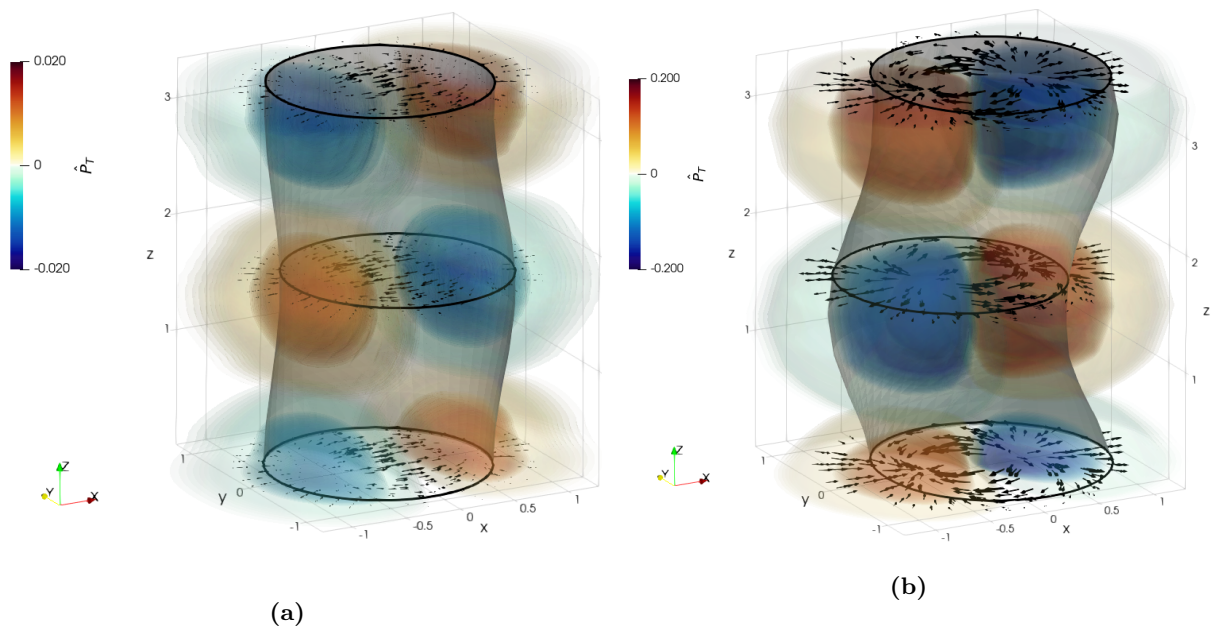


Figure 4.18: 3D visualisation of \hat{P}_T and the perturbed velocity vector field in the presence of a uniform and non-uniform background plasma flow for the slow body kink mode with eigenfunctions shown in Figure 4.16d. These correspond to the 2D velocity field vectors shown in the middle panel of Figure 4.17. (a) Case for uniform plasma flow ($W = 10^5$) (b) case with Gaussian flow with $W = 0.6$. Movies of these 3D visualisations can be found online on the PDG visualisations web-page.

propagation windows. The red shaded bands in Figure 4.15 indicate the Doppler shifted continua given by Equation 1.34, where the modes become resonantly damped. It can be seen that as the inhomogeneity of the background flow is increased, these continuum bands become wider, providing a larger frequency domain for resonant processes to occur.

The resulting eigenfunctions of \hat{P}_T , $\hat{\xi}_r$ and $\hat{\xi}_\varphi$ are shown in Figure 4.16. It is clear that fast modes are not heavily affected by the inhomogeneity of the equilibrium background plasma flow. This is mainly down to the before-mentioned amplitude of the non-uniform flow. The background plasma flow has the affect of Doppler shifting the waves which is much less clear for the dispersive fast waves. Unlike in Section 4.4.2, where the amplitude of plasma density non-uniformity was large, here the equilibrium plasma density is uniform. Slow body modes, however, feel the non-uniformity much more greatly. The local perturbation amplitude for all eigenfunctions is increased with the non-uniformity of the background flow and extra nodes and points of inflexion become visible. Furthermore, the maximum local azimuthal perturbation, $\hat{\xi}_\varphi$, is increased with a more inhomogeneous background plasma flow.

Another quantity which can be investigated is vorticity, which we define as the curl of the velocity field, $\nabla \times \mathbf{v}$. Vorticity plays an important role in the dynamics of the solar atmosphere. Granular motions in the photosphere produce a ubiquitous number of observed vortices in intergranular lanes. These vortices can have the effect of twisting the magnetic field lines which are rooted into the photosphere and exciting torsional Alfvén waves (Fedun, Shelyag, Verth, Mathioudakis & Erdélyi 2011, Fedun, Verth, Jess & Erdélyi 2011, Vigeesh et al. 2012, Moll et al. 2012, Shelyag et al. 2013, Silva et al. 2020). The background vorticity field, perturbed velocity field and the background plus perturbed vorticity field are plotted in Figure 4.17 for the slow body kink mode with eigenfunctions shown in Figure 4.16d. The left hand side column shows the background vorticity due to the equilibrium background plasma flow. Obviously, with a uniform bulk flow, there is no inhomogeneity and as a result, no associated vorticity. As the background plasma flow becomes more non-uniform in the radial direction, the curl of the velocity field now has components perpendicular to the direction of the flow. The background vorticity is localised to the interior of the magnetic cylinder, where the non-uniform plasma flow is located. The centre column in Figure 4.17 shows the perturbed velocity field for the slow body kink mode in the presence of a non-uniform flow. The uniform case on the top row has two clear nodes as predicted by uniform theory. As the background plasma flow becomes more non-uniform, these nodes shift closer together and a resulting vortical motion becomes clearer around the centre of the waveguide, where the magnitude of the background flow is greatest. It can be seen in all plots that the boundary of the waveguide, plotted as a blue line, is unaffected in all cases of non-uniform flow. This result is expected from the eigenfunctions shown in Figure 4.16d which are locally unchanged at the boundary for all background flow profiles. The right hand column of Figure 4.17 shows the resulting background plus perturbed vorticity field. It can be seen that as the non-uniformity of background plasma flow is increased (further down the Figure column), the vorticity is spread out over the whole region of inhomogeneity. Vortical motions become more apparent with increasing non-uniform flow which may act as a driver for other forms of MHD waves. Figure 4.18 again displays the 3D representation of the 2D velocity field seen in Figure 4.17. Locations of the nodes in the slow body kink eigenfunctions can be seen in Figure 4.18a in the velocity field vector for the uniform flow case. However, as expected, the locations of these nodes are pushed together when the background plasma flow is modelled as a Gaussian profile, and is transported up through the tube with the propagation of the wave seen in Figure 4.18b.

4.6 Summary & Discussion

In this chapter, the technique described in Chapter 2 and implemented in a magnetic slab in Chapter 3 and Skirvin et al. (2021) has been employed to obtain the eigenvalues for trapped MHD waves in cylindrical environments representing some cases observed in the solar atmosphere. The algorithm has been tested against well-known analytical results in a simple uniform cylindrical geometry and a scenario that takes into account the inclusion of a bulk background plasma flow. For both case studies the correct eigenvalues were obtained compared to those from previous analytical studies that derive and solve the corresponding dispersion relation. The tool was then applied to investigate the properties of MHD waves in non-uniform magnetic cylinders modelled by an inhomogeneous equilibrium plasma density and an inhomogeneous background plasma flow. When the equilibrium plasma density is modelled as a series of Gaussian profiles with varying widths, the eigenfunctions are changed under both photospheric and coronal conditions. Firstly, under photospheric conditions, slow surface waves are absorbed into the slow continuum when the background density is sufficiently non-uniform. For our studies, a width ($W \approx 0.9$) that corresponds to the internal density at the boundary being halfway between ρ_{0i} and ρ_{0e} is sufficient enough to absorb these modes into the slow continuum. Furthermore, in the thin tube limit the fundamental kink branch no longer tends to the kink speed but instead favours an averaged value between c_k and c_{kB} due to the discontinuous nature of the density profile at the boundary. Finally, as the non-uniformity is increased, the frequency of magnetoacoustic waves decreases such that the band of body modes is also absorbed into the slow continuum at larger inhomogeneities. Comparisons of the spatial eigenfunctions for different modes revealed that the fast axisymmetric modes are not affected by the radial equilibrium inhomogeneity. The fast non-axisymmetric (kink) modes however, experience an increase in the azimuthal displacement at the boundary as the equilibrium plasma density becomes more non-uniform. The internal spatial structure of slow body sausage and kink modes is greatly affected. Similar to the results found in Chapter 3, additional nodes and points of inflexion appear as the background plasma density is modelled with a profile that is increasingly non-uniform. In both cases for the slow body modes of a non-uniform photospheric cylinder, the local amplitude of the eigenfunctions at the boundary is unaffected. Under coronal conditions, similar behaviour is observed with regards to the eigenfunctions. The fundamental kink mode tends to an averaged value between c_k and c_{kB} in the thin tube limit as the background plasma density becomes more inhomogeneous. The slow body modes are absorbed into the slow continuum with increasing non-uniform equilibria and these modes are no longer trapped solutions. Comparison between the eigenfunctions for the fast body sausage and kink modes reveal similar results to the photospheric cylinder. The local maximum amplitude of perturbation for the fast body sausage mode increases with increasing non-uniform plasma density, although this is not a significant change. The boundary value of the azimuthal displacement perturbation for the fundamental kink mode increases as the background plasma density is modelled as a clear Gaussian profile. To aid understanding in observations, a visual representation of this effect was provided. It is shown that as the background plasma density is increased, the boundary shape of the fundamental kink mode becomes distorted, possibly due to the linear regime of the onset of Kelvin-Helmholtz instability (Antolin et al. 2014).

The second case study analysed in this chapter investigated the behaviour of magnetoacoustic MHD wave modes in a coronal magnetic cylinder with a non-uniform background plasma flow. The plasma flow was again modelled as a series of Gaussian profiles with differing widths and the amplitude was kept small to avoid any effects of flow related instabilities. The inhomogeneous plasma flow affected the forward and backward propagating slow body modes more than any other wave mode. Similar to the results found in Chapter 3, we have found that the non-uniform flow

creates an asymmetry between the phase speeds of forward and backward propagating slow body modes. Furthermore, like the case study investigating a background inhomogeneous density, the spatial eigenfunctions for slow kink and sausage body modes are affected due to the background flow. The eigenfunctions do not exhibit any changes at the boundary, similar to the behaviour of slow body modes in a photospheric cylinder with a non-uniform density. This is because body modes, unlike fast surface modes, propagate throughout the internal structure of the waveguide and not just amplified at the boundary. The background plasma flow introduces extra nodes into the spatial eigenfunctions at sufficient inhomogeneity and also changes the location of the local maximum in the spatial eigenfunction, this may indicate a different mode or the modification of the mode. Further investigation of vorticity due to the presence of a non-uniform background flow reveals that as the inhomogeneity of the background flow is increased, the resulting vorticity associated with the velocity perturbation also increases. We have shown that while the background vorticity increases with increasing equilibrium non-uniformity, the perturbed vorticity also increases. This is an important note to realise because it suggests that a non-uniform flow can produce a rotational perturbation. This motion may act as a driver to excite other forms of MHD waves e.g. Alfvén waves. Therefore MHD modes in an inhomogeneous equilibrium can possibly self excite other MHD wave modes within the solar atmosphere.

Chapter 5

Effect of non-linear twist and rotational flow on MHD wave modes of a magnetic cylinder

To be submitted to MNRAS.

Abstract

Modelling magnetic flux tubes in the solar atmosphere in the presence of background magnetic twist or rotational flows is expected to have an impact on the properties of magnetoacoustic waves. Previous studies have analytically modelled magnetic twist as a linear profile and in this chapter we use the numerical eigensolver to reproduce these results, as well as extending previous analysis to consider the modified continua.

Further investigations considering a magnetic flux tube embedded in both a coronal and photospheric environment with a linear background rotational flow are conducted. We find that the obtained eigensolutions for the kink mode in this scenario are similar to those of the linear magnetic twist case. For both the inclusion of a background magnetic twist and rotational flow, there is no effect on the axisymmetric $m = 0$ sausage mode. The presence of a linear background rotational flow causes the modified slow continuum to shift to faster phase speeds in the thin-tube limit. This results in the slow body modes, and slow surface modes in the photospheric cylinder, following this trajectory therefore changing their dispersive behaviour. For a photospheric flux tube in the thin-tube limit, it is almost impossible to distinguish the slow surface and fast surface kink modes upon comparison of their eigenfunctions.

This study is then extended to consider a nonlinear radial profile of background rotational flow. It is found that when the azimuthal component of the background velocity field is nonlinear, the resulting modified continua are no longer reduced to single point values at each wavenumber. The continua now occupy a band of frequencies absorbing more modes depending on the amplitude of the flow and the power of the nonlinear profile. We present a comparison between these two parameters and discuss which modes can be resonantly damped in each case. These results may have an implication for atmospheric-seismology and also provide a deeper understanding of the properties of kink modes in solar vortices.

5.1 Introduction

It is important to reiterate that the understanding of MHD waves in realistic solar structures is essential as they may play a role in chromospheric and coronal heating, in addition they can be used as a proxy to conduct solar atmospheric-seismology. However, MHD waves may also be responsible for exciting some observed phenomena, e.g. jets in the solar atmosphere (Scullion et al. 2011). The properties of MHD waves in a uniform plasma of infinite extent was presented in Section 1.4. This discussion was then extended to consider waves in uniform solar waveguides in Section 1.6, in which the $m = 0$ sausage and $m = 1$ kink modes were introduced. These particular case studies of uniform plasma can be investigated analytically, however, more complicated waveguides hosting inhomogeneous plasma, such as those investigated in Chapters 3 and 4, must be done so using a numerical approach once an analytical description breaks down, for example by using the numerical tool described in Chapter 2. Whilst the study of a radially non-uniform plasma density and flow has been essential for advancing our understanding of MHD waves in models which better represent observed solar structures, the model can be further improved to incorporate additional physical environments that may be common in magnetic flux tubes, such as magnetic twist and rotational (vortex) flow. The presence of a background magnetic twist or rotational flow would manifest themselves as non-zero azimuthal components of the background magnetic field and velocity field vectors, respectively. Considering $m = 1$ transverse kink modes, the effect of a background rotational flow or magnetic twist into the model breaks the symmetry of the system with respect to the direction of wave propagation.

Previously analytical investigations have considered a linear profile of magnetic twist, as in doing so the governing Equations (1.22)-(1.32) reduce to a simplified form. For example, Erdélyi & Fedun (2007*b*) modelled a magnetic flux tube as a uniform cylinder but with a small B_φ component and studied the effect on the $m = 0$ sausage mode. The authors derived and solved the governing equations in terms of Kummer's functions and obtain the analytical dispersion relation. They found that the presence of a background magnetic twist has no major change on the eigensolutions, however, may modify the period of the sausage mode on the order of a few percent when compared to the uniform cylinder model. An extension of this work was to also consider the $m = 1$ kink mode, which was presented by Erdélyi & Fedun (2010). In this work the authors again derived and solved the governing linearised MHD equations, this time using Whittaker's functions, which ultimately resulted in a complicated dispersion relation in terms of Kummer's functions. The resulting eigenvalues and eigenfunctions were calculated numerically for various azimuthal wavenumbers. It was shown that under both photospheric and coronal conditions, the obtained phase speeds for the $m = 1$ kink mode tend towards infinity in the long wavelength limit. Whilst the authors did not present an argument describing the physical reasoning behind this, they proposed that this may have important consequences when conducting coronal seismology of coronal loop oscillations. Furthermore, an analytical study by Ruderman (2007), investigated the $m = 1$ kink mode in linearly magnetically twisted flux tubes in both the zero plasma- β limit and also in the thin-tube limit. As this study made some mathematical simplifications, the author came to the conclusion that 'the magnetic twist does not affect the kink mode'. This statement, although true for the analysis conducted in the paper, was later proven to be only true for a linear profile of magnetic twist. A follow up study by Terradas & Goossens (2012) showed that when the magnetic twist is modelled as 'nonconstant' (or nonlinear) in a thin coronal flux tube, that the standing kink solutions are characterised by a change in polarisation of the transverse displacement along the tube. This finding is important in the context of coronal seismology, as the detection of this variation in polarisation could potentially be used as an indirect method to estimate the magnetic twist in oscillating loops.

The stability of a magnetic flux tube with a linear background magnetic twist and rotational flow component was studied by Cheremnykh et al. (2018). In order for the dispersion relation of such an equilibrium to be obtained, a simplifying assumption that waves in the thin-tube limit were only considered (Cheremnykh et al. 2018). The authors found that the $m = 0$ sausage mode becomes unstable for azimuthal flow speeds that create a centrifugal force which can overcome the magnetic tension. In other words, if v_φ^2 is sufficiently larger than $\approx (B_\varphi^2 + B_z^2)/\rho_i$ then the sausage mode is unstable. Furthermore, for the kink mode in a rotating twisted flux tube, the authors found that the kink mode can only become unstable for sufficiently large values of longitudinal flow speed, with the stability independent of the azimuthal component of flow speed. Due to the mathematical simplifications made in this study, a discussion of the properties of the wave modes in such an equilibrium was not possible.

Magnetic flux tubes with background rotational flows are a common configuration observed in astrophysical features including structures within the solar atmosphere, e.g. intergranular lanes, solar tornadoes and spicules (Bonet et al. 2008, 2010, Wedemeyer-Böhm et al. 2012, Tziotziou et al. 2018). Furthermore, they naturally appear in numerical MHD simulations of regions in the solar atmosphere with vortex drivers (see, e.g. Fedun, Shelyag, Verth, Mathioudakis & Erdélyi 2011, Fedun, Shelyag & Erdélyi 2011, Shelyag et al. 2011, 2012, 2013, González-Avilés et al. 2017, 2018, Snow et al. 2018) and also magnetoconvection simulations (Yadav et al. 2020, 2021, Silva et al. 2021). Vortex motions and flows, related to solar convective turbulent dynamics at granular scales and its interplay with magnetic fields within intergranular lanes, are ubiquitous on the solar surface and the atmosphere above. Such structures exhibit complex characteristics and excite a wide range of different waves which couple different layers of the solar atmosphere, thus enabling the channeling and transfer of mass, momentum and energy from the solar surface up to the low corona. It is to be expected that a background rotational flow should modify the observed properties of MHD waves, however, few previous analytical investigations exist for such a model, namely due to the mathematical complexity which it creates. Previous studies have investigated the stability status of rotating flux tubes, as the azimuthal velocity shear across the boundary may be susceptible to KHI (Soler et al. 2010, Zaqarashvili et al. 2015, Zhelyazkov & Chandra 2019). However, these studies assume zero plasma- β and focus on coronal conditions only, ignoring the slow modes completely.

5.2 Governing equations

The governing equations describing the perturbed plasma motions relevant to a wave investigation in a non-uniform magnetic cylinder with a background magnetic twist and plasma flow are given in Chapter 1 by Equations (1.22)-(1.32). These equations describe an initial equilibrium which is radially spatially dependant for all variables, however, for simplicity, in this chapter the equilibrium plasma density and magnetic field are taken to be spatially uniform. We will conduct separate investigations modelling the magnetic field vector in the form $(0, B_\varphi(r), B_z(r))$ and the velocity field vector as $(0, v_\varphi(r), v_z(r))$ for which Equations (1.22)-(1.32) are still valid. The modified continua given by Equations (1.33) and (1.34) are still important in the analysis of the configurations considered in this chapter. For photospheric studies, the modified Alfvén continuum exists in the leaky regime and does not overlap into the trapped wave mode domain, due to our choice of speed orderings. Unsurprisingly, for an equilibrium containing a linear (or nonlinear) magnetic twist or rotational flow, Equations (1.22)-(1.32) cannot be combined to produce an analytical dispersion relation, even when assuming the other plasma properties are uniform. As a result, the numerical tool developed in Chapter 2 is again applied in this chapter to obtain the eigensolutions.

One of the main requirements when applying the numerical tool are that the boundary con-

ditions are satisfied for \hat{P}_T and $\hat{\xi}_r$. In a magnetic flux tube with a background magnetic twist or rotational plasma flow, the continuity conditions are affected by the presence of these physical parameters. Firstly, let's consider the case of a uniformly twisted magnetic flux tube (Erdélyi & Fedun 2007b, 2010):

$$\hat{\xi}_{re}\Big|_{r=a} = \hat{\xi}_{ri}\Big|_{r=a}, \quad (5.1)$$

$$\hat{P}_{Te}\Big|_{r=a} = \left(\hat{P}_{Ti} - \frac{B_{0i\varphi}^2}{\mu_0 r} \hat{\xi}_{ri} \right)\Big|_{r=a}. \quad (5.2)$$

As it is assumed that the magnetic twist exists only inside the flux tube, there is a modification to the continuity of total pressure perturbation when compared with e.g. a uniform magnetic flux tube.

On the other hand, another case study examined in this chapter considers a uniform magnetic flux tube in the presence of a background rotational flow. In this case, the resulting boundary conditions state (Zaqarashvili et al. 2015):

$$\hat{\xi}_{re}\Big|_{r=a} = \hat{\xi}_{ri}\Big|_{r=a}, \quad (5.3)$$

$$\hat{P}_{Te}\Big|_{r=a} = \left(\hat{P}_{Ti} + \frac{\rho_{0i} v_{0i\varphi}^2}{r} \hat{\xi}_{ri} \right)\Big|_{r=a}. \quad (5.4)$$

The change in boundary conditions are accounted for in the shooting method of the numerical tool, and an eigensolution pair will only be found for values satisfying the above conditions for each respective case study.

5.3 Linear magnetic twist

It would not be unreasonable to assume that the magnetic fields permeating the solar corona may become twisted. Magnetic twist may arise from rotational motions in the photospheric intergranular lanes where the footpoints of, e.g. coronal loops, are located. Coronal loops have been shown to possess a twisted magnetic field at their footpoints (Magyar & Nakariakov 2020). Magnetic twist may have the effect of altering the observed properties of MHD waves or providing conditions where resonant absorption could take place (Ebrahimi & Karami 2016). The rate of the twist should not be very high, as otherwise the equilibrium can become unstable (see, e.g. Mei et al. 2018). Previous studies have investigated the properties of MHD waves propagating in a magnetic cylinder with a linear profile of magnetic twist (Erdélyi & Fedun 2007b, 2010, Cheremnykh et al. 2018). These models take into consideration that the majority of features observed in the solar atmosphere are likely to have twisted magnetic field due to rotational plasma motions in the photosphere. These works derive an analytical dispersion relation containing complicated Kummer functions that can be used to obtain the eigenvalues plotted on the dispersion diagram. A further test for our numerical algorithm described in Chapter 2 would be to reproduce these results without requiring the complex analytical derivations shown in Erdélyi & Fedun (2007b, 2010), for both the sausage and kink modes under photospheric and coronal conditions.

In the above studies, magnetic twist is incorporated into the model by taking the equilibrium magnetic field inside the cylinder as $\mathbf{B}_{0i}(r) = (0, Ar, B_{0zi})$, where A is the amplitude of linear magnetic twist. The magnetic field external to the cylinder is assumed vertical, straight and uniform. This choice of magnetic twist results in the governing equations taking a simplified form, as it can be seen that some quantities disappear from Equations (1.22)-(1.32) when B_φ is linear in

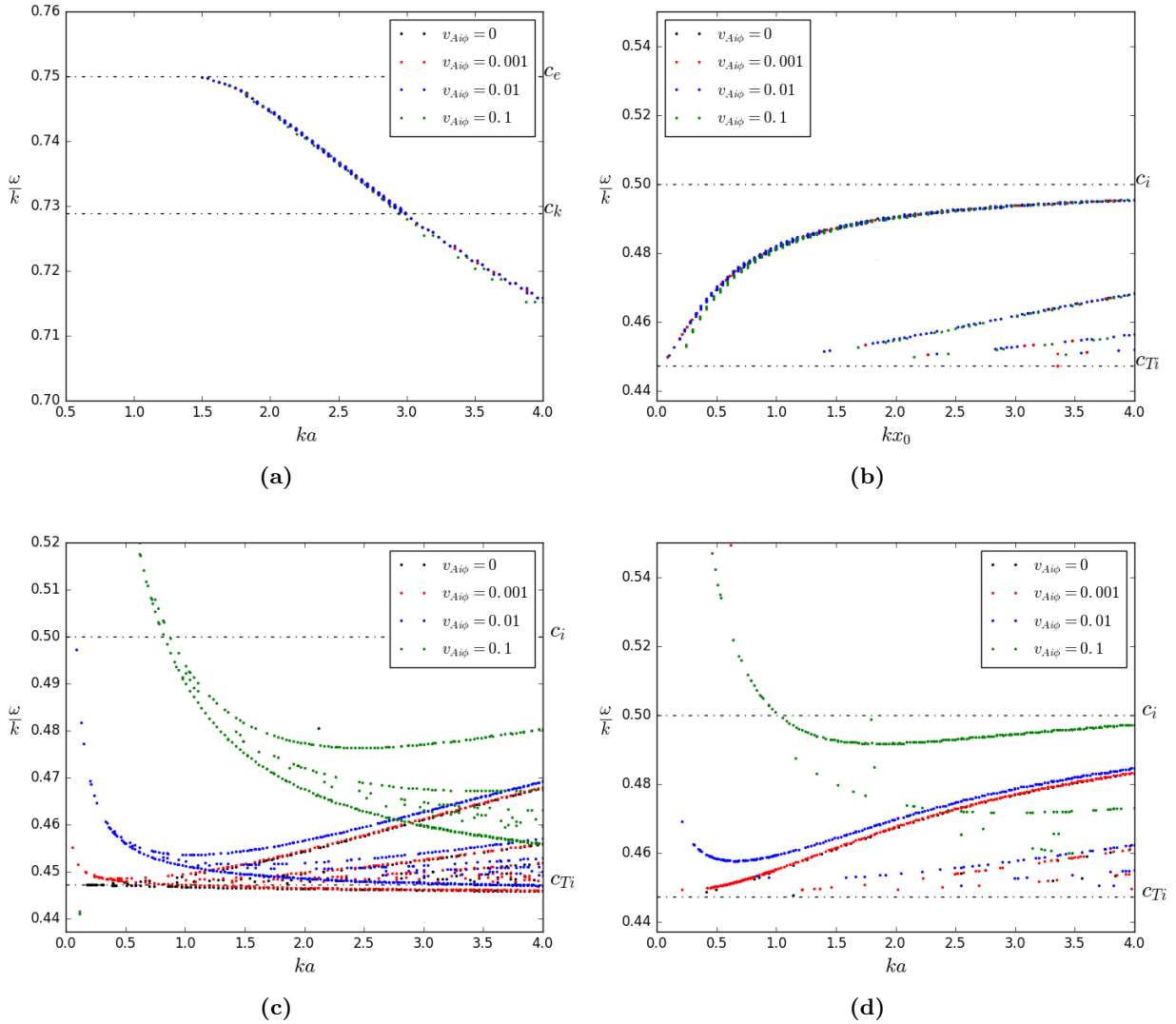


Figure 5.1: A handful of chosen numerical solutions plotted on the dispersion diagram for a magnetic cylinder with uniform magnetic twist replicated from Erdélyi & Fedun (2010). (a) fast surface sausage modes in a photospheric cylinder (b) slow body sausage modes under coronal conditions (c) slow body and surface kink modes under photospheric conditions, (d) slow body kink mode under coronal conditions. The amplitude of linear twist in each case is shown in the legend, with increasing twist ranging from no twist $A = 0$ (black), $A = 0.001$ (red), $A = 0.01$ (blue) and $A = 0.1$ (green).

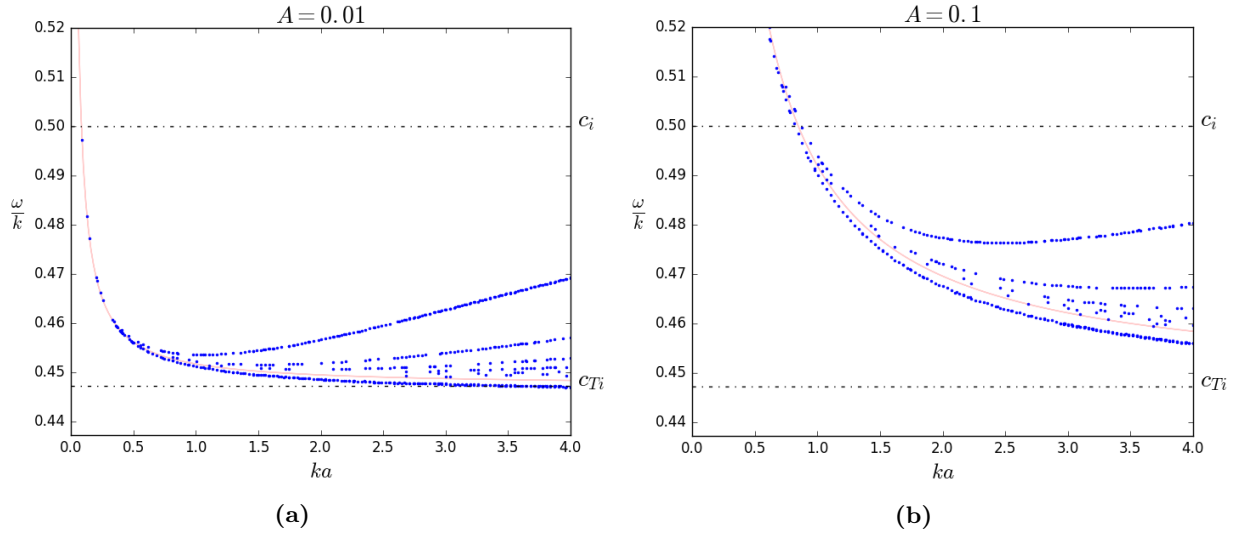


Figure 5.2: *Slow body and slow surface kink mode solutions under photospheric conditions as shown in Figure 5.1c for the cases where $A = 0.01$ and $A = 0.1$. Here the modified slow continuum is highlighted by the red curve, showing how the slow surface modes and body modes follow the same trajectory of this continuum.*

r. The full set of equations for this specific case study are given by Erdélyi & Fedun (2010) and the necessary boundary conditions are given by Equations (5.1) and (5.2).

In Figure 5.1, we show selected zoom regions of cases under both photospheric and coronal cases for different magnitudes of linear magnetic twist. Figure 5.1a and Figure 5.1b show the behaviour of the sausage mode under different configurations of magnetic twist which, as Erdélyi & Fedun (2010) have shown, has very little effect on the sausage mode and can be seen clearly in these figures. On the other hand, Figure 5.1c and Figure 5.1d show the behaviour of the slow kink modes under both photospheric and coronal conditions. These results reaffirm those found by Erdélyi & Fedun (2010) that the kink mode phase speed tends to infinity in the long wavelength limit as the magnitude of magnetic twist is increased. These results are not surprising when Equations (1.22)-(1.32) are compared under both the $m = 0$ sausage mode and the $m = 1$ kink mode. When $m = 0$ these equations are much simplified, with many terms disappearing from the equations, especially those which are proportional to the magnetic twist, B_φ . These equations are also simplified when the magnetic twist is linear, as is the case here.

Not considered in the work by Erdélyi & Fedun (2010) was the effect that the modified Alfvén and cusp continuum may have on the resulting wave modes. Equations (1.33) and (1.34) occupy a range of frequencies when the magnetic field is not constant and vertical. Even a small component of magnetic twist in the azimuthal direction modifies these continuum bands, even in the linear case considered here, where the Alfvén and cusp continua occupy varying speeds depending on the wavenumber, k . Figure 5.2 displays a couple of cases shown in Figure 5.1c but with the modified slow continuum shown. For the case of a linear magnetic twist, the modified slow continua reduces to single-point values for each value of wavenumber, indicated by the red shaded curve in Figure 5.2. It can be seen that both the slow surface modes, which are present at phase speeds underneath this continuum line, and the slow body modes which lie above it, follow the continuum which tends towards infinity in the thin tube limit. As the continuum reduces to a single value for the case of linear twist. The slow body modes are eventually absorbed into the continuum, at wavelengths

that increase with the amplitude of the twist parameter. The slow surface modes survive until extremely small values of k where, they too, become absorbed by the continuum.

5.4 Linear rotational plasma flow

In this section, a uniform magnetic cylinder in the presence of a linear rotational background flow is investigated. A profile comparable to the magnetic twist profile incorporated by Erdélyi & Fedun (2007*b*) and Erdélyi & Fedun (2010) is chosen but applied to the azimuthal velocity field component v_φ instead. A rotational flow can be either clockwise or counter-clockwise in the reference frame relative to the observer. Physically speaking, the direction of the flow does not affect the properties of the waves in a dramatic manner, similar to how a forward or backward steady field aligned flow does not alter the fundamental behaviour of the resulting MHD waves (Nakariakov & Roberts 1995*a*). The only difference between a clockwise rotational flow and an anti-clockwise rotational flow will be the sign in front of v_φ and the shifted wave frequency due to the flow.

Obtaining an equilibrium in a magnetic cylinder with a background rotational velocity component is not as mathematically simple as the scenario of a uniform magnetic cylinder. In order for total pressure balance across the waveguide the following expression must be satisfied:

$$\frac{d}{dr} \left(P + \frac{B_{0z}^2}{2\mu} \right) = \frac{\rho v_\varphi^2}{r}, \quad (5.5)$$

for the case of a background straight vertical magnetic field. Integrating Equation (5.5) with respect to spatial variable r provides more insight into the permissible function(s) of the equilibrium background flow and the relevant expression(s) for the plasma pressure in order to maintain an equilibrium. Integration of (5.5) yields:

$$P + \frac{B_{0z}^2}{2\mu} = \rho \int \frac{v_\varphi^2(r)}{r} dr, \quad (5.6)$$

before conducting the integral of the flow on the right hand side. Equation (5.6) allows us to choose specific profiles of v_φ under the constraint that it must satisfy Equation (5.5). One possible method to determine the integral on the right hand side of Equation (5.6), and hence provide insight into the required plasma pressure to maintain equilibrium, is through trial and error and seeking a relationship between the equilibrium v_φ profile and the resulting integral. A summary of this trial and error process is shown in Table 5.1. It can be seen that there is a clear relationship between whichever profile for v_φ is chosen, be it linear or nonlinear, and the resulting integral on the right hand side of the pressure balance Equation (5.6). Therefore, it does not matter whether or not the initial profile for v_φ is linear or nonlinear, an equilibrium can be obtained. The presence of a background rotational flow not only modifies the equilibrium pressure balance relationship, but also affects the continuity conditions on the boundary of the waveguide. For all the following case studies investigating the effect of a background rotational flow, the necessary boundary conditions implemented in the numerical tool are given by Equations (5.3) and (5.4).

For all the cases considered in this chapter investigating the effect of a rotational background flow, the magnetic flux tube is otherwise uniform. Explicitly, this means that the equilibrium plasma density and magnetic field is constant across the flux tube. The presence of a background rotational flow must be accounted for in the pressure balance Equation (5.5) by balancing the background rotational flow with a change in plasma pressure (i.e. in temperature) with a modification by e.g. those shown in Table 5.1. For configurations where the amplitude of the rotational flow is weak (e.g. $A < 0.5$), then the change in spatial behaviour of the plasma pressure and temperature is small but

v_φ	p	$\frac{v_\varphi^2(r)}{r}$	$\int \frac{v_\varphi^2(r)}{r} dr$	Relationship (profile & integral)
Ar	1	A^2r	$\frac{A^2r^2}{2} + C$	$\frac{A^2r^{2p}}{2p}$
$A\sqrt{r}$	0.5	A^2	$A^2r + C$	$\frac{A^2r^{2p}}{2p}$
Ar^2	2	A^2r^3	$\frac{A^2r^4}{4} + C$	$\frac{A^2r^{2p}}{2p}$
$Ar^{1.5}$	1.5	A^2r^2	$\frac{A^2r^3}{3} + C$	$\frac{A^2r^{2p}}{2p}$

Table 5.1: *The relationship between the initial choice of equilibrium profile for rotational flow v_φ and the resulting integral in the pressure balance equation. For each choice of profile, the power p is indicated along with the expressions for the term inside the integral as well as the result after conducting the integration. The constant of integration is denoted by C and is absorbed into the gas pressure. The same relationship between the initial profile and resulting integration is obtained for all trial and error case studies.*

must not be dismissed. To aid visualising the effect of a background rotational flow on the plasma equilibrium in these case studies, we show in Figure 5.3, an example scenario of the effect of a rotational background flow in a photospheric flux tube. This figure shows the case of a background rotational flow given by $v_\varphi = 0.5r$, i.e. a linear rotational flow with an amplitude of 0.5 under photospheric conditions. The amplitude of the rotational flow in this case is much greater than the case studies analysed in this chapter, however is chosen for graphical purposes to highlight how the presence of a background rotational flow affects other equilibrium plasma parameters. Figure 5.3 shows how the plasma temperature compensates for the background rotational flow to maintain constant total pressure across the flux tube by balancing the internal and external gas and magnetic pressures, which ultimately affects the plasma pressure. It can be seen that in order to achieve pressure balance in this photospheric configuration, the plasma temperature must increase towards the boundary of the flux tube, which then causes the plasma pressure and resulting sound speed to also increase in this region.

5.4.1 Rotating cylindrical magnetic flux tube under coronal conditions

In this section, a magnetic cylinder in a coronal environment with a linear background rotational flow is considered. The rotational flow is linear, such that inside the flux tube the amplitude of the flow is proportional to the radial distance r from the center of the flux tube $v_\varphi = Ar$, where A is the flow amplitude. The profiles of the rotational flow analysed in this section are shown in Figure 5.4, for varying cases of flow amplitude ranging from $A = 0$ which corresponds to no background rotational flow up to a maximum amplitude of $A = 0.05$. It should be noted here that this flow speed is incredibly small when compared to the local sound and Alfvén speeds which, under these coronal conditions, are $c_i = 1$ and $v_{Ai} = 2$. Therefore the flow is both subsonic and subalfvénic, and below the threshold for the onset of KHI. As a result, any modifications to the plasma eigenfunctions due to MHD waves are simply a result of the azimuthal component of the background velocity field.

Figures 5.5 and 5.6 show a horizontal and vertical cross-cut of the background velocity field for two amplitude cases of $A = 0.01$ and $A = 0.05$. Whilst the chosen values of A are arbitrary, they are shown to highlight the differences from an observers point of view of a rotating magnetic flux tube in the solar atmosphere. In particular, Figure 5.6 would represent the integral line of sight Doppler shift of a rotating flux tube observed at the limb of the Sun, for example that of those

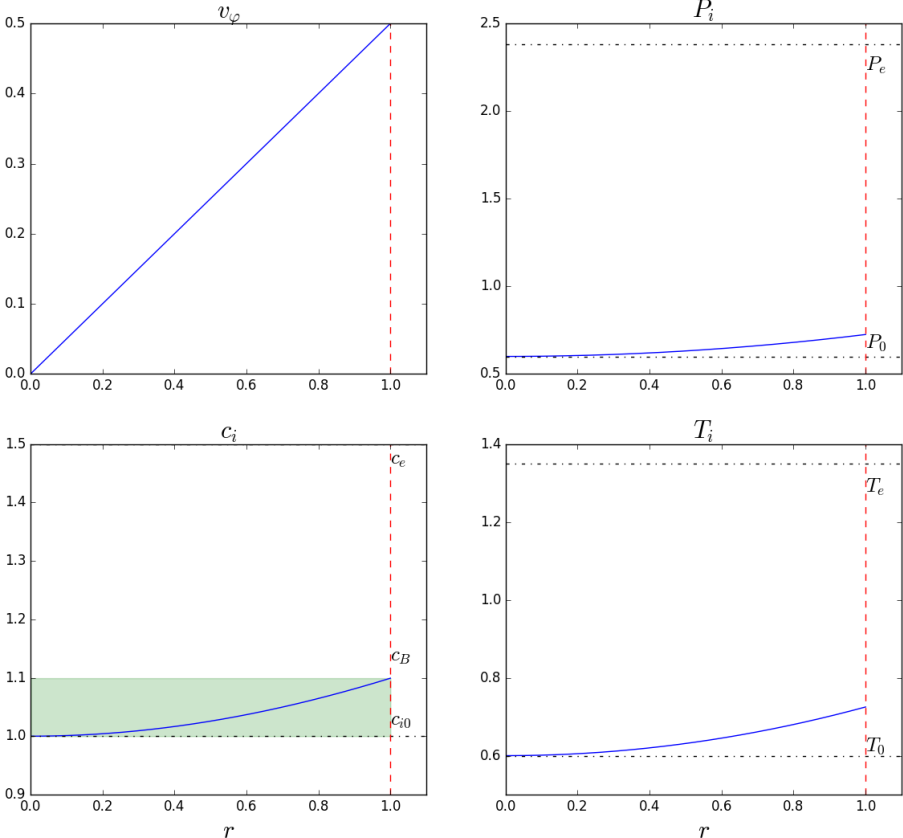


Figure 5.3: Plots of v_φ , plasma pressure, sound speed and plasma temperature inside the flux tube for an example configuration of a photospheric magnetic flux tube in the presence of a linear background rotational flow.

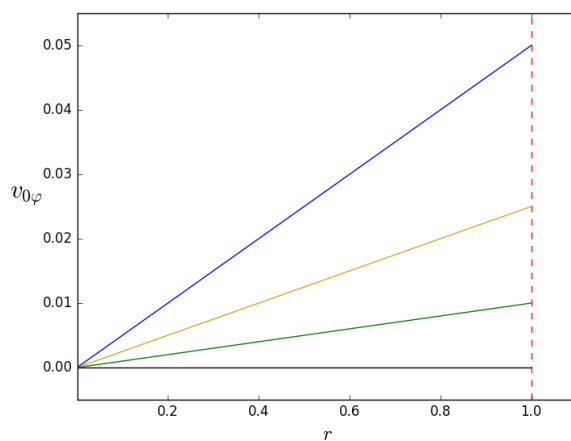


Figure 5.4: Equilibrium background rotational flow profiles for cases with increasing amplitude. In all cases the profiles are linear with respect to spatial coordinate r . The amplitude of the rotational flow increases from 0 (black line), 0.01 (green line), 0.025 (yellow line) and 0.05 (blue line).

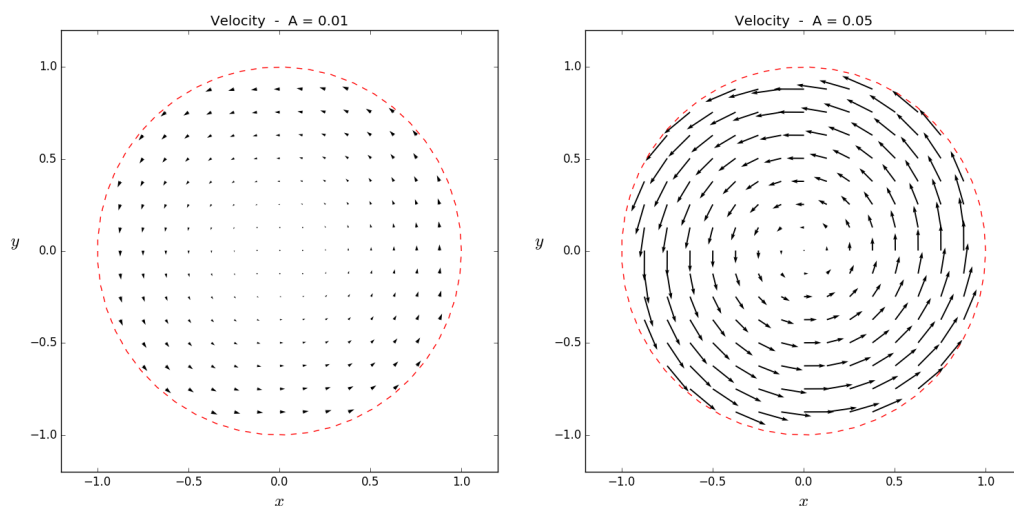


Figure 5.5: Background velocity field for a magnetic cylinder in the presence of a background rotational flow for two cases considered with (a) $A = 0.01$ (b) $A = 0.05$.

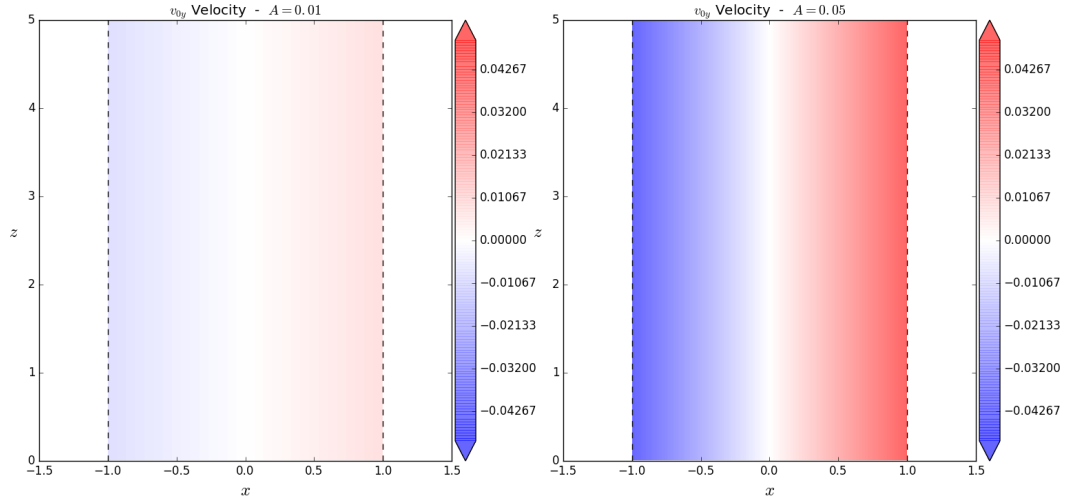


Figure 5.6: The y component of the background velocity field which would be seen by observers looking at the Doppler velocity of the structure from side on. (a) $A = 0.01$ (b) $A = 0.05$. Cross cut is taken at $y = 0$, i.e. across the centre of the flux tube.

observed in spicules (Sharma et al. 2017, Sharma et al. 2018). It can be seen that the rotational flow is only a function of r , or a function of x and y in the case of a Cartesian geometry as shown in Figures 5.5 and 5.6. The rotational flow is constant with height in all cases considered in this Chapter. In Figure 5.7, we show the resulting dispersion diagrams for both the sausage mode and kink modes in a coronal flux tube under a linear background rotational flow with varying amplitude. The whole spectrum of forward and backward propagating modes are shown. Whilst the rotational flow appears to have little effect on the fast modes, the slow modes are more greatly affected. The effect of a background rotational flow on slow modes can be seen in greater detail in Figure 5.8, which shows a zoomed-in region of the slow body mode branches on the dispersion diagrams. As expected, for the case when the velocity twist is zero, the eigenvalues of a uniform magnetic cylinder are recovered and the forward and backward slow body modes approach c_{Ti} and $-c_{Ti}$, respectively in the long wavelength limit. However, as the amplitude of the background rotational flow is increased, the dispersive properties of the $m = 1$ kink modes are altered. Similar to the comparable case of magnetic twist, the phase speeds of the slow surface and body kink modes tends to infinity in the long wavelength limit, where, beyond this, they may become leaky. As the amplitude of the rotational flow is increased, the phase speed of the obtained solutions also increases for all wavenumbers. Similar to the conclusions made by Erdélyi & Fedun (2010) for a twisted magnetic flux tube, this may have important consequences for observational findings, as the majority of observations of coronal loop oscillations are conducted in the thin tube limit (e.g. Nakariakov & Verwichte 2005). It is widely accepted that these oscillations are due to the fast body kink modes, however this result suggests that even a small background rotational flow component, similar to the case of a twisted background magnetic field, may shift the permissible phase speeds of the slow body modes into the observed phase speed ranges. For all cases of background rotational flow, the $m = 0$ sausage mode remains unaffected, suggesting that the analysis of sausage mode observations may not be appropriate for the use of coronal-seismology in flux tubes with background rotational flows.

Given that the eigenvalues are altered by a rotational background flow in a coronal flux tube for

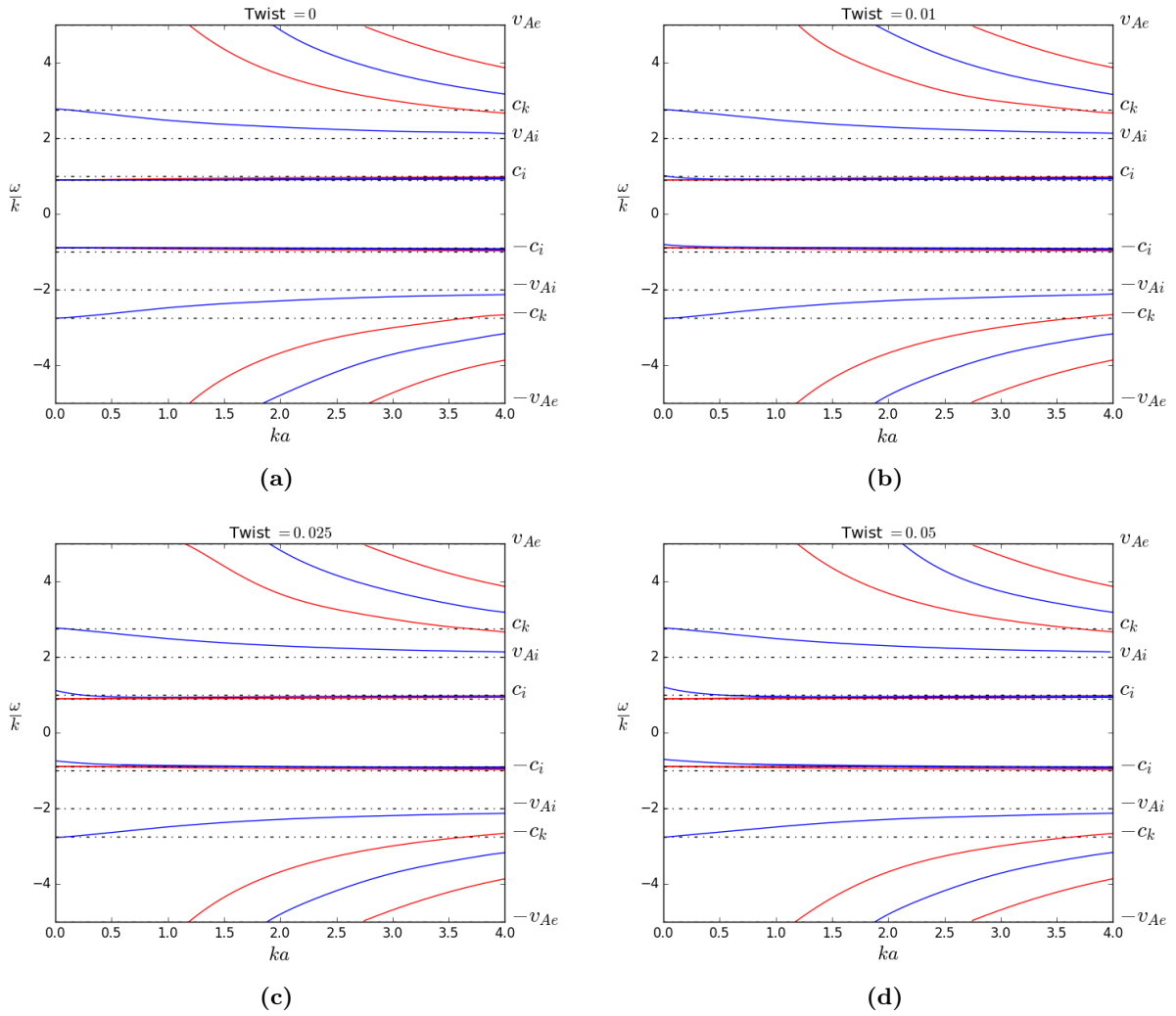


Figure 5.7: Dispersion diagrams for all cases of linear anti-clockwise rotational flow with increasing amplitude under coronal conditions (a) $A = 0$ which corresponds to uniform case with no azimuthal flow component. (b) $A = 0.01$, (c) $A = 0.025$, (d) $A = 0.05$.

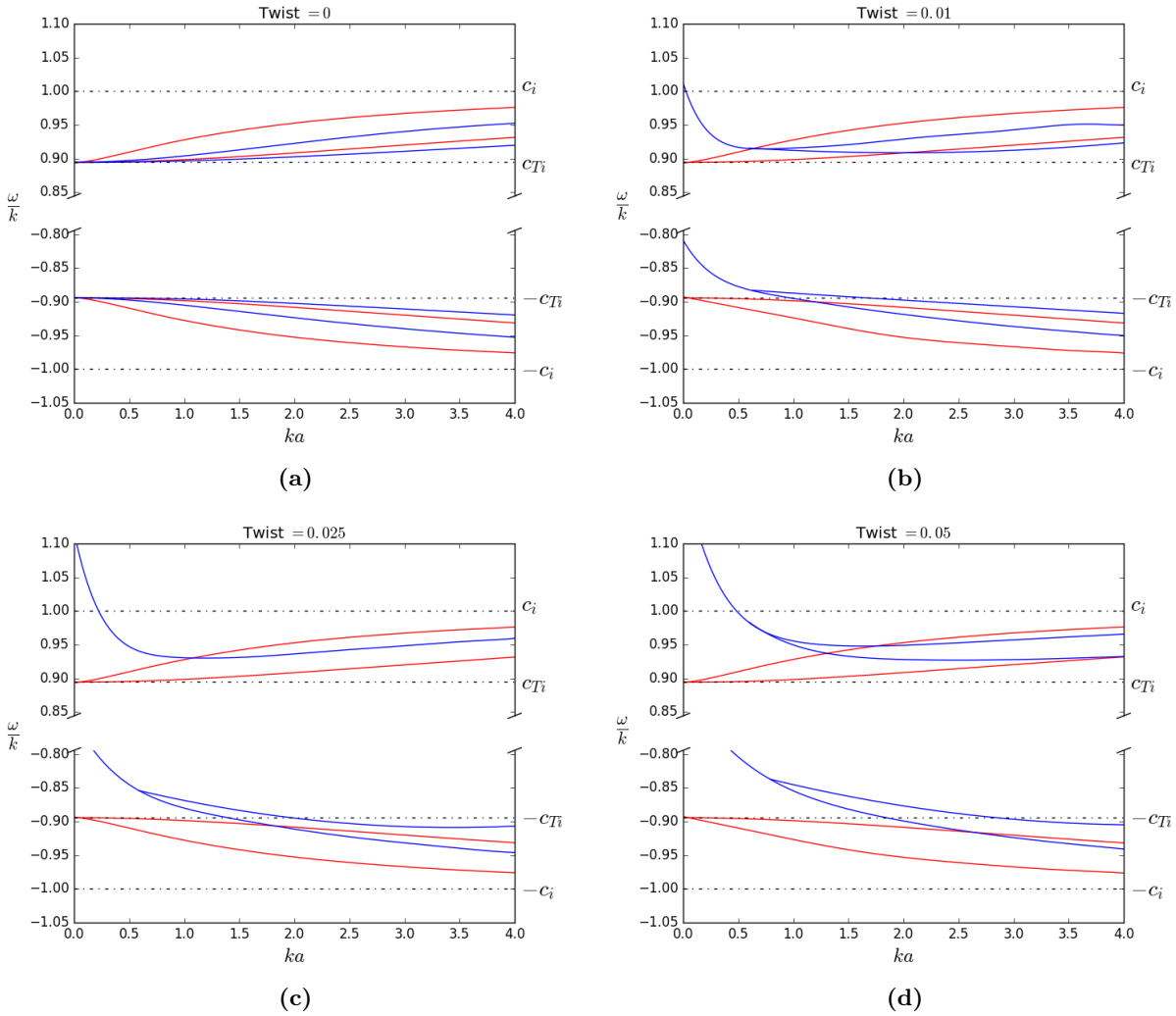


Figure 5.8: Same as Figure 5.7, however, here we show a zoom region of the dispersion diagrams on the forward and backward slow body modes for all cases of linear anti-clockwise rotational flow with increasing amplitude. (a) $A = 0$, (b) $A = 0.01$, (c) $A = 0.025$, (d) $A = 0.05$.

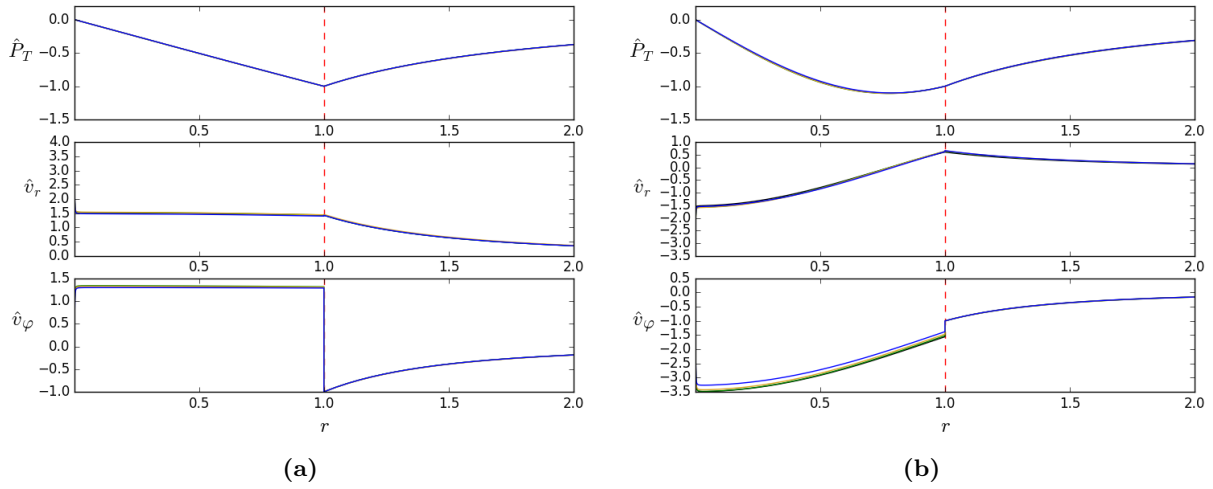


Figure 5.9: Eigenfunctions for all cases of linear clockwise rotational flow with increasing amplitude. The fast fundamental kink mode is shown in (a) whereas (b) shows the slow body kink mode. A wavenumber value of $ka = 0.55$ was chosen for all cases in both plots.

the discussed cases, it is possible to calculate the eigenfunctions to determine what affect this result may have for observational parameters. It can be seen in Figure 5.9 that the spatial eigenfunctions are unchanged for both the fast sausage and fast (fundamental) kink modes under a linear background rotational flow of different amplitudes. When compared to previous investigations discussed in earlier chapters, it may have been expected that the inclusion of a background rotational flow should have altered the spatial structure of the resulting eigenfunctions. However, it has become a common theme in this work to discover that a non-uniform background has little effect on the properties of fast magnetoacoustic modes. The same conclusion is reached here for these modes in the presence of a linear background rotational flow in a coronal flux tube, a similar analysis for slow modes in a photospheric flux tube is conducted further on in this chapter.

5.4.2 Rotating cylindrical magnetic flux tube under photospheric conditions

In this section, we consider a magnetic cylinder under photospheric conditions ($v_{Ae} < c_i < c_e < v_{Ai}$) with a linear background rotational flow. It is likely to find rotational flows in photospheric flux tubes in the solar atmosphere, due to the plasma motions in the lower solar photosphere as a result of granular buffeting. There is assumed to be no vertical plasma flow such that the background velocity vector inside the waveguide can be written as $\mathbf{v}_{0i} = (0, Ar, 0)$. Similar to the coronal case, all profiles are considered linear at this stage, with the aim to investigate how varying the amplitude of rotational flow affects the resulting perturbations. The flow outside the cylinder is zero, which results in a velocity shear across the cylinder boundary at $r = a$, however the value of A is chosen to be small and both sub-sonic and sub-Alfvénic such that the onset of KHI is avoided. In Figure 5.10, we show the linear profiles of background rotational flow considered in this section. In all cases the flow amplitude is proportional to the radial distance from the center of the flux tube up to the boundary, however the amplitude is allowed to vary.

Figure 5.11 highlights the change in eigenvalues for the different cases of flow profiles considered in Figure 5.10. The axisymmetric $m = 0$ sausage mode remains unaffected by the background flow in the long wavelength limit, although resulting phase speeds seem to increase slightly as the

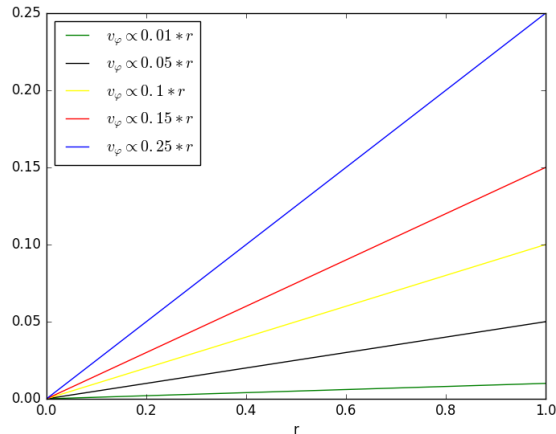


Figure 5.10: *Equilibrium background rotational flow profiles for cases with increasing amplitude for a photospheric cylinder. In all cases the profiles are linear with respect to spatial coordinate r . The amplitude of the rotational flow increases from 0.01 (green line), 0.05 (black line), 0.1 (yellow line), 0.15 (red line) and 0.25 (blue line).*

amplitude of the rotational flow is increased. On the other hand, there is a considerable effect on the $m = 1$ kink mode solutions due to the presence of a background rotational flow. The kink mode solutions in the thin-tube limit tend to infinity and may exceed c_e and enter the leaky regime. As the amplitude of the flow is increased, the solutions of the phase speeds also increases. Figure 5.12 shows the resulting dispersion diagrams for a photospheric cylinder with a linear background rotational flow.

These results bare a striking resemblance to a similar scenario of a magnetic cylinder with an equilibrium linear twisted magnetic field, such that in the long wavelength (thin-tube) limit, the phase speeds of these slow body kink modes tend to an infinite phase speed. As the amplitude of the azimuthal flow is increased, the corresponding phase speeds of the slow body kink modes is also increased for all wavelengths. The modified slow continuum given by Equation (1.34) is shown by the red shaded line in Figure 5.12. For the specific case of a linear background plasma flow, this continuum reduces to point values at every wavenumber. The wave modes follow this continuum line in the long wavelength limit and even undergo an avoided crossing where the ‘slow surface mode’ approaches the ‘fast surface mode’. Avoided crossings occur when the phase speeds of two wave modes avoid intersecting when a parameter of the system is varied, in this case v_φ . This occurs when there are constraints preventing two solutions from being equal and it demonstrates a transferal of properties between the two modes. Analysis of this phenomenon can be used to give insight into the modal structure. There is rich literature regarding avoided crossings for the eigensolutions of a wide range of physical processes including coupled spring oscillations in classical mechanics (Novotny 2010) and energy level repulsion in quantum physics (Naqvi & Brown 1972). In MHD wave theory, the subject has been covered previously, for example, between fast and slow magnetoacoustic gravity waves in a magnetically stratified plasma by Abdelatif (1990) and Mather & Erdélyi (2016) and for magnetoacoustic sausage and kink modes in asymmetric magnetic slabs (Allcock & Erdélyi 2017). Furthermore, avoided crossings have been discussed in the context of negative energy waves in hydrodynamics (Cairns 1979), in helioseismology (Pintér & Goossens 1999) and in the context of the Kelvin-Helmholtz and resonant flow instabilities (Taroyan & Erdélyi 2002, 2003). In the long wavelength limit it may not be appropriate to refer to the ‘slow surface

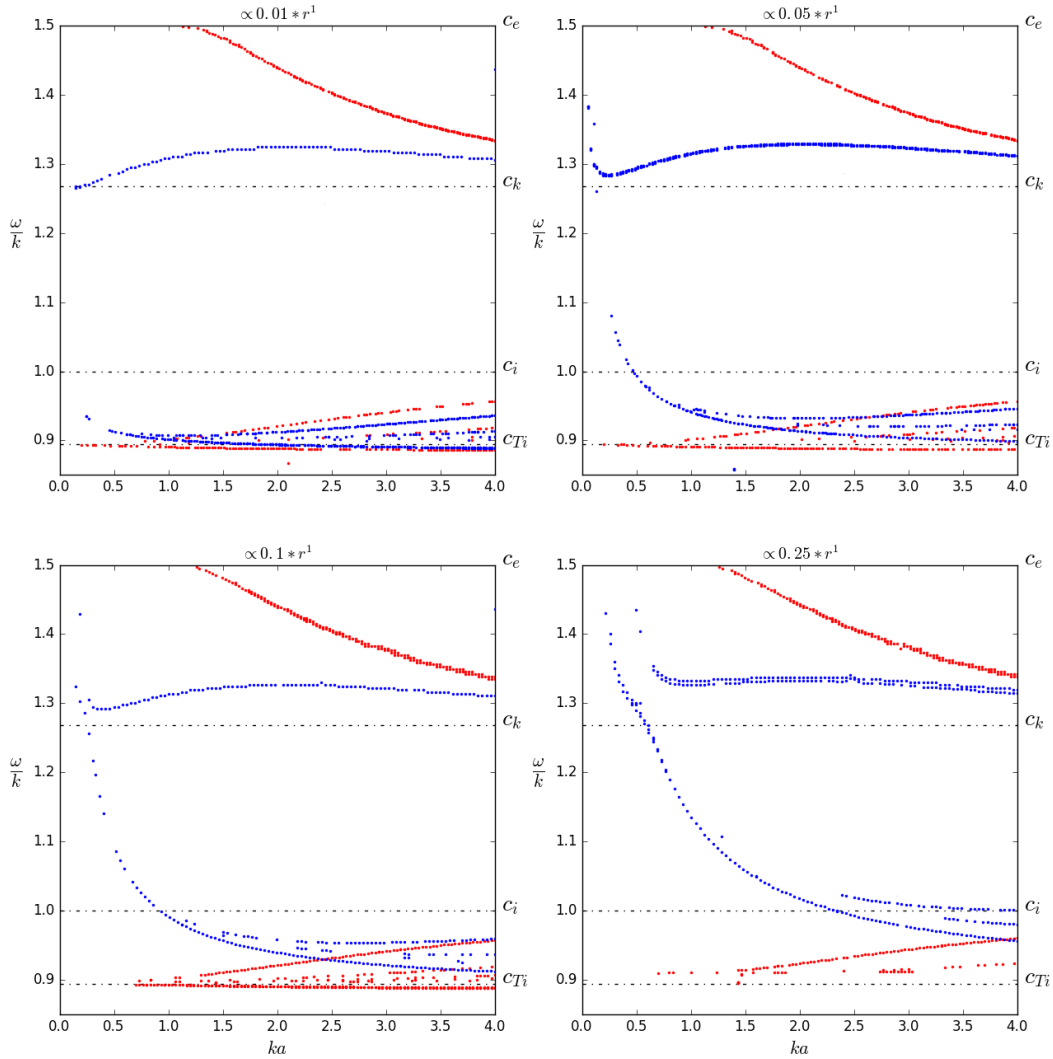


Figure 5.11: Dispersion diagrams for a photospheric cylinder with a background rotational flow of varying flow amplitudes. The different cases with varying amplitude, displayed on the top of each panel are shown corresponding to those in Figure 5.10. The red dots indicate solutions for the $m = 0$ sausage mode and the blue dots show the $m = 1$ kink mode.

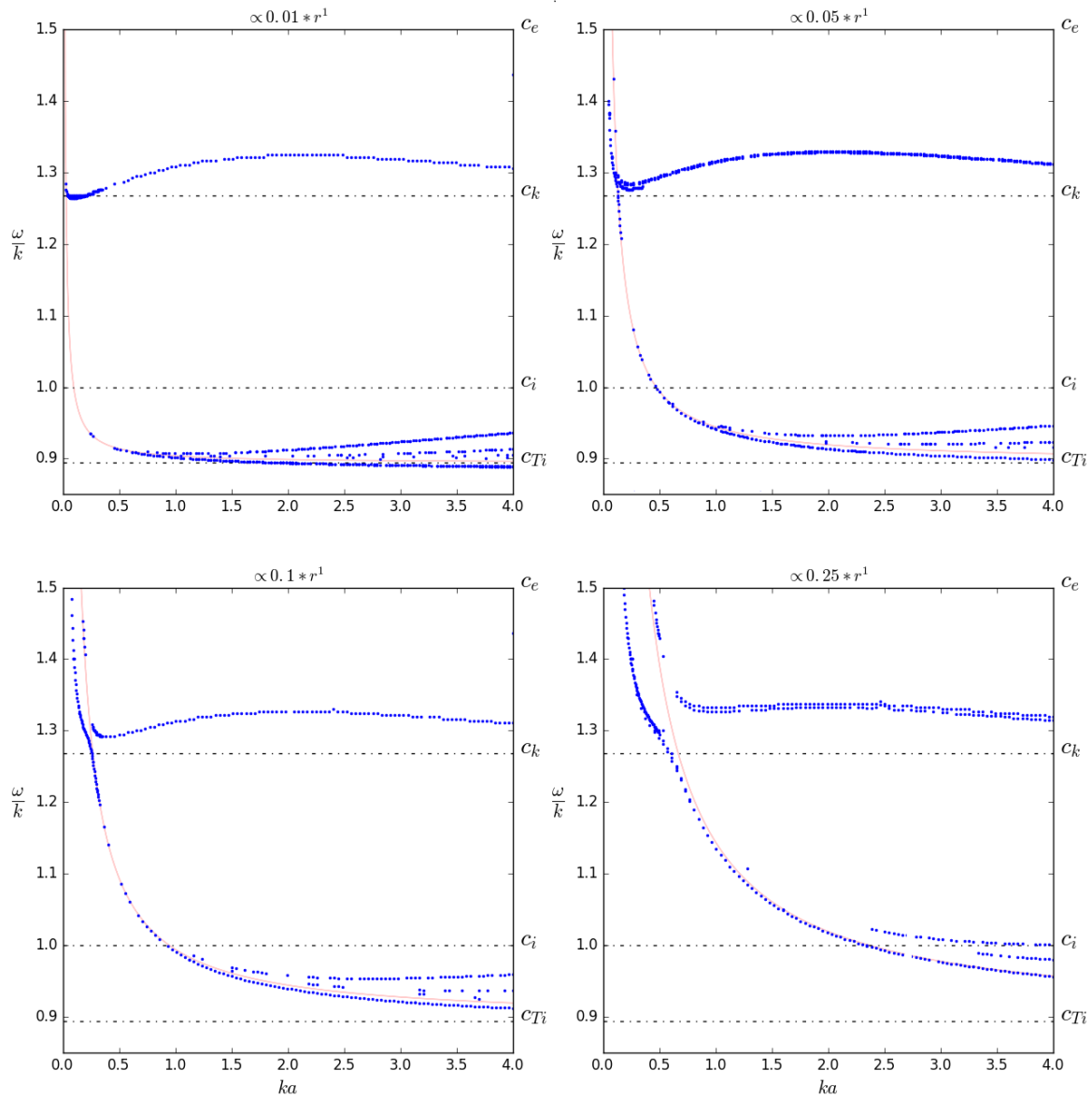


Figure 5.12: Dispersion diagrams for the $m = 1$ kink mode for a photospheric cylinder with a background rotational flow. The different cases with varying amplitude are shown where the red shaded curve indicates the modified slow continuum due to the flow.

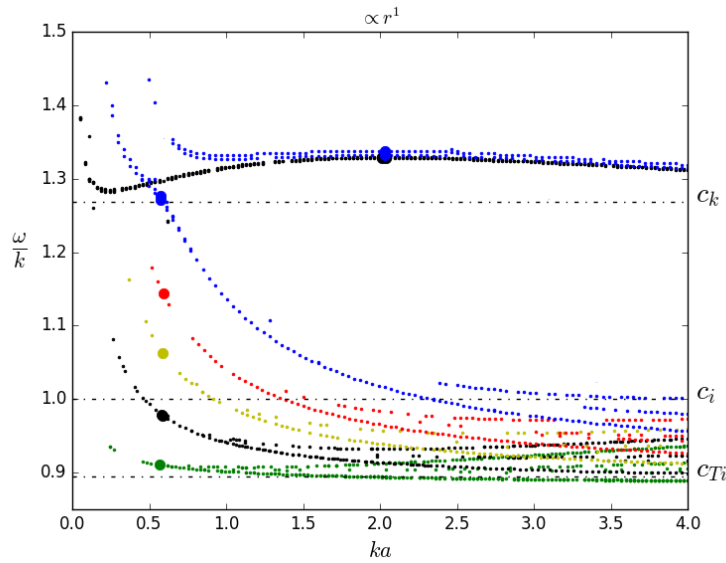


Figure 5.13: The resulting dispersion diagrams for all linear cases of rotational flow with the colour scheme consistent with Figure 5.10. These dispersion diagrams display the kink mode only, with the larger dots indicating the chosen eigenvalues for later analysis. The slow surface and slow body modes merge into a singular branch in the long wavelength limit.

mode’ as a slow mode anymore as, in the reference frame of the observer, it possesses phase speeds similar to that of the fast surface mode. In the case of a uniform photospheric cylinder, the body modes tend toward c_{Ti} in the long wavelength limit (Edwin & Roberts 1983, Priest 2014), however with the inclusion of a background rotational flow, these modes are now absorbed into the slow continuum where they become resonantly damped.

Figure 5.13 shows the resulting dispersion diagrams over-plotted on each other for the linear cases of rotational flow in a photospheric cylinder given by the profiles in Figure 5.10. The dots chosen at the same wavenumber value $ka = 0.6$ are further used for analysis of the eigenfunctions for the slow surface kink modes. Additional dots for the fast surface kink mode are shown at a wavenumber value of $ka = 2$. This figure shows nicely the effect that changing the amplitude of the background linear rotational flow has on the resulting eigensolutions of the system, such as their phase speeds increasing with flow amplitude and further how the modified slow continuum is shifted in the thin-tube limit.

In Figure 5.14, we show the spatial eigenfunctions for the slow surface kink mode for a fixed wavenumber $ka = 0.6$ but different rotational flow amplitudes. The colour scheme shown in the eigenfunctions is consistent with that for the rotational flow profiles shown in Figure 5.10. It can be seen that increasing the amplitude of the equilibrium linear rotational flow, changes the spatial behaviour of the observable eigenfunctions. For the case of $A = 0.01$ which corresponds to a very small rotational flow parameter, the eigenfunctions still obey a ‘surface-like’ structure, that is, the amplitude of the radial displacement and velocity perturbations possesses a maximum at the boundary of the flux tube. However, increasing the amplitude of the background rotational flow causes the radial displacement perturbation to increase towards the centre of the flux tube, such that the maximum displacement perturbation is no longer at the point where $r = a$. This results in an eigenfunction that shares striking similarities to that of the fundamental kink mode, and may

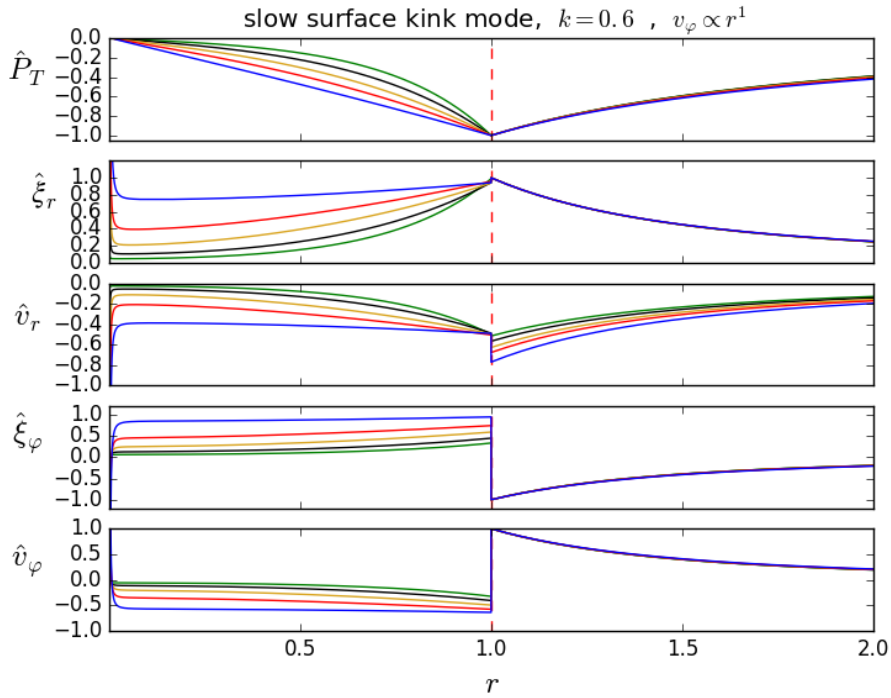


Figure 5.14: *The resulting eigenfunctions for the slow surface kink mode for all linear cases of rotational flow with the colour scheme consistent with Figure 5.10. A wavenumber value of $ka = 0.6$ was chosen for all plots.*

therefore be misinterpreted in observational data.

To further emphasise this point, it is possible to plot the eigenfunctions \hat{P}_T and $\hat{\xi}_r$ for eigenvalues of a similar phase speed on either side of the modified slow continuum. One of these solutions corresponds to the slow magnetoacoustic kink mode and the other is the fast magnetoacoustic kink mode. In Figure 5.15, we show these eigenfunctions for the slow and fast magnetoacoustic kink modes at a similar phase speed. It can be seen that the eigenfunctions are difficult to distinguish from one another and that the modes no longer display characteristics of the typical surface mode anymore. In particular, the main characteristic of a surface mode is that it possesses a maximum amplitude of radial displacement perturbation at the boundary of the waveguide, which is no longer the case when a rotational background plasma flow is present. To further investigate the similar and mixed behaviour of the perturbed eigenfunctions, it may be instructive to analyse the magnitude of the parallel and perpendicular components of the displacement. This will provide a greater insight for seismological purposes into whether the mode is slow or fast in nature, however this is a study to be conducted in future work.

5.5 Non-linear rotational plasma flow in a photospheric flux tube

In this section, we build upon the work presented in the previous section by considering a background rotational flow inside a magnetic flux tube which is non-linear in radial distance, r . The case of a non-linear rotational flow is of particular interest as it may offer a better description of the radial profiles of the observed velocity fields in solar vortex structures (Silva et al. 2020). Furthermore, a non-linear rotational flow will not cause Equations (1.22)-(1.32) to reduce to simpler

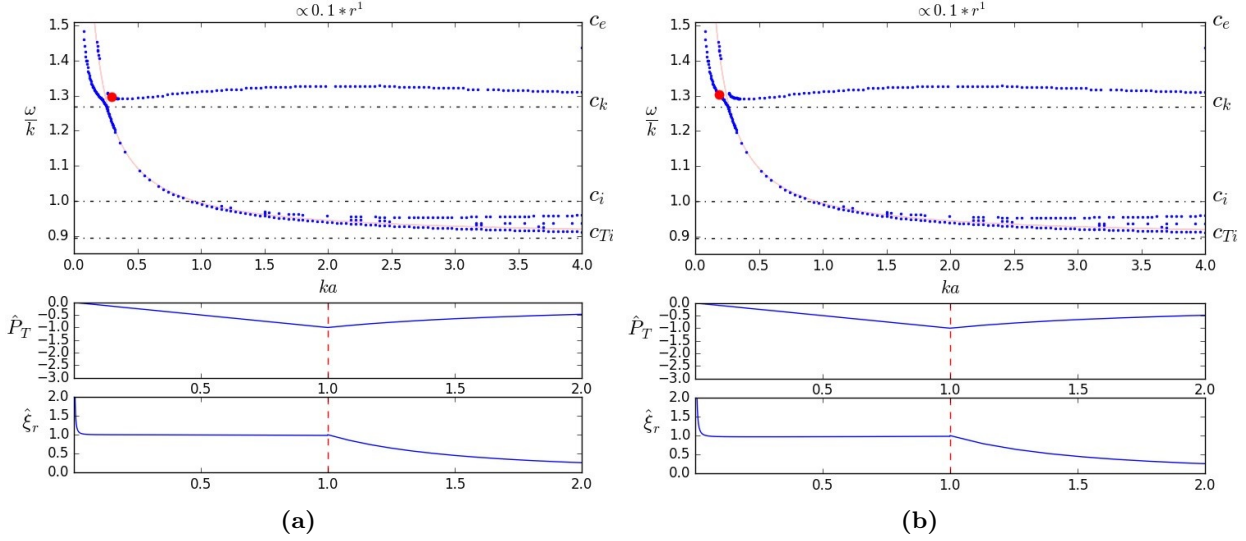


Figure 5.15: Plots showing the eigenfunctions \hat{P}_T and $\hat{\xi}_r$ for the (a) fast and (b) slow magnetoacoustic kink mode solutions in a photospheric flux tube with a background rotational flow given by $v_\varphi = 0.1r^1$. Both plots are for the same $v_{ph} = \omega/k = 1.3$ indicated by the red dot on the dispersion diagram. For both cases the resulting eigenfunctions are indistinguishable from one another.

expressions, as the radial spatial gradient of v_φ/r no longer becomes a constant value.

A magnetic flux tube in a photospheric environment is presented with an equilibrium azimuthal flow component which is spatially non-linear in the sense that:

$$v_\varphi = Ar^p, \quad (5.7)$$

where $p \neq 1$ for a nonlinear flow and A is, again, the amplitude of the flow. This scenario significantly complicates Equations (1.22)-(1.32) and furthermore, the continua modified by the flow described in Equations (1.33) and (1.34) now cover a wide range of spatial values rather than being limited to a single point for a fixed wavenumber. It should be noted that the modified Alfvén continuum is still present for these cases, however, under photospheric conditions is not important in the context of trapped modes, as it covers a range of frequencies located in the leaky regime.

As the nonlinear rotational flow contributes to the pressure balance expression given by Equation (5.5), this additional term must be accounted for by varying other plasma properties, such as plasma temperature in the case of a linear rotational flow scenario. The procedure for a nonlinear rotational flow is no different and the total pressure is balanced across the waveguide by varying the radial plasma temperature. An example of the equilibrium configuration for a photospheric flux tube with a nonlinear background rotational flow is shown in Figure 5.16. In this example, the flow is defined by $v_\varphi = 0.5r^{0.5}$, such that the azimuthal velocity describes a square root radial profile. The difference between the radial structure of plasma properties such as pressure and temperature can be seen by comparing Figure 5.3 and Figure 5.16. The difference between the linear and nonlinear examples is striking and can be expected to be important when analysing the properties of the resulting wave behaviour.

Figure 5.17 shows a comparison between the two separate variables analysed in this section. We incorporate background rotational flow into the model and compare the differences between varying the amplitude of the flow by keeping the power p constant and the alternative case by fixing the amplitude and varying the power of the rotational flow profile. By doing so, this allows us to

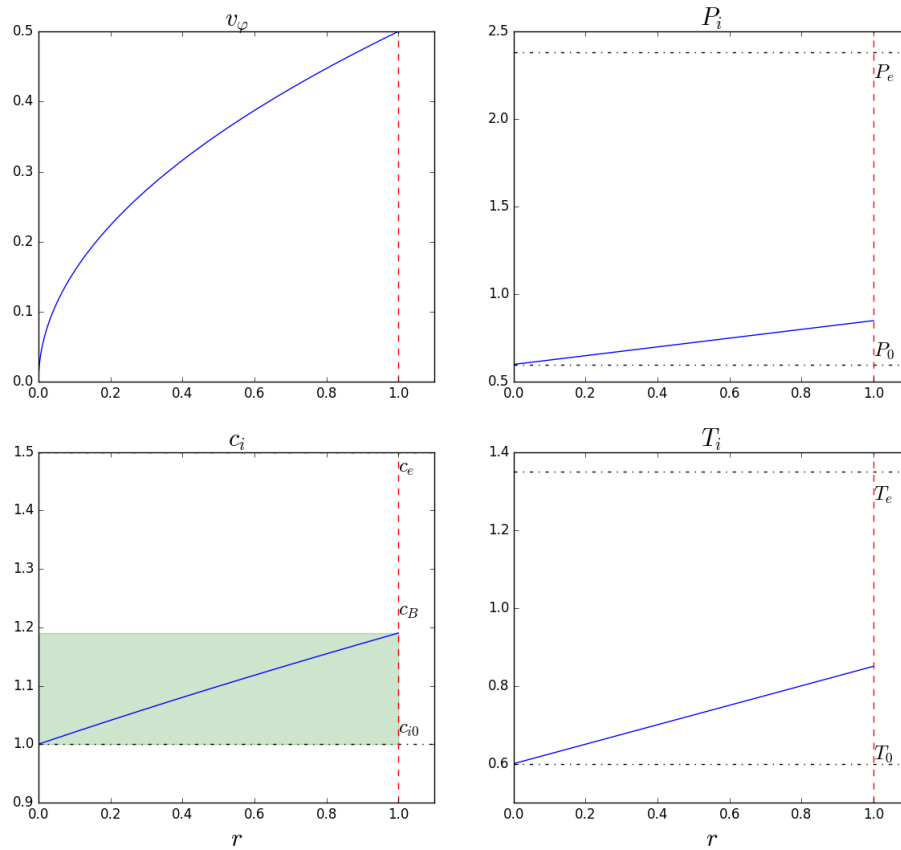


Figure 5.16: Plots of v_φ , plasma pressure, sound speed and plasma temperature inside the flux tube for an example configuration of a photospheric magnetic flux tube in the presence of a nonlinear background rotational flow given by the expression $v_\varphi = 0.5r^{0.5}$. The green shaded regions shows the inhomogeneous band of the internal sound speed, c_i , as a result of the background rotational flow.

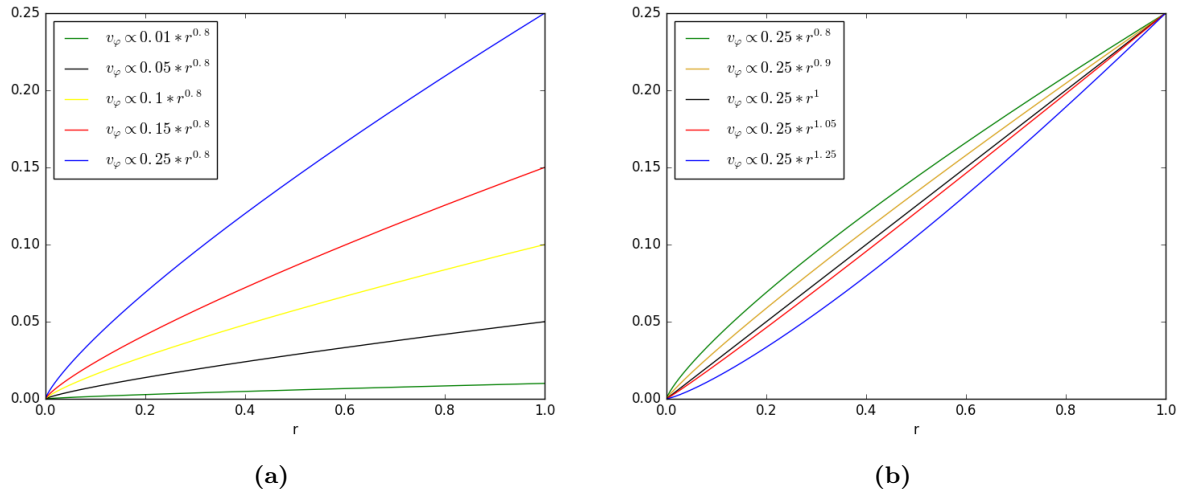


Figure 5.17: Radial profiles of the rotational flow considered in this chapter. (a) Example case where the power of the profile is kept constant but the amplitude varies (b) example case when the flow amplitude is kept constant and the power of the profile varies.

conduct a thorough analysis of the effect of the radial profile of rotational flow and its amplitude independently of one other for seismological purposes.

5.5.1 Fixed azimuthal flow profile

Similar to the analysis conducted in Section 5.4, let us assume now that the background rotational flow is non-linear and compare cases where the flow amplitude varies at the boundary, for a non-linear profile of constant power p (see e.g. Figure 5.17a). Figure 5.18 shows the resulting dispersion diagrams for the non-linear case where the power is fixed $p = 0.8$, corresponding to the profiles of the curves in Figure 5.17a. A few interesting points are deduced from this diagram. Firstly, the introduction of a non-uniform background rotational flow causes the modified cusp continuum to occupy a band of frequencies. This modified slow continuum, as a result of the background flow, becomes wider as the amplitude of the flow is increased and also shifts away from the long-wavelength limit with increasing amplitude. Secondly, the modified continuum occupies faster phase speeds as the amplitude of the flow is increased, this results in the body modes being absorbed into the continuum at larger rotational flow amplitudes for the case when $p = 0.8$, where these modes lying inside the continuum can then undergo resonant processes. For all cases when $p = 0.8$, the slow surface kink modes survive being consumed by the modified slow continuum, even for cases of larger amplitude. As the amplitude of the flow is increased, the slow surface kink modes possess similar phase speeds to those of the fast surface kink modes in the thin-tube limit, which should be considered when conducting wave analysis of propagating waves within a rotating solar structure such that the correct wave mode can be interpreted. Similarly, the obtained eigenvalues are plotted on the dispersion diagram for the case when $p = 1.25$ in Figure 5.19. For this case when $p > 1$, the notable differences when compared to the nonlinear case of $p < 1$ are that different wave modes are absorbed into the modified slow continuum. When the power of the profile is greater than unity, the slow body modes are initially absorbed by the continuum, whereas for the case when $p > 1$, the body modes initially survive unless the flow amplitude is increased sufficiently. The case of $p = 1.25$ still causes the modified slow continuum to occupy a band of frequencies, opposed

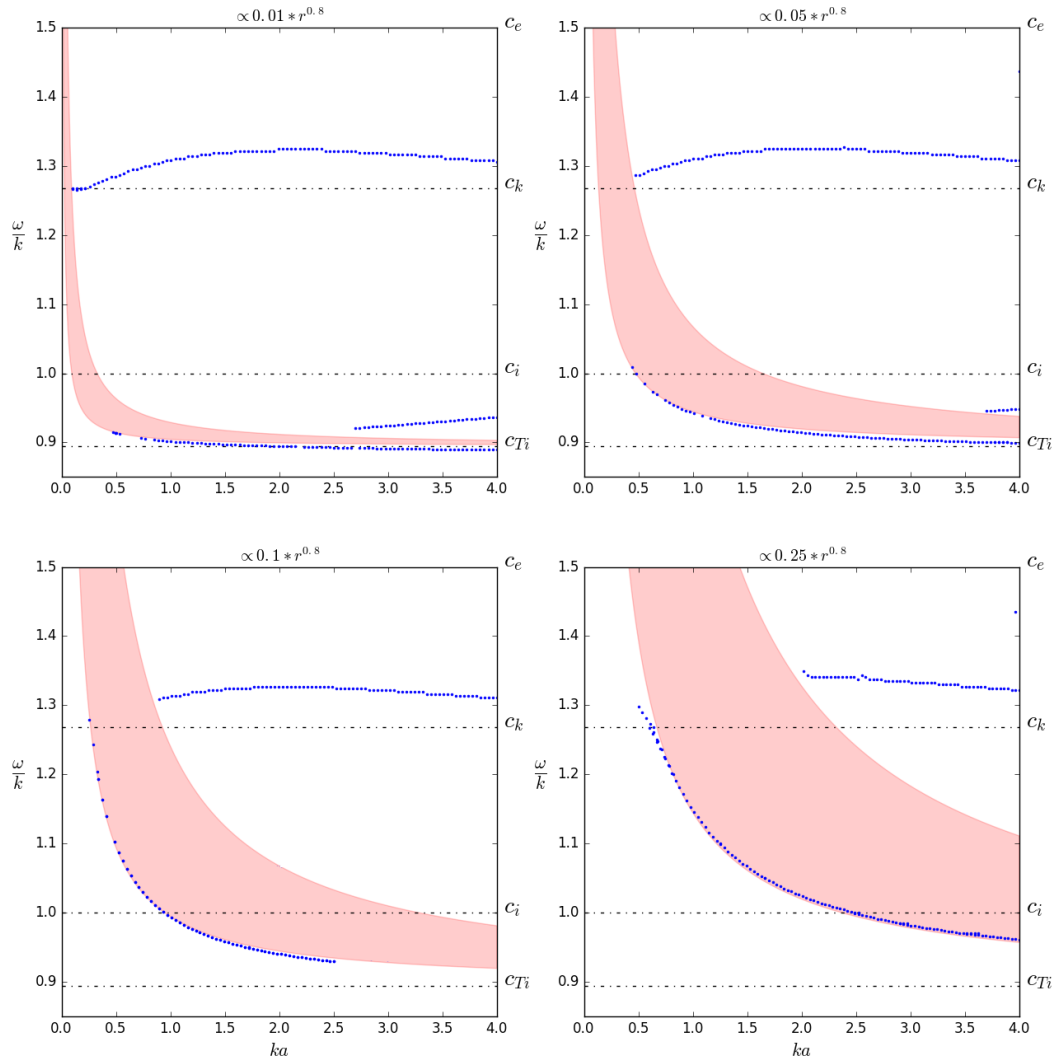


Figure 5.18: Dispersion diagrams for the $m = 1$ kink mode for a photospheric cylinder with a non-linear background rotational flow with $p = 0.8$. The different cases with varying amplitude are shown where the red shaded curve indicates the modified slow continuum due to the flow.

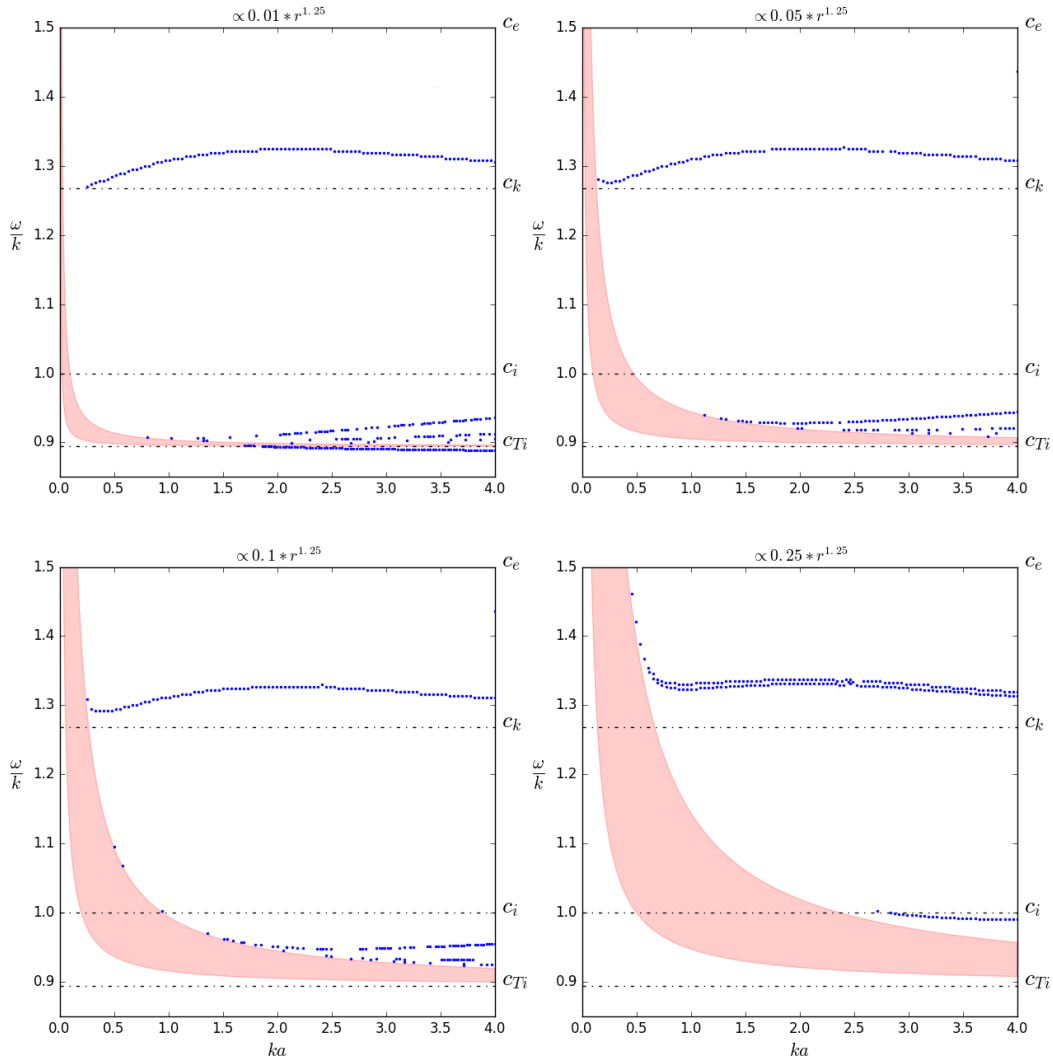


Figure 5.19: Dispersion diagrams for the $m = 1$ kink mode for a magnetic photospheric cylinder with a non-linear background rotational flow with $p = 1.25$. The different cases with varying amplitude are shown where the red shaded curve indicates the modified slow continuum.

to the single-valued nature of a linear rotational flow. Although whereas a $p < 1$ values caused the continuum to expand to faster phase speeds, a value of $p > 1$ causes this continuum to shift downwards on the dispersion diagram and consume modes with slower phase speeds.

5.5.2 Fixed azimuthal flow amplitude

Figure 5.17b shows the non-linear spatial profiles of the background rotational flow considered in this section. For all cases the amplitude of the flow is kept constant at the boundary, however the radial linearity is changed such that the power p in Equation (5.7) varies from $p < 1$ to $p > 1$. Conducting an investigation in this way will allow us to create a clearer picture of the effect that the power of the velocity profile has on the properties of the wave modes with respect to the modified slow continuum. In Figure 5.20, we show the obtained solutions for a magnetic cylinder with a nonlinear background rotational flow with a fixed amplitude of $A = 0.05$. In these plots, it is clearly seen that the width of the modified continuum depends heavily on the value of p . As the numerical code employed only seeks real solutions, the number of obtained solutions depends on the width of this region. When $p = 1$ and the flow is linear, the continuum reduces to accumulation points and the maximum number of solutions are retrieved as more eigenvalues lie on the real frequency axis. In Figure 5.20, we show the effect that the modified slow continuum has on the nature of modes entering the resonant frequency band. As explained in Section 5.5.1, when $p < 1$ the continuum consumes the slow body modes (in a photospheric cylinder) and when $p > 1$ the continuum absorbs the slow surface modes. When $p = 1$ the modes merge at the continuum line where their properties become of mixed behaviour. This nature can be seen better in Figure 5.20 as the evolution of the modified slow continuum can be compared by varying p . In all cases, the fast surface kink modes are absorbed into the continuum in the thin-tube limit.

5.6 Summary

In this chapter we have extended studies from previous chapters, which have investigated the properties of MHD waves in radially non-uniform magnetic waveguides, by including a linear and nonlinear azimuthal component to the background velocity field. In order to conduct this investigation, we ensured that the numerical code presented in Chapter 2 was capable of retrieving the correct eigenvalues for a magnetic cylinder with a background magnetic twist. The reason for this was that previous analytical studies have obtained the dispersion relation for MHD waves in linear magnetically twisted flux tubes (Erdélyi & Fedun 2007a, 2010). The eigenvalues for this particular model were retrieved and the analysis was further developed by consideration of the modified slow continuum due to the azimuthal component of the magnetic field. We managed to compliment the previous studies of magnetically twisted flux tubes by showing that the kink modes follow the trajectory of the modified slow continuum due to the background B_φ component.

A similar investigation modelling a magnetically rotating flux tube considered a uniform magnetic cylinder with a background v_φ flow component that was allowed to be either linear or nonlinear in radial direction, r . Firstly, for the case of a linear rotational flow, very similar results to those of the linear magnetic twist were recovered. Under both coronal and photospheric conditions it was found that the obtained kink mode solutions possess phase speeds which enter the leaky regime in the long wavelength limit. This was also shown to be a result of the modified slow continuum due to the background flow. The modified slow continuum reduces to single-point values in the cases of linear rotational flow and magnetic twist. Therefore, there becomes a point where, under photospheric conditions, the slow surface kink mode and the slow body kink mode merge at the point of the continuum, and their properties become mixed. Comparison of the eigenfunctions

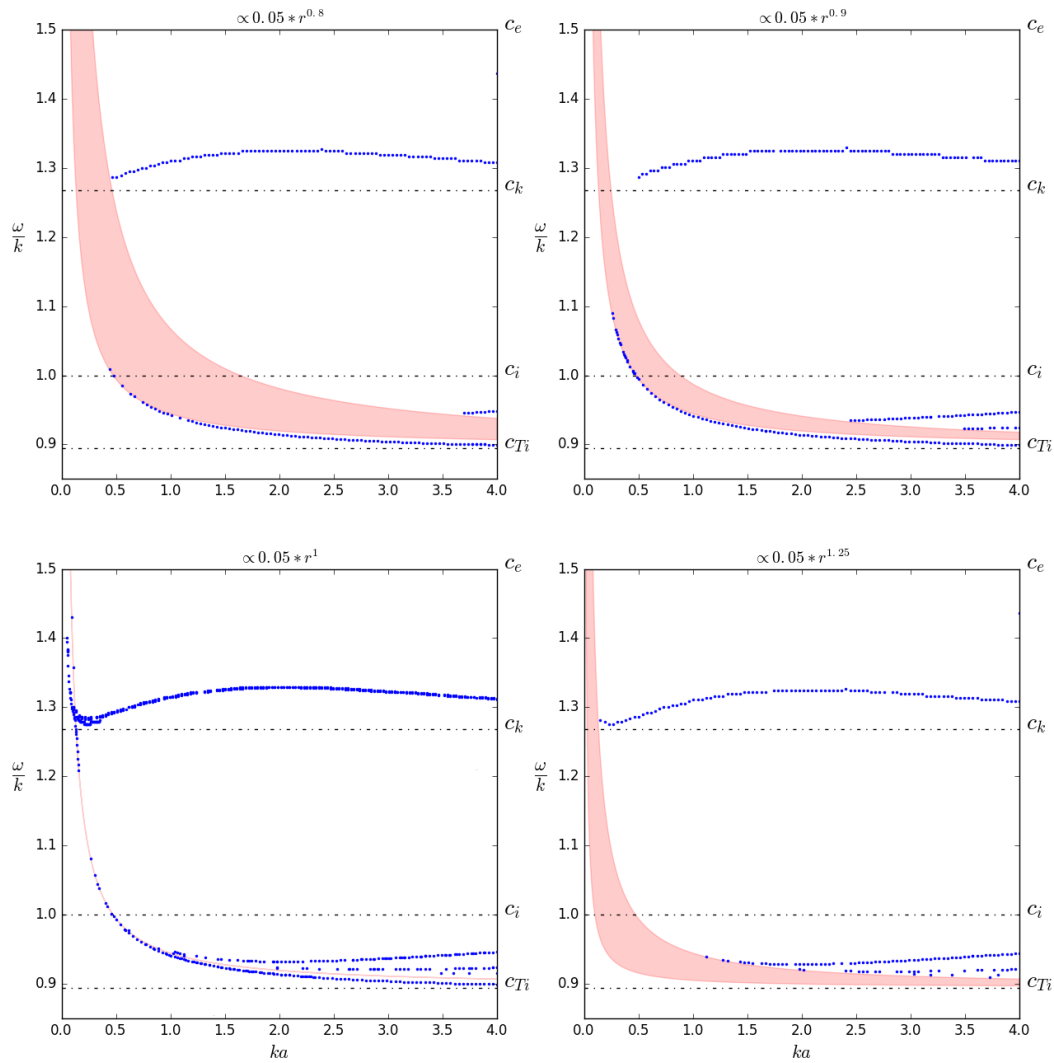


Figure 5.20: Dispersion diagrams for the $m = 1$ kink mode for a photospheric cylinder with a non-linear background rotational flow with $A = 0.05$. The different cases with varying power are shown where the red shaded curve indicates the modified slow continuum.

for the slow surface kink mode and fast surface kink mode in the presence of a linear background rotational flow at similar phase speeds, indicated that identification of the two modes becomes extremely difficult in the long wavelength limit. This is because the radial structure of the displacement and pressure perturbations for each mode become identical to each other. This could have consequences for the interpretation of these wave modes in observable solar waveguides.

An extension of this study which modelled the rotational flow as a nonlinear radial profile was then conducted in Section 5.5. A variety of case studies were compared against each other and focused on the influence of two variables, namely the amplitude of the rotational flow and the power of the spatial profile on the resulting MHD wave modes. It was found that the power of the flow profile has a significant importance on the behaviour of the modified slow continuum. The width of the modified continuum depends on both the amplitude of the flow and the power of the profile, whereas the direction of the continuum band (shifted to either faster or slower phase speeds) depends solely on the power of the profile. This has important consequences for which wave modes are absorbed into the continuum where they can undergo resonant processes, such as resonant absorption. For a linear rotational flow, with radial power equal to one, we have deduced that the continuum band reduces to single-point values, where, under photospheric conditions, the slow surface and body modes merge at the continuum point. However, for a power $p > 1$, the modified slow continuum expands from single-point values and occupies phase speeds just below the continuum line for the linear case. As a result, this causes the slow surface kink mode to enter the continuum, and is no longer present for rotational flow amplitudes that exceed a small percentage of the local sound speed, roughly 5%. However, for the case where the power of the rotational flow profile is less than linear, e.g. $p < 1$, the modified slow continuum expands to greater phase speeds and the slow body modes are now consumed by the continuum. The width of the continuum is larger as p becomes smaller and more nonlinear, causing slow body kink modes at smaller wavenumbers to become absorbed into the continuum band. For all cases of nonlinear rotational flow, the fast surface kink mode is consumed by the modified slow continuum in the thin-tube limit, suggesting that these modes may be susceptible to damping in thin rotating magnetic flux tubes that are common in the lower solar atmosphere.

For all the cases of a magnetically twisted flux tube, linear rotating flux tube and a nonlinear rotating flux tube, it was found that the axisymmetric $m = 0$ sausage mode remains unaffected by any background azimuthal component. Analytically this can be understood by examining the governing set of Equations (1.22)-(1.32) when setting $m = 0$ and noticing many terms either simplifying or disappearing altogether. Furthermore, it also suggests that sausage mode observations in the lower solar atmosphere in e.g. pores and sunspots, may not provide a suitable wave mode to conduct magnetoseismology if the structure is in the presence of any magnetic twist or background flows.

Chapter 6

Conclusions & Outlook

In this thesis we have developed a new numerical eigensolver which can be applied to multiple geometrical coordinate systems, such as Cartesian and cylindrical, to obtain the eigenvalues and resulting eigenfunctions for any arbitrary symmetrically non-uniform equilibria. The numerical algorithm utilises the shooting method and bisection method along with well known properties of fundamental trapped MHD wave modes. A more detailed explanation of the numerical code is found in Chapter 2. We have comprehensively tested this code against a number of well known, previously derived analytical results including a uniform magnetic slab with and without the inclusion of a steady background plasma flow in both coronal and photospheric environments in Chapter 3. Further testing then focused on a cylindrical geometry in Chapter 4 for which the eigenvalues for a uniform magnetic cylinder, again with and without the inclusion of a steady background plasma flow, were correctly obtained in both coronal and photospheric environments. More complex testing required retrieving the same solutions for a magnetic cylinder with a linear background magnetic twist, as done previously in Erdélyi & Fedun (2007*b*) and Erdélyi & Fedun (2010). The numerical code recovered the same eigenvalues as the previous analytical studies demonstrating the power of the newly developed algorithm to be successful in a wide variety of equilibrium configurations. The presented numerical tool has endless possible applications and, with further development, could be vital in aiding with the understanding of MHD wave properties in observed solar features.

We have found that, by modelling solar waveguides as a two-dimensional magnetic slab, that the spatial properties of slow magnetoacoustic modes are altered in the presence of a spatially non-uniform equilibrium, due to e.g. inhomogeneous plasma density and background flow (Skirvin et al. 2021). We have found that modelling the equilibrium plasma density as a Gaussian profile creates additional nodes and anti-nodes in the resulting eigenfunction solutions when compared to the eigenfunctions of a uniform magnetic slab predicted by theory. This result may have an implication for observers when interpreting observations in waveguides with a similar environment as the existence of either (a) an overtone of the mode or (b) a separate wave mode entirely. Furthermore, our results have shown that the same effect is not present for the fast magnetoacoustic modes, for which we suggest this may be because fast magnetoacoustic wave modes can propagate across the magnetic field and hence across the inhomogeneity. A full detailed discussion of the work conducted can be found in Chapter 3.

This work was then extended to investigate the properties of MHD waves in a non-uniform magnetic cylinder in Chapter 4 (Skirvin et al. 2022). A similar analysis was conducted which modelled the plasma density as a Gaussian profile under both coronal and photospheric conditions. Striking results to the case of a non-uniform magnetic slab were found that included additional nodes and anti-nodes appearing in the resulting eigenfunctions when compared to the case of a

uniform cylinder. Furthermore, it was found that the internal azimuthal displacement perturbation increased towards the cylinder boundary with increasing density non-uniformity. This creates a larger discontinuity across the boundary which results in greater shearing and may cause the onset of KHI. Similar to previous studies we have shown that a non-uniform waveguide may be susceptible to KHI and could be responsible for the disappearance of e.g. spicules fading in the upper chromosphere (De Pontieu, McIntosh, Carlsson, Hansteen, Tarbell, Schrijver, M., Shine, Tsuneta, Katsukawa, Ichimoto, Suematsu, Shimizu & Nagata 2007). An additional study of a uniform magnetic cylinder with a non-uniform background plasma flow under coronal conditions in an attempt to model a solar jet-like behaviour. We showed that the perturbed vorticity is greater in the case of maximum non-uniformity of plasma flow. This may excite torsional MHD waves in the upper layers of the solar atmosphere (González-Avilés et al. 2017, 2019).

Another study presented in this work modelled magnetic flux tubes in the presence of background magnetic twist and rotational flow. In Chapter 5 we introduced a linear magnetic twist into the model and retrieved previous analytical results. We showed how the kink mode is affected by the modified slow continuum and the wave solutions follow the trajectory of this continuum line, explaining the observed phase speed behaviour in the thin-tube limit. We then considered the effect of a linear background rotational flow on a coronal and photospheric flux tube. In both environments, it was found that there was little effect on the sausage mode, however the kink mode displayed similar characteristics to a magnetically twisted flux tube. It was determined that this behaviour was again due to the modified continuum which may have implications for interpreting observational data and conducting atmospheric-seismology. A final case study investigated the effect of a nonlinear background rotational flow in a photospheric flux tube. It was found that when the rotational flow was modelled using a nonlinear profile, the modified continua no longer reduce to single point values and instead occupy a band of wave frequencies. This results in more wave modes being consumed by the continuum where they can undergo resonant processes.

In every case study investigated in this thesis, it has become a common theme to observe that the slow magnetoacoustic modes, both body and surface, are more greatly affected than fast modes under both coronal and photospheric environments. A possible explanation of this was provided in the summary of Chapter 3. It is based on the fact that slow modes, in general, propagate along the lines of magnetic field, whereas fast modes can propagate across the magnetic field, hence can propagate across the inhomogeneity and feel the effect of non-uniform equilibria less than their slow counterparts. This result could have implications for determining which wave modes are more suitable to use when conducting solar atmospheric seismology.

6.1 Future work

1. Complex solutions

In Chapter 2 we explained the physics behind how the numerical eigensolver obtains solutions for MHD wave modes in non-uniform waveguides. One of the assumptions to allow this to be done was that the wave amplitudes are evanescent outside the waveguide, such that they are zero infinitely far from the waveguide. However, through this assumption, the investigation of complex solutions that describe leaky modes, solutions which lie inside the continua and/or instabilities are instantly ignored. Through this, a lot of interesting physics can not be studied and it would be a great advancement of the numerical eigensolver if the complex solutions were included. This can be done using a variety of techniques. Firstly, continuation of the method described in Section 2.2.1 that involves implementing the shooting method for both the real and complex components of the eigenfunctions may successfully obtain the full frequency eigenvalues, including the imaginary component. Secondly, using an alternative method than the numerical shooting method may be a more accessible approach, such as discretising the linearised MHD equations using a Finite Element approach such as the one described by the Legolas code (Claes et al. 2020).

2. Interactive eigenfunctions

Whilst the numerical eigensolver developed in this thesis has demonstrated its abilities at obtaining the correct solutions for a number of different uniform and non-uniform case studies, there is endless scope of possible improvements. One example would be to expand the usability aspect of the code, by incorporating an interactive graphical interface as a method to visualise e.g. the eigenfunctions of a particular wave solution. For example, within a separate script, the obtained solutions could be displayed on the dispersion diagram and the user could physically select each mode separately to view the eigenfunctions instantly. There could also be an option to create instant 3D snapshots/movies of this wave mode to gauge an idea as to what this mode would look like when observed propagating within a solar structure. Incorporating improved usability such as this would make the tool more accessible to the wider community.

3. Magnetoseismology with high resolution observations

In recent decades, significant progress has been made with both ground, and space-based telescopes, such as SDO/AIA, Hinode/SOT, SST, IRIS. However, even greater observations are required if we are to fully understand the physics and associated wave phenomena occurring on smaller scales in observed solar features such as jets, thin coronal loops, magnetic bright points, etc. Fortunately, the new high-resolution observational facility DKIST will provide new important information on the small-scale, fine structure and dynamics of such features. DKIST is capable of capturing the dynamic evolution of solar features with high cadence (3 seconds) and making simultaneous measurements (with 15-second cadence) of both chromospheric and photospheric magnetic fields and flows (Rast et al. 2021). The new high resolution data obtained by this telescope will create fresh opportunities to conduct detailed atmospheric-seismology using observed MHD waves. This data, complimented with the numerical tool presented in this thesis, will allow insights into the properties of MHD waves

which is at the forefront of human knowledge, surpassing what is possible from a purely analytical approach and ultimately advancing our understanding of the properties of MHD waves in non-uniform plasmas.

4. Realistic equilibrium configurations

The case studies presented in each chapter of this thesis have considered equilibria that is more representable of conditions within a solar waveguide. Although modelling of solar plasma as spatially non-uniform with background magnetic twist or rotational flows is a huge step beyond what is capable from an analytical perspective, the numerical eigensolver is capable of handling much more complex equilibria. For example, in future work it would be possible to model some of the case studies presented here, combined with each other, such as a non-uniform density flux tube with a background magnetic twist. Configurations with non-uniform plasma including a background B_φ and v_φ component are impossible to investigate purely from a theoretical point of view and must be done, at least in some part, numerically. The numerical eigensolver presented in this work is more than capable of obtaining the wave modes in observed solar configurations, so long as an equilibrium can be obtained.

5. Torsional Alfvén waves

In this thesis we have discussed and presented only the magnetoacoustic wave solutions in non-uniform magnetic waveguides. However, as we have mentioned in Chapter 1, there does exist another wave solution to Equation (1.19) that describes the Alfvén wave. It would be possible to repeat the analysis conducted in this thesis under the assumption that the perturbations are incompressible, which corresponds to the properties of Alfvén waves. This may be an interesting avenue to explore, because the presence of a non-uniform background may affect the properties of Alfvén waves in such a way that they may produce observational signatures. Because torsional Alfvén waves are incompressible, and do not perturb the plasma density or temperature, they do not leave obvious observational signatures, however, their properties in non-uniform waveguides are not well understood.

Bibliography

- Abdelatif, T. E. (1990), ‘Magneto-atmospheric waves’, *Solar Phys.* **129**, 201–219.
- Alfvén, H. (1942), ‘Existence of Electromagnetic-Hydrodynamic Waves’, *Nature* **150**, 405–406.
- Allcock, M. & Erdélyi, R. (2017), ‘Magnetohydrodynamic Waves in an Asymmetric Magnetic Slab’, *Solar Phys.* **292**, 35.
- Andries, J., Tirry, W. J. & Goossens, M. (2000), ‘Modified Kelvin-Helmholtz Instabilities and Resonant Flow Instabilities in a One-dimensional Coronal Plume Model: Results for Plasma $\beta=0$ ’, *Astrophys. J.* **531**(1), 561–570.
- Antolin, P., Yokoyama, T. & Van Doorselaere, T. (2014), ‘Fine Strand-like Structure in the Solar Corona from Magnetohydrodynamic Transverse Oscillations’, *Astrophys. J. Lett.* **787**(2), L22.
- Arber, T. D., Brady, C. S. & Shelyag, S. (2016), ‘Alfvén Wave Heating of the Solar Chromosphere: 1.5D Models’, *Astrophys. J.* **817**(2), 94.
- Arregui, I. (2015), ‘Wave heating of the solar atmosphere’, *Philosophical Transactions of the Royal Society of London Series A* **373**, 20140261–20140261.
- Arregui, I. & Goossens, M. (2019), ‘No unique solution to the seismological problem of standing kink magnetohydrodynamic waves’, *Astron. Astrophys.* **622**, A44.
- Arregui, I., Terradas, J., Oliver, R. & Ballester, J. L. (2007), ‘The influence of the internal structuring of coronal loops on the properties of their damped transverse oscillations’, *Astron. Astrophys.* **466**(3), 1145–1151.
- Arregui, I., Van Doorselaere, T., Andries, J., Goossens, M. & Kimpe, D. (2005), ‘Resonantly damped fast MHD kink modes in longitudinally stratified tubes with thick non-uniform transitional layers’, *Astron. Astrophys.* **441**(1), 361–370.
- Aschwanden, M. J., Fletcher, L., Schrijver, C. J. & Alexander, D. (1999), ‘Coronal Loop Oscillations Observed with the Transition Region and Coronal Explorer’, *Astrophys. J.* **520**(2), 880–894.
- Aschwanden, M. J., Nightingale, R. W., Andries, J., Goossens, M. & Van Doorselaere, T. (2003), ‘Observational Tests of Damping by Resonant Absorption in Coronal Loop Oscillations’, *Astrophys. J.* **598**(2), 1375–1386.
- Ballester, J. L., Alexeev, I., Collados, M., Downes, T., Pfaff, R. F., Gilbert, H., Khodachenko, M., Khomenko, E., Shaikhislamov, I. F., Soler, R., Vázquez-Semadeni, E. & Zaqarashvili, T. (2018), ‘Partially Ionized Plasmas in Astrophysics’, *Space Sci. Rev.* **214**(2), 58.

- Bareford, M. R. & Hood, A. W. (2015), ‘Shock heating in numerical simulations of kink-unstable coronal loops’, *Philosophical Transactions of the Royal Society of London Series A* **373**(2042), 20140266–20140266.
- Berger, T. E., Slater, G., Hurlburt, N., Shine, R., Tarbell, T., Title, A., Lites, B. W., Okamoto, T. J., Ichimoto, K., Katsukawa, Y., Magara, T., Suematsu, Y. & Shimizu, T. (2010), ‘Quiescent Prominence Dynamics Observed with the Hinode Solar Optical Telescope. I. Turbulent Upflow Plumes’, *Astrophys. J.* **716**(2), 1288–1307.
- Biermann, L. (1946), ‘Zur Deutung der chromosphärischen Turbulenz und des Exzesses der UV-Strahlung der Sonne’, *Naturwissenschaften* **33**(4), 118–119.
- Biermann, L. (1948), ‘Über die Ursache der chromosphärischen Turbulenz und des UV-Exzesses der Sonnenstrahlung’, **25**, 161.
- Bonet, J. A., Márquez, I., Sánchez Almeida, J., Cabello, I. & Domingo, V. (2008), ‘Convectively Driven Vortex Flows in the Sun’, *Astrophys. J. Lett.* **687**(2), L131.
- Bonet, J. A., Márquez, I., Sánchez Almeida, J., Palacios, J., Martínez Pillet, V., Solanki, S. K., del Toro Iniesta, J. C., Domingo, V., Berkefeld, T., Schmidt, W., Gandorfer, A., Barthol, P. & Knölker, M. (2010), ‘SUNRISE/IMaX Observations of Convectively Driven Vortex Flows in the Sun’, *Astrophys. J. Lett.* **723**(2), L139–L143.
- Borrero, J. M. & Ichimoto, K. (2011), ‘Magnetic Structure of Sunspots’, *Living Reviews in Solar Physics* **8**(1), 4.
- Cairns, R. A. (1979), ‘The role of negative energy waves in some instabilities of parallel flows’, *Journal of Fluid Mechanics* **92**, 1–14.
- Chandrasekhar, S. (1961), *Hydrodynamic and hydromagnetic stability*.
- Chen, S.-X., Li, B., Kumar, S., Yu, H. & Shi, M. (2018), ‘Fast Standing Modes in Transversely Nonuniform Solar Coronal Slabs: The Effects of a Finite Plasma Beta’, *Astrophys. J.* **855**(1), 47.
- Cheremnykh, O., Fedun, V., Ladikov-Roev, Y. & Verth, G. (2018), ‘On the Stability of Incompressible MHD Modes in Magnetic Cylinder with Twisted Magnetic Field and Flow’, *Astrophys. J.* **866**(2), 86.
- Cheremnykh, O. K., Fedun, V., Kryshtal, A. N. & Verth, G. (2017), ‘Incompressible magnetohydrodynamic modes in the thin magnetically twisted flux tube’, *Astron. Astrophys.* **604**, A62.
- Chitta, L. P., van Ballegoijen, A. A., Rouppe van der Voort, L., DeLuca, E. E. & Kariyappa, R. (2012), ‘Dynamics of the Solar Magnetic Bright Points Derived from Their Horizontal Motions’, *Astrophys. J.* **752**(1), 48.
- Cirtain, J. W., Golub, L., Lundquist, L., van Ballegoijen, A., Savcheva, A., Shimojo, M., DeLuca, E., Tsuneta, S., Sakao, T., Reeves, K., Weber, M., Kano, R., Narukage, N. & Shibasaki, K. (2007), ‘Evidence for Alfvén Waves in Solar X-ray Jets’, *Science* **318**, 1580.
- Claes, N., De Jonghe, J. & Keppens, R. (2020), ‘Legolas: A Modern Tool for Magnetohydrodynamic Spectroscopy’, *Astrophys. J. Suppl.* **251**(2), 25.
- De Moortel, I. & Browning, P. (2015), ‘Recent advances in coronal heating’, *Philosophical Transactions of the Royal Society of London Series A* **373**(2042), 20140269–20140269.

- De Pontieu, B., McIntosh, S., Hansteen, V. H., Carlsson, M., Schrijver, C. J., Tarbell, T. D., Title, A. M., Shine, R. A., Suematsu, Y., Tsuneta, S., Katsukawa, Y., Ichimoto, K., Shimizu, T. & Nagata, S. (2007), ‘A Tale of Two Spicules: The Impact of Spicules on the Magnetic Chromosphere’, *Pub. Astron. Soc. Japan* **59**, S655.
- De Pontieu, B., McIntosh, S. W., Carlsson, M., Hansteen, V. H., Tarbell, T. D., Schrijver, C. J., M., A., Shine, R. A., Tsuneta, S., Katsukawa, Y., Ichimoto, K., Suematsu, Y., Shimizu, T. & Nagata, S. (2007), ‘Chromospheric Alfvénic Waves Strong Enough to Power the Solar Wind’, *Science* **318**, 1574.
- Duckenfield, T. J., Kolotkov, D. Y. & Nakariakov, V. M. (2021), ‘The effect of the magnetic field on the damping of slow waves in the solar corona’, *Astron. Astrophys.* **646**, A155.
- Ebadi, H. & Ghiassi, M. (2014), ‘Observation of kink waves and their reconnection-like origin in solar spicules’, *Astrophys. Space Sci.* **353**, 31–36.
- Ebadi, H., Zaqarashvili, T. V. & Zhelyazkov, I. (2011), Wave Propagation in Solar Spicules, in I. Zhelyazkov & T. Mishonov, eds, ‘American Institute of Physics Conference Series’, Vol. 1356 of *American Institute of Physics Conference Series*, pp. 117–122.
- Ebrahimi, Z. & Karami, K. (2016), ‘Resonant absorption of kink magnetohydrodynamic waves by a magnetic twist in coronal loops’, *Monthly Notices of the Royal Astronomical Society* **462**(1), 1002–1011.
- Edwin, P. M. & Roberts, B. (1982), ‘Wave Propagation in a Magnetically Structured Atmosphere - Part Three - the Slab in a Magnetic Environment’, *Solar Phys.* **76**, 239–259.
- Edwin, P. M. & Roberts, B. (1983), ‘Wave propagation in a magnetic cylinder’, *Solar Phys.* **88**, 179–191.
- Edwin, P. M. & Roberts, B. (1988), ‘Employing analogies for ducted MHD waves in dense coronal structures’, *Astron. Astrophys.* **192**(1-2), 343–347.
- Erdélyi, R. & Ballai, I. (2007), ‘Heating of the solar and stellar coronae: a review’, *Astronomische Nachrichten* **328**(8), 726–733.
- Erdélyi, R. & Fedun, V. (2007a), ‘Are There Alfvén Waves in the Solar Atmosphere?’, *Science* **318**(5856), 1572.
- Erdélyi, R. & Fedun, V. (2007b), ‘Linear MHD Sausage Waves in Compressible Magnetically Twisted Flux Tubes’, *Solar Phys.* **246**(1), 101–118.
- Erdélyi, R. & Fedun, V. (2010), ‘Magneto-Acoustic Waves in Compressible Magnetically Twisted Flux Tubes’, *Solar Phys.* **263**(1-2), 63–85.
- Fedun, V. N., Yukhimuk, A. K. & Voitsekhovskaya, A. D. (2004), ‘The transformation of MHD Alfvén waves in space plasma’, *Journal of Plasma Physics* **70**(6), 699–707.
- Fedun, V., Shelyag, S. & Erdélyi, R. (2011), ‘Numerical Modeling of Footpoint-driven Magneto-acoustic Wave Propagation in a Localized Solar Flux Tube’, *Astrophys. J.* **727**, 17.
- Fedun, V., Shelyag, S., Verth, G., Mathioudakis, M. & Erdélyi, R. (2011), ‘MHD waves generated by high-frequency photospheric vortex motions’, *Annales Geophysicae* **29**, 1029–1035.

- Fedun, V., Verth, G., Jess, D. B. & Erdélyi, R. (2011), ‘Frequency Filtering of Torsional Alfvén Waves by Chromospheric Magnetic Field’, *Astrophys. J. Lett.* **740**(2), L46.
- Frieman, E. & Rotenberg, M. (1960), ‘On Hydromagnetic Stability of Stationary Equilibria’, *Reviews of Modern Physics* **32**(4), 898–902.
- Gafeira, R., Jafarzadeh, S., Solanki, S. K., Lagg, A., van Noort, M., Barthol, P., Blanco Rodríguez, J., del Toro Iniesta, J. C., Gandorfer, A., Gizon, L., Hirzberger, J., Knölker, M., Orozco Suárez, D., Riethmüller, T. L. & Schmidt, W. (2017), ‘Oscillations on Width and Intensity of Slender Ca II H Fibrils from Sunrise/SuFI’, *Astrophys. J. Suppl.* **229**, 7.
- Giagkiozis, I., Fedun, V., Erdélyi, R. & Verth, G. (2015), ‘Axisymmetric Modes in Magnetic Flux Tubes with Internal and External Magnetic Twist’, *Astrophys. J.* **810**, 53.
- Giagkiozis, I., Goossens, M., Verth, G., Fedun, V. & Van Doorselaere, T. (2016), ‘Resonant Absorption of Axisymmetric Modes in Twisted Magnetic Flux Tubes’, *Astrophys. J.* **823**, 71.
- Gilchrist-Millar, C. A., Jess, D. B., Grant, S. D. T., Keys, P. H., Beck, C., Jafarzadeh, S., Riedl, J. M., Van Doorselaere, T. & Ruiz Cobo, B. (2021), ‘Magnetoacoustic wave energy dissipation in the atmosphere of solar pores’, *Philosophical Transactions of the Royal Society of London Series A* **379**(2190), 20200172.
- Goedbloed, H., Keppens, R. & Poedts, S. (2019), *Magnetohydrodynamics of Laboratory and Astrophysical Plasmas*, Cambridge University Press.
- Goedbloed, J. P. H. & Poedts, S. (2004), *Principles of Magnetohydrodynamics*.
- Goedbloed, J. P., Keppens, R. & Poedts, S. (2010), *Advanced Magnetohydrodynamics*.
- González-Avilés, J. J., Guzmán, F. S. & Fedun, V. (2017), ‘Jet Formation in Solar Atmosphere due to Magnetic Reconnection’, *Astrophys. J.* **836**, 24.
- González-Avilés, J. J., Guzmán, F. S., Fedun, V., Verth, G., Sharma, R., Shelyag, S. & Regnier, S. (2019), ‘In situ generation of coronal Alfvén waves by jets’, *Monthly Notices of the Royal Astronomical Society* **484**, 1936–1945.
- González-Avilés, J. J., Guzmán, F. S., Fedun, V., Verth, G., Shelyag, S. & Regnier, S. (2018), ‘I. Jet Formation and Evolution Due to 3D Magnetic Reconnection’, *Astrophys. J.* **856**, 176.
- Goossens, M., Andries, J. & Aschwanden, M. J. (2002), ‘Coronal loop oscillations. An interpretation in terms of resonant absorption of quasi-mode kink oscillations’, *Astron. Astrophys.* **394**, L39–L42.
- Goossens, M., Andries, J., Soler, R., Van Doorselaere, T., Arregui, I. & Terradas, J. (2012), ‘Surface Alfvén Waves in Solar Flux Tubes’, *Astrophys. J.* **753**(2), 111.
- Goossens, M., Erdélyi, R. & Ruderman, M. S. (2011), ‘Resonant MHD Waves in the Solar Atmosphere’, *Space Sci. Rev.* **158**(2-4), 289–338.
- Goossens, M., Hollweg, J. V. & Sakurai, T. (1992), ‘Resonant behaviour of MHD waves on magnetic flux tubes. III - Effect of equilibrium flow’, *Solar Phys.* **138**, 233–255.
- Goossens, M. L., Arregui, I. & Van Doorselaere, T. (2019), ‘Mixed properties of MHD waves in non-uniform plasmas’, *Frontiers in Astronomy and Space Sciences* **6**, 20.

- Goossens, M., Ruderman, M. S. & Hollweg, J. V. (1995), ‘Dissipative MHD solutions for resonant Alfvén waves in 1-dimensional magnetic flux tubes’, *Solar Phys.* **157**(1-2), 75–102.
- Goossens, M., Terradas, J., Andries, J., Arregui, I. & Ballester, J. L. (2009), ‘On the nature of kink MHD waves in magnetic flux tubes’, *Astron. Astrophys.* **503**(1), 213–223.
- Gudiksen, B. V. & Nordlund, Å. (2005), ‘An Ab Initio Approach to the Solar Coronal Heating Problem’, *Astrophys. J.* **618**(2), 1020–1030.
- Hain, K. & Lüst, R. (1958), ‘Zur Stabilität zylindersymmetrischer Plasmakonfigurationen mit Volumenströmen’, *Zeitschrift Naturforschung Teil A* **13**(11), 936–940.
- Hasan, S. S. & Kalkofen, W. (1999), ‘Excitation of Oscillations in Photospheric Flux Tubes through Buffeting by External Granules’, *Astrophys. J.* **519**(2), 899–910.
- Hasan, S. S., Kalkofen, W. & van Ballegooijen, A. A. (2000), ‘Excitation of Oscillations in the Magnetic Network on the Sun’, *Astrophys. J. Lett.* **535**(1), L67–L70.
- Heyvaerts, J. & Priest, E. R. (1983), ‘Coronal heating by phase-mixed shear Alfvén waves.’, *Astron. Astrophys.* **117**, 220–234.
- Hirota, M., Morrison, P. J. & Hattori, Y. (2014), ‘Variational necessary and sufficient stability conditions for inviscid shear flow’, *Proceedings of the Royal Society A: Mathematical, Physical and Engineering Sciences* **470**(2172), 20140322.
URL: <http://dx.doi.org/10.1098/rspa.2014.0322>
- Hollweg, J. V. & Yang, G. (1988), ‘Resonance absorption of compressible magnetohydrodynamic waves at thin “surfaces”’, *J. Geophys. Res.* **93**(A6), 5423–5436.
- Howson, T. A., De Moortel, I. & Antolin, P. (2017), ‘The effects of resistivity and viscosity on the Kelvin-Helmholtz instability in oscillating coronal loops’, *Astron. Astrophys.* **602**, A74.
- Howson, T. A., De Moortel, I., Antolin, P., Van Doorselaere, T. & Wright, A. N. (2019), ‘Resonant absorption in expanding coronal magnetic flux tubes with uniform density’, *Astron. Astrophys.* **631**, A105.
- Ionson, J. A. (1978), ‘Resonant absorption of Alfvénic surface waves and the heating of solar coronal loops.’, *Astrophys. J.* **226**, 650–673.
- Ionson, J. A. (1984), ‘A unified theory of electrodynamic coupling in coronal magnetic loops - The coronal heating problem’, *Astrophys. J.* **276**, 357–368.
- Jess, D. B., Mathioudakis, M., Christian, D. J., Crockett, P. J. & Keenan, F. P. (2010), ‘A Study of Magnetic Bright Points in the Na I D₁ Line’, *Astrophys. J. Lett.* **719**(2), L134–L139.
- Jess, D. B., Mathioudakis, M., Erdélyi, R., Crockett, P. J., Keenan, F. P. & Christian, D. J. (2009), ‘Alfvén Waves in the Lower Solar Atmosphere’, *Science* **323**(5921), 1582.
- Jess, D. B., Morton, R. J., Verth, G., Fedun, V., Grant, S. D. T. & Giagkiozis, I. (2015), ‘Multi-wavelength Studies of MHD Waves in the Solar Chromosphere. An Overview of Recent Results’, *Space Sci. Rev.* **190**, 103–161.

- Jess, D. B., Van Doorselaere, T., Verth, G., Fedun, V., Krishna Prasad, S., Erdélyi, R., Keys, P. H., Grant, S. D. T., Uitenbroek, H. & Christian, D. J. (2017), ‘An Inside Look at Sunspot Oscillations with Higher Azimuthal Wavenumbers’, *Astrophys. J.* **842**(1), 59.
- Keppens, R. (1996), ‘Hot Magnetic Fibrils: The Slow Continuum Revisited’, *Astrophys. J.* **468**, 907.
- Keys, P. H., Morton, R. J., Jess, D. B., Verth, G., Grant, S. D. T., Mathioudakis, M., Mackay, D. H., Doyle, J. G., Christian, D. J., Keenan, F. P. & Erdélyi, R. (2018), ‘Photospheric Observations of Surface and Body Modes in Solar Magnetic Pores’, *Astrophys. J.* **857**(1), 28.
- Klimchuk, J. A. (2006), ‘On Solving the Coronal Heating Problem’, *Solar Phys.* **234**(1), 41–77.
- Klimchuk, J. A. (2015), ‘Key aspects of coronal heating’, *Philosophical Transactions of the Royal Society of London Series A* **373**(2042), 20140256–20140256.
- Kukhianidze, V., Zaqarashvili, T. V. & Khutsishvili, E. (2006), ‘Observation of kink waves in solar spicules’, *Astron. Astrophys.* **449**, L35–L38.
- Kuperus, M., Ionson, J. A. & Spicer, D. S. (1981), ‘On the theory of coronal heating mechanisms’, **19**, 7–40.
- Kuridze, D., Morton, R. J., Erdélyi, R., Dorrian, G. D., Mathioudakis, M., Jess, D. B. & Keenan, F. P. (2012), ‘Transverse Oscillations in Chromospheric Mottles’, *Astrophys. J.* **750**, 51.
- Kuridze, D., Zaqarashvili, T. V., Henriques, V., Mathioudakis, M., Keenan, F. P. & Hanslmeier, A. (2016), ‘Kelvin-Helmholtz Instability in Solar Chromospheric Jets: Theory and Observation’, *Astrophys. J.* **830**, 133.
- Li, B., Guo, M.-Z., Yu, H. & Chen, S.-X. (2018), ‘Impulsively Generated Wave Trains in Coronal Structures. II. Effects of Transverse Structuring on Sausage Waves in Pressureless Slabs’, *Astrophys. J.* **855**(1), 53.
- Li, H., Liu, Y. & Vai Tam, K. (2017), ‘Fundamental and Harmonic Oscillations in Neighboring Coronal Loops’, *Astrophys. J.* **842**(2), 99.
- Li, X., Zhang, J., Yang, S., Hou, Y. & Erdélyi, R. (2018), ‘Observing Kelvin-Helmholtz instability in solar blowout jet’, *Scientific Reports* **8**, 8136.
- Lopin, I. & Nagorny, I. (2015a), ‘Fast Waves in Smooth Coronal Slab’, *Astrophys. J.* **801**(1), 23.
- Lopin, I. & Nagorny, I. (2015b), ‘Sausage Waves in Transversely Nonuniform Monolithic Coronal Tubes’, *Astrophys. J.* **810**(2), 87.
- Macnamara, C. K. & Roberts, B. (2011), ‘The period ratio for kink and sausage modes in a magnetic slab’, *Astron. Astrophys.* **526**, A75.
- Magyar, N. & Nakariakov, V. M. (2020), ‘Standing Kink Waves in Sigmoid Solar Coronal Loops: Implications for Coronal Seismology’, *Astrophys. J. Lett.* **894**(2), L23.
- Magyar, N. & Van Doorselaere, T. (2016), ‘Damping of nonlinear standing kink oscillations: a numerical study’, *Astron. Astrophys.* **595**, A81.

- Mather, J. F. & Erdélyi, R. (2016), ‘Magneto-Acoustic Waves in a Gravitationally Stratified Magnetized Plasma: Eigen-Solutions and their Applications to the Solar Atmosphere’, *Astrophys. J.* **822**, 116.
- Mathioudakis, M., Jess, D. B. & Erdélyi, R. (2013), ‘Alfvén Waves in the Solar Atmosphere. From Theory to Observations’, *Space Sci. Rev.* **175**, 1–27.
- Mei, Z. X., Keppens, R., Roussev, I. I. & Lin, J. (2018), ‘Parametric study on kink instabilities of twisted magnetic flux ropes in the solar atmosphere’, *Astron. Astrophys.* **609**, A2.
- Moll, R., Cameron, R. H. & Schüssler, M. (2012), ‘Vortices, shocks, and heating in the solar photosphere: effect of a magnetic field’, *Astron. Astrophys.* **541**, A68.
- Morton, R. J., Erdélyi, R., Jess, D. B. & Mathioudakis, M. (2011), ‘Observations of Sausage Modes in Magnetic Pores’, *Astrophys. J. Lett.* **729**, L18.
- Morton, R. J., Tomczyk, S. & Pinto, R. (2015), ‘Investigating Alfvénic wave propagation in coronal open-field regions’, *Nature Communications* **6**, 7813.
- Morton, R. J., Verth, G., Fedun, V., Shelyag, S. & Erdélyi, R. (2013), ‘Evidence for the Photospheric Excitation of Incompressible Chromospheric Waves’, *Astrophys. J.* **768**(1), 17.
- Morton, R. J., Verth, G., Jess, D. B., Kuridze, D., Ruderman, M. S., Mathioudakis, M. & Erdélyi, R. (2012), ‘Observations of ubiquitous compressive waves in the Sun’s chromosphere’, *Nature Communications* **3**, 1315.
- Morton, R. J., Weberg, M. J. & McLaughlin, J. A. (2019), ‘A basal contribution from p-modes to the Alfvénic wave flux in the Sun’s corona’, *Nature Astronomy* **3**, 223.
- Nakariakov, V. M., Ofman, L., Deluca, E. E., Roberts, B. & Davila, J. M. (1999), ‘TRACE observation of damped coronal loop oscillations: Implications for coronal heating’, *Science* **285**, 862–864.
- Nakariakov, V. M. & Roberts, B. (1995*a*), ‘Magnetosonic Waves in Structured Atmospheres with Steady Flows, I’, *Solar Phys.* **159**, 213–228.
- Nakariakov, V. M. & Roberts, B. (1995*b*), ‘On Fast Magnetosonic Coronal Pulsations’, *Solar Phys.* **159**(2), 399–402.
- Nakariakov, V. M. & Verwichte, E. (2005), ‘Coronal Waves and Oscillations’, *Living Reviews in Solar Physics* **2**, 3.
- Naqvi, K. R. & Brown, W. B. (1972), ‘The non-crossing rule in molecular quantum mechanics’, *International Journal of Quantum Chemistry* **6**(2), 271–279.
- Novotny, L. (2010), ‘Strong coupling, energy splitting, and level crossings: A classical perspective’, *American Journal of Physics* **78**, 1199–1202.
- Ofman, L. & Aschwanden, M. J. (2002), ‘Damping Time Scaling of Coronal Loop Oscillations Deduced from Transition Region and Coronal Explorer Observations’, *Astrophys. J. Lett.* **576**(2), L153–L156.
- Okamoto, T. J. & De Pontieu, B. (2011), ‘Propagating Waves Along Spicules’, *Astrophys. J. Lett.* **736**(2), L24.

- Oliver, R., Ballester, J. L., Hood, A. W. & Priest, E. R. (1993), ‘Magnetohydrodynamic waves in a potential coronal arcade’, *Astron. Astrophys.* **273**, 647.
- Orszag, S. A. & Kells, L. C. (1980), ‘Transition to turbulence in plane Poiseuille and plane Couette flow’, *Journal of Fluid Mechanics* **96**, 159–205.
- Pagano, P., De Moortel, I. & Morton, R. J. (2020), ‘Effect of coronal loop structure on wave heating through phase mixing’, *Astron. Astrophys.* **643**, A73.
- Pascoe, D. J., Nakariakov, V. M., Arber, T. D. & Murawski, K. (2009), ‘Sausage oscillations in loops with a non-uniform cross-section’, *Astron. Astrophys.* **494**(3), 1119–1125.
- Pereira, T. M., De Pontieu, B. & Carlsson, M. (2011), Quantifying spicules, *in* ‘AGU Fall Meeting Abstracts’, Vol. 2011, pp. SH34B–01.
- Pietarila, A., Aznar Cuadrado, R., Hirzberger, J. & Solanki, S. K. (2011), ‘Kink Waves in an Active Region Dynamic Fibril’, *Astrophys. J.* **739**, 92.
- Pinter, B., Cadez, V. M. & Goossens, M. (1998), ‘MHD eigenmodes in a semi-infinite structured solar atmosphere’, *Astron. Astrophys.* **332**, 775–785.
- Pintér, B. & Goossens, M. (1999), ‘Oscillations in a magnetic solar model. I. Parallel propagation in a chromospheric and coronal magnetic field with constant Alfvén speed’, *Astron. Astrophys.* **347**, 321–334.
- Powell, M. J. D. (1964), ‘An efficient method for finding the minimum of a function of several variables without calculating derivatives’, *The Computer Journal* **7**(2), 155–162.
URL: <https://doi.org/10.1093/comjnl/7.2.155>
- Priest, E. R. (1984), *Solar magneto-hydrodynamics*, Cambridge University Press.
- Priest, E. R. (2014), *Magnetohydrodynamics of the Sun*, Cambridge University Press.
- Rast, M. P., Bello González, N., Bellot Rubio, L., Cao, W., Cauzzi, G., Deluca, E., de Pontieu, B., Fletcher, L., Gibson, S. E., Judge, P. G., Katsukawa, Y., Kazachenko, M. D., Khomenko, E., Landi, E., Martínez Pillet, V., Petrie, G. J. D., Qiu, J., Rachmeler, L. A., Rempel, M., Schmidt, W., Scullion, E., Sun, X., Welsch, B. T., Andretta, V., Antolin, P., Ayres, T. R., Balasubramaniam, K. S., Ballai, I., Berger, T. E., Bradshaw, S. J., Campbell, R. J., Carlsson, M., Casini, R., Centeno, R., Cranmer, S. R., Criscuoli, S., Deforest, C., Deng, Y., Erdélyi, R., Fedun, V., Fischer, C. E., González Manrique, S. J., Hahn, M., Harra, L., Henriques, V. M. J., Hurlburt, N. E., Jaeggli, S., Jafarzadeh, S., Jain, R., Jefferies, S. M., Keys, P. H., Kowalski, A. F., Kuckein, C., Kuhn, J. R., Kuridze, D., Liu, J., Liu, W., Longcope, D., Mathioudakis, M., McAteer, R. T. J., McIntosh, S. W., McKenzie, D. E., Miralles, M. P., Morton, R. J., Muglach, K., Nelson, C. J., Panesar, N. K., Parenti, S., Parnell, C. E., Poduval, B., Reardon, K. P., Reep, J. W., Schad, T. A., Schmit, D., Sharma, R., Socas-Navarro, H., Srivastava, A. K., Sterling, A. C., Suematsu, Y., Tarr, L. A., Tiwari, S., Tritzschler, A., Verth, G., Vourlidas, A., Wang, H., Wang, Y.-M., NSO and DKIST Project, DKIST Instrument Scientists, DKIST Science Working Group & DKIST Critical Science Plan Community (2021), ‘Critical Science Plan for the Daniel K. Inouye Solar Telescope (DKIST)’, *Solar Phys.* **296**(4), 70.
- Rayleigh, L. (1879), ‘On the stability, or instability, of certain fluid motions’, *Proceedings of the London Mathematical Society* **s1-11**(1), 57–72.
URL: <https://londmathsoc.onlinelibrary.wiley.com/doi/abs/10.1112/plms/s1-11.1.57>

- Roberts, B. (1981a), ‘Wave Propagation in a Magnetically Structured Atmosphere - Part Two - Waves in a Magnetic Slab’, *Solar Phys.* **69**, 39–56.
- Roberts, B. (1981b), ‘Wave propagation in a magnetically structured atmosphere. I - Surface waves at a magnetic interface.’, *Solar Phys.* **69**, 27–38.
- Roberts, B. (2019), *MHD Waves in the Solar Atmosphere*, Cambridge University Press.
- Roupe van der Voort, L., Bellot Rubio, L. R. & Ortiz, A. (2010), ‘Upflows in the Central Dark Lane of Sunspot Light Bridges’, *Astrophys. J. Lett.* **718**(2), L78–L82.
- Roupe van der Voort, L., Leenaarts, J., de Pontieu, B., Carlsson, M. & Vissers, G. (2009), ‘On-disk Counterparts of Type II Spicules in the Ca II 854.2 nm and H α Lines’, *Astrophys. J.* **705**, 272–284.
- Ruderman, M. S. (2007), ‘Nonaxisymmetric Oscillations of Thin Twisted Magnetic Tubes’, *Solar Phys.* **246**(1), 119–131.
- Ruderman, M. S., Berghmans, D., Goossens, M. & Poedts, S. (1997), ‘Direct excitation of resonant torsional Alfvén waves by footpoint motions.’, *Astron. Astrophys.* **320**, 305–318.
- Ruderman, M. S. & Erdélyi, R. (2009), ‘Transverse Oscillations of Coronal Loops’, *Space Sci. Rev.* **149**(1-4), 199–228.
- Ruderman, M. S. & Roberts, B. (2002), ‘The Damping of Coronal Loop Oscillations’, *Astrophys. J.* **577**(1), 475–486.
- Sakurai, T., Goossens, M. & Hollweg, J. V. (1991), ‘Resonant Behaviour of Magnetohydrodynamic Waves on Magnetic Flux Tubes - Part One’, *Solar Phys.* **133**(2), 227–245.
- Schwarzschild, M. (1948), ‘On Noise Arising from the Solar Granulation.’, *Astrophys. J.* **107**, 1.
- Scullion, E., Erdélyi, R., Fedun, V. & Doyle, J. G. (2011), ‘The Response of A Three-dimensional Solar Atmosphere to Wave-driven Jets’, *Astrophys. J.* **743**, 14.
- Sedláček, Z. (1971), ‘Electrostatic oscillations in cold inhomogeneous plasma I. Differential equation approach’, *Journal of Plasma Physics* **5**(2), 239–263.
- Sekse, D. H., Roupe van der Voort, L., De Pontieu, B. & Scullion, E. (2013), ‘Interplay of Three Kinds of Motion in the Disk Counterpart of Type II Spicules: Upflow, Transversal, and Torsional Motions’, *Astrophys. J.* **769**, 44.
- Sharma, R., Verth, G. & Erdélyi, R. (2017), ‘Dynamic Behavior of Spicules Inferred from Perpendicular Velocity Components’, *Astrophys. J.* **840**, 96.
- Sharma, R., Verth, G. & Erdélyi, R. (2018), ‘Evolution of complex 3d motions in spicules’, *The Astrophysical Journal* **853**(1), 61.
- Shelyag, S., Cally, P. S., Reid, A. & Mathioudakis, M. (2013), ‘Alfvén Waves in Simulations of Solar Photospheric Vortices’, *Astrophys. J. Lett.* **776**(1), L4.
- Shelyag, S., Fedun, V., Keenan, F. P., Erdélyi, R. & Mathioudakis, M. (2011), ‘Photospheric magnetic vortex structures’, *Annales Geophysicae* **29**, 883–887.

- Shelyag, S., Mathioudakis, M. & Keenan, F. P. (2012), ‘Mechanisms for MHD Poynting Flux Generation in Simulations of Solar Photospheric Magnetoconvection’, *Astrophys. J. Lett.* **753**(1), L22.
- Silva, S. S. A., Fedun, V., Verth, G., Rempel, E. L. & Shelyag, S. (2020), ‘Solar Vortex Tubes: Vortex Dynamics in the Solar Atmosphere’, *Astrophys. J.* **898**(2), 137.
- Silva, S. S. A., Verth, G., Rempel, E. L., Shelyag, S., Schiavo, L. A. C. A. & Fedun, V. (2021), ‘Solar Vortex Tubes. II. On the Origin of Magnetic Vortices’, *Astrophys. J.* **915**(1), 24.
- Skirvin, S. J., Fedun, V., Silva, S. S. A. & Verth, G. (2022), ‘II. The effect of axisymmetric and spatially varying equilibria and flow on MHD wave modes: cylindrical geometry’, *Monthly Notices of the Royal Astronomical Society* **510**(2), 2689–2706.
- Skirvin, S. J., Fedun, V. & Verth, G. (2021), ‘I. The effect of symmetric and spatially varying equilibria and flow on MHD wave modes: slab geometry’, *Monthly Notices of the Royal Astronomical Society* **504**(3), 4077–4092.
- Snow, B., Fedun, V., Gent, F. A., Verth, G. & Erdélyi, R. (2018), ‘Magnetic Shocks and Substructures Excited by Torsional Alfvén Wave Interactions in Merging Expanding Flux Tubes’, *Astrophys. J.* **857**, 125.
- Sobotka, M., Švanda, M., Jurčák, J., Heinzel, P., Del Moro, D. & Berrilli, F. (2013), ‘Dynamics of the solar atmosphere above a pore with a light bridge’, *Astron. Astrophys.* **560**, A84.
- Soler, R. (2017), ‘Fluting Modes in Transversely Nonuniform Solar Flux Tubes’, *Astrophys. J.* **850**(2), 114.
- Soler, R. (2019), ‘Transverse waves in coronal flux tubes with thick boundaries: The effect of longitudinal flows’, *Astron. Astrophys.* **623**, A32.
- Soler, R., Goossens, M., Terradas, J. & Oliver, R. (2013), ‘The Behavior of Transverse Waves in Nonuniform Solar Flux Tubes. I. Comparison of Ideal and Resistive Results’, *Astrophys. J.* **777**(2), 158.
- Soler, R. & Terradas, J. (2015), ‘Magnetohydrodynamic Kink Waves in Nonuniform Solar Flux Tubes: Phase Mixing and Energy Cascade to Small Scales’, *Astrophys. J.* **803**(1), 43.
- Soler, R., Terradas, J., Oliver, R. & Ballester, J. L. (2017), ‘Propagation of Torsional Alfvén Waves from the Photosphere to the Corona: Reflection, Transmission, and Heating in Expanding Flux Tubes’, *Astrophys. J.* **840**(1), 20.
- Soler, R., Terradas, J., Oliver, R., Ballester, J. L. & Goossens, M. (2010), ‘Kelvin-Helmholtz Instability in Coronal Magnetic Flux Tubes due to Azimuthal Shear Flows’, *Astrophys. J.* **712**, 875–882.
- Spruit, H. C. (1982), ‘Propagation Speeds and Acoustic Damping of Waves in Magnetic Flux Tubes’, *Solar Phys.* **75**(1-2), 3–17.
- Spruit, H. C. & Zweibel, E. G. (1979), ‘Convective instability of thin flux tubes.’, *Solar Phys.* **62**(1), 15–22.

- Srivastava, A. K., Ballester, J. L., Cally, P. S., Carlsson, M., Goossens, M., Jess, D. B., Khomenko, E., Mathioudakis, M., Murawski, K. & Zaqarashvili, T. V. (2021), ‘Chromospheric Heating by Magnetohydrodynamic Waves and Instabilities’, *Journal of Geophysical Research (Space Physics)* **126**(6), e029097.
- Srivastava, A. K., Shetye, J., Murawski, K., Doyle, J. G., Stangalini, M., Scullion, E., Ray, T., Wójcik, D. P. & Dwivedi, B. N. (2017), ‘High-frequency torsional Alfvén waves as an energy source for coronal heating’, *Scientific Reports* **7**, 43147.
- Stenuit, H., Keppens, R. & Goossens, M. (1998), ‘Eigenfrequencies and optimal driving frequencies of 1D non-uniform magnetic flux tubes’, *Astron. Astrophys.* **331**, 392–404.
- Stenuit, H., Tirry, W. J., Keppens, R. & Goossens, M. (1999), ‘Leaky and resonantly damped flux tube modes reconsidered’, *Astron. Astrophys.* **342**, 863–866.
- Taroyan, Y. & Erdélyi, R. (2002), ‘Resonant and Kelvin-Helmholtz instabilities on the magnetopause’, *Physics of Plasmas* **9**(7), 3121–3129.
- Taroyan, Y. & Erdélyi, R. (2003), ‘Resonant surface waves and instabilities in finite β plasmas’, *Physics of Plasmas* **10**(1), 266–276.
- Tavabi, E., Koutchmy, S. & Golub, L. (2015), ‘Limb Event Brightenings and Fast Ejection Using IRIS Mission Observations’, *Solar Phys.* **290**, 2871–2887.
- Terra-Homem, M., Erdélyi, R. & Ballai, I. (2003), ‘Linear and non-linear MHD wave propagation in steady-state magnetic cylinders’, *Solar Phys.* **217**(2), 199–223.
- Terradas, J., Andries, J., Goossens, M., Arregui, I., Oliver, R. & Ballester, J. L. (2008), ‘Nonlinear Instability of Kink Oscillations due to Shear Motions’, *Astrophys. J. Lett.* **687**(2), L115.
- Terradas, J. & Goossens, M. (2012), ‘Transverse kink oscillations in the presence of twist’, *Astron. Astrophys.* **548**, A112.
- Terradas, J., Magyar, N. & Van Doorselaere, T. (2018), ‘Effect of Magnetic Twist on Nonlinear Transverse Kink Oscillations of Line-tied Magnetic Flux Tubes’, *Astrophys. J.* **853**(1), 35.
- Thackray, H. & Jain, R. (2017), ‘Fast magnetohydrodynamic waves in a solar coronal arcade’, *Astron. Astrophys.* **608**, A108.
- Timofeev, A. V. (2000), *Resonance Phenomena in Plasma Oscillations*.
- Tirry, W. J. & Goossens, M. (1996), ‘Quasi-Modes as Dissipative Magnetohydrodynamic Eigenmodes: Results for One-dimensional Equilibrium States’, *Astrophys. J.* **471**, 501.
- Tomczyk, S., McIntosh, S. W., Keil, S. L., Judge, P. G., Schad, T., Seeley, D. H. & Edmondson, J. (2007), ‘Alfvén Waves in the Solar Corona’, *Science* **317**, 1192.
- Tsap, Y., Fedun, V., Cheremnykh, O., Stepanov, A., Kryshchal, A. & Kopylova, Y. (2020), ‘On the Stabilization of a Twisted Magnetic Flux Tube’, *Astrophys. J.* **901**(2), 99.
- Tziotziou, K., Tsiropoula, G., Kontogiannis, I., Scullion, E. & Doyle, J. G. (2018), ‘A persistent quiet-Sun small-scale tornado. I. Characteristics and dynamics’, *Astron. Astrophys.* **618**, A51.

- Van Doorselaere, T., Andries, J., Poedts, S. & Goossens, M. (2004), ‘Damping of Coronal Loop Oscillations: Calculation of Resonantly Damped Kink Oscillations of One-dimensional Nonuniform Loops’, *Astrophys. J.* **606**(2), 1223–1232.
- Van Doorselaere, T., Goossens, M., Magyar, N., Ruderman, M. S. & Ismayilli, R. (2021), ‘Non-linear Damping of Standing Kink Waves Computed With Elsässer Variables’, *Astrophys. J.* **910**(1), 58.
- Van Doorselaere, T., Nakariakov, V. M. & Verwichte, E. (2008), ‘Detection of Waves in the Solar Corona: Kink or Alfvén?’, *Astrophys. J. Lett.* **676**(1), L73.
- Van Doorselaere, T., Srivastava, A. K., Antolin, P., Magyar, N., Vasheghani Farahani, S., Tian, H., Kolotkov, D., Ofman, L., Guo, M., Arregui, I., De Moortel, I. & Pascoe, D. (2020), ‘Coronal Heating by MHD Waves’, *Space Sci. Rev.* **216**(8), 140.
- Van Doorselaere, T., Verwichte, E. & Terradas, J. (2009), ‘The Effect of Loop Curvature on Coronal Loop Kink Oscillations’, *Space Sci. Rev.* **149**(1-4), 299–324.
- Vásconez, C. L., Pucci, F., Valentini, F., Servidio, S., Matthaeus, W. H. & Malara, F. (2015), ‘Kinetic Alfvén Wave Generation by Large-scale Phase Mixing’, *Astrophys. J.* **815**(1), 7.
- Verth, G. & Jess, D. B. (2016), ‘MHD Wave Modes Resolved in Fine-Scale Chromospheric Magnetic Structures’, *Washington DC American Geophysical Union Geophysical Monograph Series* **216**, 431–448.
- Verth, G., Van Doorselaere, T., Erdélyi, R. & Goossens, M. (2007), ‘Spatial magneto-seismology: effect of density stratification on the first harmonic amplitude profile of transversal coronal loop oscillations’, *Astron. Astrophys.* **475**(1), 341–348.
- Verwichte, E., Foullon, C. & Nakariakov, V. M. (2006a), ‘Fast magnetoacoustic waves in curved coronal loops’, *Astron. Astrophys.* **446**(3), 1139–1149.
- Verwichte, E., Foullon, C. & Nakariakov, V. M. (2006b), ‘Fast magnetoacoustic waves in curved coronal loops. II. Tunneling modes’, *Astron. Astrophys.* **449**(2), 769–779.
- Verwichte, E., Foullon, C. & Nakariakov, V. M. (2006c), ‘Seismology of curved coronal loops with vertically polarised transverse oscillations’, *Astron. Astrophys.* **452**(2), 615–622.
- Verwichte, E., Haynes, M., Arber, T. D. & Brady, C. S. (2008), ‘Damping of Slow MHD Coronal Loop Oscillations by Shocks’, *Astrophys. J.* **685**(2), 1286–1290.
- Vigeesh, G., Fedun, V., Hasan, S. S. & Erdélyi, R. (2012), ‘Three-dimensional Simulations of Magnetohydrodynamic Waves in Magnetized Solar Atmosphere’, *Astrophys. J.* **755**(1), 18.
- Voitenko, Y. & Goossens, M. (2002), ‘Nonlinear excitation of small-scale Alfvén waves by fast waves and plasma heating in the solar atmosphere’, *Solar Phys.* **209**(1), 37–60.
- Voitenko, Y. & Goossens, M. (2004), ‘Cross-Field Heating of Coronal Ions by Low-Frequency Kinetic Alfvén Waves’, *Astrophys. J. Lett.* **605**(2), L149–L152.
- Walsh, R. W. & Ireland, J. (2003), ‘The heating of the solar corona’, *Astron. Astrophys. Rev.* **12**(1), 1–41.

- Wedemeyer-Böhm, S., Scullion, E., Steiner, O., Rouppe van der Voort, L., de La Cruz Rodriguez, J., Fedun, V. & Erdélyi, R. (2012), ‘Magnetic tornadoes as energy channels into the solar corona’, *Nature* **486**(7404), 505–508.
- Wentzel, D. G. (1979), ‘Hydromagnetic surface waves on cylindrical fluxtubes.’, *Astron. Astrophys.* **76**(1), 20–23.
- Williams, T., Walsh, R. W., Peter, H. & Winebarger, A. R. (2020), ‘Evidence for and Analysis of Multiple Hidden Coronal Strands in Cross-sectional Emission Profiles: Further Results from NASA’s High-resolution Solar Coronal Imager’, *Astrophys. J.* **902**(2), 90.
- Wilson, P. R. (1979), ‘Hydromagnetic wave modes in magnetic flux tubes.’, *Astron. Astrophys.* **71**(1-2), 9–13.
- Wilson, P. R. (1980), ‘The general dispersion relation for the vibration modes of magnetic flux tubes’, *Astron. Astrophys.* **87**(1-2), 121–125.
- Wilson, P. R. (1981), ‘Free and forced oscillations of a flux tube’, *Astrophys. J.* **251**, 756–767.
- Withbroe, G. L. & Noyes, R. W. (1977), ‘Mass and energy flow in the solar chromosphere and corona.’, *Annual Review of Astronomy and Astrophysics* **15**, 363–387.
- Yadav, N., Cameron, R. H. & Solanki, S. K. (2020), ‘Simulations Show that Vortex Flows Could Heat the Chromosphere in Solar Plage’, *Astrophys. J. Lett.* **894**(2), L17.
- Yadav, N., Cameron, R. H. & Solanki, S. K. (2021), ‘Vortex flow properties in simulations of solar plage region: Evidence for their role in chromospheric heating’, *Astron. Astrophys.* **645**, A3.
- Yu, D. J., Van Doorselaere, T. & Goossens, M. (2017*a*), ‘Resonant Absorption of Surface Sausage and Surface Kink Modes under Photospheric Conditions’, *Astrophys. J.* **850**(1), 44.
- Yu, D. J., Van Doorselaere, T. & Goossens, M. (2017*b*), ‘Resonant absorption of the slow sausage wave in the slow continuum’, *Astron. Astrophys.* **602**, A108.
- Yu, H., Li, B., Chen, S. & Guo, M. (2021), ‘Resonant Damping of Kink Modes in Solar Coronal Slabs’, *Solar Phys.* **296**(6), 95.
- Zajtsev, V. V. & Stepanov, A. V. (1975), ‘On the origin of pulsations of type IV solar radio emission. Plasma cylinder oscillations (I).’, *Issledovaniia Geomagnetizmu Aeronomii i Fizike Solntsa* **37**, 3–10.
- Zaqarashvili, T. V. (2011), Solar Spicules: Recent Challenges in Observations and Theory, in I. Zhelyazkov & T. Mishonov, eds, ‘American Institute of Physics Conference Series’, Vol. 1356 of *American Institute of Physics Conference Series*, pp. 106–116.
- Zaqarashvili, T. V., Zhelyazkov, I. & Ofman, L. (2015), ‘Stability of Rotating Magnetized Jets in the Solar Atmosphere. I. Kelvin-Helmholtz Instability’, *Astrophys. J.* **813**, 123.
- Zhelyazkov, I. (2012), ‘Magnetohydrodynamic waves and their stability status in solar spicules’, *Astron. Astrophys.* **537**, A124.
- Zhelyazkov, I. (2013), Kelvin-Helmholtz instability of kink waves in photospheric, chromospheric, and X-ray solar jets, in I. Zhelyazkov & T. M. Mishonov, eds, ‘American Institute of Physics Conference Series’, Vol. 1551 of *American Institute of Physics Conference Series*, pp. 150–164.

Zhelyazkov, I. & Chandra, R. (2019), ‘Can High-Mode Magnetohydrodynamic Waves Propagating in a Spinning Macrospicule Be Unstable Due to the Kelvin-Helmholtz Instability?’, *Solar Phys.* **294**(2), 20.

Zirker, J. B. (1993), ‘Coronal Heating’, *Solar Phys.* **148**(1), 43–60.

Appendices

Appendix A

Derivation of governing equation for a non-uniform flow in a magnetic slab

Here we will derive the governing differential equation for horizontal velocity perturbation \hat{v}_x in a magnetic slab with a non-uniform vertical background plasma flow in the form $U_{0i}(x)$

First start from the linearised ideal MHD Equations (1.7)-(1.10):

$$\frac{\partial \rho_1}{\partial t} + \rho_0(\nabla \cdot \mathbf{v}_1) + \rho_1(\nabla \cdot \mathbf{v}_0) = 0, \quad (\text{A.1})$$

$$\rho_0 \frac{\partial \mathbf{v}_1}{\partial t} = -\nabla p_1 + \frac{1}{\mu}(\nabla \times \mathbf{B}_1) \times \mathbf{B}_0, \quad (\text{A.2})$$

$$\frac{\partial p_1}{\partial t} - c_0^2 \frac{\partial \rho_1}{\partial t} = 0, \quad (\text{A.3})$$

$$\frac{\partial \mathbf{B}_1}{\partial t} = \nabla \times (\mathbf{v}_1 \times \mathbf{B}_0) + \nabla \times (\mathbf{v}_0 \times \mathbf{B}_1). \quad (\text{A.4})$$

Seeking wave-like solutions where each perturbed variable (denoted subscript 1) is put proportional to $\exp(ikz - i\omega t)$ yields:

$$-i\Omega(x)\hat{\rho}_1 + \rho_0(\hat{v}'_x + ik\hat{v}_z) = 0, \quad (\text{A.5})$$

$$-i\rho_0\Omega(x)\hat{v}_x = -\hat{P}'_1 + \frac{B_0}{\mu_0}(ik\hat{B}_x - \hat{B}'_z), \quad (\text{A.6})$$

$$-i\rho_0\Omega(x)\hat{v}_z + \rho_0 U'_{0i}(x)\hat{v}_x = -ik\hat{P}_1, \quad (\text{A.7})$$

$$-i\Omega(x)\hat{P}_1 + c_0^2\rho_0(\hat{v}'_x + ik\hat{v}_z) = 0, \quad (\text{A.8})$$

$$-i\Omega(x)\hat{B}_x = ikB_0\hat{v}_x, \quad (\text{A.9})$$

$$-i\Omega(x)\hat{B}_z = \hat{B}_x U'_{0i}(x) - B_0\hat{v}'_x, \quad (\text{A.10})$$

where $\Omega(x) = \omega - kU_{0i}(x)$ is discussed in the text and a prime denotes a differential with respect to spatial coordinate x . Combining Equations (A.9) and (A.10) isolates \hat{B}_z :

$$\hat{B}_z = -iB_0 \left(\frac{\hat{v}'_x}{\Omega(x)} - \frac{\Omega'(x)}{\Omega^2(x)}\hat{v}_x \right), \quad (\text{A.11})$$

and Equation (A.11) can be differentiated with respect to spatial coordinate x to yield:

$$\hat{B}'_z = \frac{-iB_0}{\Omega^2(x)} \left[\Omega(x)\hat{v}''_x - \Omega''(x)\hat{v}_x - 2\Omega'(x)\hat{v}'_x + 2\frac{(\Omega'(x))^2}{\Omega(x)}\hat{v}_x \right]. \quad (\text{A.12})$$

Substituting Equation (A.12) into Equation (A.6) and multiplying the resulting expression by $i\Omega(x)$ after dividing the expression by ρ_0 yields:

$$\begin{aligned} \Omega^2(x)\hat{v}_x = & \frac{c^2}{[\Omega^2(x) - k^2c^2]} \left[\Omega''(x)\Omega(x)\hat{v}_x - \frac{2(\Omega'(x))^2\Omega^2(x)}{[\Omega^2(x) - k^2c^2]}\hat{v}_x - \Omega^2(x)\hat{v}_x'' + \frac{2\Omega^3(x)\Omega'(x)}{[\Omega^2(x) - k^2c^2]}\hat{v}_x' \right] + \\ & + v_A^2 \left(k^2\hat{v}_x - \frac{1}{\Omega(x)} \left[\Omega(x)\hat{v}_x'' - 2\Omega'(x)\hat{v}_x' - \Omega''(x)\hat{v}_x + \frac{2(\Omega'(x))^2}{\Omega(x)}\hat{v}_x \right] \right). \end{aligned} \quad (\text{A.13})$$

Using Equation (A.13) it is possible to now collect the coefficients of \hat{v}_x'' , \hat{v}_x' and \hat{v}_x separately. Introducing a new variable $m_0^2(x)$ which can be written as:

$$m_0^2(x) = \frac{[k^2v_A^2 - \Omega^2(x)][k^2c^2 - \Omega^2(x)]}{(c^2 + v_A^2)[k^2c_T^2 - \Omega^2(x)]}, \quad (\text{A.14})$$

the coefficients become:

$$\hat{v}_x'' : (c^2 + v_A^2) (\Omega^2(x) - k^2c_T^2), \quad (\text{A.15})$$

$$\hat{v}_x' : \frac{2\Omega'(x)}{\Omega(x)} \left[\frac{c^2\Omega^4(x)}{[\Omega^2(x) - k^2c^2]} + v_A^2 [\Omega^2(x) - k^2c^2] \right], \quad (\text{A.16})$$

$$\begin{aligned} \hat{v}_x : & \frac{\Omega''(x)}{\Omega(x)} (c^2 + v_A^2) (\Omega^2(x) - k^2c_T^2) - \frac{2(\Omega'(x))^2}{\Omega^2(x)} \left[\frac{\Omega^2(x) [\Omega^2(x) - k^2v_A^2]}{m_0^2} - k^2c^2v_A^2 \right] - \\ & - (\Omega^2(x) - k^2c^2) (\Omega^2(x) - k^2v_A^2). \end{aligned} \quad (\text{A.17})$$

Dividing all Equations (A.15)-(A.17) by the factor $(c^2 + v_A^2) (\Omega^2(x) - k^2c_T^2)$ such that the coefficient of the largest derivative is equal to 1 yields the governing equation:

$$\hat{v}_x'' + D(x)\hat{v}_x' + \left[-\frac{\Omega''(x)}{\Omega(x)} - \frac{\Omega'(x)}{\Omega(x)}D(x) - m_0^2(x) \right] \hat{v}_x = 0, \quad (\text{A.18})$$

with,

$$D(x) = \frac{2\Omega'(x)}{\Omega(x)} \left[\frac{\Omega^2(x)}{\Omega_c^2(x)} - \frac{k^2c_T^2}{\Omega_T^2(x)} \right]. \quad (\text{A.19})$$

Given that the non-uniform flow is taken inside the waveguide, the parameters in this expression can be sub-scripted by i .